Cranfield University

Sebastiano Sorato

Methodology to analyse three dimensional droplet dispersion applicable to Icing Wind Tunnels

School of Engineering

PhD

Cranfield University

School of Engineering

PhD Thesis

2009

Sebastiano Sorato

Methodology to analyse three dimensional droplet dispersion applicable to Icing Wind Tunnels

Supervisor: David Hammond

Academic Year 2006 to 2009

This thesis is submitted in partial fulfilment of the requirements for the degree of Doctor of Philosophy

© Cranfield University, 2009. All rights reserved. No part of this publication may be reproduced without the written permission of the copyright holder.

ABSTRACT

This dissertation presents a methodology to simulate the dispersion of water droplets in the air flow typical of an Icing Tunnel. It is based on the understanding the physical parameters that influence the uniformity and the distribution of cloud of droplets in the airflow and to connect them with analytical parameters which may be used to describe the dispersion process. Specifically it investigates the main geometrical and physical parameters contributing to the droplets dispersion at different tunnel operative conditions, finding a consistent numerical approach to reproduce the local droplets dynamic, quantifying the possible limits of commercial CFD methods, pulling out the empirical parameters/constant needing to simulate properly the local conditions and validating the results with calibrated experiment.

An overview of the turbulence and multiphase flow theories, considered relevant to the Icing Tunnel environment, is presented as well as basic concepts and terminology of particle dispersion. Taylor's theory of particle dispersion has been taken as starting point to explain further historical development of discrete phase dispersion. Common methods incorporated in commercial CFD software are explained and relative shortcomings underlined. The local aerodynamic condition within tunnel, which are required to perform the calculation with the Lagrangian particle equation of motions, are generated numerically using different turbulent models and are compared to the historical K-ε model. Verification of the calculation is performed with grid independency studies. Stochastic Separated Flow methods are applied to compute the particle trajectories. The Discrete Random Walk, as described in the literature, has been used to perform particle dispersion analysis. Numerical settings in the code are related to the characteristics of the local turbulent condition such as turbulence intensity and length scales.

In order to acquire turbulence data, at different tunnel operating conditions, to be used as input boundary condition for the numerical solver, hot wire probe measurements have been performed. After presenting instrumentation and method details, turbulent

statistics results and relative uncertainties are discussed, underlying the connection with Lagrangian dispersion models. Measured turbulence profiles are used to define boundary input conditions for CFD simulations. The choice of the input plane location referred to the position of the spray bars is discussed concerning the conditions of near-nozzle-field and far-nozzle-field. Evolution of the particle's statistics, as mean and standard deviation, are presented in relation to tunnel geometry and the three dimensional droplets cloud behaviour is shown. Probability density function type results are presented to be compared to the experimental results. The icing blade measurement is used to acquire Liquid Water content distribution in the test section at several tunnel operating conditions in order to provide support and validation to numerical droplets dispersion predictions.

The results are discussed and summarized defining a dispersion indicator related to the shape of the probability density function through the Half Width at Half Maximum value. The droplets dispersion evolution along the tunnel is presented for both the K-ε and Reynolds Stress turbulence models and compared with the experimental measurements. For each turbulence model different type of injection have been tried in order to check the sensitivity of the methodology to different injection characterization. Both the K-ε model and the RSM model provide similar trends of the water droplets distribution along the vertical and horizontal directions in a plane normal to the tunnel axis. The effect of the different nozzle air pressures (different operating conditions) can be caught by the solver and input variance of pressure values of the order of 2%, have reflected, through different turbulence inlet profiles, in final STD differences less than 1% of the test section length. The level of the droplets dispersion prediction is close to the measurement but the trend with the spray bars cannot reproduce the local small effects. The accuracy of the models cannot catch higher gradient of the standard deviation, more than 2% of the test section length. The local differences between the K-ε and RSM models have been estimated and found to be small in comparison to characteristic length of the droplets cloud. Similar results have been found for the different injection types, where local relative differences have been estimated to be on average less than 5% of the "single injection" baseline, which reflect in a difference on cloud spread of about 0.4% of the characteristic test section length.

Keywords:
Lagrangian dispersion, Icing Tunnel, CFD, Discrete phase, Stochastic models

ACKNOWLEDGEMENTS

I would take advantage here to express the gratitude to the people within the department of Power & Propulsion that provided the necessary background for the work on this thesis. I would like to thank my supervisor Dr. David Hammond for the collaboration he offered me during my research and the freedom he granted me to pursue my own ideas. A special thanks is directed to Prof. Pericles Pilidis to have given me the opportunity to begin this valuable experience and to have supported me during the challenging phases of my research.

The years of research spent at Cranfield provided valuable professional and private life experiences with pleasant and though moments, which enrich the memories of life. At the end of the days I did not only receive notions, but teachings that became part of my personal culture, contributing to the development, hopefully in the right direction, of my character. This improvement has also been possible with the presence and support of friends that participated to this experience. A very restricted number of friends, which actively shared with me situations, discussions, thoughts and fun during my years of living in Cranfield. I express my gratitude to all of them (that sure can recognize their names between the lines), hoping to have positively contributed to their experience too.

As final remark, a special thanks to my family that always gave me the freedom and the opportunity to choose the way for my future, just providing the necessary advises when I needed those most.

TABLE OF CONTENTS

TABLE OF FIGURES

TABLE OF TABLES

1 Introduction

1.1 Icing Science overview

The icing phenomenon is a mixing of several physics factors that contribute to the formation of the ice distributed on aircraft parts. This formation is a consequence of the freezing of suspended cloud droplets on airplane structures causing a growth of a specific-shaped ice. The altitudes and temperatures typical of the flight envelop of the modern aircraft mean this phenomenon occurs both to the light and commercial aviation. The effects of the built up of an ice structure on the aircraft surface give rise to unwanted aerodynamic disturbances, usually called “degradation effects”, causing lift losses and control problems when referring to external wings or causing mass flow losses and pressure losses when referring to internal duct and intake systems. In borderline cases, as has sadly happened in the past, they can cause serious accidents.

Particular attention has then been paid to this problem in order to guarantee the safeness of the passenger and the crew involved. The modern aircraft have now to certify their ability to flight under specified maximum atmospheric icing conditions, being equipped with an appropriate anti-icing system and following precise de-icing procedures. The way to specify and quantify these maximum conditions it is still an open position in the icing community, however the Appendix C to Part 25 of the FAR is usually used as reference for the icing conditions envelope. The difficulty of how to characterize the icing envelope in order to give a better concrete support to the development and improvement of the anti-icing system is due to the complexity of the physical phenomena involved and to the wide range of atmospheric flight conditions typically encountered.

The Appendix C to Part 25 actually characterizes two icing envelope referring to different icing intensity associated to the stratified and cumuliform clouds. The envelope refers to the Continuous maximum icing (associated to stratiform clouds) and intermittent maximum icing (associated to cumuliform clouds). The continuous

maximum icing is defined by the variables of the cloud liquid water content (LWC), the mean effective diameter of the cloud droplets, the ambient air temperature, and the interrelationship of these three variables as shown in figure 1-1. The limiting icing envelope in terms of altitude and temperature is given in figure 1-2. The inter-relationship of cloud liquid water content with drop diameter and altitude is determined from figures 1-1 and 1-2. The cloud liquid water content for continuous maximum icing conditions of a horizontal extent, other than 17.4 nautical miles, is determined by the value of liquid water content of figure 1, multiplied by the appropriate factor from figure 1-3. The intermittent maximum icing is similarly characterized with the difference to consider the variables described by the envelope of the figure 1-4 and 1-5 and the horizontal extent, other than 2.6 nautical miles, is determined by the value indicated in figure 1-4, multiplied by the appropriate factor of figure 1-6.

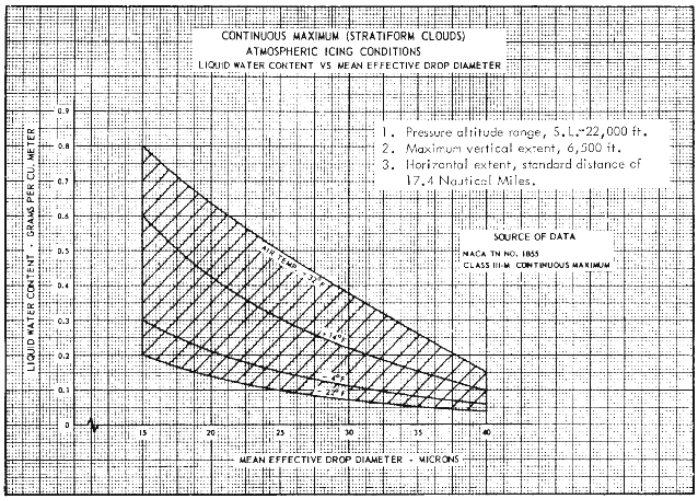

Figure 1-1: LWC vs. drop diameters envelope (Continuous)

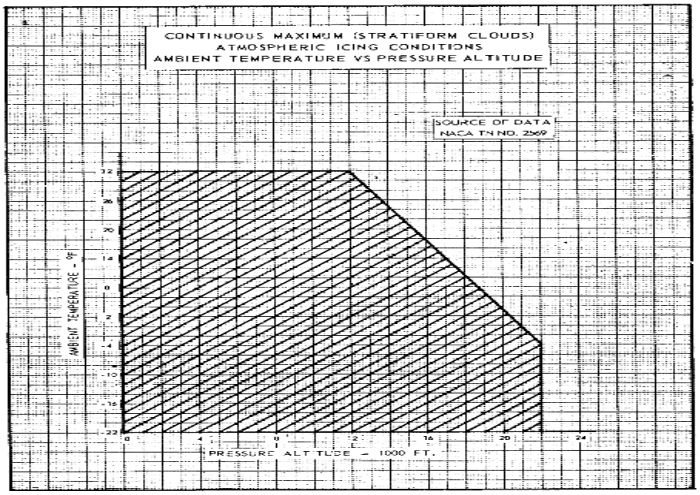

Figure 1-2: Ambient temperature vs. Pressure altitude (Continuous)

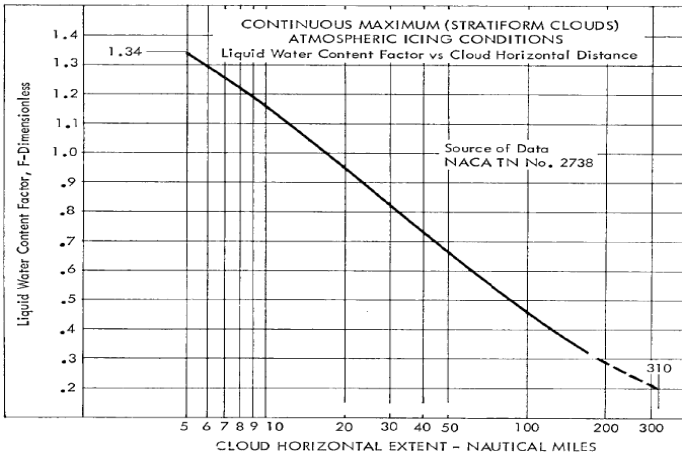

Figure 1-3: LWC factor vs. Cloud horizontal distance (Continuous)

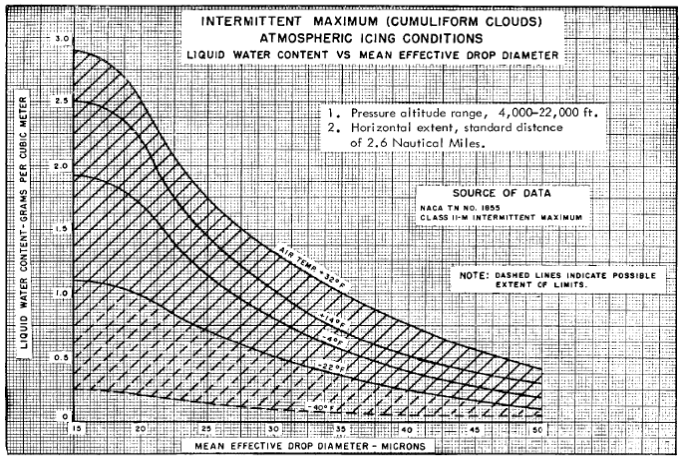

Figure 1-4: LWC vs. drop diameters envelope (Intermittent)

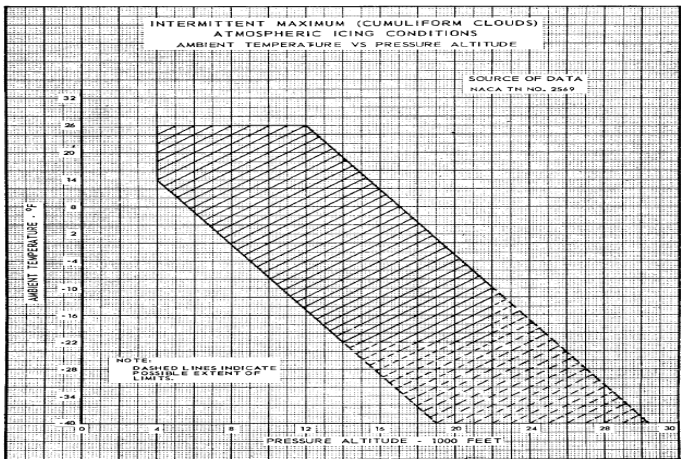

Figure 1-5: Ambient temperature vs. Pressure altitude (Intermittent)

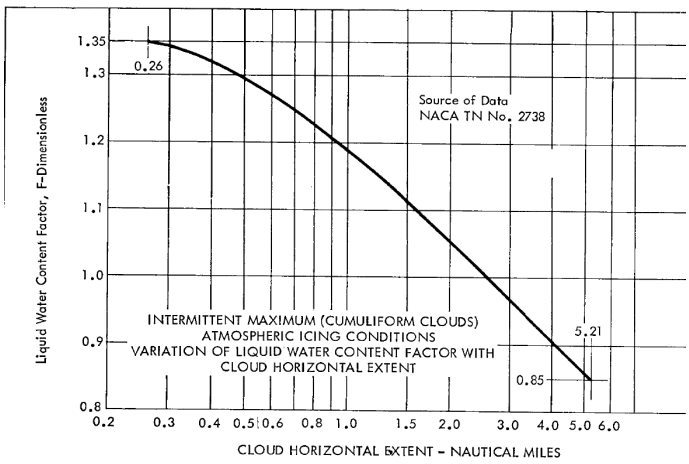

Figure 1-6: LWC factor vs. Cloud horizontal distance (Intermittent)

The variables chosen to define the envelope are also significant for the icing physics phenomena and usually characterize the icing shape, structure and accretion dynamics. The freezing of the water droplet at the impact on the aircraft surface can have different kinetic rate that produce different ice shape and structure. Typically the icing structural types are identified as follows:

- Glaze ice: it is characterized by supercooled water droplets that strike a surface but do not freeze completely at the point of impact. The remaining water fraction is then transported by the airflow while it freezes on the icing film. Under this condition often "horns" or protrusions are formed and project into the airflow.

- Rime ice: formed by supercooled drops that rapidly freezing on impact. It forms mostly along an airfoil's stagnation point generally conforming to the shape of the airfoil.
- Runback ice: occurring on wings with thermal anti-icing system when the system does not evaporate 100% of the water that impinges on the surface. The water runs back from the impingement zone, leaving the leading-edge region without ice. When the water reaches the region where the added heat no longer raises the surface temperature above freezing, the water begins to freeze and a ridge line develops. Frozen rivulets follow the ridge line in cases where the air temperature is close to freezing, which leads to ice shapes with large chord wise extent
- SLD ice: ice formed in SupercooledLargeDroplet conditions. Due to the larger droplet size often extends to unprotected parts of the aircraft and forms larger ice shapes characterized by the not instantly freezing of the water droplets mass.

The interaction between airflow and water droplets, combined with atmospheric conditions with temperature well below the zero and presence of water droplets clouds with concentration between 0.2-3.0 grams per cubic meter, drives the ice accretion phenomena. In order to clarify the aspect of this process, considering how the ice structures previously described are related to the impact process and the dynamic of the interaction with the airflow, a part of the research activities in the icing community is focused on analysing the behaviour of the droplet splash depending on aerodynamic condition and surface properties. Concerning the “icing science” this research field represents the main field to proper study and to describe the icing phenomena when seen as interaction between water droplet and target surface that evolves in an aerodynamic background depending on the local operative conditions. On the other hand the results coming from this investigation not only contribute to clarify some hidden aspects but also underline the importance of disciplines related to the icing science that can have application concerning the water-airflow interaction.

These disciplines, for example the dispersed phase turbulent transport that will be object of this thesis, can receive contribution in their specific research field, by the results coming from the their application to the icing technology. Icing wind tunnel test is a typical example where discrete phase dispersion, expressed by water droplets distribution and consequent icing cloud uniformity, is coupled with the icing field having a benchmark to test its models and a possible source for the identification of new phenomena. At the same time the inter-related fields of aerodynamics, turbulence and discrete phase transport are key features of the icing tunnel itself and contribute and support the development and improvement of its performance with the objective to better reproduce the atmospheric cloud uniformity.

In terms of icing technology that characterize by the whole of several application as probes for liquid water content, supper cooled large droplets detectors, numerical model and system to predict the icing accretion, the icing wind tunnel will be the main object of this thesis and its use is of primary importance to test anti-icing system, certifying the capability to flight in simulated icing condition and to support with in-flight test the validation of numerical codes.

1.2 Icing Wind Tunnel overview

The icing tunnel can be considered as an instrument to support the icing academic research as well as a tool for aerospace industrial applications. Research interest in atmospheric icing, both in civil and aerospace engineering, needs to better understand the physics of the formation of the ice, its interaction with different materials and surfaces and the possibility to predict and prevent its growth. In addiction to the numerical codes with capabilities to predict the story of the ice, experimental processes are needed to verify and analyze the real effects of the icing and, at the same time, to proof the efficiency of the anti-icing systems. In this respect icing atmospheric conditions have to be simulated in ground laboratories with the objective to reproduce the airflow and clouds characteristics encountered in in-flight situations.

Icing wind tunnels are usually built up following the general layout of standard aerodynamics wind tunnel, with the main difference being in the inclusion of a refrigeration plant, to cool the airflow at a range of temperatures between 0 and -35 degree and to include a droplet source of bar spray rake with nozzles able to produce droplet sizes required from the FAR specification and usually until to the SLD specification. The main configuration, common to several industrial and research icing tunnel, is a closed loop circuit of the type shown in the figure 7.

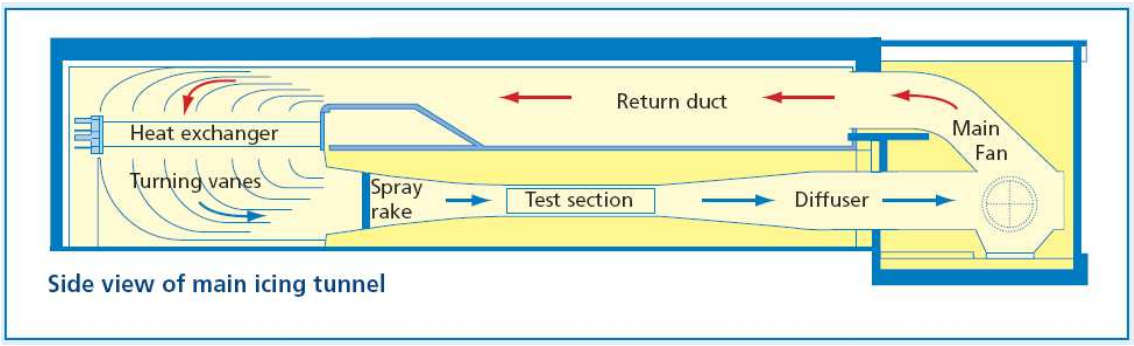

Figure 1-7: Cranfield Icing Wind Tunnel view

Specifically the Cranfield Icing Wind Tunnel comprises a 100 Kg/s fan/engine that with a series of different working sections, depending on the model size to be used, allows obtaining a test mach number until 0.5. The atmospheric icing condition are simulated with a refrigeration plant with a cooler of 400 KW able to decrease the temperature until -35 deg. and with six spray bars of nozzles able to produce droplet sizes from 20 to 80 microns. Several pressure and temperature transducers are fixed and connected to the digital data acquisition system and used to monitor and control the tunnel running conditions. Though the dimensions and performance of other icing tunnels can be different respect the Cranfield IWT, the dynamic of the processes involved can be representative of general physics phenomena.

The individual parts of an icing tunnel defined by test section, divergent section, turning vanes, plenum chamber and convergent section are designed to satisfy several criteria and deal with various constrains. Aerodynamic performance, such as a maximum efficiency in converting kinetic energy in pressure and reducing the pressure losses and constrain in space-cost and versatility are can affect the design process. In addition, specifically for icing tunnel, temperature uniformity and water

cloud uniformity have also to be considered as performance parameters depending on the airflow quality and features.

Water droplets and temperature distribution appear to be direct related to the turbulent scalar transport, where scalar is the temperature or the water concentration, and in parallel, when referring to mass particles, to the discrete phase transport or dispersion. In contrast with the standard aerodynamic tunnel, the local turbulence can play an important role to improve the performance of the icing tunnel, always in respect to the requirement of low turbulence levels in the test section.

The distribution of water droplets is closely connected with the airflow feature, through the interaction between water droplets and the turbulence structures. These structures are generated by aerodynamic disturbances within the icing tunnel such as the heat exchanger and the bar spray rake. Those components, affecting the airflow quality, may contribute to the final quality of the cloud uniformity. Considering the position of the heat exchanger, upstream the spray bars, its turbulence could affect the local airflow there contributing to create a higher turbulence background that, if not dissipated, could enhance the water droplets dispersion in proximity to the nozzles. At the same time the nozzle themselves, characterized by an injection of air with defined pressure and flow structures, are sources of turbulent that contributes to the dispersion of water droplets.

Measurements of the quality of the airflow in the Icing Tunnel has been performed and published in the literature. Gonsalez J.C. & Arrington E.A.[1, 2] performed airflow quality measurement in the NASA Glenn Icing Research Tunnel before and after the changing in the heat exchanger. Overview of the improvements in the airflow is reported by Irvine T.B. & al.[3]. Data were collected at single cross-sectional plane and included total pressure, static pressure, Mach number, total temperature, flow angle and turbulence intensity. The description and calibration of the instrumentation is reported in Gonsalez J.C. & Arrington E.A.[4]. Results show that the heat exchanger makes a major contribution to the turbulence production. Considering the injection process of water droplets in the flow as possible source of turbulence, the effects of the air nozzle spray were taking in account acquiring and comparing turbulent statistics at different nozzles operative pressures. They show that the injection of the

droplets interacts with the background turbulence and modify the final dispersion in the test chamber. The higher the pressure of nozzle's air, the higher the turbulence modification and the better the distribution of droplets becomes, as showed in Ide R.F. & Oldenburg J.R.[5]. However, as will be shown later, depending on the flow and turbulent structures, different air pressure not necessarily gives significant changes to the droplets distribution.

The interaction between droplets and airflow can be idealized as an exchange of momentum between flow and droplets with intensity driven by the local airflow unsteadiness, expressed in terms of turbulence statistics. The evolution of these statistics and their contribution to the particle dispersion within the tunnel is characterized by the tunnel geometry and consequently by the characteristic flow scales, leading each tunnel to its own case. However the similarity of the phenomena involved leads to research a methodology that permits to investigate the uniformity of the dispersion in a general point of view and, as presented in this thesis, to support icing tunnel design and test.

1.3 Icing Wind Tunnel Test overview

To test the anti-icing system the customers ask for a range of airspeeds and tunnel temperature. For each combination of these values a specific amount of water in the airflow is required to reproduce the flight conditions. It is expressed in terms of LWC (Liquid Water Content) and represents the grams of water per kilograms of air. At the same time a specific size distribution of droplets is needed, typically 20 microns, being possible with an appropriate combination of atomizing air pressure and water pressure of the nozzles, deriving from their calibration curves and selected on the control panel. With these specifications and with the model fixed in the test chamber it is possible to start the process of calibration of the cloud to obtain a uniform distribution of the droplets on the part of the model to test.

The optimization procedure can be summarized by the following main steps:

- Selection of the spray bars to use depending on the position of the model in the test section

- Selection of the number and relative position of the nozzles depending on the water spatial distribution required
- Run the tunnel in icing condition spraying water for a reference time
- Observe and measure the spatial distribution of the thickness of the ice (icing blade technique)
- Verify the uniformity and whether necessary change the position/number of the nozzles.

This trial & error way to calibrate the cloud is time & energy consuming due to the use of the cooler. The main factors in determining the number of iterations in this process are the shape and complexity of the model and the experience of the user. Thus, a computational method for tracking the turbulent water droplet dispersion as they move from the nozzle to the test section will help to simplify and speed up the calibration process. Such a procedure would also allow the testing of different icing tunnel configurations and operating conditions having cloud uniformity prediction for a wide range of droplet size including SLD droplets.

The cloud uniformity can be considered a parameter of the icing wind tunnel and values are often referred in a clean configuration without any model in the test section. The presence of the model modifies the aerodynamic field changing the momentum exchange with the droplets and their relative distribution. Under this circumstances the calibration procedure, ideally, should compensate the effect of the aerodynamic disturbances created by the blockage effects of the model, leaving the aerodynamic field of the model unchanged or properly in similitude with respect to a real in-flight situation. In this context the similitude criteria include other than the usual aerodynamics non-dimensional numbers also the similitude in the cloud seen by the model.

Every change in the operative conditions, associated with different points of the flight envelope, that affect the interaction between droplets and airflow could produce some alteration in the cloud uniformity. The calibration procedure, in this circumstance, could mean more setting up for particular test point, mainly in having to change the water nozzle configuration. The eventual evolution of the water droplet distribution cloud upstream the test chamber is only affected by the aerodynamic forces and the

water droplet defined size and there is not further means of control by the user during the test.

It raises, then, the interest to investigate the relations between the source of water droplets cloud and its final dispersion in the test section with theoretical models that could be translated in numerical procedures useful to support and simplify the calibration process. The methodology to perform this computational analysis, based on physical phenomena involved, could then underline the validity and limits of the numerical simulations giving a scenario for possible coupling of numerical calculation to support laboratory cloud calibration test.

1.4 Physical background

Research interest connected with this work is focused on the behaviour of multiphase flow where two or more phases, not chemically related, are present. Each of the phases is considered to have a separate volume fraction, the sum of which is unity, and conservation equations can be written in order to obtain the dynamic of each phase depending on its features and on the interaction with the other phases. The form of the conservation equations and the approach how to consider the coupling of the different phases, one of the major challenging of multiphase theories, will be described in the next chapters.

Two-phase flow, of the type encountered in the Icing Wind Tunnel, is found in many engineering systems including aerospace, biological, chemical, civil, mechanical, and nuclear applications. In particular, many combustion and energy systems involve dilute two-phase flow, ranging from droplet sprays and dispersion in gas turbine combustor flow to bubbly pipe flows of nuclear reactors and atmospheric pollutant dispersion. A greater understanding of the two-phase interactions can lead to increases in performance, reduction in cost and/or improved safety for such systems. In parallel, computational fluid dynamics (CFD) has now become an indispensable tool for gathering information to be used for design and optimization. Thus, the combination of these two disciplines, computational two-phase flow, has emerged as an important research area with unique characteristics and issue.

The interaction between the phases depends on the momentum and energy exchange between them and can be idealized as something partially related to the individual phase properties such as mass density, viscosity and partially related to the flow conditions depending on the problem under examination. The aerodynamic forces generated by the phases and contributing, for the Newton's third law, to the motion of each phase are connected to the operative conditions for the case, such as pressure and velocity, and to the case local geometry.

The operative and geometric conditions, which in computational fluid dynamic translate as input and boundary conditions, characterize the phase motion, seen as the whole of the phase kinematic features expressed by the velocity field defined by its turbulent regime. Consequently it has to be described and investigated to be properly coupled to the modelling of inter phase momentum exchange terms. As seen in the previous paragraphs, the Icing tunnel is characterized by turbulence sources, i.e.: heat exchanger and nozzles spray rake that exchange energy with the background velocity field defined by the tunnel geometry itself. This process is defined by the result of a local changing in the tunnel turbulence field described by its energy cascade, as available in the literature (Hinze, Tennekes, Pope)[6,7,8] due to the break up of large structures (or eddies) into smaller eddies until the viscous dissipation is dominant and the remainder of energy is converted into heat.

The turbulent regime in the Icing Wind Tunnel can then be characterized by the large scale structures associated the tunnel characteristic length scale. Typically they can be assumed to be a fraction of the hydraulic tunnel diameter. The cascade process evolves then with the help of the heat exchanger than contributes to break up the large structures transferring energy to the smaller eddies. This aspect generates the background turbulence level at the nozzle location downwind the exchanger. The nozzles contribution then act as a new turbulent energy source where energy is injected into the flow and interact and mixes with the turbulent existing field.

The effect of the turbulent field, characterized by its energy and spatial-temporal scales, is translated, through its contribution to the phase's velocity field, to the aerodynamic forces that affect the motion of the suspended phase. Not only design

and operative conditions influence the turbulence production and transfer within the flow, but also the presence of more phases itself is cause of turbulent production. It depends on the intrinsic property of the phases and on their relative motion, i.e.: relative speeds, which could produce aerodynamic disturbances or turbulence damping effects. This phenomenon represents an active research sector within multiphase flow and turbulence theories and it is called in the literature as “turbulence modulation”. It can be seen as a part of the whole picture of the phenomena related to the interaction between the phases. Though it is an element that can alter the turbulence effects on the particle motion itself, its dynamic it is still under investigation and for engineering computational purposes, under circumstances that will be discussed in the next chapters, its contribution can be neglected.

In the Icing Wind tunnel case the multiphase flow and turbulence disciplines can contribute into investigation of the motion of the water droplets, considered as dispersed discrete phase, coupled to a continuum carrier phase that is the tunnel airflow. The paths of individual droplets, typically around 20 microns of diameter, seen as ensemble, describe the position and behaviour of the icing cloud during its evolution within the tunnel. The domain of interest of the computational/theoretical analysis of the cloud evolution should include the elements that contribute, through an exploitation of the disciplines above cited, to characterize a “well posed” problem able to represent and solve the physical problem. In the Icing tunnel case presented in this research the attention has been focused on the volume from the spray bars to the test section, considering it able to properly supply the data sufficient to solve the engineering computational simulations.

In this sense the investigation of the variables, parameters and procedures necessary to describe and solve the physic problem leads to research a methodology that adds to the determination, approximation and solution to compute, in the Icing tunnel case, the numerical calculation and prediction of water droplet distribution.

1.5 The aim of the research

The aim of this research is to find a methodology to simulate the dispersion of water droplet in the air flow typical of an Icing Tunnel. It is going to proceed by understanding the physical and analytical parameters that influence the uniformity and the distribution of the cloud of droplets in the airflow and to connect them with the physical and operative parameters of the icing tunnel. This will help to improve the process of setting up the nozzle system for the cloud required before each test with the possibility at the end to be able to have an ensemble of methods to predict the dispersion of the droplets. The study involves different very general topics, such as turbulence and multiphase flow, with application in many fields of the industry and science. Depending on the situations, different models could be more appropriate than others, and the investigation is going to proceed considering the connection with the Icing Tunnel environment.

2 Transport processes in turbulent flow

2.1 Assumptions and criteria regarding two phase flow regimes

As seen in the previous chapter the interaction between particle (referred here to droplets or solid particles) and gaseous carrier phase, that control the dispersion process, is depending on local flow properties and on the mixture properties, characterized by the discrete phase material (density), geometric properties (particle/droplet size and shape) and its volume fraction. Depending on the loading of the discrete phase on the carrier phase different mechanism of mutual interaction can exist and produce different coupling regimes between the phases. The amount of particle dispersed in the flow, identified in terms of loading, gives a primary classification of the mixture characteristic.

The dilute condition, pictured as a lean concentration of the dispersed phase, it is here considered, following Loth [9], if the effects of the particle-particle interaction are treated as not significant. These interactions refer to two different situations, namely particle - particle direct collision (where the particle can coalesce or collide with each other) and particle – particle fluid dynamic interaction (where the proximity of the particles and their wake affect their aerodynamic forces). The direct collision of particles typically happens when the particle collision time scale is longer than either the particle response time to the fluid variations (τ_p) or the particle – eddy interaction time scale (τ_{int}), (the time scale where the particle interact with a particular eddy).

Details of the genesis of the criteria for the evaluation of particle-particle interaction can be found in Loth [9]. The frequency of particle collision is proportional to the number of particle in a reference volume, defined by the particle-number density $n_p=N/\Omega$, which is the number of particles (N) per unit volume (Ω), and to the number of collisions per unit time per particle associated to n_p value, relative particle velocity, and swept particle area πd^2 (d equal to particle diameter). Considering the relative

particle velocity upper-bounded by the particle terminal velocity (U_{term}) in a quiescent flow, the criteria for negligible particle-particle collision is:

$$n_p U_{term} \pi d^2 << 1 / \max(\tau_p, \tau_{\text{int}}) \qquad (2.1).$$

The term on the right hand side can be adjusted in a more explicit form considering the particle- eddy interaction time dependent on the flow features and structures [9]. The criteria, then, turns into two final conditions for negligible mutual particles collisions, whether the turbulence scale or the macroscopic mean flow scale is considered [9]:

$$n_p \Lambda \pi d^2 \Big/ (\gamma^2 + 1)^{1/2} << 1 \text{ for negligible particle–particle collisions in turbulence} \qquad (2.2).$$

$$n_p U_{term} L \pi d^2 << 1 \text{ for negligible particle–particle collisions} \qquad (2.3).$$

Where Λ, L and γ are respectively the turbulent eddy integral length scale, the smallest macro scale representative of the geometry and the particle drift parameter, as defined by Stock [10] $\gamma = V_{term}/u'$ (with u' equal to the turbulent fluid root mean square fluctuation). The particle-number density n_p, affecting the particle collision, can be related to the macroscopic features of the case considered where a particular volume, characterizing the geometry, can be chosen as a reference. However, due to particle preferential concentration or inertia effects, local changes in the number density, expressed as some peak value, can give different local particle-particle coupling regimes.

Differences in local particle concentration also characterize the local particle volume fraction (α) defined as volume occupied by particles divided by the mixture reference volume. This parameter is useful to identify the particle-particle fluid dynamics interaction criteria, that is usually more restrictive that the particle-particle collision criteria. It can be typically expressed as:

$\alpha^{1/3} << 1$ for negligible particle-particle fluid dynamic interaction [9]. (2.4).

At the same time the volume fraction can be used to characterize the particle-fluid interaction defining the regimes where the momentum transfer terms between the phases become significant. Differently by the dilute criteria, that investigates when the particle dynamics is affected by the particle-particle interactions, the criteria defining the process of fluid-particle interaction investigates the effects of the phases on their relative motion. The different regimes are usually summarized in the literature with the following classification [11]:

- **One-way coupling**: this particular regime considers the particulate effect on the carrier phase to be negligible and only the action from the carrier phase to the discrete phase is considered. The state of the airflow is then taken to be independent on the presence of the particle (droplet) and calculation for its motion can be done "a priori" solving its own set of equations. The particle behaviour can then be idealized and calculated through the equation of motion depending on the specified airflow solution. Rules-of-thumb found in literature state that this regime ends at a volume load of 10^6 (Elghobashi [11]) to 10^5 (Elghobashi and Truesdell [12]). The particles behave as passive (non-ideal) tracers, following a range of fluid instantaneous fluctuations. Due to the fact that particles may not follow all fluid motions, so-called preferential concentration (or 'clustering') can occur (Eaton and Fessler [13]).
- **Two-way coupling**: in two-phase flows this generally denotes that inter phase transfer of mass, momentum or energy is important to the fluid dynamic description of both phases. With a higher particle load, the particle phase starts to influence the motion of the fluid phase. Under this circumstance, the turbulence level can be attenuated or augmented, depending on the particle characteristics and relative velocities. The fluid phase and particle phase equations should be solved simultaneously. Boundaries for the two-way coupling regime are often stated at volume loads of 10^5 and 10^2. Despite numerous suggestions, there is no single parameter that seems capable of

prediction this behaviour. The inertia of the particle referred to the fluid fluctuation can be a discriminating for this behaviour [11]. The idea behind this is the fact that a less responsive particle will exhibit a greater instantaneous slip velocity. If this slip velocity is large enough, it may generate significant turbulence. Another often-cited rule [14] suggests that the ratio of particle size and fluid length scale is the discriminating parameter. This criterion was based on a large survey of experimental data.

- **Four-way coupling**: if the particle load is increased even further, particle-particle interactions should be taken into account (collisions, hydrodynamic interactions). In this regime, the distribution of the particles can become significantly non-random, with large regions devoid of particles. These large-scale structures can for instance be observed in fluidized bed reactors.

In the case of small particle size, which exists in many engineering applications, the interactions between the particle and fluid are expressed on the background assumption of the continuum property of the fluid seen by the particle. It establishes that the size of the particles is much greater than the free mean path of the fluid molecules and it can be written as (Loth [9]): $da_f \rho_f / \mu_f >> 1$ for continuum flow around the particle.

3.1 Assumption and criteria applied to Icing Wind Tunnel

The result of the application of the discussed criteria leads to different choices of the models describing the particle-fluid interaction characterized by appropriate simplifications and approximations. Starting from a macroscopic point of view that identify the upper-bounded features of the simplification applicable to the case examined, the criteria allow to identify particular regions and regimes where different local approach can be considered. This aspect can then produce different local solution procedures and strategies for the dynamic of the two phases.

The Icing Tunnel, seen as a macroscopic level, is a two-phase flow system where the carrier phase is the tunnel airflow and the discrete phase is composed by water droplets. The overall volume fraction between the two phases is usually bounded by the specification in the Appendix C to FAR 25 and can be assumed proportional to the

Liquid Water Content (LWC), identified as the grams of water per cubic meter of air. In this respect the volume fraction so chosen represents a macroscopic estimation of the regimes concerning the particle-fluid interaction. The desired value of the LWC is usually required and verified in the tunnel test section, where the model is fixed. Local variations of the volume fraction, however, can be present in different part of the tunnel, possibly affecting the dynamic of the inter phase exchange terms. They would be mainly dependent on two factors: local sources of water droplets i.e.: nozzles, or local non uniformity of the particle distribution caused by interaction with aerodynamic structures.

From the Appendix C to FAR 25 droplets size is also specified within the "icing" envelope. The size of the droplets combined to the volume fraction, combination that represents the number of droplets to whom that volume has been distributed to, identify the dilute condition. The number of droplets in a reference volume is $n_l = \frac{N}{\Omega}$

where the macroscopic total number of water droplets is $N = \frac{m_{water}}{\rho_{water} V_{particle}}$, with m_{water}, ρ_w and $V_{particle}$ respectively the total mass of water, the water density and the particle volume. Considering the total mass of water $m_{water} = \alpha \rho_w V_{air}$ and $\alpha = LWC / \rho_w$ being the macroscopic volume fraction, the macroscopic particle density number is $n_l = \frac{\alpha}{V_{particle}}$.

Considering the terminal velocity dependent on the water droplet diameter, assuming a macroscopic length scale as fraction of the tunnel test section and using arbitrarily an operative velocity of 60 m/s, the criteria for negligible particle-particle collision, for the macroscopic conditions coming from the Appendix C, without considering the turbulence effects, can be calculated and plotted as function of particle diameter and parametric with LWC.

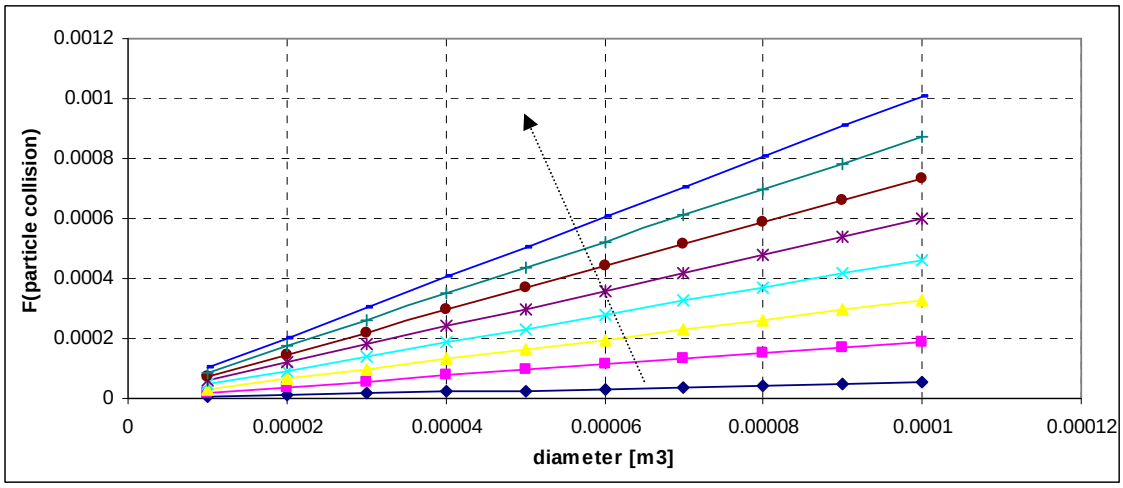

Figure 2-1: Particle collision function vs. Diameter, (for different LWC)

The results, expressed as function of particle collision (*F(particle collision)*), are much lower than unity indicating that the criteria for negligible particle mutual collision is satisfied. Estimation of the appropriate length scale, linearly contributing to the criteria, to a different order of magnitude does not affect the qualitative result.

When the turbulence effects are included the turbulent structures act on the particle motion producing a pseudo-random particle motion that changes the probability of the particle collision. In this case the criteria to the evaluation of the particle collision effects require a preliminary estimation of the turbulent scales and statistics moments. The behaviour of a particle to be suspended in a turbulent flow by the turbulent motion and then by its periodic random force, opposing to the gravity falling forces, is described by the particle drift parameter that requires an estimation of the turbulent root mean square fluctuations (u'_{rms}). The turbulent fluctuations are depending on the (different) local flow condition, determined by the local geometry, on the tunnel and are usually connected to the turbulence intensity defined as $T_u = U_{mean} / u'_{rms}$. In principle the turbulence intensity in an Icing Tunnel can be considered to be bounded by some high local values at in regions with low local velocity, i.e. : Heat exchanger or spray nozzle rake before the contraction, and by low values in high speed region such as the test section. The choice of the values is dependent on the geometry considered and on the operating tunnel testing conditions. The same characteristics also affect the turbulent length scale. Its preliminary estimation is more complicated

by the fact that not only the macroscopic geometry but also the coupling, generally non-linear, with other tunnel parts and component affects its values. However, imaging the overall tunnel geometry weakly scaling as the test chamber dimension, a fraction of the test section hydraulic diameter, typically one order of magnitude less, can be assumed as first approximation.

In order to include the turbulence effect on the estimation of the significance particle-particle interaction regime, it is possible to proceed as follow. Assuming the turbulent intensity range between 1%-10% as possible values for the icing tunnel, the turbulent fluctuation can be extracted by the local velocity depending on the tunnel geometry. The particles will generally experience different fluid fluctuations, due to the various mechanisms of production/dissipation of turbulent kinetic energy, along their path and as a first try the conservative maximum values can be used. In this case the particles will be considered always exposed to the maximum fluctuation present in the tunnel. Using the same particle diameter of the figure1-1 the particle-particle collision criteria, with turbulence, gives the results shown in the figure 1-2.

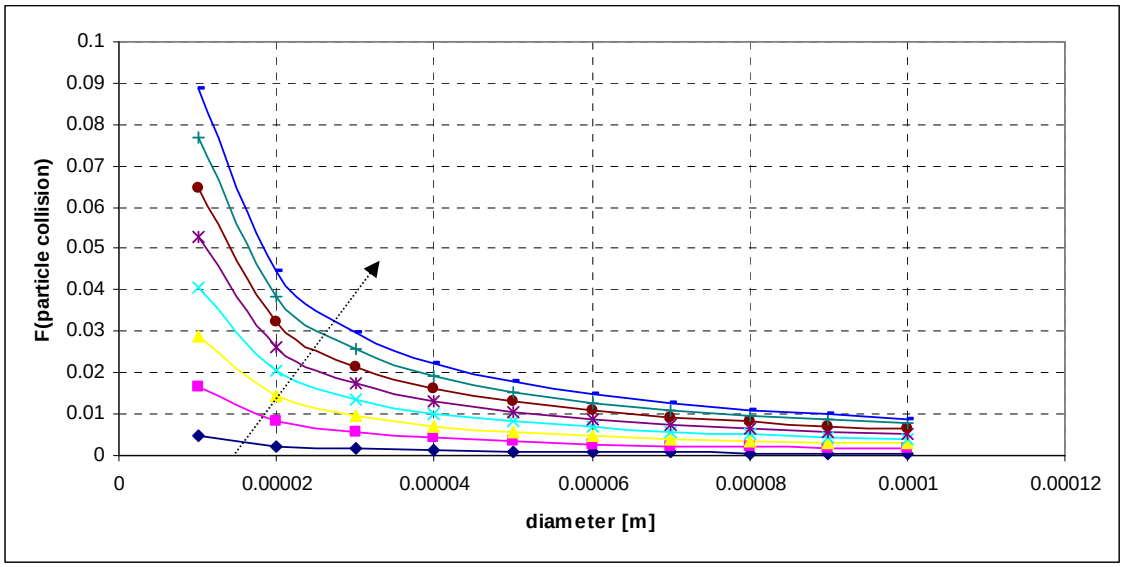

Figure 2-2 Particle collision function vs. Diameter, (different LWC), with turbulence

The turbulence length scale has been chosen to be 5% of the Cranfield Icing Tunnel diameter and according to the criteria for particle-particle collision its contribution

follows a linear trend. Doubling its value it will double the value of the final solution. The trend with the diameter follows the coarse consideration that the higher the particle diameter is, the higher the particle inertia is, the lower is the effect of the turbulence on the random motion and collision of the particles. The values calculated, also when considering changes in the length scale as doubling/halving, are one order of magnitude lower than unity suggesting a negligible contribution of the particle-particle collision to the phase motion.

The particle-particle fluid dynamic effects can also be estimated by the macroscopic volume fraction in the tunnel that comes from the LWC specification of the Appendix C. The criteria give the results plotted in the figure 3.

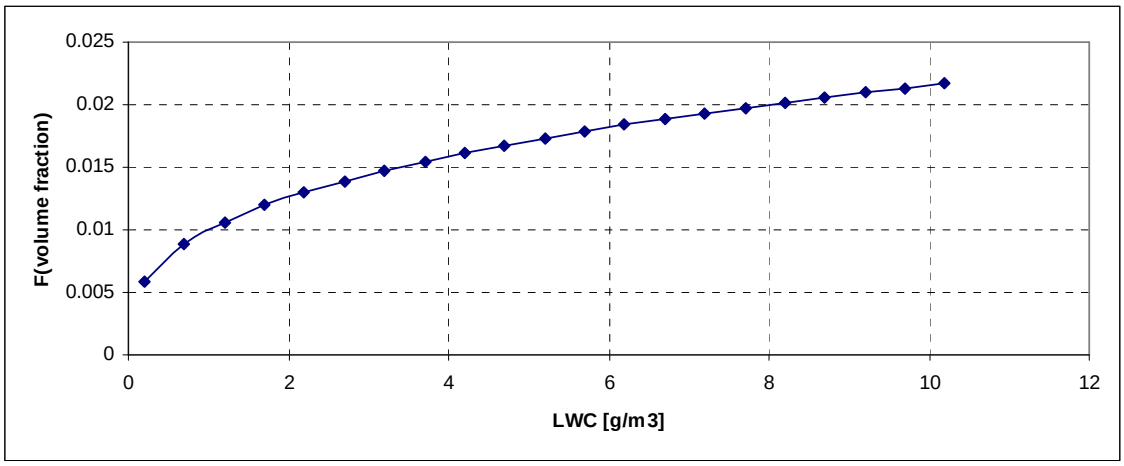

Figure 2-3: Volume fraction function vs. LWC

The graph shows a negligible contribution of particle-particle fluid dynamic interaction (*F(volume fraction)*<<1) till values much higher than the FAR 25 specifications. This macroscopic volume fraction is usually requested and encountered in the test section but can change in other tunnel parts. The water droplets are injected in the tunnel, upwind the test section, by nozzles and then disperse moving to the test section. The dispersion is generated by the nozzles themselves, close to the nozzle region, and then by the tunnel background turbulence. The local volume fraction, then, is going to change from higher values near the nozzles to the lower values after the dispersion process leading that the behaviour of the particle and the coupling regimes fluid-particle to be different near the spray bars.

To investigate the local volume fraction the nozzle jet shape has been considered as conical with an angle depending on the nozzle specifications and the operative tunnel conditions i.e.: tunnel velocity, nozzles air/water pressures. The local volume fraction can be estimated by the volume of water within the conical volume of the jet. It gives:

$$\alpha = \frac{m_w}{\rho_w V_{cone}} = \frac{m_w 3}{\rho_w x^3 \pi (\tan\alpha)^2} \qquad (2.5).$$

Where (α) is the half cone angle and (*x*) is the cone height, representing the distance from the nozzle exit. In this approach local differences in volume fraction are due to the high concentration of water coming out from an "almost punctual" source, defined by the nozzle exit area. Inhomogeneous turbulence effects on the particle dispersion are neglected and a uniform distribution of water droplets within the reference cone volume will be assumed. The continuous injection process is considered, picturing the nozzle spraying continuously and constant mass of water will be assumed within the reference volume: $div(u_{water}) = 0$. The axial velocity component, referred to the aligned nozzle/tunnel axis, is considered to be dominant in this circumstance. Then, the constancy of the mass of water roughly turns into the constancy of the droplet axial velocity component (u_x). This aspect implies that the axial acceleration of the air/water mixture is negligible near the nozzles and the effects of the tunnel contraction ratio are neglected. With these assumptions the local volume fraction near the nozzle can be estimated, using the operating conditions of the Cranfield Icing Tunnel, and it is shown in the next figure.

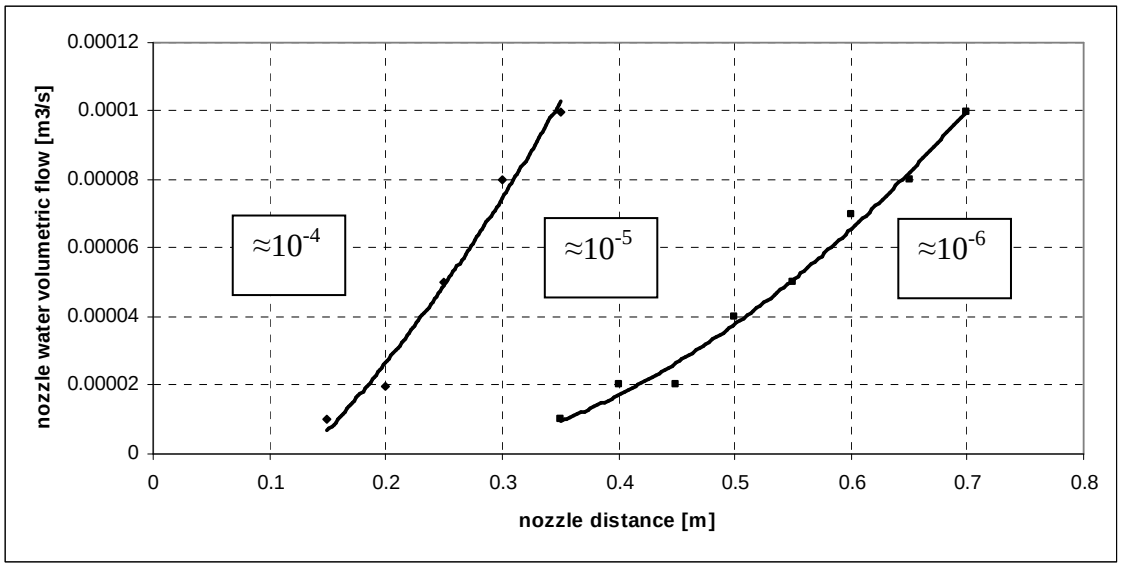

Figure 2-4: Volume fraction regions vs. Nozzle distance

The lines identify three regions of volume fraction. The values show that, following the coupling criteria, the effect of the water droplets on the carrier phase can be considered negligible for distance from the nozzle more than 30 cm. For closer distance, the values indicate regions of the two-way coupling regimes and show as different zones of the tunnel can have different coupling behaviour. Despite of this fact, the effects of the different coupling regimes in the small volume considered can still produce negligible contribution on the overall particle dispersion.

The local particle density-number can be estimated from the local volume fraction leading the possibility to estimate the local effect of particle-particle collision. In the case on negligible turbulence it gives the result of figure 2-5:

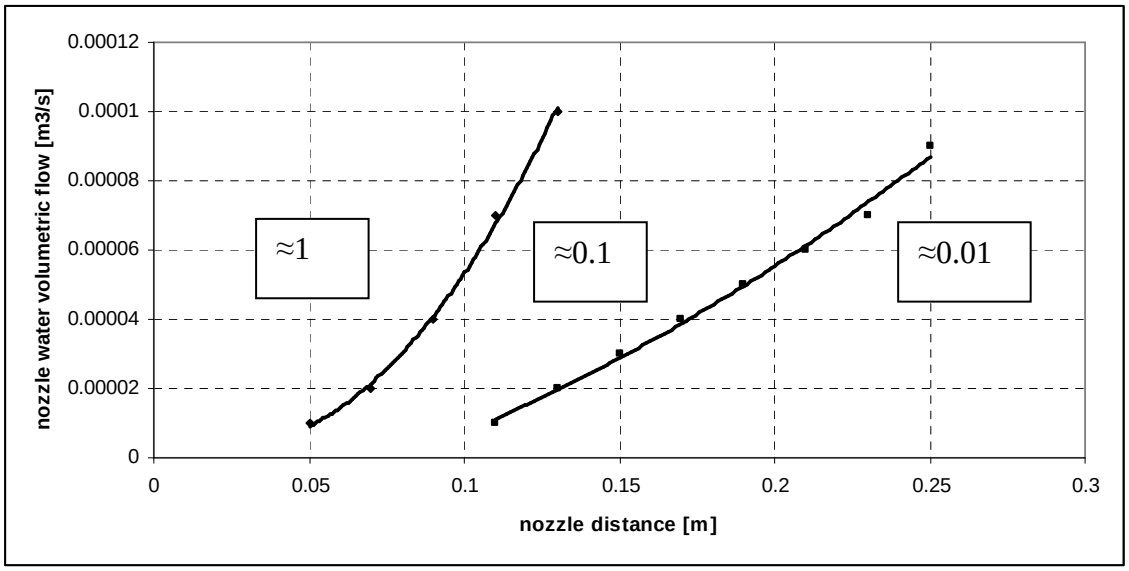

Figure 2-5: Particle number density vs. Nozzle distance

The particle-particle collision criterion is linearly proportional to the product of the particle diameter and mass of water in the reference volume and for this reason the choice of the particle diameter, represented as parameter, has been fixed to its maximum considered value of 100 micron. The lines shown in the graph represent, then, the upper bound boundary for the identification of the local particle-particle collision effects with the range of particle diameters less than 100 microns and masses of water chosen.

As shown in the previous figures the Icing Wind Tunnel can produce different droplet transport regimes, typically associated with variations in the volume fraction, which characterize the fluid-particle interaction behaviour. The near nozzle region is characterized by a two-way coupling regime where the effects of the momentum and energy of the particles (water droplets) can affect the local air flow dynamics. The local turbulent structure can be modified by this interaction which contributes to a modified local turbulence spectrum. Particle-particle collisions can also be present in this region, influencing the water droplet spray behaviour. Outside the near nozzle field the flow regimes in an Icing Tunnel, in terms of water cloud features, fall within the range of validity for a one-way coupling regime where the momentum and energy exchange from particle to fluid are negligible for the dynamic of the carrier phase.

To analyze the particle dispersion within the two regions of the tunnel, it should be possible, in principle, to consider the “near nozzle” and “far field” dispersion using two separate descriptions. This would imply to define a “near nozzle region” where the jet coming out from the nozzle is resolved and then coupled with the background tunnel flow, improving the range of parameters available for the further dispersion computation at the expenses of higher computational resources. In terms of a methodology focused on an engineering application and considering the small length of this “near nozzle region”, a simplified approach can be used trying instead to discuss the characteristics of the nozzle in terms of general parameters coming from experiment. This would allow having a synthetic description of the near nozzle region that could be conveniently coupled with the one-way description of the fluid-particle interaction in the tunnel.

2.3 Role of turbulence, time and length scale

One of the main factors in particle dispersion is the interaction of the dispersed phase with the turbulent eddies and flow structures. An important characteristic of the turbulent flow is its ability to improve the mixing and transport of the fluid with respect to the laminar condition, playing an important role in many engineering applications where fluid streams are brought together to mix. The picture of the two mixing fluids can be seen also as representation of a carrier fluid that interact with a second fluid composed as a whole of fluid-particles that are transported by the carrier phase fluid dynamic structures. In this respect the theoretical visualization of a fluid particle is understood as a macromolecular volume of fluid small enough to have average properties equal to local properties all over its volume. If we consider that the continuum comprising the fluid particle remain intact for time scale larger than the turbulent time scale, the fluid particle preserves its internal properties longer than characteristic time of the flow in which it is immersed. Pressures, temperature, density, velocity within this volume are essentially uniform.

This turbulent mixing visualization can be extended such that the fluid particle becomes a real physical entity identified by the discrete dispersed particles characterized by different internal properties and consequent relative inertia effects. In

the limiting case of negligible particle inertia the dispersed phase behaves like a fluid element being for this reason to be able to follow all the fluid structures. In practical applications, approximation to this limiting condition leads to the definition of discrete particle as "*tracer*" particles.

Normally turbulent flows contain eddies of a range of sizes, each having different amounts of energy. The process of turbulence decay allows the large-scale structures to break down into smaller structure (energy cascade process) until the effects of the viscous forces become dominant. Each turbulent eddy has an associated length and time scale referred as *eddy characteristic size* and *eddy lifetime*. The eddies in the largest size range have characteristic length scale comparable with to the flow macroscopic scale and their velocity is typically on the order of the r.m.s. turbulence intensity. This eddies are considered the energy containing eddies and represent the large scale flow structures that contribute to the production of turbulent kinetic energy and to the of transfer energy from the mean motion to the turbulent motion. The energy is transferred to successively smaller and smaller eddies until the Reynolds number of these eddies is sufficiently small, $\mathrm{Re}_{\upsilon} = o(1)$, that the viscosity is effective in dissipating the energy. From the Kolmogorov's first similarity hypothesis (see Pope Textbook [9]), stating that the statistics of the small-scale motion have a universal form uniquely determined by viscosity (υ) and dissipation rate (ε), it is possible to link the scale of motion [7,9]:

$$\left\{ \begin{array}{l} \eta / l_0 \approx \mathrm{Re}^{-\frac{3}{4}} \\ u_\eta / u_0 \approx \mathrm{Re}^{-\frac{1}{4}} \\ \tau_\eta / \tau_0 \approx \mathrm{Re}^{-\frac{1}{2}} \end{array} \right\} \qquad (2.6).$$

Where the suffix η refers to the Kolmogorov scales and l_0, u_0 and τ_0 are the integral scale of the energy-containing eddies. The rate of energy transfer from the large scale to the smaller scale, through the constant rate of energy transfer in the inertial sub-

range, determines the dissipation rate within the dissipative range of the energy-cascade.

The turbulent field can then be considered as an ensemble of flow structures with different and scaling length and time scales. In principle each of these structures contributes, in parallel to its amount of energy, to the mixing of the fluid particles and to the transfers of momentum and energy within the flow. The same process place for the motion of discrete particles whereas the energy of the eddies is transferred to the motion of the particles. Because of the finite timescale of the turbulent eddies their contribution to the particle motion will be dependent on the ability of the discrete particles to respond, in the associated time frame, to the fluctuation and, also, to the amount of turbulent energy available at the characteristics particle time scales. The size of the particle with respect to the eddy size is an important parameter in determining the outcome of the eddy-particle interaction and concerning characteristics non-dimensional numbers will be defined further.

The energy cascade process of the turbulence is originated by a three dimensional motion of vortex stretching due to the mean strain rate and the turbulence phenomena would require a complete description considering the whole of the spatial and temporal variables. Simplification to the problem can be done defining some special conditions that can reasonably be approximated in the reality. Turbulence flow is considered *homogeneous* if statistical properties of turbulent quantities are independent of space; *isotropic* if statistical features show no preference for any direction; *statistically steady* if the spatial statistics are time-independent. Based on these assumptions theoretical model for particle dispersion in turbulent flow have been developed.

To better underline the effects of the turbulent energy and scales on the particles dispersion the statistical theory of Taylor [15], applied to fluid particle, will be presented.

2.4 Historical background: Taylor fluid particle dispersion

The first attempt to describe dispersion in turbulent flow is by Taylor [15]. It describes dispersion of fluid particles in homogeneous, stationary turbulence. Furthermore it can be extended to study the dispersion of passive scalar (such as temperature), whose behaviour can be approximated to that of fluid particles for a given flow condition, or to the study of "heavy" particles, providing that some their statistics are given "a priori". The term "dispersion" is in this case meant to characterize the behaviour of a cloud of particles which is described by the evolution of its statistical moments that define the location and the shape of the cloud. Considering the simplified one dimensional situation with particles originating from the origin of the reference frame, injected with an initial velocity $u(t_0)$, their position after a time t can be expressed, following the notation of Shirolkar et al. [16], by:

$$x(t) = \int_0^t u(t_1)dt_1 \tag{2.7}.$$

If we follow trajectories of a large number of particles the ensemble averaged fluid particle location as function of time is given by:

$$\langle x(t)\rangle = \int_0^t \langle u(t_1)\rangle dt_1 \tag{2.8}.$$

The expression for the variance of the position as function of time can be derived as follow:

$$x = \langle x\rangle + x' \tag{2.9}.$$

$$x'(t) = \int_0^t u'(t_1)dt_1 \tag{2.10}.$$

$$\frac{dx'^2}{dt} = 2x'(t)\frac{dx'(t)}{dt} = 2\int_0^t u'(t)u'(t_1)dt_1 \qquad (2.11).$$

$$\frac{\langle dx'^2 \rangle}{dt} = 2\int_0^t \langle u'(t)u'(t_1)\rangle dt_1 \qquad (2.12).$$

$$\langle x'^2 \rangle = 2\int_0^t \int_0^{t_2} \langle u'(t)u'(t_1)\rangle dt dt_1 \qquad (2.13).$$

Thus the mean fluid particle location and its variance can be determined given the ensemble averaged fluid particle velocity and the covariance of the fluctuating velocity at different times. Defining a *Lagrangian autocorrelation function* similar to one used by Taylor [15]:

$$R^L(t,t_1) = \frac{\langle u'(t)u'(t_1)\rangle}{\langle u'^2(t)\rangle} \qquad (2.14).$$

And considering the fluid velocity as stationary random function of time, the autocorrelation depends only by the time lag (ξ) becoming:

$$R^L(\xi) = \frac{\langle u'(t)u'(t+\xi)\rangle}{\langle u'^2\rangle} \qquad (2.15).$$

The expression for the variance can be rewritten as follow:

$$\langle x'^2 \rangle = 2\langle u'^2\rangle \int_0^t \int_0^{t_2} R^L(\xi) d\xi dt_1 \qquad (2.16).$$

Thus, from a simplified turbulent motion the problem of particle dispersion is based on considering the Lagrangian autocorrelation function. This is related to the Lagrangian fluid time scale, roughly the time interval over which the fluid velocity is correlated with itself, by the expression:

$$\tau_{fL} = \int_0^\infty R^L(\xi) d\xi \qquad (2.17).$$

Usually one of the simplest forms of the autocorrelation is the exponential form given by:

$$R^L(\xi) \approx \exp\left(-\frac{|\xi|}{\tau_{fL}}\right) \qquad (2.18).$$

This expression is just an assumption and different expressions taking in account more complex phenomena in a turbulent flow (as the loops around the zero of the autocorrelation) are discussed by Frankiel [17]. However this simple exponential form is connected and consistent with another family of particle dispersion model coming from the Langevin equation [18].

After some mathematical manipulation derived by Kampe de Feriet [19] and using the Venkatram [20] approximation of the autocorrelation, which is assumed equal to one for time less than the Lagrangian timescale and zero otherwise, it is possible to derive two limiting conditions for the variance:

$$\left\langle x'^2 \right\rangle = \left\langle u'^2 \right\rangle t^2 \quad \text{for } t \le \tau_{fL} \qquad (2.19).$$

$$\left\langle x'^2 \right\rangle = 2\left\langle u'^2 \right\rangle t \tau_{fL} \quad \text{for } t >> \tau_{fL} \qquad (2.20).$$

It can be seen that the variance in the dispersion of fluid particles, in homogeneous turbulence, released from a fixed point grows as the square of the time of travel when this is less than the Lagrangian fluid time scale and became linear in time for time of travel much larger than the Lagrangian time scale (asymptotic behaviour). The fluid properties required for this analysis are the velocity fluctuation statistics and the fluid Lagrangian autocorrelation function. Note that all properties are that of the fluid phase and that we are dealing with the dispersion of a fluid element. However it is true that all above equation can be applied to a dispersed phase if properties such as the autocorrelation function are available for that phase. For example considering a dispersed phase that behaves like a fluid element; increasing its inertia will damp its fluctuation but will increase its Lagrangian timescale. The dispersion of this particle for "long" time is affected by both the contribution of these inertia effects as expressed by the above equations.

It has to be noted that the required statistics of the fluid are in the Lagrangian reference of frame and one limitation of this theory is that they are more difficult to obtain than the Eulerian statistics. The Lagrangian fluid autocorrelation is usually unknown and the Lagrangian fluid time scale is approximately related to its Eulerian time scale [21]. When extended to a discrete phase it is even more difficult to estimate some Lagrangian particle statistics, requiring measures following the particle path. Theoretical model are used to relate the statistics between phases and reference of frame [22].

2.5 Physical mechanisms for heavy particle dispersion

The previous analysis has been focused on the dispersion of the fluid particles characterized by the evolution of the variance of the cloud of particles which is affected by the turbulence statistics, namely fluid root mean square fluctuation and autocorrelation function. In industrial applications the particles of interest can have density that is much larger than the carrier fluid causing the dynamic response of the discrete particles to be different from the fluid particles. The mechanisms that control the dynamic response of a heavy particle will be discussed in the next paragraphs.

2.5.1 Inertia effect

If the particle is dense ($\rho_p >> \rho_f$) the inertial force at the fluid-particle interface will dampen its velocity fluctuations produced by the surrounding fluid fluctuations. A dense particle will typically have less fluctuation as compared to the one of the fluid-particle. This aspect produces a consequent reduction in the particle root mean square fluctuating velocity is known as *inertia effect* and it is characterized by a time scale called *particle relaxation time*. It is defined as the rate of response of particle acceleration to the relative velocity between the particle and the carrier fluid. Its expression is:

$$\tau_p = \frac{24\rho_p d_p^2}{18\mu_f C_D \mathrm{Re}_p} \qquad (2.21).$$

where ρ_p, d_p, and Re_p are the particle density, diameter, Reynolds number respectively, μ_f is the fluid viscosity, and C_D is the fluid-particle drag coefficient. The particle Reynolds number is defined by:

$$\mathrm{Re}_p = \frac{\rho_f \left| V_p - V_f \right| d_p}{\mu_f} \qquad (2.22).$$

The particle response time and the time scale characteristic of the turbulent motion can be combined to define the non-dimensional Stokes number:

$$St = \frac{\tau_p}{\tau_f} \qquad (2.23).$$

The reference fluid dynamic timescale τ_f does not have a unique value and in principle can be referred to the whole turbulent spectrum. When referring to the Kolmogorov time scale, the smallest one, the Kolmogorov Stokes number indicates the capability of the particle to follow the high frequencies of the fluid fluctuations.

Negligible contributions of that scale typically are considered when St >> 1, otherwise the particle is considered to be able to follow the fluctuation when St << 1. In the case of high Reynolds number flow, typically encountered in wind tunnel application, the separation between the turbulent scales can be of the order of 10^4 and the Kolmogorov scales can be similar or smaller than the particle response time. The particles, however, are still able to follow the larger scale fluctuations that, in parallel, are more energetic. When evaluating the importance of the turbulent dispersion could then be appropriate to compare the particle response time to the integral turbulent time scale identifying the inertia behaviour between particles and most energetic eddies.

The effects of the particle inertia can also be visualized considering an idealized situation of a particle continuously forced by a periodic fluctuation. If only the particle drag force is considered, the applied equation of motion is:

$$\frac{du_p}{dt} = \frac{\left(u_f - u_p\right)}{\tau_p} \qquad (2.24).$$

Where u_f and u_p are respectively the fluid and particle velocities. Applying the Laplace transform the transfer function between the periodic fluid velocity (input) and the particle velocity (output) can be obtained as function of the particle response time. Considering a range of particle diameters from 10 to 100 microns the “damping” effects are summarized in the figure 2-6:

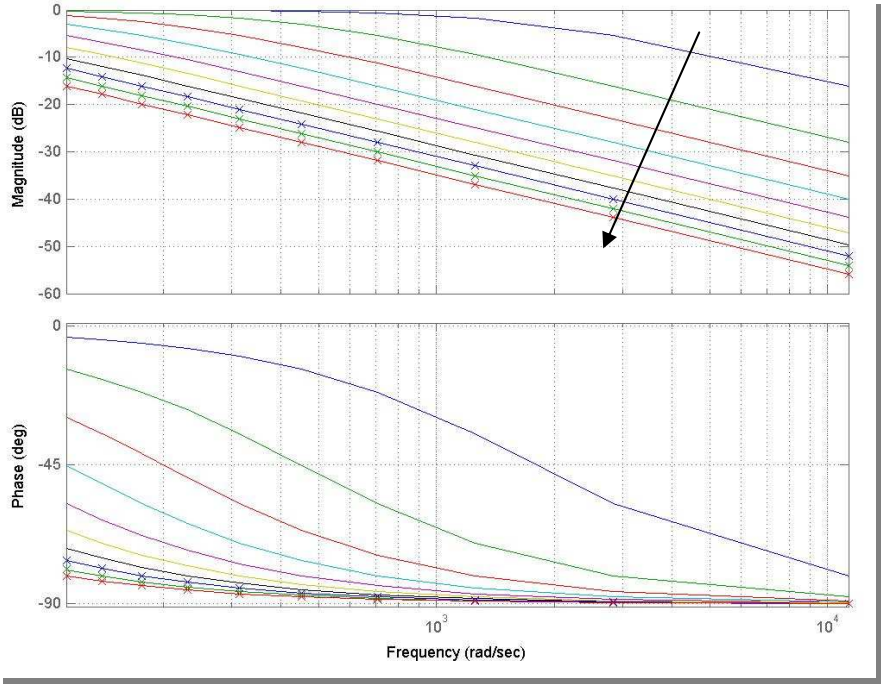

Figure 2-6: particle response to periodic fluctuations.

Referring to figure 1-6, the higher is the particle response time the lower is the inversely proportional cut-off frequency where amplitude variation from fluid and particle fluctuation, expressed in dB, are negligible. The phase response shows, also, that the particles follow the carrier phase with phase lag that increase with the particle inertia.

Another interesting inertia effect, presented with numerical calculation by Wang & Stock [22], is that the fluid timescale seen by a heavy particle is function of the Stokes number. When applying the Taylor theory [15] to heavy particles the Lagrangian autocorrelation between the particles velocity is required. If discrete particles have negligible inertia their motion can be assumed to be the same of the fluid particles and their correlation would coincide with the fluid Lagrangian autocorrelation. Increasing the particle inertia, the motion of the particle will be less affected by the fluctuation and less “chaotic”. If we picture a particle trapped in the eddy-one and its velocity just before migrating eddy-two as initial velocity, the effect of this velocity will have greater influence on the outcome of the eddy-two as particle inertia increases. This means that it is more difficult to change the trajectory or velocity of a particle with higher inertia and this aspect translate in a higher correlation of the particle motion at different time lags. The consequent correlated time is known as *particle Lagrangian*

time scale and it is related, scaling with the inertia effect, to the fluid time scale at the heavy particle position as shown in figure 2-7:

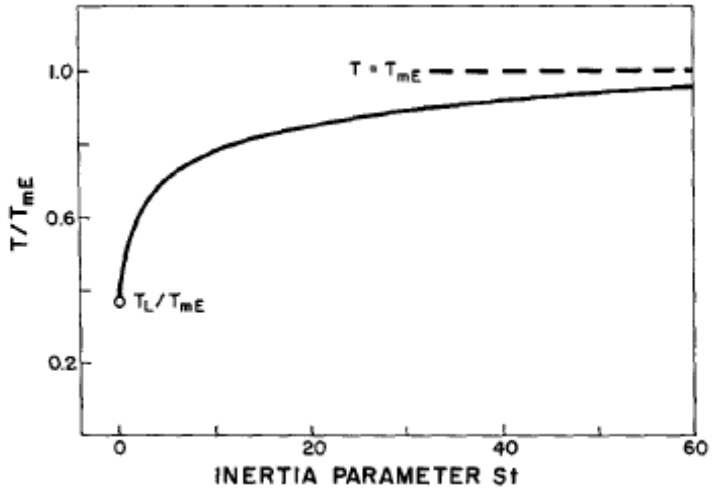

Figure 2-7: Particle Lagrangian Timescale (from Wang & Stock[22])

With Referring to figure 1-7, zero particle inertia the time scale coincides with the Lagrangian time scale of the fluid fluctuation (T_L). Increasing the Stokes number the time scale increases with asymptotic behaviour, so that when the inertia is very high we can consider the particle to be standing still with respect the fluid fluctuation, tending to the Eulerian time scale. In the figure 7 the time scale of the heavy particle in a reference frame moving with the mean flow velocity has been considered (T_{mE}).

In conclusion, increasing particle inertia decreases the particle fluctuation velocity and at the same time increases the particle Lagrangian time scale. According to the statistical theory of turbulent dispersion [15] the degree of the dispersion is determined by both the contributions through the product of RMS of velocity and Lagrangian time scale for the particle. The inertia effects so fare considered do not include the effect of the body force applied on a heavy particle. This cause a drift velocity between fluid particle and heavy particle that affect the interaction between eddies a particles as will be described in the next paragraph.

2.5.2 Crossing trajectory effect

When a body force, like gravity, is considered, the heavy particle would be subject to a falling velocity producing a mean drift velocity respect to the fluid particles. As a consequence of this the particle may not remain trapped inside the eddy for the entire lifetime of that eddy and the fluid-particle interaction is affected by this limited available time. The phenomenon of migration of a particle from one eddy to another one within the eddy lifetime is known as the *crossing trajectory effect (CTE)* [23]. The importance of the drift velocity can be identified by the non dimensional drift parameter introduced in the previous paragraphs:

$$\gamma = \frac{U_{drift}}{u'_{rms}} \qquad (2.25).$$

where u'_{rms} represents the root mean square fluid velocity fluctuation. The ratio between the drift velocity and particle fluctuation can be seen as a power of the turbulence to keep the heavy particles suspended in the flow. For high value of the drift parameter the eddy-particle interaction time can be significantly reduced. A particle drift velocity, representing the "fluid-particle mean motion", or the difference of velocity between them, is used to determine the time a particle would take to cross a given eddy. The minimum time to cross the eddy with length scale l_e is given by:

$$t_c = \frac{l_e}{V_{drift}} \qquad (2.26).$$

If the minimum *crossing time* is smaller than the eddy lifetime the particle would jump to another eddy. The *crossing time* concept is used for numerical application to account for CTE by allowing the particle to interact with an eddy for a time that is the minimum between the crossing time and eddy lifetime.

2.5.3 Combined effects of St and γ

The dynamics of heavy particle motion differs from that of the fluid elements due to the higher density of the discrete particles and the bigger sizes respect to the ideal fluid particles. The statistical Taylor theory [15], based on specific turbulent assumptions previously described, can be applied to the dispersion of heavy particle once the appropriate heavy particle statistic moments have been specified. The process to link the measurable fluid particles statistics with the heavy particle statistics has been developed in algebraic form by Wang & Stock [22]. It mainly consists in two steps. The first one is to relate the Lagrangian autocorrelation of the heavy particles to the one of the fluid particles at the heavy particle positions. In this step the inertia effects of the discrete particles are included. The second step is to relate the Lagrangian autocorrelation of the fluid particles at the heavy particle position with the available statistics for the fluid turbulence typically measured or expressed in the Eulerian form. The details of the process can be found in the reference and only the main outcomes will be discussed here.

The final form of their particle Lagrangian autocorrelation is expressed as function of three parameters: the Stokes number, the drift parameter and the turbulence structure parameter defined as $m = T_{mE} u_0 / L_f$ where $u_0 \equiv u'_{rms}$ represents the fluid root mean square fluctuation and L_f is the fluid spatial integral length scale. In the results presented in the paper the turbulence parameter was fixed to one allowing the specifying of the eddy turn-over time as the moving Eulerian time scale. The resultant particle integral time scale contours, normalized by the fluid Lagrangian time scale, as function of Stokes and γ are shown in figure 2-8:

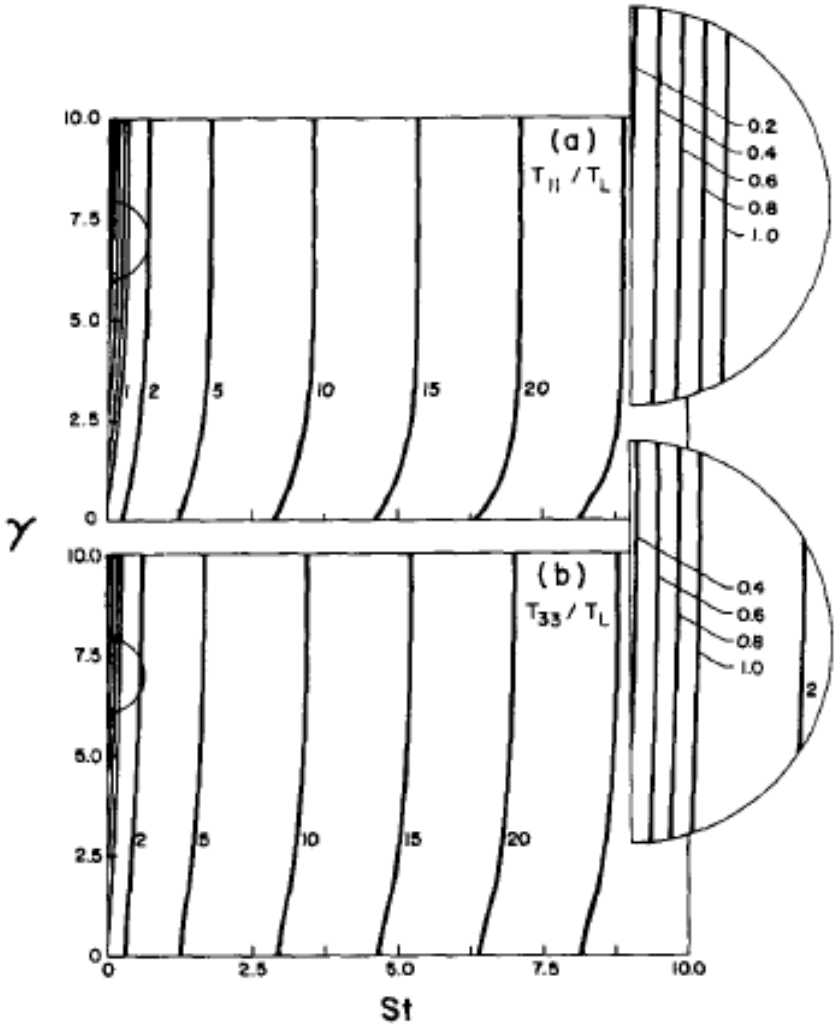

Figure 2-8: Particle Timescale vs. Stokes & gamma (from Wang & Stock[22])

The T_{11} and T_{33} in figure 1-8 refer to the time scale of the fluctuations oriented respectively normal to and parallel with the direction respect to the drift velocity caused by the gravity i.e.: gravity axis. In the limiting case of $\gamma = 0$ the particle time scale increase with the Stokes number. This situation is analogous to the one already presented of an idealized condition of a particle continuously forced by a periodic fluctuation; considering that there is no drift, the relative velocity between particle and eddy, representing the periodic force, is zero. The trend of the particle time scale with *St* can be assumed to be the same of the figure 2-6.

The particle root mean square velocity fluctuation contours, normalized by the fluid root mean square fluctuation, as function of St and γ are presented in the figure 2-9:

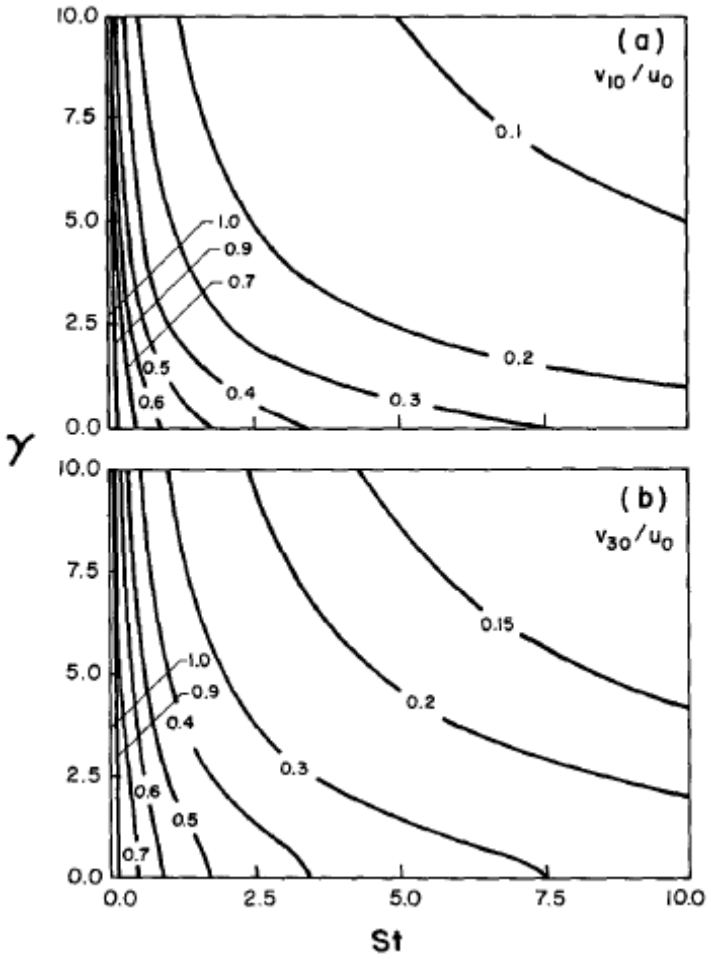

Figure 2-9: RMS velocity fluctuation vs. Stokes & gamma (from Wang & Stock[22])

The v_{10} and v_{30}, in figure 1-9, refer to the time scale of the fluctuations oriented respectively with the normal and parallel direction respect to the drift velocity. The role of inertia and drift velocity is to reduce the energy of the fluctuation of the particle motion. For the limiting condition of $\gamma = 0$ the cut-off frequency mechanism visualized in the figure 6 is responsible for the lower particle turbulent energy. Considering the particle dispersion, applying the Taylor theory, in the limiting condition $\gamma = 0$ the authors found that the ratio between heavy particle and fluid particle long time dispersion is proportional to the ratio of their Lagrangian time scale. Following the same notation:

$$\frac{\varepsilon^p(\infty)}{\varepsilon^f(\infty)} = \frac{T(St)}{T_L} \qquad (2.27).$$

Where $\varepsilon(\tau) = \int_0^{\tau} \langle u(0)u(\tau) \rangle dt$ is the dispersion coefficient respectively for fluid particle (^{f}) and heavy particle (^{p}). The dispersion of heavy particles can thus be in excess of what it would be for fluid particles considering the values of particle time scales bounded between T_L and $T_{mE} > T_L$. This situation is usually referred to the *inertial limit behaviour*. If the two time scales are approximately equal, the inertial-limit behaviour will not considerably increase mean particle dispersion from that of a passive scalar. However, the investigations to date are not conclusive. The ratio between the two scale has been reported by ~ 0.4. Sato and Yamamoto [24] which measured the ratio T_L/T_{mE} in the range of 0.3–0.6 as a function of flow Reynolds number. Experimental works by Wells and Stock [25] and Loth and Stedl [26] suggesting T_L/T_{mE} ~1. Isotropic DNS simulations of the decaying turbulence by Elghobashi and Truesdell [27] obtained T_L/T_{mE} ~1.

In the case of St = 0 and large drift parameters the root mean square veocity fluctuation of the discrete particle has been found the same of the fluid particle. The inertia of the particle is in this case negligible and the dispersion coefficient is inversely proportional to the drift velocity. The drift parameter controls the dispersion phenomena because the drift velocity affects the particle time scale. The correlation between the fluctuations seen by the particle and produced by eddies is shorted due to the falling particle velocity through eddies. This is the case where the crossing trajectory effects are dominant.

The general trend of the dispersion coefficient contours, as function of St and γ, is presented in the figure 2-10:

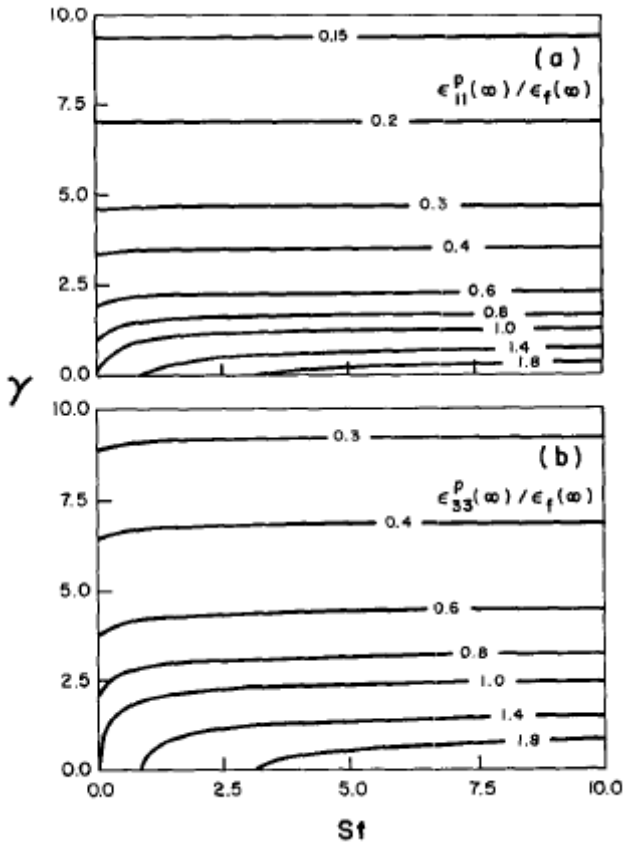

Figure 2-10: Dispersion coefficient vs. Stokes & gamma (from Wang & Stock[22])

The ε_{11} and ε_{33} refer to the time scale of the fluctuations oriented respectively normal to and parallel with the direction of the drift velocity. The ratio between particle and fluid dispersion coefficient is reported. The heavy particles disperse faster than the fluid particles for small values of the drift parameter. The situation is reversed when γ is sufficiently large.

2.5.4 Force acting on the particle

The dispersion of fluid particles is the results of the chaotic turbulent action of the fluid molecules, which can be expresses in terms of characteristic time scales and intensity. The fact that the turbulence is applied to fluid element is an idealization because the fluid elements motion is the turbulence itself and the variance of the position of fluid elements in time can be seen as a statistical moment coming from a

more general probability density function describing the status of the whole fluid elements in the flow.

When heavy particles are introduced, the dispersion phenomena have to account for the inertia and the drift of the particles with respect to the fluid elements. This phenomenon, synthetically described by St and γ, originates from the response of the heavy particle to fluid fluctuations. In this case the turbulent field results really applied to heavy particles through the aerodynamic forces done by the fluid and a description of those one will be given here.

Considering the equation of motion of a particle in a Lagrangian reference frame the forces acting on the particle can be summarized as body forces, surface forces, and collision forces [29]:

$$m_p \, dv/dt = F_{body} + F_{surf} + F_{coll} \qquad (2.28).$$

The body force, if electromagnetic are neglected, is usually based on gravitational forces and the resulting expression for a particle sphere is $F_{body} = g\rho_p V_p$ where ρ_p and V_p are particle density and volume.

The surface force arises from the local fluid dynamic interaction between fluid and particle. It mainly represents the effects of the pressure and shear stress integrated on the particle surface. No specific decomposition and synthesis of lift, drag and other surface effects is needed if direct integration of the aerodynamic interactions is performed on the particle surface. Thus, not even limiting assumptions of particle shape, particle Reynolds number, and flow gradient are required in this case. This approach is referred to *resolved-surface* and avoids empiricism associated with the prescription of fluid dynamic forces. However, the spatial grid resolution for the fluid flow field in the region of the particle has to be fine enough to allow description of the stresses around the particle i.e.: the grid scale has to be small when compared to the particle diameter: $\Delta x << d_p$. For the range of sizes typically involved in engineering applications, of the order of 10^{-5} in the Icing Wind Tunnel, the computational cost to compute the surface forces would become too expensive.

A different approach can be used to specify the surface force based on the interaction between fluid and particle, as the linear combination of several different components, surface-averaged and specified by analytical or empirical expressions. It has been discussed by Loth [9] that this point-volume formulation requires two important characteristics for a rigorous application, specifically: the spatial and temporal gradients of the flow of the fluid eddies are moderate and seen as linear by the particle; and that the instantaneous fluid fluctuations are know in the proximity of the particle (about a diameter away from the particle surface). For engineering applications, operating through the Reynolds Average Navier Stokes (RANS) formulation of the equation of motion of the fluid, those requirements are not met because no resolved turbulent structures are present. The details of the temporal/spatial variations of the flow field have to be modelled to predict their influence on the particle motion. In this circumstance the only condition to be satisfied for the point- volume treatment is, as opposite to the resolved-surface treatment, $\Delta x >> d_p$. Comparison of the point-volume and resolved-volume treatment is shown in figure 2-11:

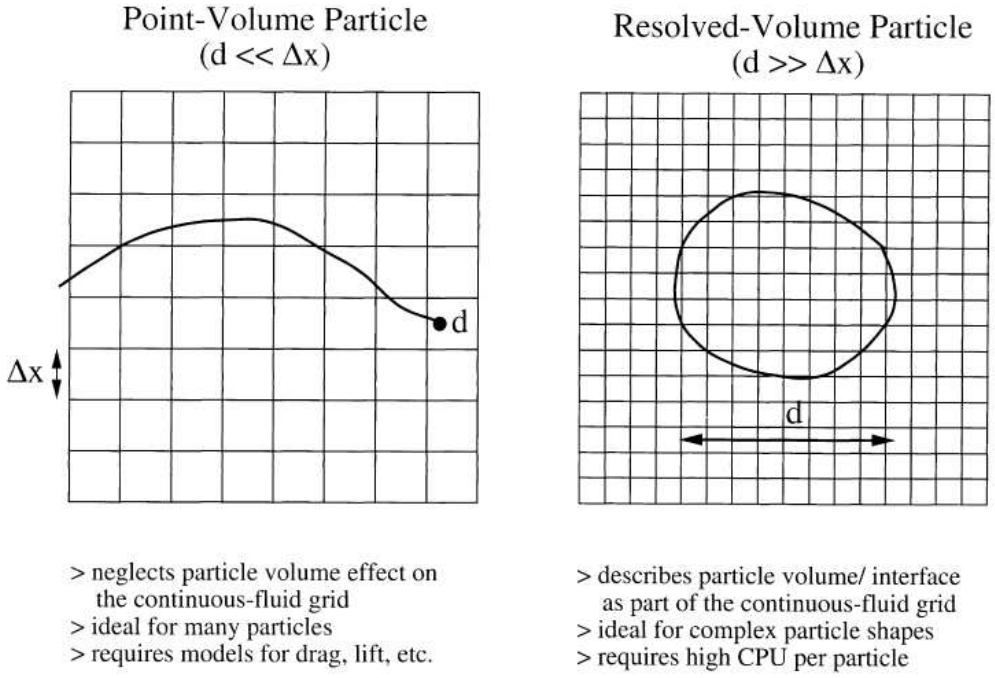

Figure 2-11: Point-Volume & Resolve-Volume (from Loth[9])

This point-force description of the linear momentum particle dynamic is the Maxey-Riley equation [29], derived analytically for incompressible creeping flow around a single solid spherical particle. The surface force in this case includes the contribution of drag (F_d), added mass (F_A), stress gradient (F_S) and a history term (F_H):

$$F_{surf} = F_d + F_A + F_S + F_H \tag{2.29}$$

Following the notation of Crowe [28], the expressions for the separate components are given by:

$$\left\{\begin{array}{l} F_D = -3\pi d\mu_f w \\ F_A = -0.5\rho_f V_p (dv/dt - Du_{@p}/Dt \\ F_S = \rho_f V_p \, Du_{@p}/Dt - g\rho_f V_p \\ F_H = -\frac{3}{2} d^2 (\pi\rho_f \mu_f)^{1/2} \int_0^t \left[\frac{dw/dt}{\sqrt{t-\tau}}\right] d\tau \end{array}\right\} \tag{2.30}$$

where the sub script $_f$ and $_p$ referring to the fluid and particle and ρ, μ, V, w, τ and $u_{@p}$ refer to density, viscosity, volume, relative fluid particle velocity, time and fluid velocity at particle location. In the case of a heavy particle with $\rho_p >> \rho_f$, (for water droplets the ratio is of the order of 10^3), the terms associated with ρ_f can be reasonably neglected under several circumstances. The resulting equation of motion for heavy particles, as used by Wang & Stock [22], is then composed by the significant contribution of drag and body forces only.

2.5.5 Drag Force

For heavy particles immersed in a flow field with moderate velocity gradient the most significant contribution to the particle acceleration comes from the drag force. Several physical mechanisms can affect the nature of this force and the trend of its C_d. Because of the wide range of engineering condition of interest several expressions for this force have been developed in the literature. The shape of the C_d curve has been

historically and experimentally related to the particle Reynolds number Re_p, particle shape, flow Mach number and terms concerning the non linear coupling effects between the parameters. For a general spherical particle the force can be written as:

$$F_D = \frac{1}{2}\rho_f \left|u_f - u_p\right|^2 SC_D = \frac{\pi}{8}\rho_f d^2 \left|u_f - u_p\right|^2 C_D \qquad (2.31).$$

For Stokes flow, where $Re_p << 1$, the C_d takes the form: $C_d = 24/\mathrm{Re}_p$. The creeping flow condition assumes that the particle and the fluid are in kinetic equilibrium and no slip velocity occurs. In view of its common occurrence, the Stokesian drag is also often used as a baseline for many other conditions, where Re_p depart from unity, by including a correction factor *f* which is the ratio of particle drag coefficient to the Stokesian drag coefficient. Experiment data from Clift et al. [30] indicated the trend, for *f* as function of Re_p for solid sphere in incompressible flow, as shown in figure 2-12:

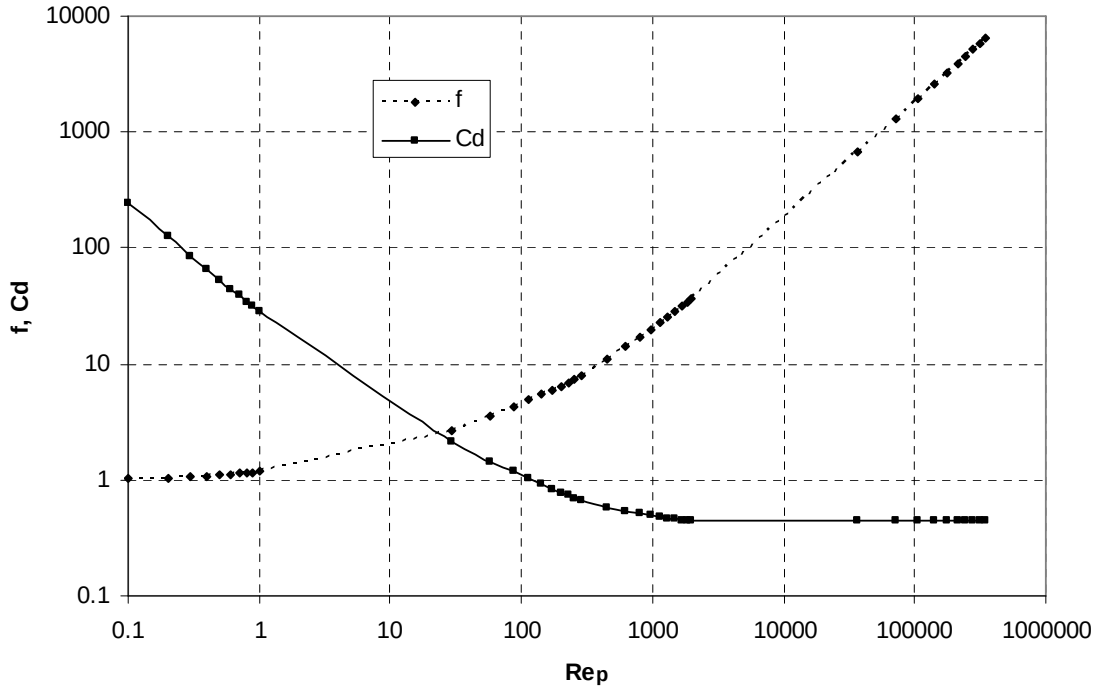

Figure 2-12: Drag Coefficient & Correction Factor vs. Reynolds$_p$

In case of droplets the shape of the particle can be considered to be dependent on the local actions of the flow and deformation respect the sphere can be present.

Deformations would occur at sufficient high Reynolds number where the liquid surface tension no longer dominates. For a heavy particle at terminal velocity the criteria to consider to describe the droplet deformation can be expressed by the Bond number [Loth [9]]:

$$B = \left|\rho_p - \rho_f\right| g d_p^2 \Big/ \sigma << 0.14 \qquad (2.32).$$

In this condition, the deformation is of most interests when the particle diameter is in excess of 10^{-3} meters. For small water droplets with diameter of the order of 10^{-5} meters, in steady-state conditions where only the falling velocity is significant, the deformation effects can be easily neglected.

Another example of the dependence of the C_d with Re_p for spherical particles, is included in the commercial CFD code "FLUENT", is the relation of Morsi-Alexander [31]. As in the case presented by Clift et al. [30] the expression for the C_d is function of parameter depending on several range of the Re number [Fluent manual [32]]. It shows:

$$C_d = a_1 + \frac{a_2}{\mathrm{Re}} + \frac{a_3}{\mathrm{Re}^2} \qquad (2.33).$$

2.5.6 Icing Wind Tunnel Considerations

The heavy particle condition of the Icing tunnel environment allows the simplification of the particle equations of motion for the drag force and the body forces. When inertial forces are considered, the gravity is typically used as reference acceleration to obtain an order of magnitude of the phenomena involved (i.e.: the gamma parameter). If this idealization is extended to the Icing Wind Tunnel it would require the particle to be in dynamic equilibrium with aerodynamic forces applied by the fluid motion within the tunnel, leaving the relative fluid-particle motion only produced by the gravity force. This condition can be pictured considering the flow in steady condition

moving through the test section or through a straight duct component with particle in kinetic equilibrium with the mean axial flow velocity.

In the icing tunnel the injection of the particles is located upwind of the contraction where the flow is accelerated to the required test section speed. The acceleration of the particle is consequently affected by the fluid acceleration, but the particle inertia would produce a relative acceleration particle-fluid that would produce inertial force acting on the particle. In this circumstance the body forces can be characterized by the combination of gravity and inertial forces.

To investigate and isolate the effects of the inertial forces produced by the relative acceleration between fluid and particle in the convergent section, neglecting the contribution of the gravity component, a simplified one-dimensional approach can be followed. The tunnel shape is represented by a general function of the distance along the axis parameterized with contraction ratio and contraction length. It is assumed that the tunnel has a square section and the contraction profile represents both the horizontal and vertical contraction. However the case can represent axial acceleration in asymmetric contraction tunnel with the same contraction ratio. The square section convergent shape can be represented by the general function:

$$f(x) = a\left(\frac{x}{l}\right)^3 + b\left(\frac{x}{l}\right)^2 + c\left(\frac{x}{l}\right) + d \qquad (2.34).$$

expressed by the non-dimensional variable x/l where l is the length parameter. The constant are determined by the boundary conditions:

$$\begin{aligned} & f\left(x/l\right)_{x/l=0} = 1 \\ & \frac{f\left(x/l\right)_{x/l=1}}{f\left(x/l\right)_{x/l=0}} = A \\ & f'\left(x/l\right)_{x/l=1} = 0 \\ & f'\left(x/l\right)_{x/l=0} = 0 \end{aligned} \qquad (2.35).$$

where A is the contraction ratio parameter. Once the geometry has been specified the axial velocity component in the contraction is know by the area ratio for incompressible flow regimes characteristic assumed for low speed wind tunnels. The vertical velocity component has been neglected in this simplified case. The particle motion along the axis has been calculated using only the contribution of the drag force produced by the slip fluid-particle velocity. Considering the particle initial velocity to be the same of the fluid, which is a reasonable approximation for small response time particle, the Stokesian drag has been used i.e.: Re < 1. The result of the simulation is shown in figure 2-13:

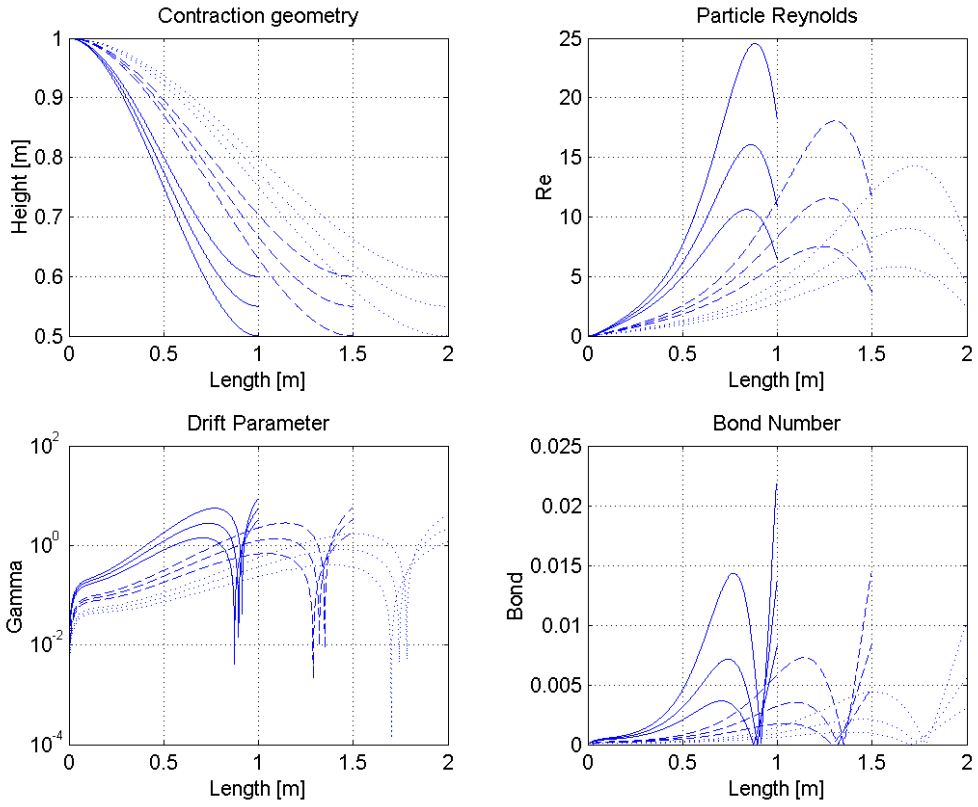

Figure 2-13: Inertial Forces effect on the particle

Three different contraction ratio and contraction length have been used. For each condition the Re_p, based on the slip velocity, the drift parameter, based on the relative inertial acceleration, and the Bond number, based on the inertial forces, have been calculated. Clearly, the more gentle the contraction the lower is the relative inertial acceleration.

3 Fluid-Particle Numerical Models

3.1 Introduction

In the previous chapter the underlying physical phenomena concerning fluid-particle interaction has been presented as the mechanisms that lead and modify heavy particle dispersion compared to the scalar / fluid element dispersion. The investigation of these mechanisms generally contributes to the improvement of treatment of the particle dispersion represented by the understanding of the interaction and coupling of the particle motion with the turbulence fluid structures. For engineering purposes these mechanisms need usually to be incorporated in methodologies and methods, through a numerical approach, that allows qualitative representation of the phenomena involved, giving quantitative results for practical applications.

The particle dispersion is dependent on the local airflow conditions that in turn affect the forces acting on the particle. In the simulation of the carrier phase, then, details of the turbulent structures and instantaneous fluctuations contribute to characterizing the forces. As has been previously discussed the forces can be derived by integration of shear stress and pressure along the particle surface, or by synthetic description where individual components are identified and expressed in terms of flow dynamic parameters. In both the cases, the details of the carrier phase determine the outcome from the force treatment process.

Because of the wide range of turbulent length/time scales involved in practical engineering problems the computation of particle trajectories, which is affected by the whole turbulent spectrum, would require the carrier phase resolution to the smallest time/length scales. Such calculations can be ideally performed using DNS calculation where the full-time dependent Navier-Stokes equations are solved without any filtering or approximation. Typically, the high resolution required to solve the smallest scale, for grid-independent solutions, results in low Reynolds numbers, simple geometries and the use of spectral methods if flow discontinuities are not critical to the flow physics. The primary advantage of DNS is that the eddy structures

are duly specified and no (empirical) turbulence modelling is necessary. The particle dispersion is then determined by solving the particle equations of motion based on the aerodynamic forces calculated for the carrier flow. However, for most engineering flows, DNS computations are simply too computationally intensive. DNS requires resolution of all scales in the turbulent flow where the smallest scales are on the order of the Kolmogorov scale. Based on the ratio between the integral scale and the computational domain, following Piomelli [33], we can conservatively write $L/\eta_K \approx \mathrm{Re}_L^{3/4}$; thus the total number of points required for the fluid resolution scales approximately with the cube of this ratio, $\mathrm{Re}_L^{9/4}$. As the largest present computers do not allow for simulations in excess of 10^9 nodes, this limits engineering computations to values of Re_L on the order of 10^4. Further, wall-bounded flows with resolution of the viscous sub-layer can even be more restrictive, e.g. $\mathrm{Re}_L^{7/2}$ based on Piomelli [33].

Typical laboratory flows in wind tunnels have Reynolds numbers of the order of 10^5-10^6, much higher than those possible using DNS calculations. Moreover for practical engineering purposes supporting laboratory tests, the computational resources available are usually insufficient to deal with the theoretical number of nodes required. To reduce the computational cost for carrier phase simulation a filtered formulation can be introduced into Navier-Stokes equations. The most energetic eddies, represented by the large flow structures in the energy cascade, are dependent on and related to the geometry considered. As discussed in the previous chapter, the particle dispersion is significantly affected by these large scales eddies which contribute to the energy transfer from the fluid to the particle motion. The smaller scales, in the inertial sub range, can be assumed, instead, to have universal behaviour independent by the local geometry. Their effects on discrete particle motion, except for very responsive particle, i.e.: tracer, with very low inertia, can be considered small if compared to the large structures when the particle inertial cut-off frequency is much higher than the characteristic small scale frequency. In this case, details of the carrier phase flow structures at the integral scales would allow for calculating discrete particle motion neglecting the aerodynamic contribution of the smallest scales in the fluid-particle interaction. This approach for the carrier phase is referred to Large Eddy Simulation (LES) simulation.

The governing equations are obtained by a low-pass spatial filtering of the Navier–Stokes equations. This spatial filtering is applied at sufficiently small-scales that the filtered turbulence is at or below the inertial range and thus can be considered homogeneous and isotropic. The filter width should vary with space for non-homogenous turbulence, e.g. smaller near walls for boundary layer flow, and a dynamic sub grid model can be used to allow energy transport to and from the unresolved scales [34, 35]. This technique is perhaps the most promising for low to moderate Reynolds number engineering flows because, with proper care, it can reproduce complex separated flow in both the mean and root mean square statistics. For particle dispersion, the key advantage of LES is the detailed spatial temporal evolution of the unfiltered large-scale turbulent motions that provide the input with which to determine the forces acting on the particles allowing computation of particle trajectories through integration of the equation of motion of the particles. A rough approximation for the number of nodes required for a wall-bounded simulation, following Piomelli [33], can be $N_n \approx 0.2\,\mathrm{Re}^{1.2}$.

For wind tunnel Reynolds macroscopic number, based on the characteristic test section dimension, of 10^5, the number of nodes required would be of the order of several millions exceeding the practical limit for test-support computation. The geometry of the duct, for an Icing Wind Tunnel simulation, is not only the cause of turbulent flow structure, as additional sources of turbulence should also be considered and modelled. Typically these sources include a heat exchanger, turning vanes and nozzle jets. These all involve local flow structures with high computational complexity. Their characteristic macroscopic length scale might well be one or two order of magnitude smaller than the tunnel dimension (10^{-2}, 10^{-3} meters). Also simplifying the problem and restrict the computational domain to the water droplets injection till the test section, detailed input condition of the flow structure, required as input boundary condition, would not be easily available from experiments. In this circumstance even the LES approach is likely to be too computational expensive to be coupled with a practical icing test.

Reduction in computational cost can be achieved when the filter of the Navier-Stokes equation is shifted from the inertial range to the very largest scale of motion. In the

limit of considering only the mean flow structures and variations, the unresolved-eddy formulation is adopted and will be discussed below. In this case, the consequent particle dispersion would be characterized only by statistical moments, i.e.: mean position and variance. Any details of local dynamic-kinematic interaction with turbulent structures, then, are neglected.

3.2 Unresolved eddy formulation

The category of unresolved-eddy simulations chiefly includes RANS (Reynolds Averaged Navier–Stokes) simulations, whereby all spatial velocity components are separated into their steady and fluctuating components and the fluctuating components are predicted in terms of statistical moments. The result is that only mean velocity distributions and flow variation at very low frequency can be determined. Overviews of methods in this field for both incompressible and compressible flow are reported by Vandromme [36] and the main aspects of this formulation will be presented below.

When the velocity is decomposed into mean and fluctuating components additional terms appear in the Navier-Stokes equations from the non-linear acceleration terms, relating the momentum transport produced by the turbulence on the mean motion. These terms are referred to the Reynolds-stress terms, $\overline{u_i' u_j'}$, and six independent unknowns that cannot be derived by number of equations available. The primary aim of RANS models, then, is to empirically represent the Reynolds-stress terms, appearing in the source term of the momentum transport equations, using some of the mean flow velocity features.

Turbulence models are generally divided into the traditional eddy viscosity models and the more advanced Reynolds-stress closure models. For the eddy viscosity models, $\overline{u_i' u_j'}$ is related to the mean velocity gradients and a mean turbulent viscosity, ν_t, synthesising the turbulent diffusion effects. These terms require modelling. The eddy–viscosity models are generally classified according to the number of partial differential transport equations which must be solved in addition to those for mean

mass, momentum, and energy conservation to compute ν_t. These generally range from zero-equation (algebraic) models where the turbulence is essentially assumed to be in a state of local equilibrium, to three-equation models where finite-rate production, diffusion and dissipation processes are individually modelled. For particle dispersion characterization and computation both an eddy time and length scale are needed such that two-equation models such as k-ε or k-ω are typically employed for the continuous-phase descriptions used for two-phase simulations. The k- ε model is the most popular technique for free shear layer flows because of its somewhat robust performance with a common set of empirical coefficients [37]. Because of that, it is also commonly used in modelling particle turbulent diffusion. However, the exact transport equations for k (turbulent kinetic energy) and ε (turbulent dissipation) contain many terms which require significant empiricism or outright neglect. Similar aspects concern the k-ω model, first proposed by Wilcox [38] , which examines instead the dissipation of k per unit kinetic energy (defined as ω). The kinetic energy equation and the specification of the turbulent viscosity are the same of the k- ε model but an equation for ω is used instead. The k-ω model shows superior behaviour in the near-wall region and in its accounting for the effects of the stream wise pressure gradient [8]. It is frequently used for separated flow regions. For wind tunnel applications focused on the bulk region flow field, of interest for particle dispersion, in general, any of these models can be used for predicting mean particle diffusion. However, their ability to reproduce the continuous-fluid characteristics (especially the mean velocity field and the turbulent length and time scales) should be the primary determinant for their use in two-phase flows.

The eddy viscosity models are based on the assumption that the Reynolds stress terms are related to the mean velocity gradient. Experiments concerning wind tunnel and shear flows [8], however, showed that this assumption is not generally valid, but for simple flows, whit turbulent characteristics evolving slowly (following the mean flow) this assumption can be considered reasonable. A different class of models, the Reynolds-stress closure models, seek to avoid a gradient transport approach for the turbulent stress tensor terms by employing individual equations for the individual turbulent stresses (and potentially the turbulent fluxes as well). Unfortunately, the large number of transport equations (a total of six equations for the independent stress terms) results in a much more computationally intensive and complex CFD solution.

As Reynolds-stress closure models are well suited to the framework of particle diffusion computation in anisotropic turbulence, they are expected to become increasingly important as they mature in fidelity and convenience. They usually perform better than the two equation models in calculating flows with significant streamline curvature, flow with swirl and rotation and flow with rapid variation in the mean flow quantities [8]. In Icing Tunnel applications the individual Reynolds stresses can capture the anisotropic effects of the convergent section, i.e.: contraction ratio effects, allowing the particles to be subjected to different flow structures, expressed in terms of statistical moments, along the three reference frame coordinates.

The continuous phase methods described are usually implemented in the commercial fluid dynamic codes (Fluent, CFX) and represent ordinary tools for engineering calculations. When multiphase flow is present, they are properly coupled with the discrete phase solution providing inputs for determine particle dispersion and behaviour. The simulation of the particles trajectories can be generally computed in both Lagrangian and Eulerian reference frame, whereby the Navier-Stokes equations for the carrier phase and associated turbulence models are implemented in the Eulerian frame. The choice of the reference frame for particle calculation is dependent on the characteristic conditions of the multiphase flow and the need for computational efficiency. A brief overview of the difference between the two approaches will be described next.

3.3 Particle Tracking Reference Frame

3.3.1 Eulerian reference frame

The Eulerian description of fluid motion basically consists of a set of partial differential equations for the fluid motion, in the time-space domain, that can be solved in a fixed reference frame. The time history of fluid elements is then described by their history within the fixed reference volume at marked positions that are function of time itself. The flow variables characterizing the fluid behaviour can then be specified at these marked locations, which are generated by meshing the volume in

discrete smaller parts. Once the algorithm for the numerical flow solution in these "nodes" is available in the numerical solver it can, in principle, be efficiently used to compute at the same points the discrete particle calculations. Therefore it is convenient to define a particle dispersion model, which depends on the solution of the fluid phase differential equations, in an Eulerian reference frame. This is the primary motivation for Eulerian particle dispersion models. This approach is usually adopted with particle loads of more than 10% or in case when significant amount of particles have to be considered in the reference volume [32].

The problem of describing particle dispersion in an Eulerian system requires developing appropriate partial differential equations (or transport equations) for the different particle properties of interest, such as particle velocity and particle number density. Once these equations, with valid assumptions, are developed, then it is easy to implement, solve, and interpret them along with the fluid phase transport equations. The simplest Eulerian approach to account for the dispersed phase is to treat the particles with a conserved scalar variable called a *mixture fraction* [39]. This approach, when applied to discrete particles, is known as the *locally homogeneous flow* (LHF) model. The main assumption of the LHF models is that the transport rates between the fluid and the particles are very fast compared to the rate of development of the entire flow [40]. The implication of the assumption is that the particles will have the same local velocity and temperature as those of the fluid. In general, the fluid and particles can be assumed to be in both mechanical and thermodynamic equilibrium at every point in the flow field. With this approximation, the two-phase problem is reduced to a variable-density single-phase problem [40]. The Navier-Stokes equations are written in term of mixture variables (ρ_m, u_m, p_m), expressed as a combination of discrete/carrier phase variables, weighted by the local particle volume fraction. Due to the gross oversimplification of the two-phase flow, this approach has a very limited use.

When the assumption of mechanical equilibrium is inapplicable to practical engineering problems concerning transport of high inertia particles the full Eulerian approach can be followed. This separated-fluid approach for an Eulerian description of the particle phase assumes that the carrier fluid and the particles are two separate, but inter-mixed, continua. This is also called the two-fluid method, and it accounts for relative inter phase mechanical and thermodynamic differences. Two set of equation

are solved, each one for each phase, containing the coupling terms regarding mass, velocity and energy transfer. The computational cost of the two fluid approach is then highly increased respect the LHF model.

The hypothesis of mechanical equilibrium between the particle and fluid elements can be reasonable for small/light particle with small response time leading a Stokes number less than one. For a water droplet of 20 micron, in air, the response time is of the order 10^{-3} seconds and the Stokes number in a typical icing tunnel application is well below than unity. The mixture model can then be applied to compute the particle volume fraction (LWC) instead of using the more demanding two-fluid model. However the very low loading factor also allows treating the discrete phase computation in a Lagrangian reference frame following the path of individual particles, which ensemble describe the phase characteristics.

3.3.2 Lagrangian reference frame

In the Lagrangian description a fluid element (or a droplet/particle) is described as a point that moves as its own velocity with characteristic variables, describing its properties, that are updated along its own path. In this circumstance the particle can be pictured moving through the Eulerian reference domain following a path that is generally not coincident with the Eulerian grid. The motion of the particle is determined by the aerodynamic interaction with the carrier phase, which is solved in the Eulerian frame. Interpolation schemes are used to interpolate along the particle path within the carrier phase where flow variables are known at the grid nodes.

In principle the Lagrangian frame can be considered the natural frame to describe the motion of a dispersed phase once the environment, represented by the carrier phase volume, has been specified. The particle history can then be computed by solving the momentum equation of motion, with force treated as described in the previous chapter, for individual or parcels of particles with specific size and properties.

Lagrangian approaches are typically more physically robust when describing phenomena such as turbulent diffusion, particle-particle interaction and particle

reflection from surfaces [28]. If the particles are not of the same shape or size the lagrangian approach also allow the employment of a statistical representation of particle distribution to include the effects of different inertial response. For the Eulerian approach this would require a set of equations for each particle shape and size, greatly increasing the computational cost. The Lagrangian approach also allows consideration of the effects of the aerodynamic particle-particle interaction when the particles cross over the wake of other particles where the steady state Eulerian treatment does not allow his phenomenon.

When applied to low volume fraction flow, as in the case for the Icing Tunnel condition, the Lagrangian approach is usually performed as a post-processing step where the particle equation of motion, usually represented by an ordinary differential equation, is integrated with its own numerical scheme and it is decoupled from the carrier phase solution. Because the particle variables are not calculated at the grid nodes, the grid resolution is not directly connected with the particle variable resolution required to show trends and gradients smoothly. However, the grid resolution has to be sufficient to describe the gradient of the flow variables that affect the particle motion. This aspect can help to simplify the numerical simulation of the carrier phase in situation where the flow spatial gradients are not significant but particle distribution is required on a smaller relative length scale. However, using the Lagrangian approach to compute a set of particle paths to reach statistical convergence can be comparatively memory intensive.

Another advantage to consider for the Lagrangian approach, described also as the *discrete approach*, in particular referring to Icing Tunnel applications, is the possibility to change the particle injection parameters in the domain without modifying the structure of the carrier phase computational domain. In terms of methodology for applied particle trajectory computation, this approach has the advantage that it simplifies the procedures required for the final solution. Once the carrier phase solution has been calculated, different configurations of particle injection, at different locations and different conditions, can be tried and computed. Also the possibility to specify the injection conditions, without the mixture constraint of mechanical fluid-particle equilibrium, also adds more parameters, as the injection velocity, to the local injection phenomenon characterization. The Lagrangian

approach is then chosen to be the main method of this research and will be applied for computation of particle trajectories. The approach is implemented in commercial CFD codes as well as the related particle injection options [32]. It performs the integration of the particle equation of motion, with the point-force description related to the local carrier phase solution and with stochastic characterization of the instantaneous local flow field.

3.4 Stochastic characterization of the instantaneous velocity field

The unresolved eddy simulation performed with the RANS approach neglects the instantaneous details of the local flow field and only the temporal variations of the mean local flow can be calculated. The fluctuating components of the velocity field, typically characterized by higher frequencies than the mean motion, can be generally connected to the turbulence model outcome, where the turbulent kinetic energy defined as an isotropic second order statistical moment. To solve the integration of the particle equation of motion the local characterization of the turbulence structure, expressed in terms of turbulence intensity and characteristic length/time scales, that in turn affect the aerodynamic interaction with the particle phase, need to be reconstructed. This is usually done in connection with the turbulent variables available from the solver together with a random number generator in order to simulate the chaotic effect of the turbulent structures. The primary goal of this stochastic approach is then to fully determine an instantaneous fluid velocity, as seen locally by the particle, and compute the trajectory of a statistically large number of particles in the flow to obtain mean particle diffusion information.

3.4.1 Discrete Random Walk model (DRW)

Considering the simplified particle momentum equation including drag and gravity forces only, such as experienced by heavy particles (particle density much higher than carrier phase density):

$$\frac{du_p}{dt} = \frac{\left(u_f - u_p\right)}{\tau_p} + g \qquad (3.1).$$

where u_f and u_p are the fluid and particle velocities respectively, τ_p is the particle response time and g the gravity force. The key problem is to determine the instantaneous fluid velocity along the particle trajectory. Considering the Reynolds decomposition of the velocity it is possible to write:

$$\frac{du_p}{dt} = \frac{1}{\tau_p}\left(\bar{u}_f - u_p + g\right) + \frac{u_p'}{\tau_p} \qquad (3.2).$$

Thus, being the mean fluid velocity available from a turbulence model, the unknown is the fluctuating fluid component. With the eddy-lifetime model [41, 42] the particle is assumed to interact with a discrete succession of eddies as it moves along the computational domain. Typically the broad spectrum of eddies is synthesised and idealized in simplified mean eddies characterized by a convection velocity (related to the mean stream wise velocity), eddy strength (based on local turbulent intensity) and a time scale and length scale which are derived by the local turbulent properties available from the RANS turbulence models. The fluctuating fluid velocity component associated with the eddy's strength is sampled randomly from a Gaussian distribution with variance proportional to the local turbulent kinetic energy value (k) under the assumption of turbulence isotropy [32], as shown below:

$$P(u') = \frac{1}{\sqrt{2\pi}\sqrt{\frac{2}{3}k}} \exp\left[-\frac{(u')^2}{\frac{4}{3}k}\right] \qquad (3.3).$$

The particle dynamic equations are then integrated for a series of eddy-particle interaction times, resampling independent fluctuating velocities, through a new random number, after the eddy-particle interaction time has elapsed. A typical representation of the trend of the fluctuation is given in the next figure:

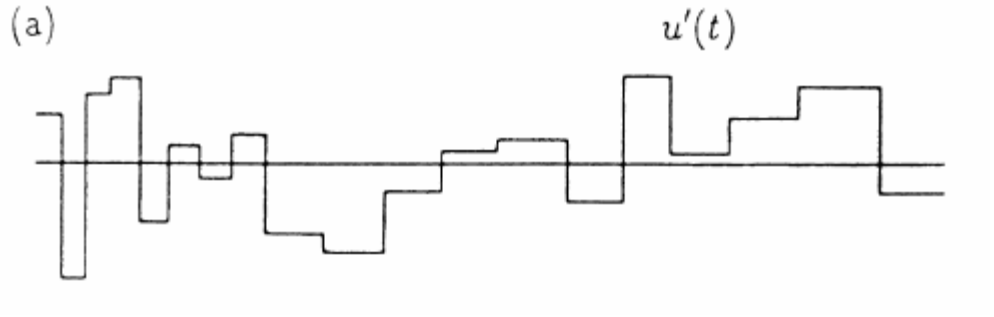

Figure 3-1a: DRW fluctuation samples (from MacInnes & Bracco[43])

The interaction time (time step) is determined to be the minimum between the eddy life time and the eddy transit time defined in the previous chapters. The advantage of the eddy lifetime model is that it can easily account for the crossing trajectory effects, particularly relevant, with heavy particles, in respect of the particle dispersion. However in this formulation some spurious drift of the particle from higher lo lower region of turbulence can be present [43].

When the stochastic model is coupled with typical two-equation turbulence models the condition of isotropy is usually adopted and the local velocity fluctuations in the coordinate directions are assumed to be the same and proportional the turbulent kinetic energy, $\overline{u'^2} = \overline{v'^2} = \overline{w'^2} = \frac{2}{3}k$. To consider anisotropic effects, the Reynolds stress tensor components would be required to characterize the turbulence directional behaviour. The commercial CFD codes, as in the case FLUENT, allow the incorporation of these effects by coupling the stochastic discrete particle model with the turbulence Reynolds Stress Model. In this case the diagonal components of the Reynolds stress tensor are used to define the velocity fluctuation required for the eddy-life-time model. The variance of the randomly distributed velocity sample for each direction is, then, proportional to the respective diagonal term.

The model can be improved to better represent more complex flow relaxing the condition of turbulence isotropy according to the procedure of *Yuan, Y. and Crowe, C. T.,[Particulate Sci. Technol. 7,129 (1989)*]. Considering a two dimensional case, the fluctuation u_f' and v_f' are required. Two different fluctuations u'_1 and u'_2 can be sampled from the PDF defined above. The two component of the velocity can then be related as:

$$u'_f = u'_1$$

$$v'_f = Ru'_1 + \sqrt{1-R^2}\,u'_2 \text{ with } R = \frac{\overline{u'_f v'_f}}{\sqrt{u'^2_f v'^2_f}}$$

When the cross-correlation (R) is zero the velocities correspond at two different independent samples as in the eddy life time model.

3.4.2 Continuous Random Walk Model (CRW)

One primary problem with the DRW model is that it employs step-function type perturbations yielding infinite continuous-fluid accelerations. This shortcoming can be solved by correlating the turbulence statistics with stochastic sampling continuously in time, thus yielding finite fluid accelerations. Though this model is not included in the commercial FLUENT code it has been widely reviewed in the literature and it is here presented as part of the state of the art models available. This approach gives the advantage of including, when necessary, stress-gradient (due to a finite fluid acceleration) and Basset history effects (due to finite time correlation) [37]. The model considers the particle to interact with a discrete series of eddies along its path as shown in the next figure:

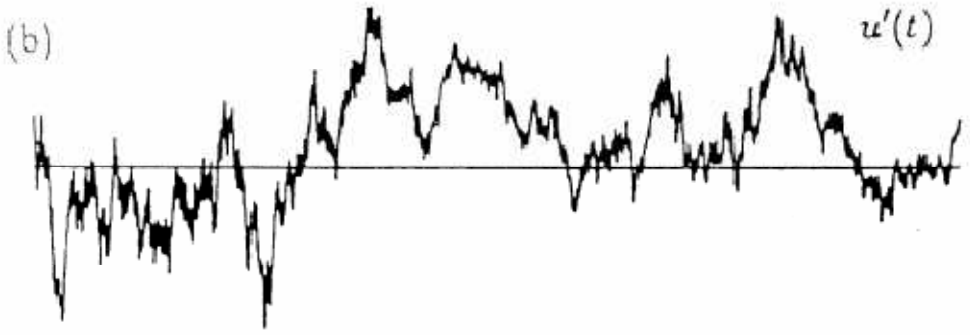

Figure 3-1b: CRW fluctuation samples (from MacInnes & Bracco[43])

It is possible to use a different approach accounting for a continuous time series of eddies including the effects of the autocorrelation between the time steps. With the assumption of a Markov-chain model between different velocity fluctuation, where the time dependent fluctuation is affected only by the previous time step, it is possible to write at the time (t + dt):

$$u'_f(t+dt) = R^L(dt)u'(t) + \varepsilon\sqrt{u'^2_f}\sqrt{1-(R^L(dt))^2} \quad \text{with}$$

$$R^L = \exp\left(-\frac{\Delta t}{T_L^*}\right) \tag{3.4}.$$

Where R^L is the Lagrangian autocorrelation function and ε is a normally distributed random number. In the case of zero correlation between time steps it gives the same result as the eddy life time model. The expression above can be seen as the finite differences of Langevin equation [44, 45] and requires the knowledge of the Lagrangian timescale of the fluid as seen by the particle T_L^*. This is usually unknown and can approximated using the approach of Csanady [46].

Instead of approximating T_L^*, a two step approach can be used as discussed by Berlemont et al. and Burry & Bergelez [47, 48]. The discrete particle and the fluid particle are assumed to be coincident at time t. After a time step, due to the inertia effect, their position will be usually different. Using the fluid Lagrangian autocorrelation it is possible to relate the velocity of the fluid particle at time t and (t + dt). This is the first step. Then it is necessary to transfer the velocity at time (t + dt) from the fluid particle position to the discrete particle position. This is the second step and is done using Eulerian fluid spatial correlation in the form similar to the time correlation substituting the time variables by their spatial equivalent [49, 50, 51]. Advantages and shortcomings related to this choice are extensively described by Pozorsky & Minier [52] and will be not discussed here.

3.4.3 Behaviour of Stochastic models in Inhomogeneous flows

The stochastic models determining the instantaneous velocity fluctuation, such as the DRW model implemented in the commercial CFD codes, can produce non physical dispersion of particles in inhomogeneous flows. This aspect has been analyzed by MacInnes & Bracco [43] where spurious drift of particle from higher to lower region of turbulence intensity has been found. Their analysis has been based on the dispersion

of tracer particles in inhomogeneous flows where both discontinuous random walk and continuous random walk models predict unphysical results. This statement has been proven by reducing the dispersion problem to a case where the fluid motion is divergence free and the particles follow the same path as the fluid particles, i.e., tracer particles. When a uniform concentration of particles is injected along the entire inlet region of a system, the same uniform concentration should remain throughout the system, regardless of the inhomogeneity of the turbulence (in the same way that an isothermal flow would remain isothermal irrespective of the turbulence). It has been found, however, that the models predict an unphysical migration of particles from the region of high turbulence intensity to the region of low turbulence intensity. This behavior of the stochastic models is a consequence of the relation between the Lagrangian and Eulerian description of the fluid particle motion. This consequence can be seen expressing the instantaneous acceleration of the fluid particle:

$$a_i = U_j \frac{\partial U_i}{\partial x_j} \tag{3.5}$$

where the Einstein convention of summing up over repeated indices is adopted. Expressing the instantaneous velocity as the sum of the mean and fluctuating parts, one writes

$$U_i = \overline{U_i} + u_i \tag{3.6}$$

where, by definition:

$$\overline{u_i} = 0$$

The mean acceleration is obtained combining the previous equations, and averaging over time. After algebraic manipulations the acceleration of the fluid particle is:

$$\overline{a_i} = \overline{U_j} \frac{\partial \overline{U_i}}{\partial x_j} + \overline{u_j \frac{\partial u_i}{\partial x_j}} \tag{3.7}$$

One can therefore break down the mean acceleration of a fluid particle into a component due to the mean flow, and a component due to random turbulent fluctuations in an inhomogeneous flow field. The drift acceleration gives rise then to a drift velocity that one needs to add into the stochastic particle equation of motion to take into account turbulence inhomogeneities:

$$\partial u_i = \overline{u_j \frac{\partial u_i}{\partial x_j}} dt = \frac{\partial \overline{u_i u_j}}{\partial x_j} dt \qquad (3.8).$$

where the second equality is a consequence of the assumption of the divergence-free fluctuating velocity field. From the previous equation it can be seen that the inhomogeneity of the turbulence field can produce a non zero Lagrangian mean fluid particle velocity in an Eulerian field with zero mean velocity. The drift correction velocity as expressed before is in principle applicable only to tracer particles which perfectly follow the fluid fluctuations. An extension of this correction to inertial particles was performed by Bocksell & Loth [54] who derived a drift correction that applies to particles with arbitrary inertia. Using the instantaneous acceleration of a fluid particle along the path of an inertial particle, Bocksell & Loth [54] showed that the drift correction for an inertial particle can be obtained from the drift correction of a fluid particle through a multiplicative factor as follows:

$$\partial u_i = \frac{\partial \overline{u_i u_j}}{\partial x_j} \left(\frac{1}{1 + St} \right) dt \qquad (3.9).$$

Where St is the particle Stokes number. The correction behaves correctly at the limiting case of zero particle inertia, where reduce to the tracer correction, and for the case of particles with high inertia, where correction tends to zero decoupling the fluctuating flow field and the particle motion.

An overview of the correction available for the inhomogeneity effect has been reported by Strutt & Lightstone [54] for the tracer particles case. They considered a two dimensional duct, as shown in figure 3-2, with an arbitrary turbulent kinetic energy profile along the direction normal to the duct axis (y direction). The first choice for the turbulent kinetic energy profile was the step function:

$$\begin{Bmatrix} k = 0.1 \; y < 0 \\ k = 0.5 \; y > 0 \end{Bmatrix}$$

The calculation of the particles dispersion has been done with the baseline model of Shuen, Chen and Faeth [55] and then corrected for inhomegeneity effects.

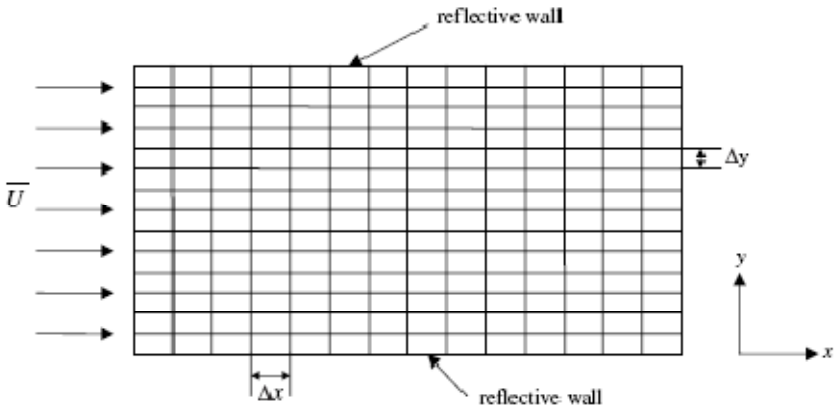

Figure 3-2: Computational domain (from Strutt & Lighstone[54])

Particle concentration profiles have been calculated for several downstream locations and normalized by the particle concentration at the inlet. If there were no net particle migration, the normalized particle concentration profiles would be uniform and equal to unity at all downstream locations. The figure 3-3 shows the predicted particle concentration after 1, 5, and 9 eddy lifetimes. From the figure 3-3 the Shuen, Chen & Faeth model [55] predicts a clear migration of particles from the region of high turbulent intensity to low turbulent intensity. This particle migration is amplified downstream from the inlet.

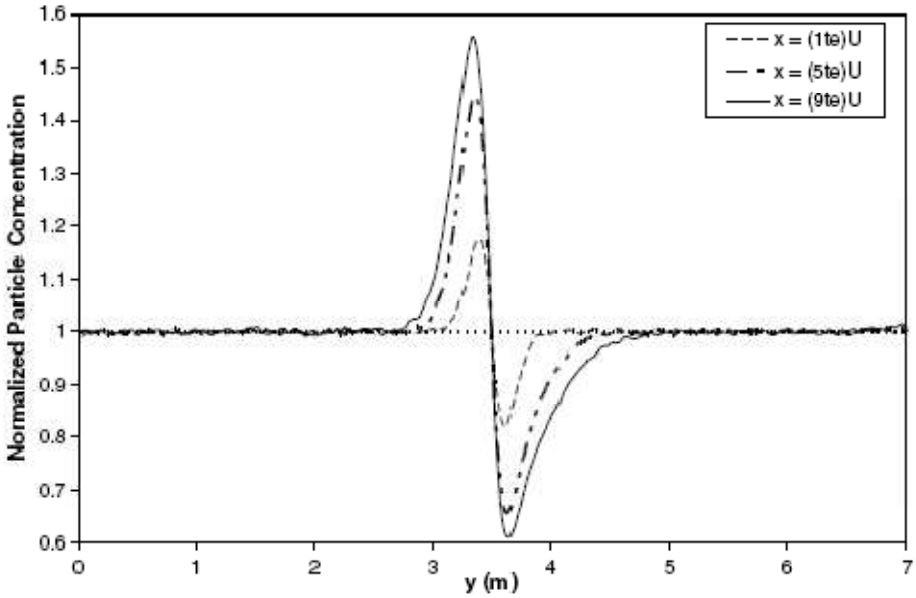

Figure 3-3: Concentration along vertical distance y (from Strutt & Lightstone[54])

The reason is because on average particles in higher turbulence regions can travel a greater distance than particles from a lower turbulence region during the same time interval [43]. Thus the high velocity particles from the high kinetic energy region have a higher probability to penetrate into the low kinetic energy region, yielding a non-uniform particle concentration.

The same phenomenon of particle migration has been analysed in a more real situation, with a continuous turbulence kinetic energy gradient profile as shown in figure 3-4:

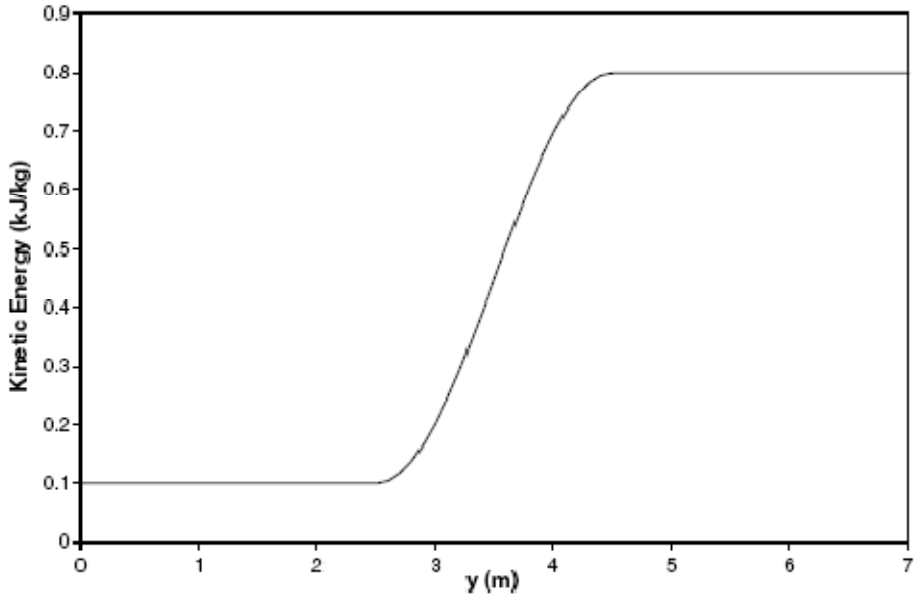

Figure 3-4: Turbulent kinetic energy profile along y axis (from Strutt & Lightstone[54])

The normalized particle concentration relating to this case in shown in figure 3-5. The amplitude of the concentration profile is reduced compared to the previous step-function case but is still present along the duct.

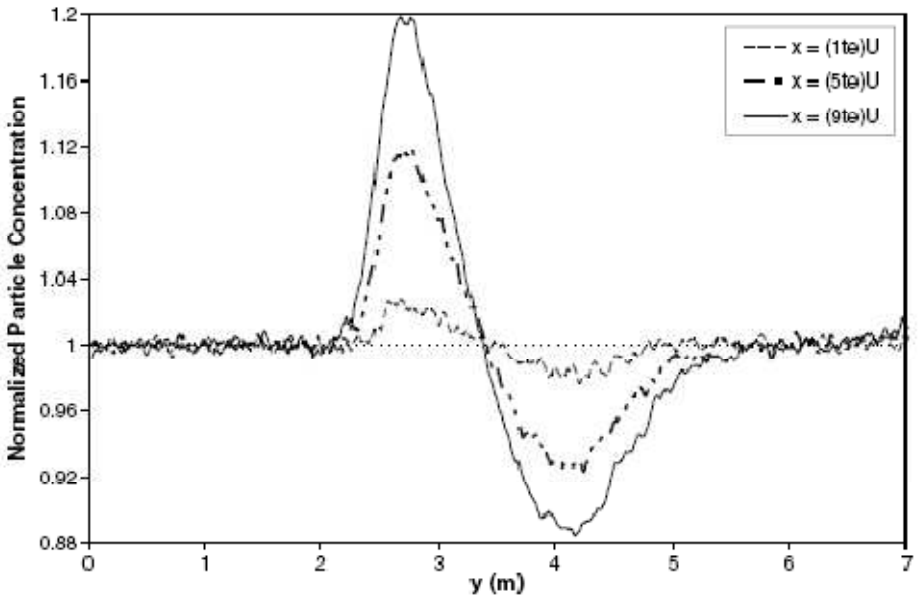

Figure 3-5: Concentration along vertical distance y (from Strutt & Lightstone[54])

The main reason for false migration of fluid particles, in the discontinuous random walk model, is because the turbulent fluctuation, determined at the start of the eddy

lifetime, is held constant for the duration of the eddy lifetime. In their paper Strutt & Lightstone [54] have tested different types of correction for turbulence inhomogeneity applied to the turbulent kinetic energy gradient previously described. The correction model, available from the literature, mainly consisted of adding a correction velocity to the particle equation of motion and/or updating the turbulence intensity value during the particle/eddy interaction time.

The MacInnes and Bracco model [43] combines the updating of the kinetic energy along the particle sub-time steps with a correction velocity. At each sub-time step, The instantaneous fluctuating velocity is updated using the local value of turbulence kinetic energy defined as $u'_{new} = \varepsilon\sqrt{\frac{2}{3}k_{new}}$, where the random number ε is held constant during the particle- eddy interaction time (as required by the discontinuous random walk model). The correction velocity, to be added as additional term in the particle equation of motion, was derived by estimating the mean fluctuating velocity from the characteristic distances particles travel during an eddy lifetime. The final form of the transverse correction velocity can be written as:

$$v'_c = \frac{1}{3}\frac{dk}{dy}t_e \qquad (3.10).$$

The correction velocity is applied at the beginning of every particle/eddy interaction.

The Chen [56] model tested updates the turbulent intensity sub-time step fraction of the particle/eddy interaction time. Using an anisotropic discontinuous random walk model, Chen used the normal stress found from a second moment closure model to approximate the turbulence intensity. In the analysis of Strutt & Lightstone [54], isotropy has been assumed and the turbulent fluctuation is approximated as $\sqrt{\frac{2}{3}k}$. At every sub-time step the fluctuation is updated with reference to the local turbulence kinetic energy.

Another correction velocity that is applied in conjunction with updating the kinetic energy is that of Bocksell & Loth [53]. Bocksell & Loth's correction velocity accounted

for the particle acceleration due to the gradient in the turbulent fluctuation variance [53]. This was done by analyzing the Lagrangian derivative of the fluid velocity along the fluid path. For isotropic, thin free-shear flows, the transverse correction velocity takes the form:

$$v'_c(t + \Delta t) = v'_c(t) + \frac{1}{3}\frac{dk}{dy}\Delta t \qquad (3.11).$$

The final model tested was the one of Strutt & Lightstone [54] that use a probability theory applied to the eddy fluctuations to formulate the condition for the correction velocity. The idea was to calculate the expected value of the negative fluctuation on the top half of the eddy and the expected value of the positive fluctuation of the bottom half of the eddy. At the midsection of the eddy (symmetry plane) the net flow of particles should be zero. Because the expected value of the positive/negative fluctuations is dependent on the local (top, bottom) turbulence kinetic energy, a correction velocity is required in case of inhomogeneity to balance the net flow. Their final correction velocity is then expressed as (using the same original notation):

$$v'_{ci} = 0.212\frac{dk}{dy}\Big|_{yi} + v'_{ci-1} \qquad (3.12).$$

The result of the application of these corrections to the case of a linear gradient of turbulent kinetic energy is summarized in the next figure. It shows the application of the Chen model, only updating the turbulent kinetic energy, is shown. Strutt & Lightstone [54] have discussed how the an effective limit of the model is reached and the performance of the model are no more improving, when the number of sub-samples are sufficiently increased. In the figure a case of 5 and 50 sub-sample has been shown.

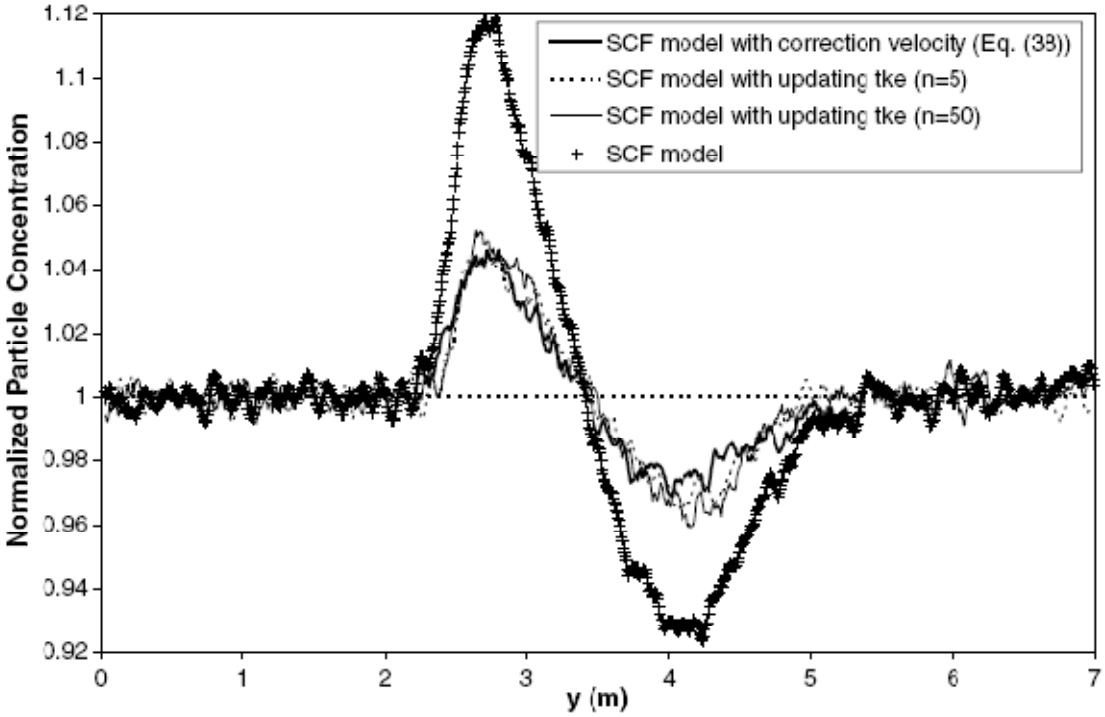

Figure 3-6: Concentration along vertical distance y (from Strutt & Lightstone[54])

In the figure 3-8 the result coming from the other models are shown. The normalized particle concentration curves were obtained by MacInnes and Bracco [43], Bocksell & Loth [53] and the Strutt & Lightstone [54], using correction factors after 5 eddy lifetimes. All three correction factors take similar forms, however, they differ in the empirical constant used and the frequency at which they are applied. Compared to the Chen correction the application of both updating the kinetic energy and correction velocity has been found to be the most effective way to account for turbulence inhomogeneity.

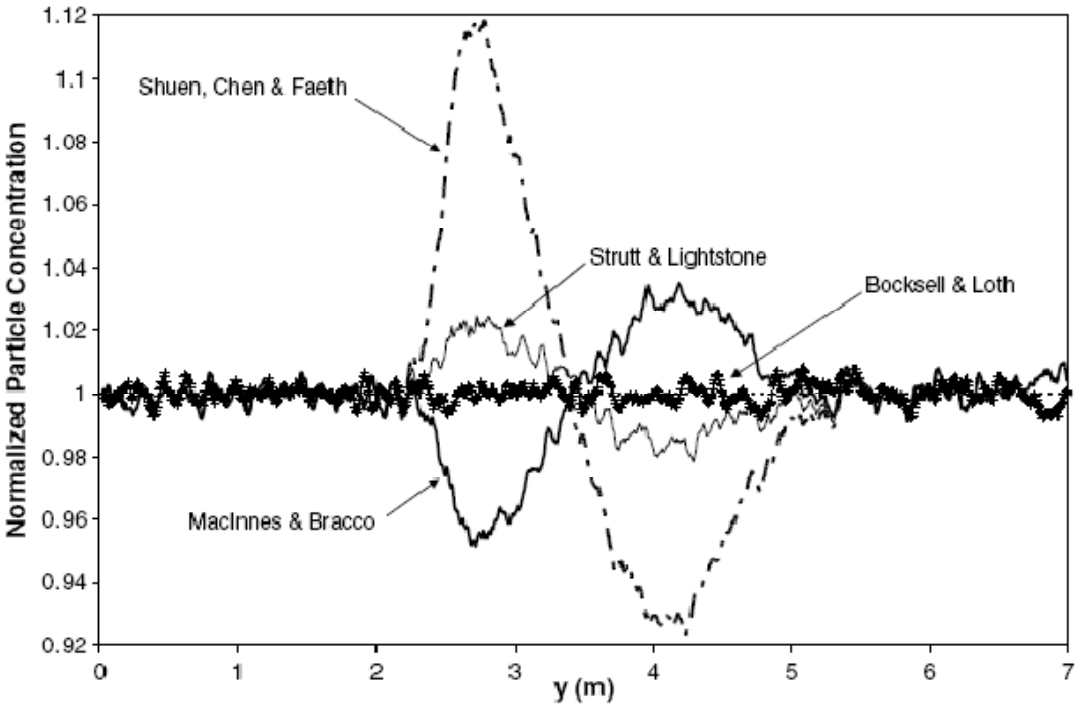

Figure 3-7: Concentration along vertical distance y (from Strutt & Lightstone[54])

The behaviour of stochastic models in inhomegeneous turbulence field has been presented and described, within this work, because the correction methods are a significant research field that belong to the state of the art discrete phase dispersion models. As has been previously stated, the commercial CFD code FLUENT does not include such correction methods and as its manual says: " *The DRW model may give nonphysical results in strongly nonhomogeneous diffusion-dominated flows, where small particles should become uniformly distributed* ".

4 Experimental Measurement

4.1 Introduction

In order to develop a methodology based on the available state of the art models for particle dispersion and being able to compare and select the more appropriate ones, the experimental approach is necessary to validate the results of the prediction of particles dispersion. In this sense the validation, as referred in the literature, is itself a well established methodology that has been extensively and used combined with numerical calculation. In the present work, however, the experimental results would be used also to identify phenomena that are related to the particle dispersion physics and are relevant to the trace the route for the set of procedures required for the engineering prediction. The experiments, then, provide not only a baseline test case to be used for further comparison, but also help to characterize and describe physical phenomena that can be used within the numerical calculation.

The choice of the experiments required in the methodology development contest, in parallel at the investigation of the numerical models available for engineering calculation, has been done having a preliminary look at the general methods available from the literature and then choosing the ones within the boundary condition dictated by the resources available to achieve the objective of the study. This process has been carried out along the development of the project and the selection of the experimental work has been focused on the necessary aspects to characterize and adapt the state of the art dispersion model to the Icing Wind Tunnel environment. In this sense, general experiments focused on the improvement of the models, also whether indirectly contributing to the development of methodology because changing the relative weight of the models, have been substituted by experiments used to identify, characterize and measure conditions and parameters relative to the available particle dispersion models applicable for icing tunnel engineering calculations.

4.2 Selection of the experiments for Icing Tunnels airflow characterization

As has been seen in the previous chapter, the engineering approach for the dispersion of water droplets in the icing tunnel, as well the general dispersion of particles in turbulent flows, is based on numerical methods that approximate the solution of the Navier-Stokes equations coupled with the particle equation of motion. Because the turbulence it is involved and mainly responsible for the dispersion phenomena in the icing wind tunnel, the numerical methods are affected by empiricism associated to the turbulence models. The first consideration would be then related to whether or not investigate the validity of the turbulence model constants for the specific case of the Icing Wing tunnel. In order to keep the attention focused on the engineering objective of the methodology, without deeply investigate the general turbulence models behaviour, it has been assumed the constants of the turbulence models, which appear in the equation of the turbulent kinetic energy and dissipation rate and have been originally calculated to cover a wide range of case history, to be unchanged respect their reference values. The literature available on the application of the turbulence model for practical calculation also supports this consideration.

The numerical calculation, generally, required the specification of local boundary conditions to properly represent the physics of the problem examined. These boundary conditions are applied to the computational volume in order to completely characterize the fluid dynamic solution of the problem. In the Icing Wind Tunnel case, as has been seen before, the flow quality can be affected by contribution usually generated outside the numerical computational domain. The heat exchanger geometry, for example, can be responsible for turbulence generation as well as the tunnel turning vanes and the very local flow coming out from the nozzle. In order to reduce the computational cost of the simulations the computational domain has been sad to be considered by the spray bars to the test section. For the same reason the internal nozzle air flow and the very local external structure has been sad to be not resolved with numerical simulation but to be synthesized from experimental work.

It appears, then, that part of the experimental work has to be focused on the characterization of the boundary conditions required for the numerical simulation. These conditions besides providing the necessary constrain to “well-pose” the numerical problem, have also to capture the necessary information to synthesize and describe the initial relevant physics phenomena that would characterize the water droplets dispersion along the tunnel.

In order to specify the turbulence characteristic, in terms of kinetic energy and length/time scales, at the beginning of the computational domain, experimental measurements would be required to map the turbulence profile along a plane normal to the tunnel axis and close or coincident with the input plane in the CFD simulation. Measurements of turbulence acquired at the input plane would directly provide the necessary information on the inlet flow condition for the fluid dynamic simulation, but would not characterized the effects of the air coming out from the nozzle. Because the nozzle effects contribute to the dispersion of the water droplets in the near nozzle field, an investigation of the flow quality downwind the spray bars has been considered necessary to obtain information and indication of the turbulence behaviour in the near nozzle field.

4.3 Water droplets dispersion measurement in the Icing wind tunnel

From the Taylor theory has been seen that the dispersion of particle is usually indicated and quantified with the variance of the particles displacement. The same approach will be used here to characterize the behaviour of the water droplets cloud. The water droplets cloud, originating from the nozzle injection and moving along the tunnel, can be pictured as an ensemble of independent stochastic realization of individual droplets path. The cloud spatial characteristic can then be defined by the ensemble statistic moments of the spatial displacement of the individual droplets.

In order to characterize the cloud of droplets, the position of its centre and the diameter of the cloud would be required as function of the distance covered along the tunnel (or function of the residence time along the tunnel). If the cloud is pictured as stochastic realization of single droplet events, the statistical mean value of the droplets displacement and its standard deviation can be used to express centre position and spread (i.e.: diameter) of the cloud.

To calculate these statistic moments an instantaneous picture of the droplet distribution taken at some place within the tunnel is required to allow detecting the spatial coordinates of the single droplet and being able to compute the statistical analysis. This approach has been followed in the literature where images of particles moving through the wind tunnel, at different locations, have been recorded with optical camera [57]. The practical problems concerning the installation of optical device in the tunnel and the difficulties to find or provide the proper optical access often make this approach not feasible for Icing Wind Tunnel application. In general the facilities used for these approaches were specifically built for this type of application.

To overcome this difficulty and find an easier approach for detect the particle dispersion in the tunnel it has been decided to exploit the formation of the ice as indication of the liquid water content distribution. If it is pictured that the ice formation is dependent on the local impingement and freezing of the singles droplets and it is assumed that the droplets collection efficiency is not affected by the ice presence, i.e.: the aerodynamic field seen by the droplets is undisturbed by the presence of the ice, the ice thickness would be indicative of the number of droplets present in the reference volume considered. This consideration strictly holds if also the droplets size is uniform.

To measure the icing thickness and to relate that to the liquid water content distribution, the icing blade approach can be used. The icing blade is a very simple device and it is frequently used in Icing test [58] . It consists of a piece of metal (aluminium) that is usually placed in the centre of the tunnel, normal to the tunnel axis. After the desired spray condition has been stabilized the bar is exposed to the icing cloud. The appropriate exposure time results in an ice thickness accretion on the

bar that is proportional to the local LWC. The icing blade has been used at an air temperature to ensure that rime icing occurred thereby minimizing the width of the ice, which would change the collection efficiency. The LWC is determined from the ice thickness by the following equation:

$$LWC = \frac{C * \varrho_{ice} * \Delta S}{E_b * V * t} \qquad (4.1).$$

where: C is a constant ϱ_{ice} is the density of ice ΔS is the ice thickness on the blade E_b is the blade collection efficiency V is the airspeed t is the exposure time. The blade collection efficiency represents the ratio of the mass-flux of the impinging droplets to the mass flux in the free stream and it is an indication of how much the droplets are disturbed by the aerodynamic field close to the blade. In this experiment the collection efficiency of the blade has been assumed equal to one. Though in the reality this is a limiting case, for the condition tested in this experiment, with small and thin icing thickness, this assumption can be considered reasonable. It is also to be considered that the error on the collection efficiency would affect the value of the LWC but the distribution of the water (droplets), assuming the collection efficiency to be constant along the blade, would be not affected by that. Moreover the objective of the test is to obtain information of the distribution of water in different tunnel operative conditions and in this respect is mainly focused on a qualitative analysis.

The Icing blade test has then been performed to acquire a set of experimental measurements for particles distribution to be used further for validate the CFD prediction. Though the measurement is conceptually simple it can be time and energy consuming. The tunnel is required to run at low temperature, in order to get the rime ice necessary for the correlation of thickness and LWC, and the measure of the ice thickness has to be manually done, at several stations on the blade, with the caliper kept at low temperature to avoid melting the ice.

Considering this aspect the test matrix has been chosen to characterize and describe an envelope for typical icing test without being too much energy and time expensive.

A description of the condition chosen for the icing blade test is presented in the next chapter.

4.3.1 Description of the test

The cloud uniformity is a requirement that is usually verified and adjusted in the test section during the icing test. The objective of the icing blade measurement would be then to provide a set of baseline measurement in the test section characterizing the water droplets distribution for different icing tunnel operative conditions.

The test has been carried on with an icing blade vertically positioned in the test section. Three reference speeds have been chosen, nominally 40 m/s, 60 m/s, 90 m/s. The nozzle configuration has been kept the same for the whole test. Central nozzles have been chosen in number of 4 and 5, depending on the spray bars, to keep the configuration symmetrical to the vertical medium plane of the tunnel. Three different combination of water/air pressure have been chosen to have low, medium and high LWC with droplet size of 20 and 40 micron. The test has been structured as follow:

1. To measure the distribution of each spray bar for each of the velocities and for each of the three different LWC settings with droplets size of 20 micron. One spray bar at time has been switched on spraying water with all the others spray bars spraying air. The results would represent the individual contribution of the bars to the LWC in the test section with all the bars contributing to the turbulence modulation.[1]
2. To measure the influence of the neighbouring nozzles/bars on the dispersion of the water droplets. In this case the central bar only, (bar 3), has been used spraying water, with the neighbouring bar, (bar 2 & 4), spraying air sequentially. Two combination of air/water pressure have been chosen, low and high. The test has been repeated for two different droplets size of 20 and

[1] The Gaussian function represents a special distribution widely analysed and discussed in the literature of stochastic particle dispersion. It is the typical profile that is associated to a stochastic Langevin equation, for the motion of particles, with linear drift and diffusion coefficient. This equation just take the form of the droplets equation of motion when only drag and gravity forces are considered significant. However, the nature of the stochastic methods for particle dispersion, coming from Langevin equations type and widely used in atmospheric particle dispersion, is not discussed in this thesis, but further details can be found in Gardiner [79], Thomson [80], Gillespie [81].

40 micron. The results would represent the contribution to the turbulence modulation coming from the neighbouring bars.

4.3.2 Icing blade results

The thickness of the ice, for each run, has been measured with a “cold” calliper and the values translated in LWC distribution. The typical distribution profile on the blade is well approximated by the Gaussian distribution where the standard deviation can be related to the measured Full Width at Half Maximum value. This is a parameter commonly used to describe the width of a function, given by the difference between two extreme values of the independent variable at which the dependent variable is equal to half of its maximum value, as shown in figure 4-1:

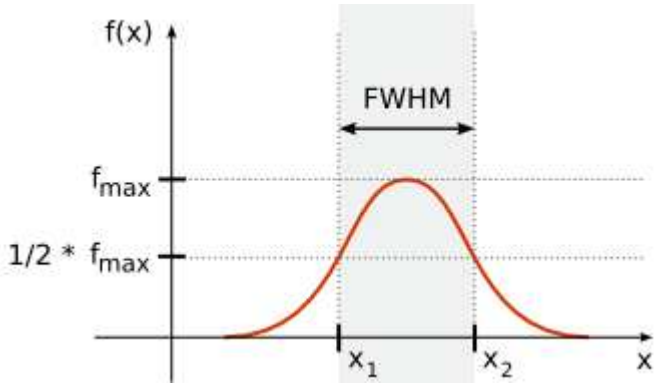

Figure 4-1: Full Width at Half Maximum

When the relation of the FWHM and the standard deviation related to the normal distribution is:

$$\mathrm{FWHM} = 2\sqrt{2\ln 2}\,\sigma \approx 2.35482\,\sigma. \qquad (4.2).$$

From the set of measurement acquired at different speeds and different combination of nozzle’s water and air pressure, as defined in the point 1 paragraph x.3.1, has been obtained a set of Gaussian-like shapes of water droplets distribution. From each of these curves the mean value and standard deviation of the water droplet cloud relative to that condition have been extracted. Typical profile acquired is shown in the next figure for the test section velocity of 40 m/s. The graphs shown on Y axis the LWC

concentration [g/m^3] and on X axis the position in the test section [m] with origin at the centre.

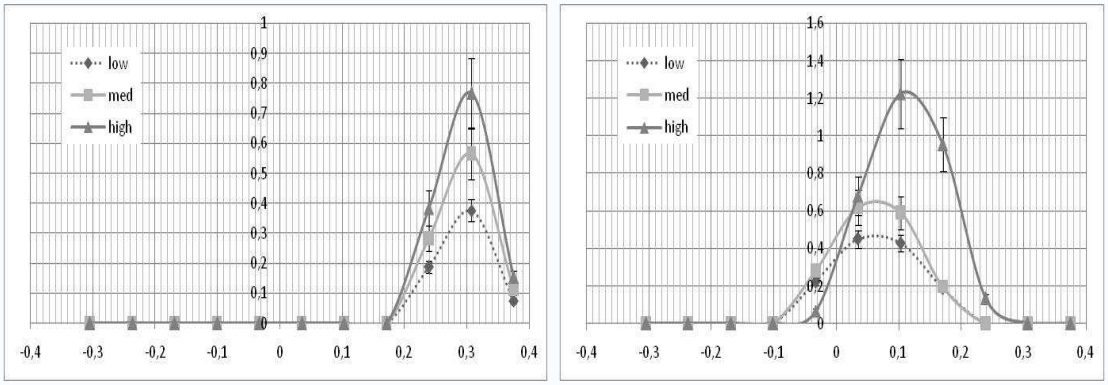

Figure 4-2 a, b: Water droplets distribution, bar 1 (a), bar 2 (b)

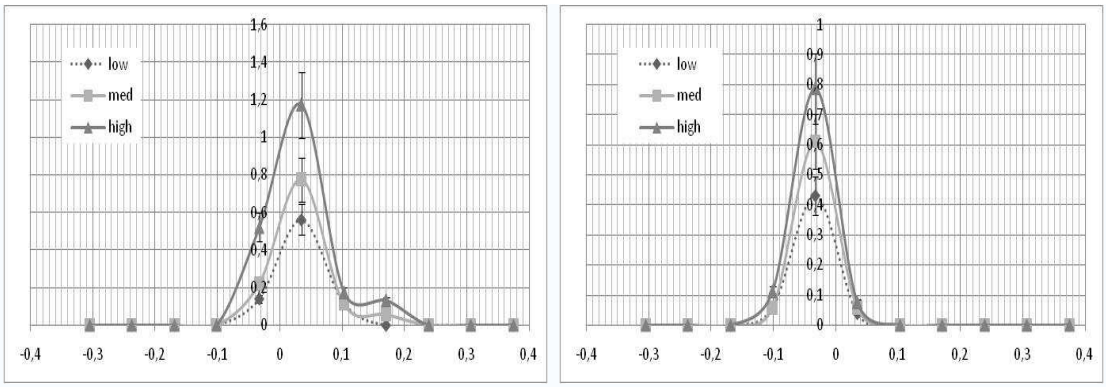

Figure 4-3 a, b: Water droplets distribution, bar 3 (a), bar 4 (b)

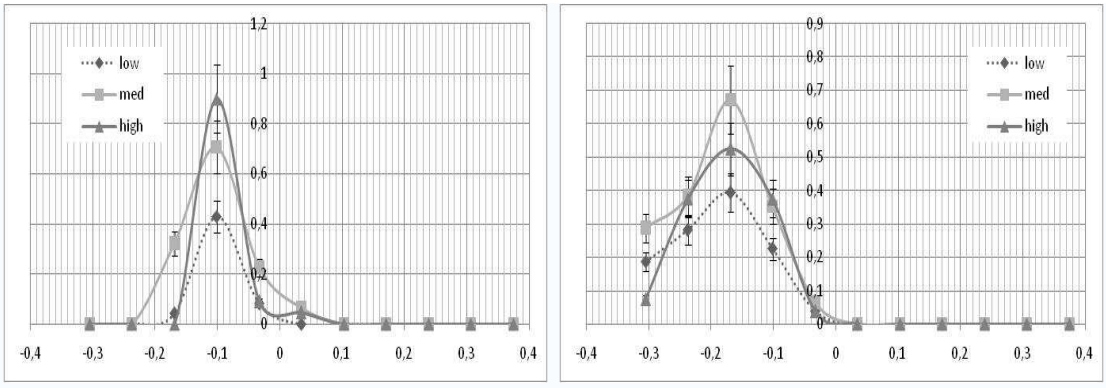

Figure 4-4 a, b: Water droplets distribution, bar 5 (a), bar 6 (b)

The single figures indicate the LWC distribution along the blade that has been marked following the vertical height of the test section. Each figure corresponds to the distribution relative to a spray bar, from the spray bar number 1 on the top left side to

the spray bar number 6 on the bottom right side. The estimation of the error associated to the LWC value has been calculated directly from the bias error affecting the thickness measurement. Considering a LWC_0 associated to a thickness ΔS and LWC_1 associated to a thickness $\Delta S + \varepsilon$, the error percentage associated to the LWC is equal to the error percentage associated to the thickness measurement:

$$\frac{LWC_1 - LWC_0}{LWC_0} = \frac{\varepsilon}{\Delta S} \qquad (4.3).$$

The error associated to the ice thickness measurement, depending on the resolution of the caliper and on the randomness related to the manual procedure, has been considered to be 15% of the mean value of the thickness. This value has been added with error bars to the LWC graphs. The figure 2 shows the position and density of the water cloud coming from the single spray bars and for different liquid water content levels.

From this type of measurement, available for the other velocity conditions, the mean cloud position and the its standard deviation, through the FWHM, can be extracted. The standard deviations of the 40, 60, 90 m/s conditions, normalized by the test section characteristic length, are shown in the next graphs:

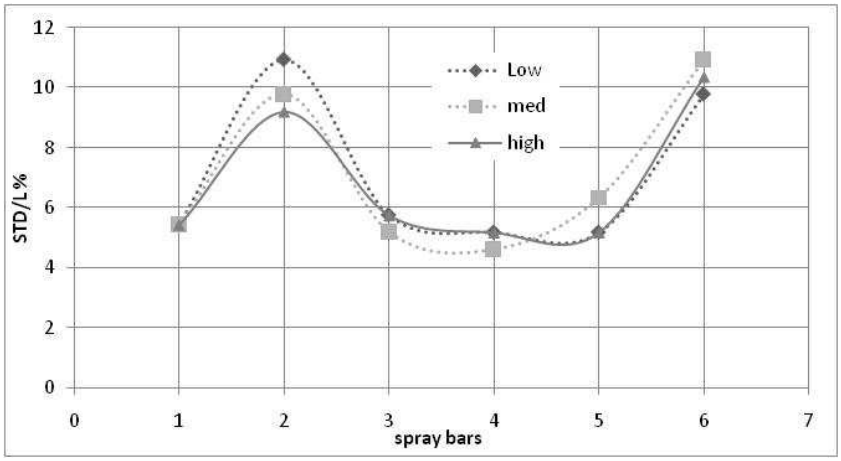

Figure 4-5: Normalized Standard Deviation vs. spray bars, 40 m/s

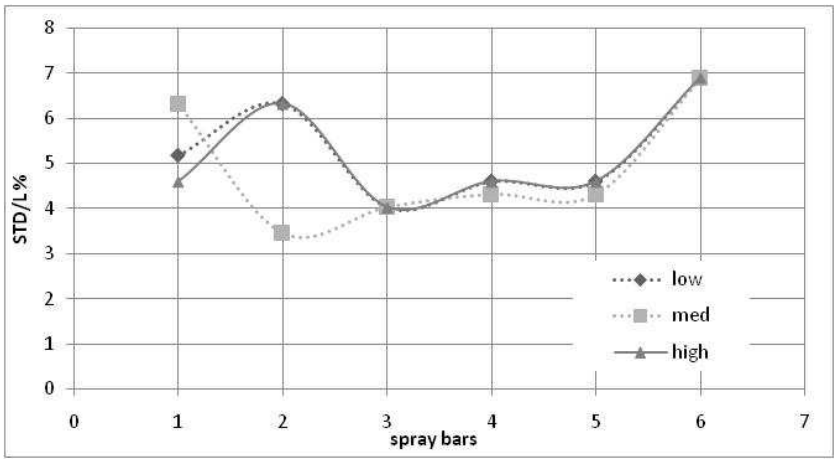

Figure 4-6: Normalized Standard Deviation vs. spray bars, 60 m/s

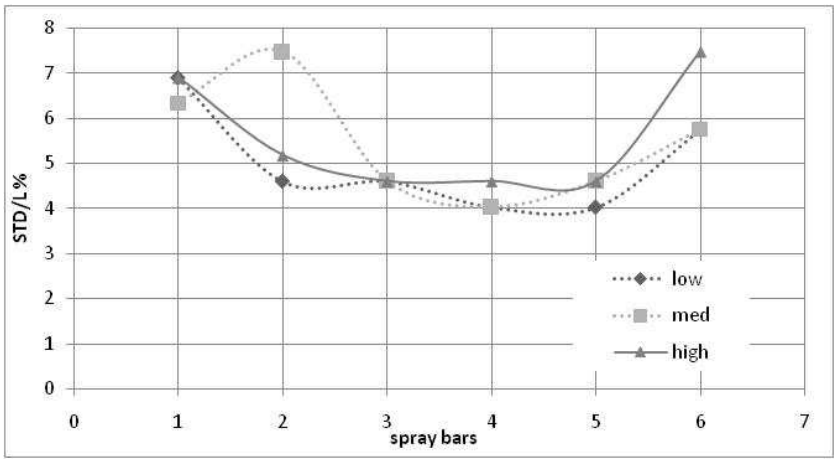

Figure 4-7: Normalized Standard Deviation vs. spray bars, 90 m/s

From the figures it can be seen that the standard deviation increases at the extremities of the test section and is smaller generally in the centre region. Typically the bottom of the tunnel, covered by the spray bars number 4, 5 and 6, showed a wider distribution of the icing thickness. It can be seen also from the figure 4-4 that the distribution of the bar 6 does not go to zero at the extremity but tend to go to a constant non-zero value indicating a presence of a constant small ice thickness on the blade. The trend of the standard deviation also shows a non monotonic behaviour with the liquid water content value and then with the nozzle air pressure. In the centre region the influence of the nozzle air pressures chosen are often indistinguishable. However, depending of the Icing Wind Tunnel geometry and configuration, the nozzle air pressures may affect the distribution of water droplets in the test section, through a changing on the local turbulence level, and the results coming from this experiment has to be considered in relation to the value chosen in this test matrix.

To investigate a possible effect of the air coming from the neighbouring nozzle on the water droplet distribution a test has been done following the test matrix indicated at the point 2 paragraph 1.3.1. The central spray bar three has been used spraying water while the neighbouring bars, respectively two and four, have been used to spray water sequentially. The effect on one bar at time has been considered first and then both the bar two and four have been used at the same time spraying air. The test has been done at 40 m/s speed only and with the two extreme value of liquid water content, indicated with “low” and “high”, previously chosen. The nozzle air pressure has been chosen respectively of 23.5 and 24.1 psi and the water pressure adjusted to get water droplet of 20 micron first and then 40 micron. The results are summarized in the next figure:

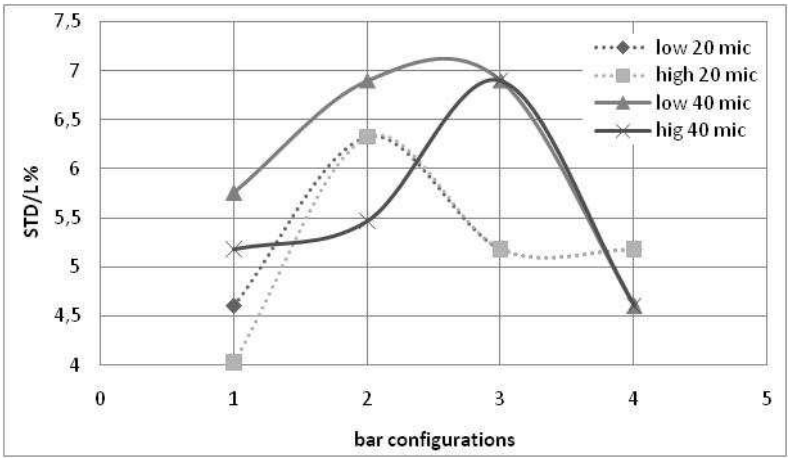

Figure 4-8 Normalized Standard Deviation vs. spray bars, 20/40 microns

The bar configurations 1, 2, 3, 4 correspond respectively to the use of bar 3 only, bar 3+2, bar 3+4, bar 3+2+4. For the 20 micron droplets the effect of the neighbouring jets is to increase the standard deviation with the major contribution given by the jet coming from the bar two only. When combined the neighbouring jet give a reduced contribution on the spread of the water cloud. This may be given by a “squeezing” effect of the two jet that overcome the general increasing in the local turbulence filed that contributes to improve the water droplets dispersion. For 40 microns droplets the contribution of the single jets is to increase the standard deviation of the distribution where the effect of the jet coming from the bar 2 is less significant with higher liquid water content. When combined, in this case, the neighbouring jets reduce the spread of the cloud respect the baseline configuration suggesting that the “squeezing” effect

is in this case less balanced by the local turbulence. However, for the configuration chosen was not possible to identify a monotonic trend describing the interaction of the neighbouring turbulence with the water spray.

The icing blade test has been performed also for the horizontal distribution of water droplet at the condition of 40 m/s with the same three different level of liquid water content used for the vertical distribution measurements. The nozzle configuration has been kept the same of the vertical measurements and the horizontal distribution is, in this case, given by the combined effect of four or five central nozzles, depending on the spray bar. It was not possible to acquire the distribution profile of the bar one due the difficulties to place the icing blade at the desired position through the test section. The results of the bars from two to six (top left to bottom centre) are shown in the next figure:

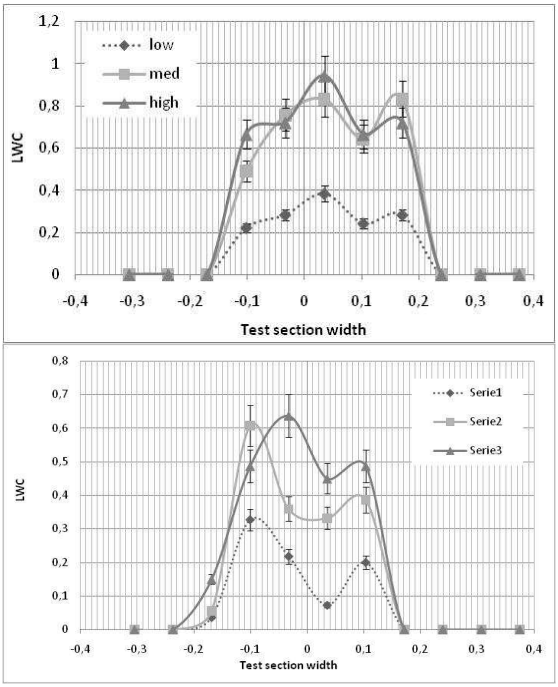

Figure 4-9 a, b: LWC horizontal distribution, bar 2(a), bar 3 (b)

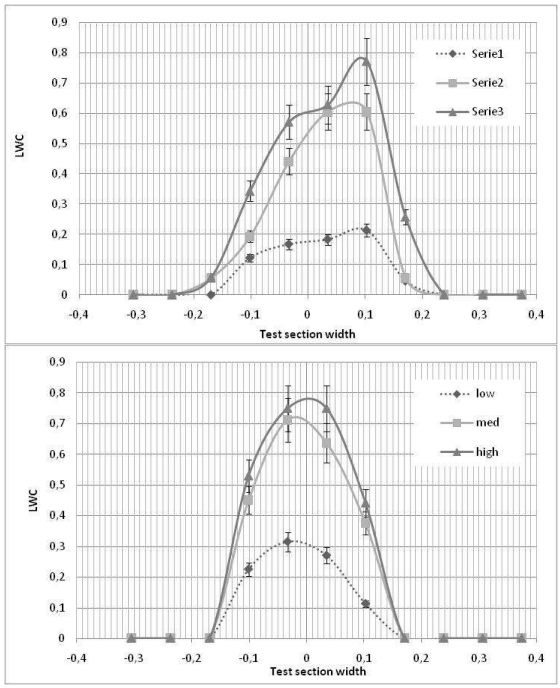

Figure 4-10 a, b: LWC horizontal distribution, bar 4(a), bar 5 (b)

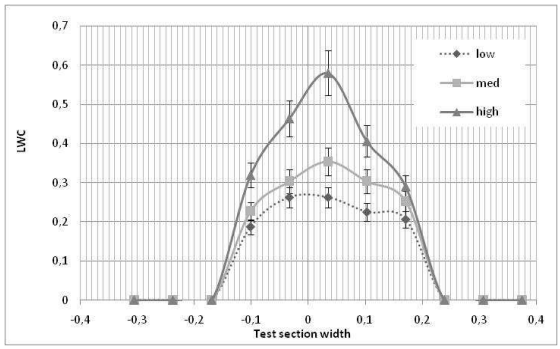

Figure 4-11 : LWC horizontal distribution, bar 6

In this case the total distribution is the result of the overlapping of the individual distribution coming from the single nozzles. Generally it can be considered dependent on the individual standard deviation and on the relative nozzles spacing. The effects of these parameters are then discussed in the next paragraph.

4.3.3 Consideration on the total water distribution

As first approximation the mean position of the cloud can be considered to be transported by the aerodynamic streamlines within the tunnel. The variation of the

centre of the cloud along the blade is then proportional to the aerodynamic projection of the spray bars mutual distance from the spray bar plane to the test section plane. Depending on this variation different overlapping regions can occur, producing a total water distribution with variable uniformity. The next figure shows the total distribution calculated from measurements of single distributions for the condition of 40 m/s at different level of LWC:

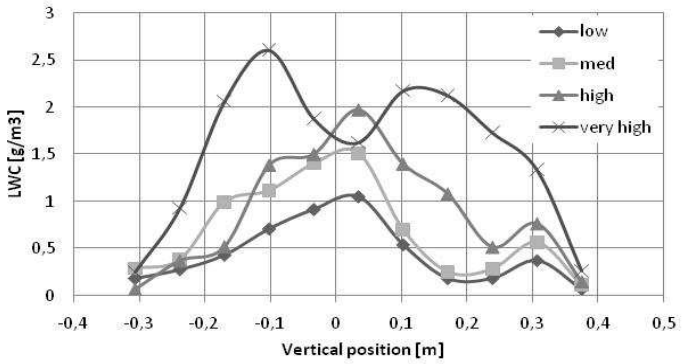

Figure 4-12: LWC distribution for different LWC conditions

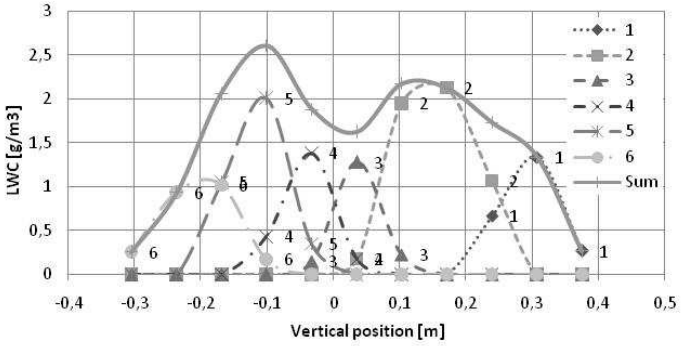

Figure 4-13: Spray bar contribution to LWC distribution (very high LWC)

The uniformity improves as long as the LWC and then the air pressure coming from the nozzle increase. For very high value of nozzle air pressure, in this case until 30 psi, the total distribution improves as a consequence of the increasing of the standard deviation of the distribution coming from a single spray bar. The standard deviation is in turn dependent on the local turbulence level seen by the cloud that can be affected by the nozzles air pressure. For the condition of very high LWC the contribution of the single distribution are shown in figure 4-13. The higher standard deviation of the spray bar two and five contributes to a better uniformity spreading the LWC over a

wider length but at the same time the higher peak of their relative LWC gives the opposite effect.

The total distribution, sum of the single spray bars distributions, can be pictured as function of the standard deviation of the single component, the overlapping region and the total LWC value of the single component. The total amount of water coming from the nozzle is dependent on the nozzle water mass flow as a function of the nozzle water pressure. Typically, the spray bar systems used in Icing Wind Tunnel have the same water pressure along each single bar. In this way the nozzles connected to the bar provide the same water mass flow once the pressure has been chosen. For each single bar, then, the peak of liquid water content and the standard deviation of the distribution are related and are not independent variable. The possibility to change independently the overlapping region is something that can be generally done, in discrete way, switching on/off the nozzles of the spray bar (controlling the horizontal overlapping), or moving vertically the spray bars and controlling the vertical overlapping. To analyze the effect of the overlapping region and the local standard deviation on the total distribution a simplified case is considered.

Two distributions of LWC have been arbitrarily chosen, respectively the bar three and four at 40 m/s, and summed each other to obtain a total distribution. The sum has been repeated for different values of overlapping regions, defined here as the distance between the mean values of the distributions, and scaled with different values of standard deviation of the bar four distribution. In this way the distribution of the bar three has been kept constant and the distribution of the bar four act as a parameter. The quality of the uniformity of the total distribution has been quantified by the fourth order statistical moment of the total distribution i.e.: kurtosis. It can give an indication on the "peakedness" of a probability distribution of a real-valued random variable. The Gaussian distribution has a kurtosis equal to 3. Values higher than that indicate generally more "peaked" distribution respect the normal one, while lower values indicate a tendency to a more "flat" distribution. The figure 4-14 shows an example of the total distribution when shifting the bar four respect the mean position of the bar three:

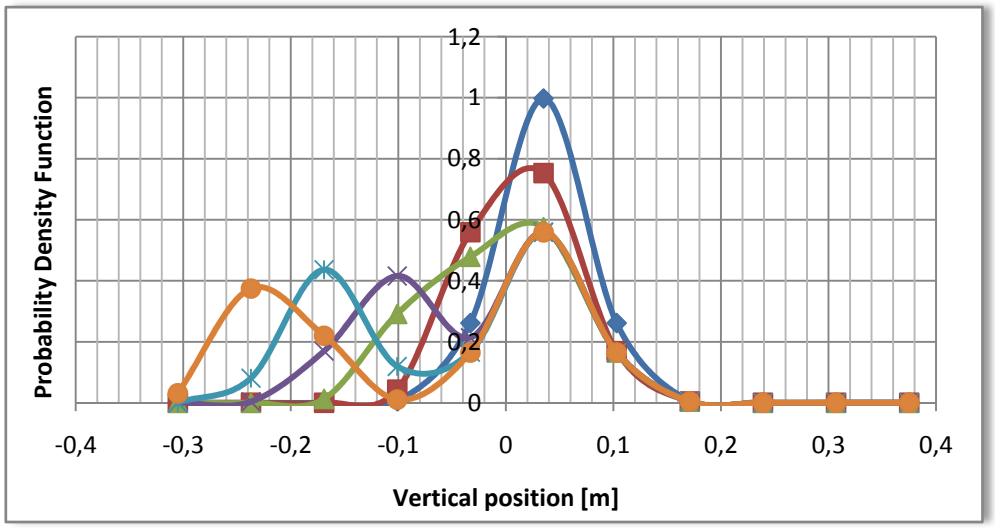

Figure 4-14: PDF for relative shifting of bar 4 to bar 3

Results in terms of kurtosis as function of the difference between the centre of the distributions and parameterized by the standard deviation are shown in the next figure:

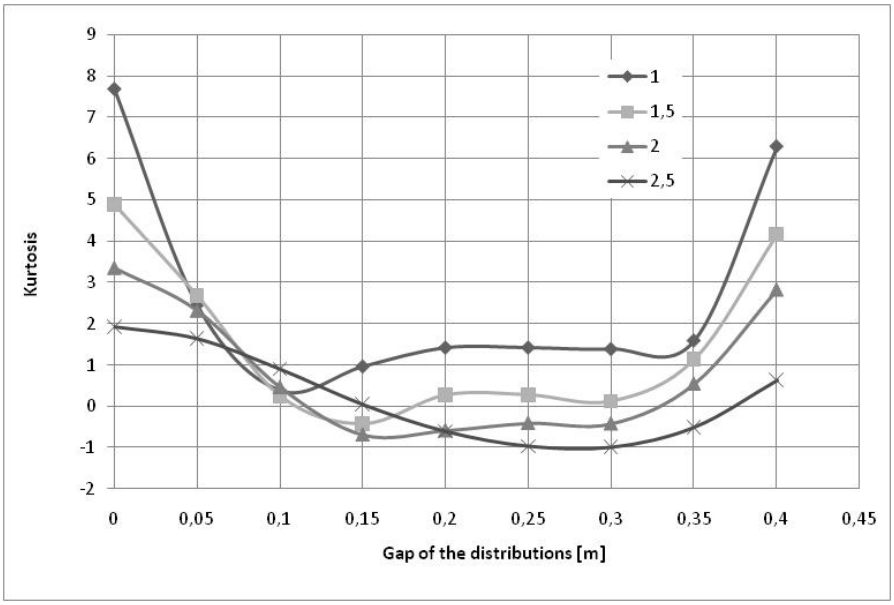

Figure 4-15: Kurtosis vs. Distance between mean of distributions

The trend of the kurtosis for the case of figure four is shown by the curve with the baseline standard deviation i.e.: 1. It can be seen that depending on the standard deviation of the distribution and then depending on its spread, the minimum value of

the kurtosis, indicating a more “uniform” distribution, moves on higher value of distance of the centre of the distribution.

4.4 Water distribution within the nozzles in the near field

4.4.1 Introduction

In the general approach of finding a methodology for water droplets distribution prediction, as has been discussed in the previous chapter, different regions of the tunnel should be separately and specifically investigated in order to get the necessary information to synthesize the physics of the problem accordingly to the practical requirement of the numerical models used for engineering calculation.

To analyze the behaviour of the spray in the near nozzle field the measurement of the water distribution of the spray, expressed in terms of LWC, has been performed with a thermal probe. The icing blade could not be used in this case to extract the water droplets distribution because there is not sufficient time for the droplets to be supercooled before the impact on the blade. The characterization of the water distribution allows for estimating the spread and the diameter of the nozzle jet and to have an indication on its angle through the calculation of the FWHM value for the distribution.

The spray angle is the opening angle which the nozzle jet of droplets forms at the moment when it leaves the nozzle orifice and it is one of the fundamental parameters characterizing of a given nozzle. In fact the amplitude of the spray angle determines, in connection with the distance between the nozzle orifice and the target to be covered, the spray coverage and the density of liquid sprayed with respect to the cover area. It is important to note that, because of several factors like gravity forces and aerodynamic drag, the initial spray angle value cannot be maintained but in a limited distance from the orifice. The spray angle is affect by the local interaction by nozzle air jet and nozzle fluid jet and by the characteristic of the fluid. Depending upon the type of nozzle, a different percentage of the available energy is used to break up the

jet and give the desired spray pattern and spray angle. The transfer of the energy from air jet to the liquid film and then to the liquid ligaments and droplets depends on the characteristic aerodynamic design of the nozzle and also the local nozzle turbulence field.

The characterization of the nozzle behaviour in terms of the spray angle and consequent spray diameter can be considered then as a simplified approach to synthesise phenomena typical of internal and very local nozzle performance. The measurement of the jet diameter has been done, within this work, to have information of the spray characteristics to be used and compared with the numerical results coming from the CFD calculation and also to investigate the behaviour of the nozzle spray with different icing tunnel operating conditions

4.4.2 Description of the thermal probe

A method of measuring the LWC was an RAE/Plessey thermal probe [59], showed in the next figure. RAE (Royal Aerospace Establishment) refers to a previous name of the organization of what is now called QinetiQ. The probe was originally developed for helicopter icing flight trial use but was never taken forward into commercial production.

Figure 4-16: RAE/Plessey thermal probe

The probe operates by measuring the power dissipation from a cylindrical probe maintained at near constant temperature (~70° C). To achieve this, a semiconducting Barium Titanate ceramic is used which has a positive temperature coefficient of resistance (PTCR) that allows it to be thermally self-stabilizing. For a constant supply voltage, the current varies with the ambient conditions. Changing in the electrical resistance of the probe as a function of the heat loss rate due to the evaporation of water droplets from the surface of the cylinder can be used to measure the amount of flowing water. The LWC can therefore be deduced from the power dissipation, which increases with LWC owing to the additional energy required to evaporate the impinging water droplets. When the LWC rises above a certain level, the power supplied to the probe head is insufficient to evaporate all the water film, rendering the output inaccurate [60].

The probe utilizes the relative large cooling effect due to the evaporation of the droplets of liquid deposited on the surface of the ceramic cylinder from an impinging gas stream, compared with the cooling effect of convection, conduction and radiation. The device requires relative movement between the probe and the gas for the measurement of the liquid water content to take place. In the Icing Wind Tunnel test the probe would be directly exposed to the wind tunnel flow with water cloud conditions and connected to an electrical power supply able to provide and shown the amount of power and current used.

When a potential difference is applied to the ceramic cylinder the initial current is large and the resistivity of the material is low. The heat loss on the surface of the material at constant temperature is balanced by the electrical power input. If the potential difference increase to a sufficient high level, the joule heating effect raises the temperature of the ceramic material to the value where the slope of the resistivity/temperature function is very high. At this temperature a small change in ceramic temperature would give large change in resistance and large change in dissipated heat. Therefore, large changes in heat lost at the ceramic surface can be tolerated with only small changes in ceramic temperature. At the same time any increase or decrease of the heat dissipation causes a corresponding increase or decrease in current flowing to the material and then a change in power dissipated. In this condition the ceramic material behaves like a self-stabilizing material tending to

stabilize at specific temperature that is generally dependent on the potential difference applied and on the ambient condition at the surface of the ceramic cylinder.

4.4.3 Description of the test

To measure the distribution and then the dimension of the cloud of water coming from the nozzle the thermal probe has been placed to a reference distance from the central nozzle and moved normally to the nozzle axis spanning the whole area covered by the spray. The electrical signal recorded by the probe has been acquired at discrete stations in order to mapping the water distribution of the spray. The reference distance has been chosen to ensure enough spread of the jet, to provide a reasonable spatial resolution with the thermal probe measurement and also to be able to obtain a description of the spray close to a plane already used for airflow quality measurement with the hot wire probe.

Generally, distance too close to the nozzle, with smaller cloud diameter, could have been affected by higher uncertainty due to the probe spatial resolution. At the same time too high local water mass fraction could have affected the reading of the probe if the power supplied had been insufficient to evaporate all the water on the probe surface. Based on the previous icing tunnel testing experience and based on visual indication on the behavior of the spray the distance approximately of one meter downwind the spray bar has been chosen. The probe has been inserted longitudinally in the tunnel as shown in the following figure:

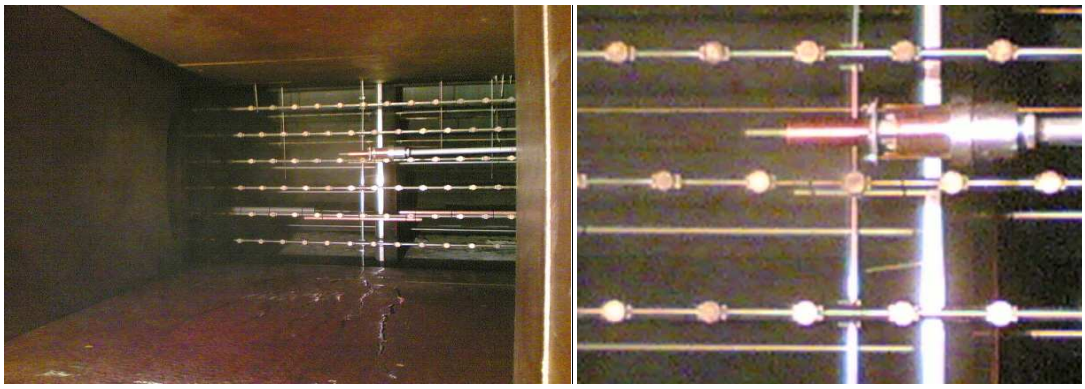

Figure 4-17: probe positioning within the tunnel

The test has been performed with droplets size of 20 microns and repeated for different tunnel operative conditions, respectively:

- Only the air coming from the nozzle and three values of LWC
- The test section velocity of 40 m/s and three value of LWC
- The test section velocity of 60 m/s and three value of LWC

For each run the values of the current intensity in dry condition have been acquired as baseline and then subtracted to the values recorded in wet spraying conditions. During the test, the probe has been visually checked to verify that no water film was present on the surface and all the mass of water impinging was evaporated.

4.4.4 Results of the test

The LWC distribution has been measured at different stations moving the probe through the area covered by the spray. The power supplier has been fixed to a constant voltage and the current intensity has been recorded as indication of power changes due the heat losses. Though a rigorous error analysis for the equipment used was not available, the data has been recorded in order to check repeatability of the test and the statistical convergence of the data series. The results are expressed in terms of distribution of the current difference by the baseline dry condition, where only the convection heat exchange is considered and the wet condition with the nozzle spraying respectively at three different value of LWC corresponding to air pressure of 24psi, 26psi, 28psi. The following figure shows the current distribution when only the air coming from the nozzle is flowing through the probe and the tunnel flow is off:

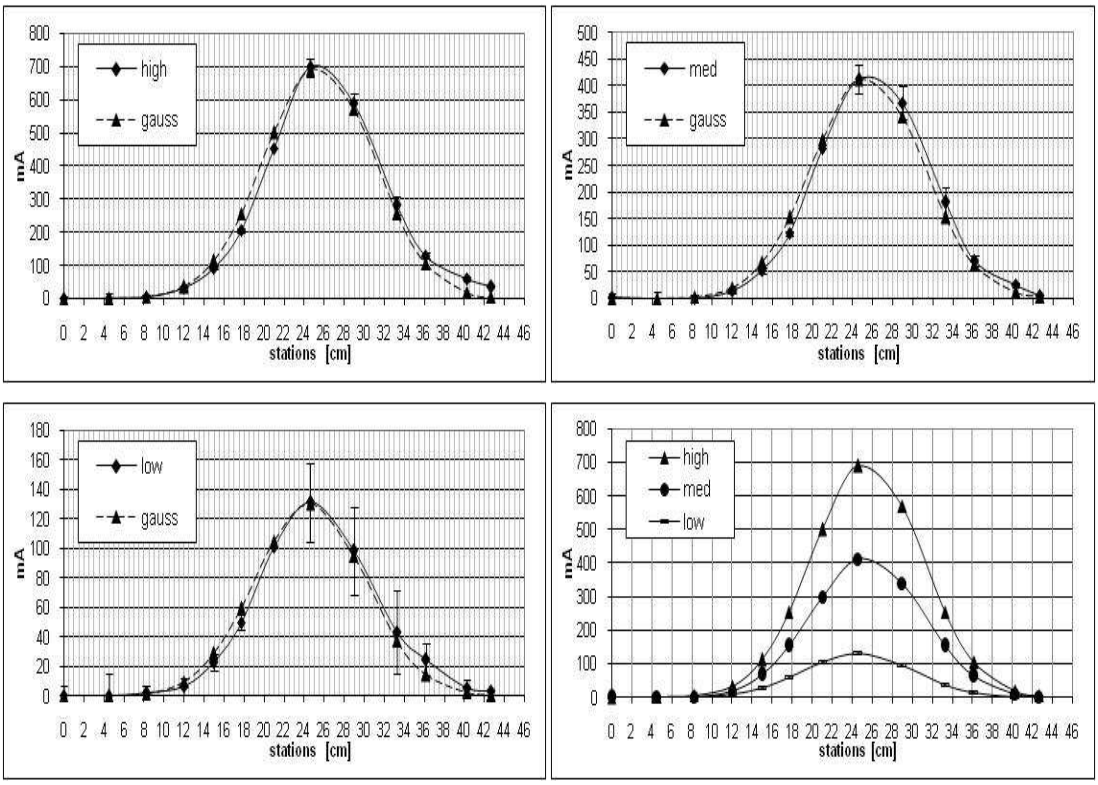

Figure 4-18: Ampere readings vs. Traverse distance

The figure 4-18 show the trend of the distribution, expressed in milliampere, as function of the marked distance of the support. The distribution is shown to be well approximated by the Gaussian distribution (last picture) with standard deviation calculated from the FWHM parameter. Without the airflow of the main tunnel the standard deviation takes values around 5 cm and it is approximately constant for the three values of LWC and then of the air pressures. This would suggest that the higher energy injected by the higher air pressure is proportionally used to break up the ligament of the increased mass flow of water flowing through the nozzle, but the resolution of the measurement only allow to have a preliminary indication on this aspect. The error of the measurement has been considered to be represented by the statistical error associated to the series of the data and with a confidence level of 95% and it is added to the graph with the error bars.

The next figure shows the results of the measurement performed at the test section speed of 40 m/s:

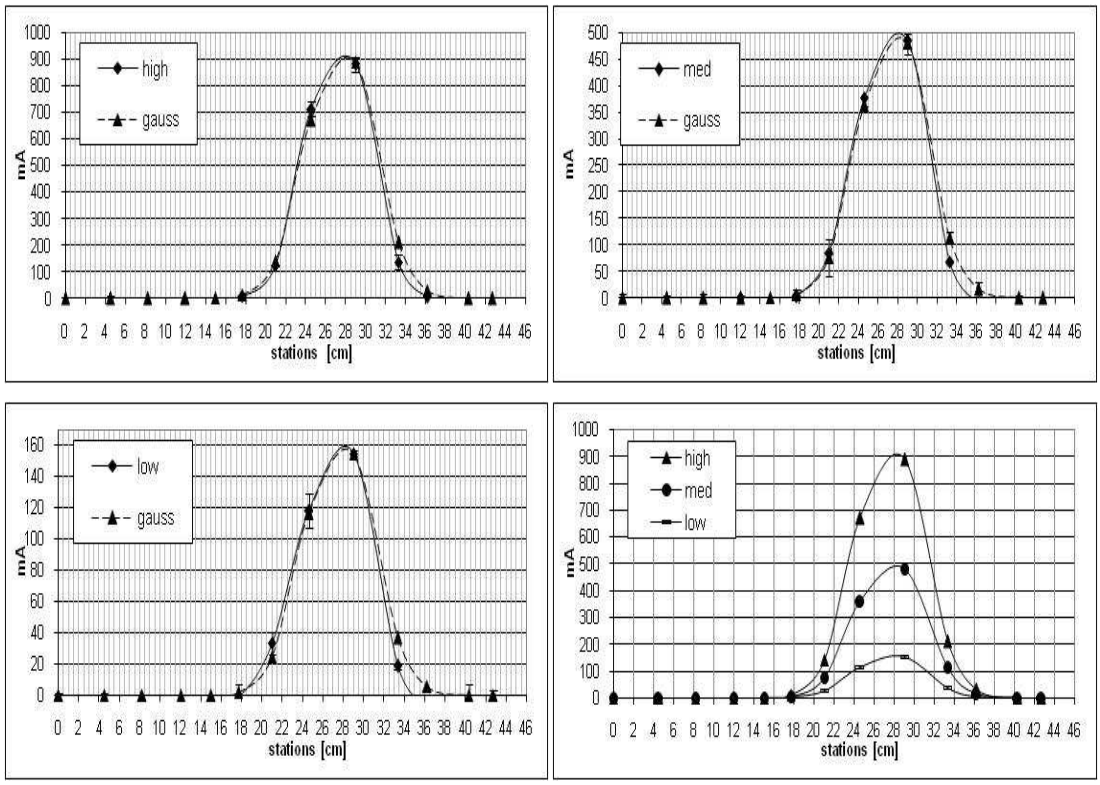

Figure 4-19: Ampere readings vs. Traverse distance, 40 m/s

Also in this condition the distribution is well approximated by the Gaussian shape. The standard deviation is reduced respect the condition at zero tunnel speed by the squeezing effect of the tunnel airflow. In this case the values of the standard deviation are around 3,3 cm and are mainly constant with the nozzle air pressures. The measurement in this condition showed a good repeatability with lower statistical error on the mean distribution profile.

The measurement at 60 m/s are shown in following figure:

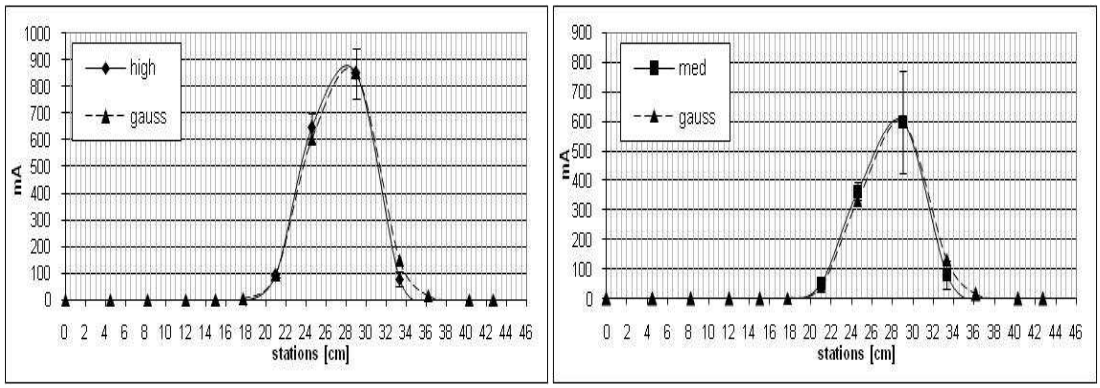

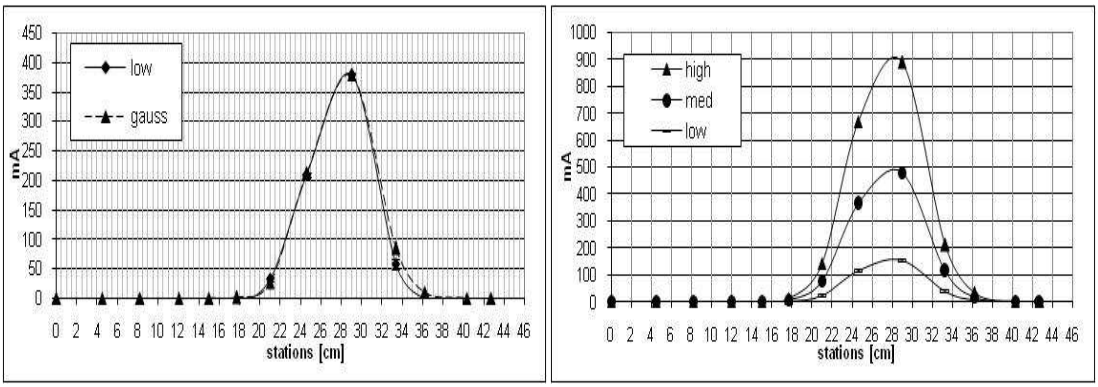

Figure 4-20: Ampere readings vs. Traverse distance, 60 m/s

The standard deviation for this condition is a bit lower of the 40 m/s condition and approximately of 3 cm. Considering the resolution of the measurement the two conditions do not show significant macroscopic changes in the LWC distribution. The effect of the increased airflow of the tunnel is in this case of the order of 10% of the standard deviation of the 40 m/s case. For the two velocity conditions tested the standard deviation of the spray can be assumed, within the limits for practical engineering calculation, to be approximately constant.

4.5 Characterization of the turbulence in the Icing Wind Tunnel

4.5.1 Introduction

The CFD calculation for particle dispersion generally requires the flow boundary condition necessary to specify the problem considered. In the Icing Wind Tunnel case the geometry of the problem, as will be described further, can be reduced to considering the part of the tunnel from the spray bars, specifying the water droplet source (injection), to the test section, characterizing the target location of the problem. As typical in turbulent flow, the models require, in parallel with the conditions of the main flow velocity, also the turbulent characteristics generally expressed at

appropriate points in the domain. For Icing Wind Tunnels they can be generally specified at the input flow plane/ domain.

The particles dispersion, whatever model is considered, is strongly influenced by the turbulence properties, defining intensities and characteristic scales, of the carrier phase. As has been discussed in the chapter 4 the stochastic dispersion models based on the Eulerian-Lagrangian approach all require turbulence statistics to calculate the fluctuating velocity component of the carrier phase at the discrete particle position. Using the RANS equation the evolution of turbulence statistics, at least for the low order ones as the turbulence kinetic energy, can then be tracked once specified an appropriate input condition.

In the optic of a general methodology, the choice of the approach to characterize the turbulence has been driven by the requirement to synthetically describe the physics phenomena that would affect the water droplets dispersion within the tunnel. The choice of the approach has also to consider a level of complexity of the description of the physics that can be conveniently utilized and coupled with the numerical models for particle dispersion, avoiding energy and time consuming approaches. The main objective of the selected approach is then to acquire a turbulence profile that given as input condition to the RANS solver, as turbulent kinetic energy and dissipation rate profile, could specify the turbulence history.

4.5.2 Aim of the test

The jets coming from the sprays in the Icing Tunnel configuration, as discussed in the chapter 2, are a source of turbulence that affect the aerodynamics characteristics of the near nozzle field. Generally the interaction between the nozzles air field and the main tunnel airfield can be considered depending on the tunnel geometry, the nozzles characteristics and the typical operating regimes of the tunnel. The combination of those contributions is typically non linear and very often is unpractical to derive a trend of their effects by macroscopic/definition of the parameters. The air coming from the nozzles, however, can in principle affect the turbulence field within the whole tunnel contributing to the water droplets dispersion. Therefore, the nozzle's air

effects should included in the synthetic description of the turbulent field specified for numerical calculation.

To investigate the effects of the nozzles on the aerodynamic of the main tunnel air flow, to be included in the characterization of the turbulence inlet profile needs by the CFD simulation, the turbulence measurement can be generally acquired in a plane downwind the spray bars. The results of this type of test is not only to have an indication of the contribution of the nozzle air pressure of the turbulence trend but also to provide, as will be described further, an input turbulent condition that can include, though in a simplified form, the nozzles contribution. This approach is also driven by the intention to characterize and reproduce the nozzle spray effects by experimental information simplifying the cost of the consequent numerical procedure.

The measure has been acquired in a plane one meter downwind the spray bars. Considering a typical cone spray angle, at that location the jets coming from of the singles nozzle start to mix. The dry condition has been chosen and only the contribution to the air coming from the nozzle has been added to the main flow. Two main velocity has been tested, respectively 40m/s and 60m/s test section velocities, each of that with three different liquid water content. Different LWC represent different air pressure of the spray bars. A number of 3x3 points, on a normal plane to the axis, has been measured for each condition.

It was not possible to acquire data for test section velocity of 90 m/s due the short life of the probes in that conditions. It has to be noted that also if the local speed at the probe position was much less than that and well in the range of the velocities supported by the probe, persistent problems of breakage of the probes have been experienced in that conditions.

4.5.3 Constant Temperature Anemometer (CTA)

The measures of turbulence have been acquired with Constant Temperature Anemometer, with measuring chain shown in figure 16a, with single-sensor straight wire Dantec Dynamics (55P11) connected to an acquisition card Keitlhey (KPCI-

3101) with maximum sampling frequency of 225 KHz. The hot-wire anemometer is a transducer that senses the changing in heat transfer from a small electrically heated sensor exposed to fluid motion. Its operation relies on the variation of the electrical resistance of the sensor material with temperature due to the cooling effect of the flow. When the temperature, composition and pressure of the fluid are constant the only variable affecting heat transfer is the fluid velocity. The hot-wire anemometry is popular due to their small size which results in high spatial resolution and little interference to the flow, a high-frequency response, a high sensitivity at low velocities, generally low cost, and an output signal in the form of voltage that can be easily recorded and stored for convenient data analysis.

When a current is passed through wire, heat is generated. During equilibrium, the heat generated is balanced by the heat loss (primarily convective) to the surroundings. If the velocity changes, then the convective heat transfer coefficient will also change resulting in a wire temperature change that will eventually reach a new equilibrium with the surroundings. These equilibrium points, in static conditions, are usually recorded and plotted as wire voltages versus fluid velocities to obtain the static calibration curve.

In the reality the wire would be exposed to flow conditions that are typically unsteady and would present a wide range of frequency of characteristics fluid velocities variations. When the wire is exposed to these changes in flow velocity it will not react instantaneously to the fluctuations due to its thermal inertia. This will dampen the variations in wire resistance (and then in wire voltage) resulting in measured flow fluctuations smaller than they actually are. The wire response would then be too slow for most turbulence studies, and compensation in the electronics circuit of the anemometer is therefore necessary. The constant temperature anemometer uses a feedback amplifier to maintain the average wire temperature and wire resistance constant {i.e., $dT/dt = 0$}, within the capability of the amplifier. In this case the changes in wire resistance due to the velocity fluctuations would be quickly compensated by increasing in the wire current produced by the current regulating amplifier. Because of the high gain of the current regulating amplifier, a condition of bridge balance exists, which is practically independent of the flow velocity past the wire. The wire time constant is thus reduced by a factor of several hundred times from

fractions of a millisecond to some few microseconds. The practical upper frequency limit for a CTA is the frequency at which the feedback amplifier becomes unstable. The probe current is represented by the voltage drop across the bridge.

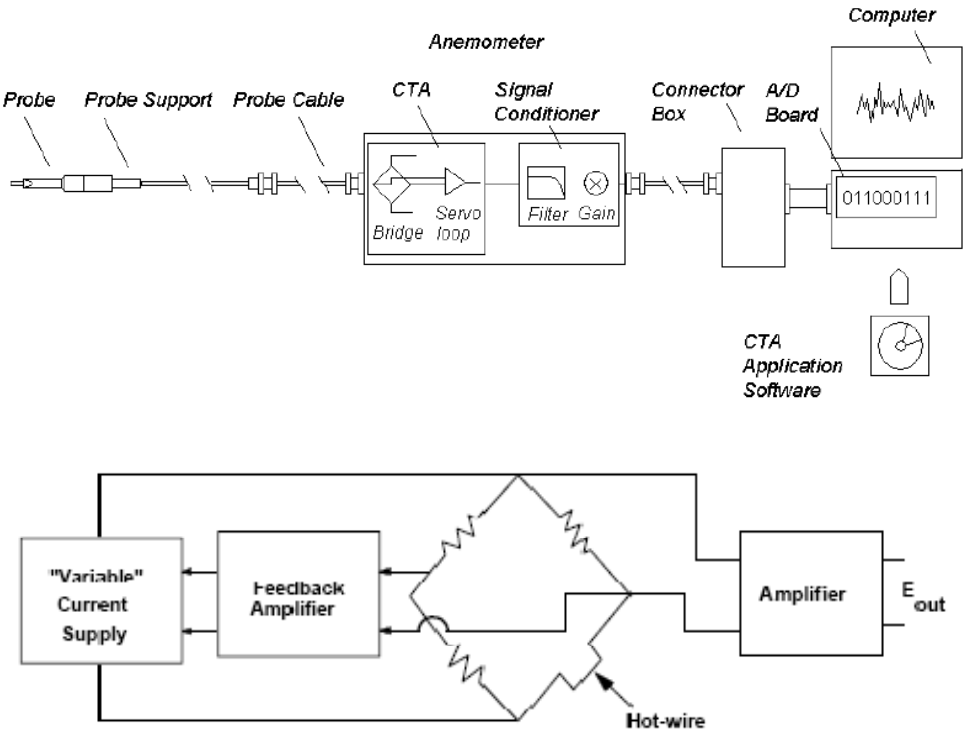

Figure 4-21: CTA scheme and amplifier bridge

4.5.4 Selection of the hot wire probe

The selection of the type of probe is generally based on the flow regimes and on the turbulence statistics required from the measurements. From an engineering point of view these requirements have to be coupled also with the aspects and problems related to the design of the experiment in order to reduce its complexity and increasing its robustness and repeatability. In this work the selection of the probe suitable to acquire the turbulence statistics has been done as compromise between the level of information measurable to have a description of the turbulence field sufficient

for CFD calculations, the requirement of simplicity to get that information and the availability of the instrumentation.

To fully characterize the turbulence flow field the components of the Reynolds stress tensor would be required and the calculation of the second orders cross moments would then require simultaneous measurement of the fluctuating components along the three axis of the reference fame. Despite the advantage to have a fully description of the instantaneous velocity components in the 3D space, this measurement, performed with triple-wire probes, would have increased the cost and the complexity of the experiment beyond the limits dictated by the scope of this work.

As has been described in the previous chapter, for engineering calculation of water droplet dispersion, the stochastic Lagrangian models, based on the two-equation turbulence models, typically consider the airflow velocity fluctuation to be proportional to the turbulent kinetic energy with the further assumption of isotropy. In this case nor the detailed description of the trace of the Reynolds tensor, neither its evolution along the tunnel is required for droplets trajectory calculation. A detailed description of the inlet profile of the fluctuating component along the three direction of the reference frame would then be lost in the further numerical calculation.

The assumption of isotropy can simplify the measurement of the turbulence to one-component measurement, allowing from that to define the turbulent kinetic energy and dissipation rate required as input condition. This measurement is typically performed with a single-straight hot wire probes, which can be repaired and are the most affordable sensor type, with the advantage to sensibly reduce the complexity and the cost of the experiment. Though the turbulence is a typical three dimensional phenomena, in the case of an Icing Wind Tunnel where the spray bars are usually placed close the settling chamber the assumption of isotropy in that particular region can be considered reasonable within the aim of this work.

When the Reynolds Stress model is used as turbulence closure model the water droplets trajectory can, in this case, be affected by anisotropic characteristic of the carrier phase. In this case the evolution of the Reynolds tensor component is calculated and a detailed input condition for those would be, in principle, an

advantage for the further solution. However even with the Reynolds Stress model it is possible to specify the turbulent kinetic energy and dissipation rate as input condition leaving the geometry of the computational domain to further define the anisotropic part of the final solution. Considering reasonable the assumption of isotropy at the measurement region, the same input condition can be used also for the Reynolds Stress model and the single-straight wire has been chosen for the turbulence test performed in the Icing Wind Tunnel.

4.5.5 CTA calibration

High-quality measurements using hot-wire probes require an accurate calibration procedure. The objective of the calibration is to establish the relationship between the anemometer output voltage of the sensor to the magnitude and direction of the velocity vector. The calibration is typically carried out by holding the probe stationary in a well defined flow of low-intensity turbulence. This method in which the probe is held stationary in a moving fluid or traversed at constant speed through a quiescent fluid is known as 'static' calibration and is the most popular [61]. The calibration in air flow is usually performed by placing the probe in the potential region of a round jet at a point where the static pressure is atmospheric or in the free stream of a turbulence free wind tunnel.

The velocity calibration of such a hot-wire probe usually consists of a series of measurements of the velocity *U* and the anemometer voltage *E*. To obtain sufficient accuracy it is common practice to carry out several readings, typically 10-20, of *(E*, U) equally spaced over the selected velocity range. The 'raw calibration data' must then be smoothed over the entire velocity range of interest, either through an interpolated 'look-up' table , or a fitted analytical function [62]. The most commonly used calibration methods are related to analytical expressions for the relationships between the velocity *U* and anemometer voltage *E*. The selection of an analytical calibration function is in general a balance between the degree of its mathematical complexity and the goodness of its fit to the calibration data [63]. In this study the Kings law has been used to relate the voltages to velocities as follow:

$$E^2 = A + BU^n \qquad (4.4).$$

Many previous investigations have shown that good approximation can be obtained with this relation [64, 65]. The calibration of the probe has been performed with a turbulence free nozzle, in the range of speeds of interest between 1 m/s and 30 m/s at standard air temperature.

4.5.6 Uncertainty of CTA measurements

The uncertainty of the results obtained with the CTA anemometer is a combination of the uncertainties of the individually acquired voltages converted into velocity and the uncertainty of the statistical analysis of the velocity series. The uncertainty of each individual velocity sample is determined by non-statistical means based on detailed knowledge about the instrumentation, calibration equipment and experimental conditions. The uncertainties presented below are relative standard uncertainties. The *relative standard uncertainty* $u(y_i)$ of a dependent variable is a function of the standard deviation of the input variance and can be expressed as follow [66]:

$$u(y_i) = \frac{1}{y_i} \cdot S \cdot \left(\frac{\Delta x_i}{k_i} \right) \qquad (4.5).$$

where $S = \partial y_i / \partial x_i$ is the sensitivity factor and k_i is the coverage factor related to the distribution of the input variance (Gaussian, rectangular etc.). The major sources of uncertainty involve calibration equipment, linearization, A/D board resolution, temperature variations during the experiment, probe positioning. The *total relative uncertainty* then becomes:

$$u(tot) = 2\sqrt{\sum u(y_i)^2} \qquad (4.6).$$

where the factor 2 express the 95 % confidence level. The relative standard uncertainties have been calculated for the whole range of velocity of interest of the case study for each of the sources listed above. Details of the procedure can be found

in Dantec Dynamic user guide [67]. Errors bars and percentage errors are shown in the next figure:

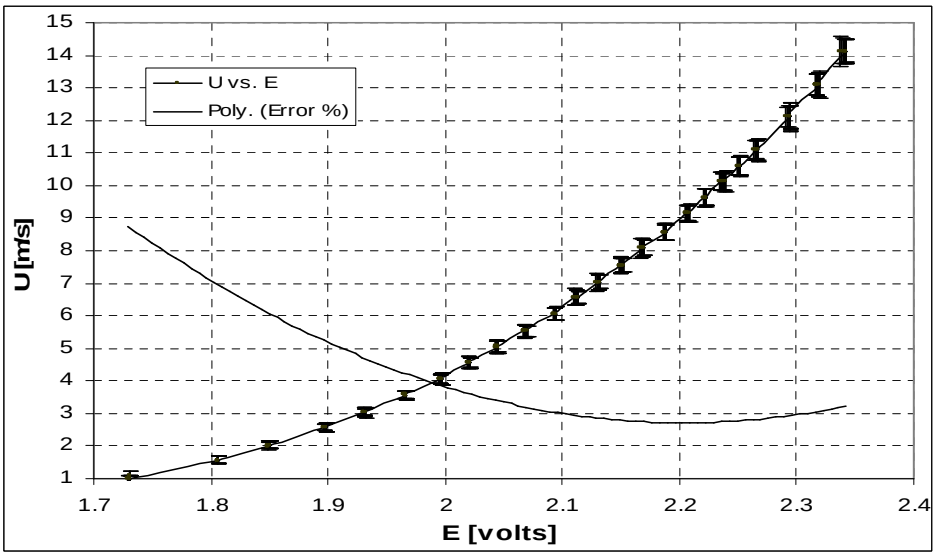

Figure 4-22: hot wire total relative standard uncertainty

Typical values of temperature variation and probe angle positioning have been chosen to be a conservative 6°C and 5° angle. The individual typical contribution of the sources of error is shown in the next table for a reference speed of 7 m/s:

Source	Input variants	Typical value	Relative output variants	Typical value	Coverage Factor	Relative standard uncertainty
	Δx_i	Δx_i	$\frac{1}{U}\Delta y_i$	$\frac{1}{U}\Delta y_i$	k	$\frac{1}{k}\frac{1}{U}\Delta y_i$
Calibration	ΔU_{cal}	0.01	$2\cdot\mathrm{STDV}(\Delta U_{cal})$	0.02	2	0.01
Linearization	ΔU_{fit}	0.0066	$2\cdot\mathrm{STDV}(\Delta U_{fit})$	0.0132	2	0.0066
A/D resolution	E_{AD} n	10 V 12 bit	$\frac{1}{U}\frac{E_{ad}}{2^n}\frac{\delta U}{\delta E}$	0.008	$\sqrt{3}$	0.0049
Temperature variations	ΔT	6	$\frac{1}{U}\frac{\Delta T}{(T_w - T_0)}\left(\frac{A}{B}U^{-0.5}+1\right)$	0.0053	$\sqrt{3}$	0.0031
Probe positioning	Θ	5	1-cos Θ	0.0036	$\sqrt{3}$	0.0021

Table 1: Hot wire sources of error

Other source un uncertainty is related to the statistical uncertainty when calculating the statistic moments from a finite length of samples acquired. The output of an how wire signal, after linearization and conversion, is generally a time-varying signal representing the instantaneous velocity component. In a turbulent flow this signal can be considered of typical random nature and statistical description is used to extract the required information. Random data observed on a finite time interval, as acquired in the hot wire anemometry, are referred to single-time history record. The collection of all possible single-time records that a process could have produced defines the general stochastic process. The general description of the stochastic process is then defined by this ensemble of the single-time records. The statistical quantities of interest can be calculated, at each time value, by the ensemble average all over the single-time record. When these statistical quantities are independent on the time the random process is said to be stationary. If the process is stationary and a single-time records, thought as ensemble of independent events, can be representative of the behaviour of the whole stochastic process, the random process is said to be ergodic. In this case the statistical moment can be calculated by averaging over the time of a single-time record. This assumption, widely used in turbulence experiments, is used in this work to compute the flow and turbulence statistic from the velocity time series acquired with the anemometer.

The calculation of the statistic moments is typically affected by the error associated to the finite length of the time series. Details of the genesis of these errors and their derivation can be found in Bendat & Piersol [68] and Bruun [69]. Only the main aspect will be discussed here. During the acquisition process the continuous signal is replaced by the discrete signal composed by the digital sample record where the number of acquired points are depending on the sampling frequency of the acquisition board and by the total time of record. The estimate for the mean value $\overline{X_e}$ and variance $\overline{x_e^2}$ of the finite sample record of length N are:

$$\overline{X_e} = \frac{1}{N}\sum_{1}^{N} X(n) \qquad (4.7).$$

$$\overline{x_e^2} = \frac{1}{N-1}\sum_{1}^{N}(X(n) - \overline{X_e})^2 \qquad (4.8).$$

Considering the probability density function of the statistically independent (N) samples to be of Gaussian type, the estimate of the mean and variance would fall within the interval defined by:

$$\overline{X_t} - \epsilon\sigma[\overline{X_e}] < \overline{X_e} < \overline{X_t} + \epsilon\sigma[\overline{X_e}] \qquad (4.9).$$

$$\overline{x_t^2} - \epsilon\sigma\left[\overline{x_e^2}\right] < \overline{x_e^2} < \overline{x_t^2} + \epsilon\sigma\left[\overline{x_e^2}\right] \qquad (4.10).$$

Where $\overline{X_t}$, $\overline{x_t^2}$ are indicating the "true" mean value and variance for an infinite length series, ϵ is a coefficient used to identify the confidence level required as expressed in the table 2 and σ is the standard deviation of the variable considered :

ϵ	Confidence level %
1.65	90
1.96	95
2.33	98
2.57	99

Table 2: Confidence levels

The uncertainty of the measurement, chosen the confidence level desired, can be determined once the standard deviation of the quantity of interest has been specified. It has been shown by Bruun [69] that the standard deviation of mean and variance can be expressed as:

$$\sigma[\overline{X_e}] = \sigma_x/\sqrt{N} \qquad (4.11).$$

$$\sigma\left[\overline{x_e^2}\right] = \sigma_x^2/\sqrt{N} \qquad (4.12).$$

Where σ_x is the standard deviation of the measured random process. The statistical uncertainty of the measurement is then related to the number of independent samples acquired during the experiment. The number of independent samples can be estimated, following Bruun [69] and Tennekes & Lumley [7], as the samples acquired every twice integral time scale. In this case, for the calculation of the statistical quantities and their relative uncertainty only the point acquired at interval time equal to twice integral scale have to be used. Generally the integral time scale is not known a priori and is has to be calculated first through the calculation of the autocorrelation function of the velocity time series.

4.5.7 CTA hardware settings

The typical hardware set-up for an hot wire anemometry package consists of an *overheat adjustment* (static bridge balancing) and a *square wave test* (dynamic balancing). When a signal filter is part of the CTA, the hardware set-up also includes *low-pass filter* and optional *gain* settings.

The overheat adjustment determines the working temperature of the sensor through the adjustment of the overheat resistor in the bridge arm, so that the wanted sensor operating temperature is established when the bridge is set to operating condition. The practical use of overheat adjustment depends on how the temperature varies during setup, calibration and experiment. When temperature variation are experienced during the test, or between the test conditions and the calibration conditions, the overheat ratio should be adjusted to minimize the effect of those variations. An alternative simplified approach consist to keep the overheat ratio constant during the experiment, recording the temperature variation and correct the anemometer voltage before conversion and reduction. This latest approach has been followed in this work. The adjustment of the bridge has been performed to keep the overheat ratio of 0.8, as suggested by the manual, with an over temperature of approximate 220°C. This ratio has been left unchanged for the whole test and temperature corrections have been applied before conversion and reduction of the data following Jørgensen [70].

The square wave test, or dynamic bridge balancing, serves two purposes: it can be used to optimize the bandwidth of the combined sensor/anemometer circuit, through changing in the bridge settings for gain, or simply to check that the servo-loop operates stable and with sufficiently high bandwidth in the specific application. It is carried out by applying a square wave signal to the bridge top. The time it takes for the bridge to get into balance is related to the time constant, and hence the bandwidth, of the system. Most CTA anemometers have built-in square-wave generators. The square wave test applied to the bridge with reference velocity of ~ 10m/s revealed a bandwidth response about 50 KHz with a stable servo-loop.

Before to digital acquire the data is necessary to analogically filter the signal to prevent the higher frequency to folding-back (aliasing phenomena). From the Nyquist-Shannon theorem the sampling frequency of the acquisition card should be the double the maximum frequency expected in the flow to properly rebuilt the original signal. Because a signal contains an infinity amount of frequency is necessary to cut-off the higher undesired frequencies to avoid that their energy is transferred to the lower ones. The analogical Low-Pass filter, employed for this operation, has then been adjusted to be the half of the digital board sampling frequency.

4.5.8 Probe positioning and Test matrix

The positioning of the probe within the tunnel has been determined in relation to the information required to characterize the turbulence profile. With the assumption of isotropy the fluctuating component of the velocity would be considered to be the same and have the same weight on the total turbulence kinetic energy (k). Because in the reality these fluctuating components would be not generally the same, the turbulent kinetic energy profile would be dependent on the choice of the measured component used for the estimation of k under the assumption of isotropy, i.e.: $k = \frac{3}{2}\bar{u}^2$ or $k = \frac{3}{2}\bar{v}^2$ or $k = \frac{3}{2}\bar{w}^2$.

With the single-straight hot wire probe it is not possible to directly measure the single component of the velocity but the quantity measured is the effective cooling velocity

U_e that is primarily affected by the velocity components normal to the wire axis [70]. In the Icing Wind Tunnel case the dispersion of the droplets and the consequent cloud uniformity is mainly required and verified in section normal to the tunnel axis. In this case, in order to have a better estimation of the turbulent kinetic energy profile for the computation of particle dispersion, the fluctuating components in a plane normal to the tunnel axis have been measured putting the wire axis parallel to the tunnel axial velocity component. The component normal to the wire axis is represented by the sum of the velocity components lying in a plane normal to the tunnel axis and, though it is not possible to distinguish the single contributes, the overall trend of the turbulence kinetic energy so estimated can be pictured to be representative of the fluctuating field normal to the axial direction experienced by the water droplets.

To verify possible effects and errors on turbulence statistics due to the prongs interference, measurements have been acquired, at the same conditions, rotating the probe of 90° and putting it normal to the tunnel axis. As will be shown further the difference on the standard deviation of fluctuations, between the two cases, has been found to be less than 10% and close to the uncertainty due to the measurement. The prongs interference has been then neglected.

When the probe is normal to the tunnel axis with a pitch angle of 90° (referring to figure 18), as in this test with the stem normal to tunnel axis and main axial velocity component, there might be some interference due to the vortex shedding [69]. This effect has been experienced during the test, at some location, expressed as periodic noise at very high frequency, close to the bandwidth limit of the anemometer, over imposed to the velocity time series. Its contribution to the standard deviation of the fluctuation has been analyzed comparing the original signal with the one filtered cutting off the noise frequency. The result showed negligible contribution of the vortex shedding to the standard deviation value due to the very small amplitude of its noise. Similar results have been obtained in other turbulence test performed with the same equipment at the Luton ACT Icing Tunnel. It has to be noted as the effect of the vortex shedding has been not experienced when the wire was positioned parallel to the tunnel axis indicating as the low sensitivity of the probe to the parallel velocity fluctuation act as a filter for the low amplitude noise caused by the vortex shedding.

The sensitivity of the wire to the axis parallel component of the velocity vector has been extensively analyzed in the literature. The simples approximation is to consider the contribution of the velocity parallel to the axis [70], expressing the cooling velocity with a cosine law depending on the yaw angle as:

$$U_e = U \cos^{m} \alpha \qquad (4.13).$$

In this case at 90° the contribution of the parallel component to the cooling of the probe is neglected. Generally, the heat transfer strongly depends on the angle between the velocity vector and the wire. In the case of an ideal sensor, where there is no heat conduction to the prongs, the heat transfer varies with the cosine of the angle between the velocity and the wire normal. In reality heat is conducted to the prongs and a directional sensitivity factor *k* (yaw-factor), which describes the prong interference is typically introduced expressing the cooling velocity as [67]:

$$U_e = U(cos^2\alpha + k^2 sin^2\alpha)^{0.5} \qquad (4.14).$$

Where U is the velocity of the airflow, α is the yaw angle as shown in figure 18 and k is the yaw coefficient that indicates the weight of the component parallel to the wire axis on the heat exchange of the probe.

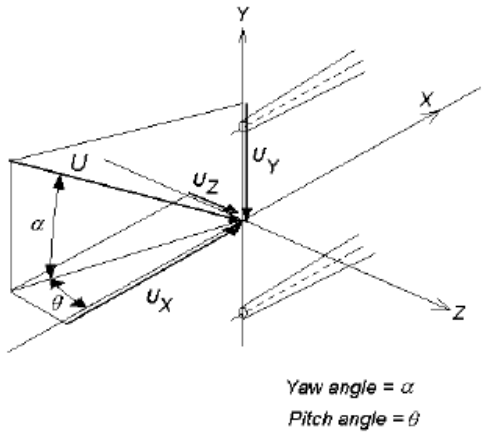

Figure 4-23: Characteristic positioning angles (from Jørgensen F.E.[67])

Bruun and Tropea [63] have discussed the calibration of different hot wire probe including the effects of pitch angle. The typical trend they found for the yaw coefficient k is reported in figure 4-24:

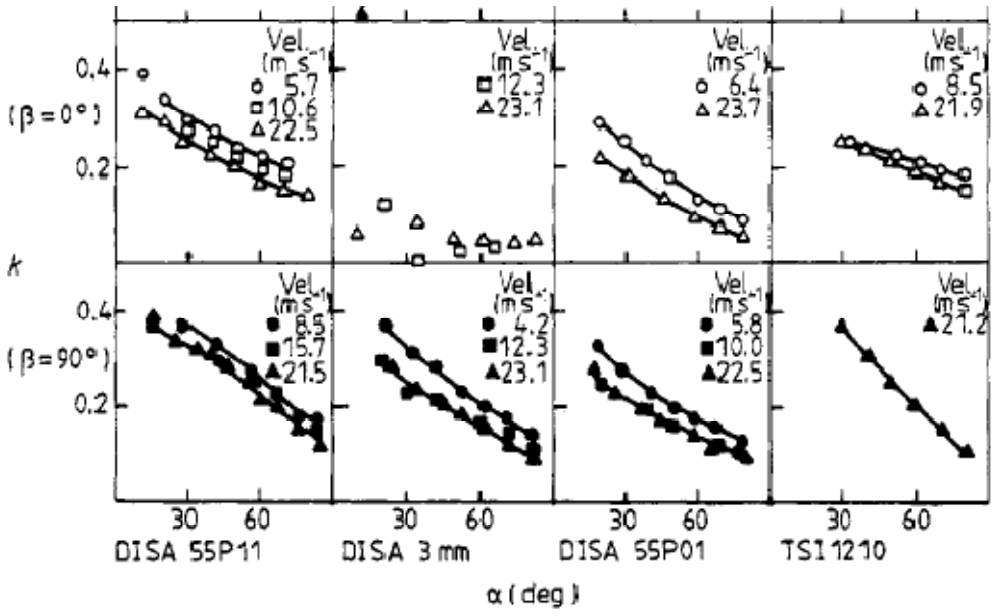

Figure 4-24: k yaw coefficient vs.yaw angles (from Bruun & Tropea[63])

They measured the trend of k with two pitch angles, β=0°,90°, three different calibrating velocities and different yaw angles α. The probe DISA 55P11 was the single-straight hot wire. Similar procedure has been repeated in this work to verify the sensitivity of the probe to the parallel component of the velocity vector. Following Bruun & Tropea [63] the calibration of the probe has been performed first at pitch angle zero, α = 0°, in order to get the A,B and n coefficient of the King law. Then the probe has been fixed at a yaw angle α = 90°, respect the axial velocity of the calibrator nozzle and the for several value of the velocity the coefficient k has been calculated being α and U_e (calculated from the voltages reading with the King law) known. The trend of k^2 versus the calibrating speed at α = 90° is shown in the following figure:

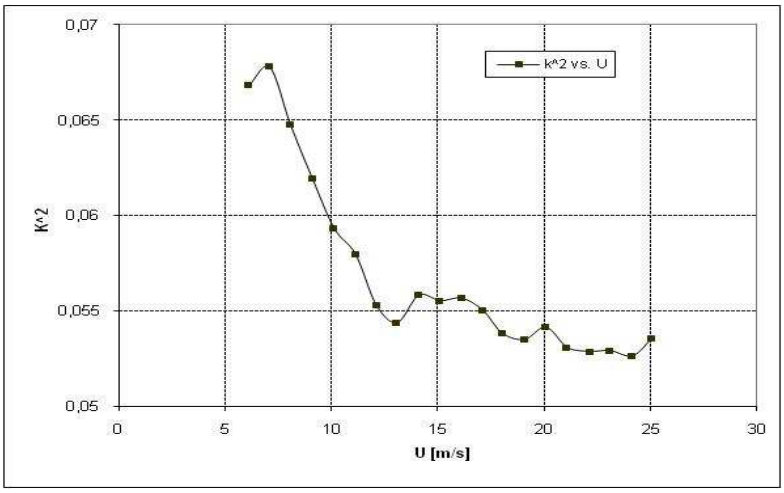

Figure 4-25: k^2 vs. Speed for 90 degree pitch

The value of k can then be estimated to be around the average 0.2 for the range of velocities considered in this test. This imply a contribution of the parallel component of the tunnel velocity to the effective cooling velocity, in a real condition, typically limited at a maximum of about 20 %. This aspect would reflect in the measurement of the mean velocity component, in the plane normal to the tunnel axis that should be scaled by the contribution of the parallel component. Also the fluctuations produced by the parallel component would generally contribute to the standard deviation of the velocity time series, but this contribution, considered of the order of the uncertainty of the measurement, can be neglected if compared to the contribution of the two components lying in the plane normal to the tunnel axis.

To scale the contribution of the parallel component of the velocity to the estimation of the mean velocity value of the time series, the angle between the probe and the airflow is required and generally it is not known a priori. An approach to estimate this angle has been tried in this work, exploiting the fact that both measurements with the wire parallel and normal to the tunnel axis were acquired. If neglecting the contribution of the pitch angle to the effective cooling velocity its expression for the wire normal and parallel to the tunnel axis is:

$$U_{e\_nor} = U(cos^2\alpha + k^2 sin^2\alpha)^{0.5} \text{ normal} \qquad (4.15).$$

$$U_{e\,par} = U(cos^2(\alpha + 90) + k^2 sin^2(\alpha + 90))^{0.5} \text{ parallel} \qquad (4.16).$$

Where $U_{e\,nor}$, $U_{e\,par}$ are the velocity read by the hot wire, U is the flow velocity and α is the unknown angle between the flow and the normal to the wire, assumed to be aligned with the tunnel axis in the reference position. Dividing the two equations each other and solving for α it is possible to get an estimation of the angle between reference axis and airflow. However, this approach has shown too much uncertainty related to the estimation of the angle. Those uncertainties were mainly determined by the probe positioning misalignment, when rotated of 90° and by uncertainties related to the acquisition of the time series not at simultaneous time. Though the approach could provide some useful information on the direction of the velocity vector, in the circumstances of the test was not possible using it to increase the level of detail of the velocity and turbulence input profile.

The probe has been finally placed in the tunnel in a plane one meter downwind the spray bars. The test matrix has been chosen with a number of 3x3 point along the height-width of the tunnel, namely Top-Center-Bottom x Left-Center-Right. The measurement points have been placed 15cm far from the upper and bottom walls and 20 cm far from the side walls.The nozzle configuration has been chosen to be the same as the icing blade test in “clean” configuration, i.e. without adding any turbulence generators. The time series have been acquired for each point at the conditions of 40 and 60 test section speeds, with the probe positioned normally and parallel to the axial tunnel direction.

4.5.9 Results from the velocity time series

The main results of the hot wire test have been analyzed to be used for CFD simulation of water droplets dispersion. The main objective of the test was to obtain a profile of the variables of interest for droplets trajectory calculation that would characterize the general quality and behaviour of the airflow in the Icing Wind Tunnel including the local effects of the jet coming from the nozzles.

Considering the test matrix of the measurement plane, the measurement points will be indicated with the number from 1 to 9 to represent the location of the next figure where the main airflow is pointing out of the page:

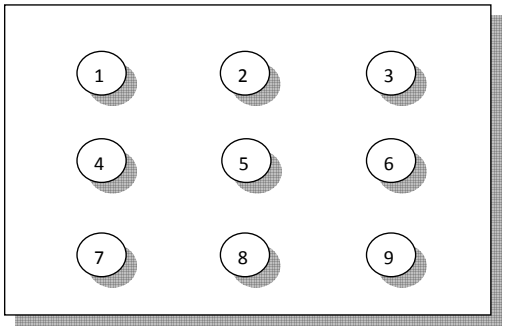

Figure 4-26: Measurement plane labels

Mean value of the velocity and standard deviation (then variance) have been computed, with their relative errors, by the statistical analysis of the time series. For the test section speed of 40 m/s and 60 m/s the mean value of the effective cooling velocity, acquired with the wire normal to the tunnel axis, is shown in next figure:

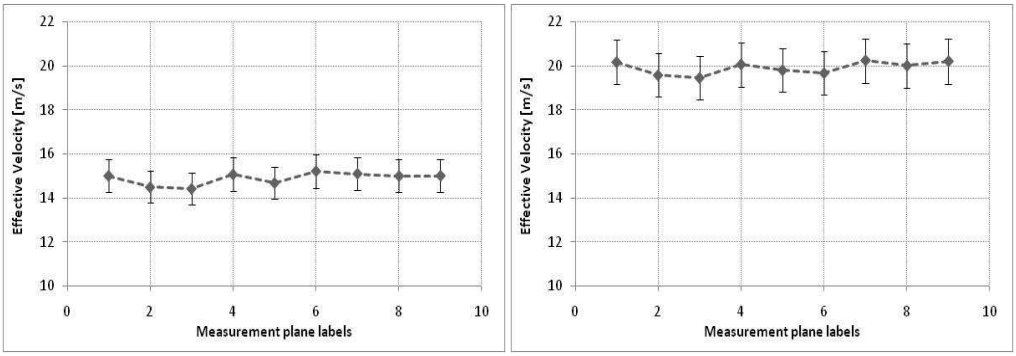

Figure 4-27: Mean velocity value vs. Measurement labels

The error of the mean component has been estimated to be of the order of 6% mainly determined by the uncertainties on the acquired voltages. The statistical error on the mean value calculation is in this case very small and typically less than 1%. The mean value of the effective cooling velocity is in general affected by the component outside the axial direction of the tunnel. In an idealized case the components of the velocity within a wind tunnel, characterizing the streamlines, are depending on the shape of

the tunnel wall and on the contraction ratio. Very high local contraction ratio can produce, near the tunnel wall, velocity components that can contribute to the heat exchange on the wire. When the measurement points are sufficiently far from the tunnel wall and for gentle local contraction, however, the axial component is typically dominant and can be approximated by the effective cooling velocity. The profile of the mean axial component can then be estimated by the measured cooling velocity. The variation along the measurement points, as shown in the figure 4-28 with non-dimensional coordinates and colorbar indicating the velocity in m/s, indicate some expected non-uniformity of the profile. However, the variations are often within the uncertainty of the measurement and as first approximation the overall profile can be considered uniform as shown in the next figure, where profiles for the two reference velocities of 60 and 40 meters/second, interpolated on a finer grid with cubic interpolation scheme, have been plotted with the colorbar scale chosen to be ± 10% of the mean values.

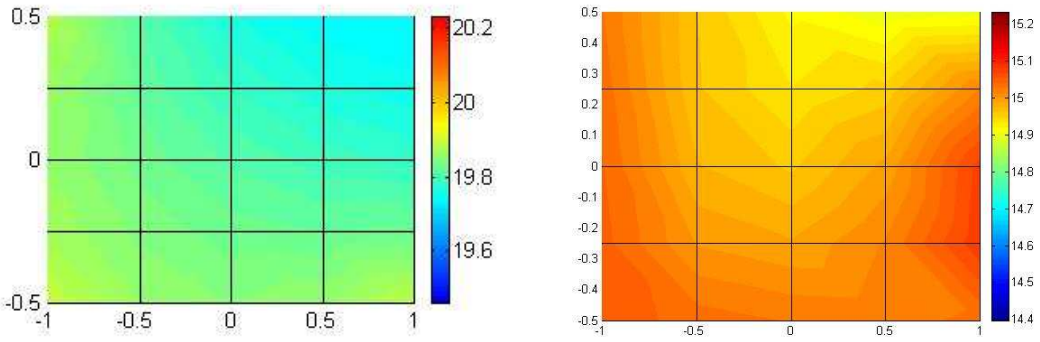

Figure 4-28 a, b: Mean velocity profile 60 m/s (a), 40 m/s (b)

The standard deviation of the velocity fluctuations has been computed by the statistical analysis of the time series. The results include the baseline value, acquired without the effect of the spray bars and the values corresponding to the three level of LWC in the test section depending on the values of the air pressure coming from the nozzle. The results for the velocities of 40 and 60 m/s are shown in the following figures:

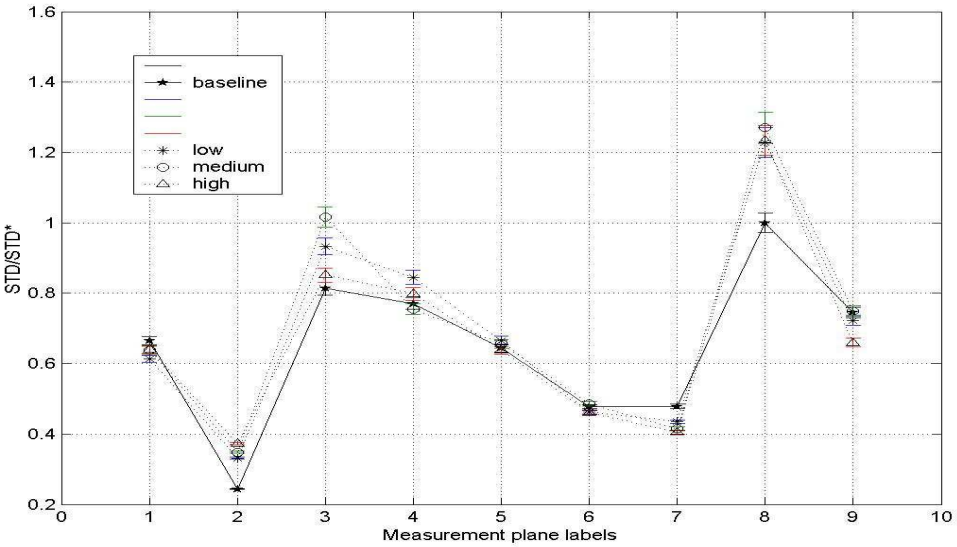

Figure 4-29: STanDard deviation trend at 40 m/s

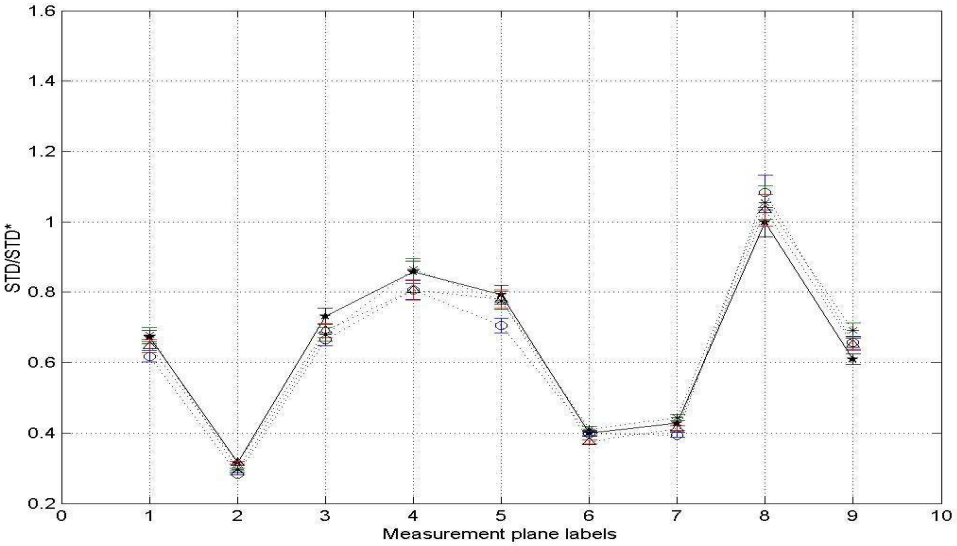

Figure 4-30: STanDard deviation trend at 60 m/s

The figure shown the non-dimensional standard deviation, with error bars calculated by the uncertainty on the voltages acquisition and the statistical uncertainties of the finite time series. For the air pressure conditions chosen for the test, considering the uncertainty associated with the measurement, monotonically trends are difficult to detect because the differences can be of the order of the errors. The mean trend shows that the nozzle contribution is reduced as the velocity is increasing and its effect on the turbulence level is varying with the velocity. Indications from other turbulence

test done at the GKN Icing Tunnel and discussion with its staff [71] suggest that the effect of the air coming from the nozzles on the production of the turbulence energy is generally function of the slip velocity jet-airflow that is dependent not only by the nozzles characteristics but also by the local tunnel geometry. However general trend for nozzle contribution to the turbulence, in conditions relative to icing test, are often not readily identifiable.

The standard deviation profiles on the measurement plane are shown in the following figure for the condition of 40 and 60 m/s without the air coming from the nozzle (baseline configuration):

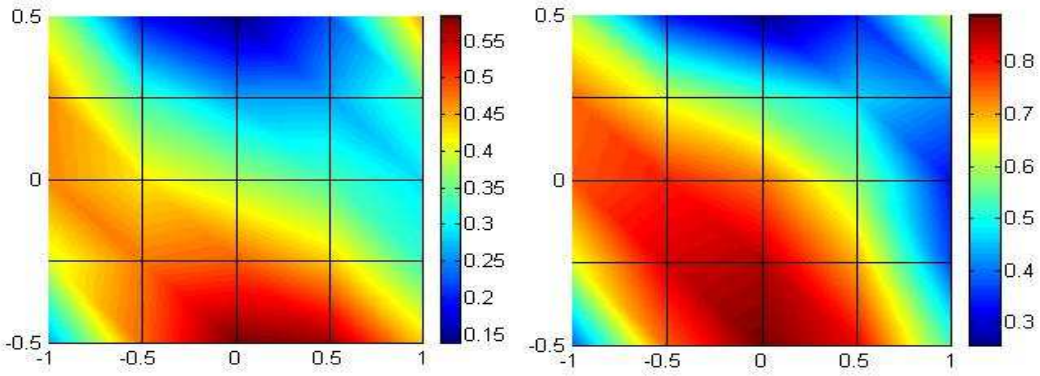

Figure 4-31 a, b: Turbulent fluctuation profile 40(a) and 60(b) m/s

The profiles shown in the figure 4-31 have been acquired with the wire parallel to the axial direction of the tunnel. As discussed in the paragraph 1.5.8 the intention was to characterize and quantify the turbulence kinetic energy in the plane normal to the tunnel axis to better approximate the turbulence experienced by the particle in that direction. The effect of the prongs has been investigated comparing the values of the standard deviation so acquired with the ones acquired with the wire normal to the tunnel axis. The difference percentage by the two measurements is shown in the next figure:

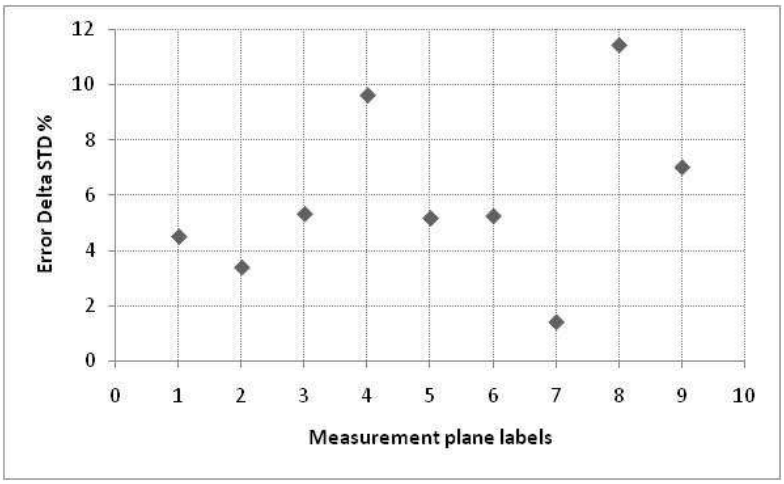

Figure 4-32: Difference % between measurements

Considering the difference of the two measurements of the order of the experimental uncertainty the prongs effect on the turbulent fluctuation has been neglected for the case of the wire parallel to the tunnel axis.

5 CFD simulation of particles dispersion

5.1 Introduction

The CFD approach for calculation of flow characteristics, regimes and state is a common practice used in the engineering application. It is widely used in research and industrial applications where the solution of the flow helps to investigate and predict the behavior of mechanical systems. As discussed in the chapter 3, for engineering application the most widely used approaches for the numerical solutions are based on the averaged Navier-Stokes equations that allows to contain the computational cost giving, at the same, sufficient accuracy to investigate phenomena related to practical applications.

Two-equation models have been used over the past two decades as the basis of considerable research on turbulence flow computation. Although several different models have been suggested to describe the turbulence field, the most accepted is the turbulence energy-dissipation model. Differential equations for the turbulence energy and dissipation are incorporated into the numerical codes, and the effective eddy viscosity is related to the energy and dissipation rate. The turbulence field predicted by this model can then be used to calculate the particle dispersion. The simulations discussed in this section are based on models using averaged properties for the fluid phase.

5.2 Carrier Phase Simulation

5.2.1 Geometry and Boundary conditions

The computation of the dispersion of the water droplets and, generally, of a discrete phase, require the solution of the carrier phase to provide turbulent statistics required for the stochastic models usually employed in commercial CFD codes. The airflow

quality of the carrier phase depends on the geometry of the tunnel, scales with the operating conditions of velocity and nozzle air pressure and can be affected by the presence of the dispersed phase.

As has been discussed in chapter 2, the interaction between water droplets and the carrier phase, characterized by the momentum inter phase transfer, is depending on the local volume fraction of the dispersed phase. Depending on the volume fraction and by the consequent regimes of interaction, different strategies can be followed to compute the carrier phase solution. The commercial CFD codes allows for simulating the momentum and energy exchange between discrete phase and carrier phase. When this type of simulation has to be solved the solution of the carrier phase has to be computed including the presence of the dispersed phase. In this case the interphase momentum exchange terms are added to the averaged Navier-Stokes equations and the two-way coupling is resolved by alternately solving the discrete and continuous phase equations until the solutions in both phases have stopped changing. This interphase exchange of heat, mass, and momentum from the particle to the continuous phase is qualitatively shown in Figure 1:

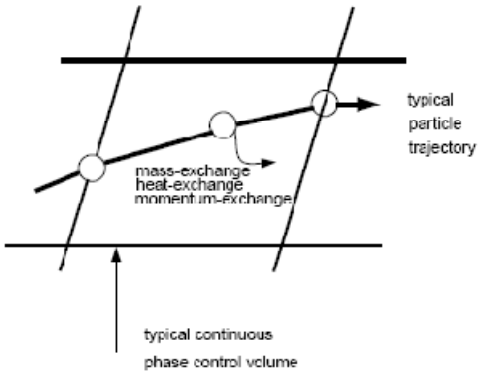

Figure 5-1: from Fluent 6.3 user manual

The momentum transfer from the continuous phase to the discrete phase is generally computed by examining the change in momentum of a particle as it passes through each control volume. It is mainly determined by the drag force acting between fluid and particle, especially in the Icing Tunnel operating conditions, but other forces can be included when their contribution is assumed to be significant. This momentum exchange appears as a momentum sink in the continuous phase momentum balance in

any subsequent calculations of the continuous phase flow field. When stochastic tracking is performed, the interphase exchange terms are computed for each stochastic trajectory with the particle mass flow rate divided by the number of stochastic tracks computed. This implies that an equal mass flow of particles follows each stochastic trajectory. In case where the interphase exchanges can be neglected the computation of the carrier phase can be done “a priori” without considering the effects of the injection of the dispersed phase. The geometry and the boundary condition are affecting the carrier phase solution in this case.

In CFD simulation the geometry should typically include the necessary details to obtain an accurate description of the flow field. The quality and the accuracy of the geometry are then problem-related and are depending on the variables that are going to be investigated. For simulation of the dispersion of a discrete phase, a description of the turbulence field is required with the mean flow variables. In the Icing Wind Tunnel the aerodynamic field is affected by elements present in the tunnel circuit as turning vanes, heat exchanger, spray bar rake and convergent/divergent section design. As has been discussed in the chapter 3, detailed description of these elements would increase the computational cost beyond the resources typically available for engineering application of CFD and for testing support and a simplified description of the geometry is then necessary. The simplified model, however, has to be able to:

- Isolate a piece of a complete physical system
- Contain boundaries with sufficient information to describe the physical phenomena
- Accommodate those information in the boundary conditions available in the commercial CFD codes

The geometry used in this work describe the Cranfield Icing Wind Tunnel from the section where is placed the spray bar rake to the outflow section, placed at the beginning of the diffuser, as shown in figure 2. The geometry of the spray bars has been not reproduced in this case because its contribution to the turbulence has been assumed to be represented by the turbulence field measured downwind with the hot wire probe. The outflow section has been investigated in order to analyze its

contribution to the overall solution. The geometry of the diffuser has been included in preliminary simulations and the distance of the outflow plane from the center of the test section has been used as parameter. The mean flow field and the turbulence field have been found not affected by the description of the diffuser and the outflow plane has been finally placed at the end of the test section to reduce the computational cost.

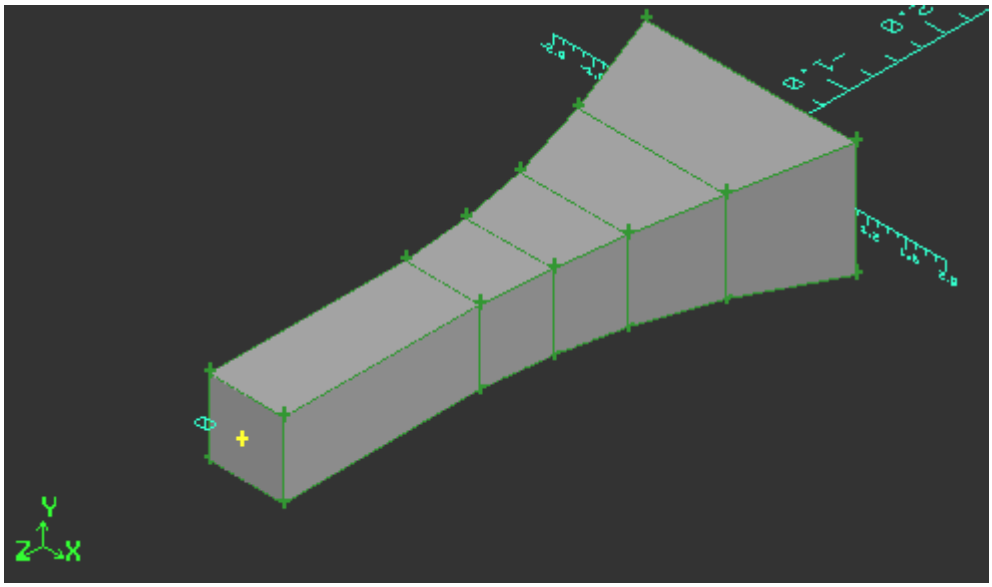

Figure 5-2: Cranfield Icing Wind Tunnel geometry

The boundary conditions available in FLUENT have been used to characterize the problem examined. The wall condition has been used for the tunnel wall. This condition does not require further specification and settings in the code. Once the tunnel walls have been specified the inlet and outlet condition need to be defined. The choice of the outlet condition is represented by the outflow or by the pressure outlet conditions. For incompressible flow where there is no backflow at the outlet plane i.e.: no recirculation zones, the outflow condition can be used. For compressible flow the pressure outlet condition is more appropriate and requires the value of the static pressure at the exit plane [32]. This value can be measured with pitot tube or static taps at the chosen location. For the speeds analyzed in this work the outflow condition has been used for the simulations.

The choice of the inlet condition, similarly to the outlet condition, is also depending on the flow regimes considered. For incompressible flow, where the density can be

considered constant, the velocity inlet condition can be used. This condition allow to specify the values and the direction of the mean velocity vector at the inlet plane as well as the turbulence characteristics of the inlet flow field. In this study the mean velocity has been assumed enter in the computational domain normally to the input plane. In principle the velocity vector at the spray bar section might have some non uniformity in its direction and the amount is depending on the tunnel design i.e.: design and geometry of the turning vanes. As has been discussed in the chapter 4, the three dimensional mean velocity profile could be extracted from hot wire measurement, however for simplified case where this measurement is not available, the assumption of "normal direction" can be used to approximate the local wind tunnel flow field. For compressible flow simulation, the mass flow inlet is more appropriate to describe the physical phenomena. The same turbulence characteristic of the velocity inlet condition can be specified for the inlet plane.

The turbulence conditions can be specified with different combination of characteristic parameters. When a profile is required the choice is typically based on the specification of turbulent kinetic energy k and turbulent dissipation rate ε. From the hot wire measurement, turbulence statistics have been measured in a plane downwind the spray bars in order to catch the effects of the nozzle air pressure. To adapt the measured profile to an appropriate inlet condition it has been scaled backward to the inlet plane according to the turbulence decay profile in the domain [57, 72]. Similar decay curves have been showed in the Snyder & Lumley experiment [57] where, during the initial period, the turbulent energy follows the inverse law $u'^2 \propto A(x - x_0)^{-1}$ and the dissipation rate $\varepsilon = -\frac{3U}{2}\frac{du'^2}{dx}$ where the hypotheses of isotropy and frozen turbulence have been applied. To better account for tunnel geometry effects, the production terms P, due to contraction ratio, have been added to the turbulent kinetic energy equation, expressed as $\frac{dk}{dt} = P - \varepsilon$ for homogeneous turbulence, which has been solved coupled to the dissipation rate equation of the k-ε model. The numerical solution has been implemented in MATLAB to obtain the required decay, at a distance several times that of the turbulence length scale from an inlet virtual origin, in order to match the measured profile. The inlet profile has been then interpolated on the higher grid resolution with a cubic order. It can be assumed

that for a low wind tunnel turbulence level, the particles see a “locally homogeneous” turbulent field within characteristic dimension of the order of the cloud diameter. This assumption reduces the error impact of the interpolation procedure on the particle dispersion solution, however, the required number of measurement points would be still connected to the desired level of accuracy specified by the user.

5.3 Verification Procedure for Carrier Phase Simulation

5.3.1 Introduction

As for experimental measurement also in CFD simulations is appropriate to investigate the uncertainties related to simulation of the engineering problem examined. Though the CFD commercial codes are verified in their consistency to properly numerically solve the fluid dynamic equations, further user verification are required to assess the validity of the simulation in relation to the specific problem under consideration.

As discussed in Stern F & al. [73] sources of errors and uncertainties in CFD simulations can be divided into two distinct categories: modeling and numerical. Modeling errors and uncertainties are depending on the mathematical representation of the physical problem such as geometry, boundary conditions, turbulence models, assumption on the fluid dynamic regimes and properties (i.e.: incompressibility conditions, Newtonian flows, etc…). Numerical errors and uncertainties are depending on numerical solution of the mathematical equations, such as discretization, artificial dissipation, incomplete iterative and grid convergence, lack of conservation of mass, momentum, and energy, computer round-off, etc…In this case the attention is focused on the investigation of the code to properly solve, numerically, the set of equations specified and whether or not those equations are modeling the physics of the problem is not significant for the investigation of the numerical error so defined.

The methodologies to assess the quality of the simulation respect the modeling and numerical error are typically referred to the validation and verification procedures. Following Roche [74], the succinct description of verification can be stated as "solving the equations right," and of the validation as "solving the right equations." When transferred to engineering simulations these methodologies allow to investigate, following different routes, the uncertainties present in the final calculated solution. When the attention is specifically focused on the uncertainty related only to the numerical solution of the partial differential equations, the verification procedure allow to identify whether the numerical settings for the iterative procedures and discretization (such as spatial and time step sizes) are sufficient to calculate the solution within a desired level of uncertainty.

To compare a numerical solution of modeling equations with their exact or true (expected) values, the relative difference between the solutions is often considered. In this sense, accuracy indicates the closeness of agreement between a simulation/experimental value of a quantity and its true value and it typically increases as error approaches zero. The true values of simulation/experimental quantities are rarely known. Thus, errors must be estimated. An uncertainty U is an estimate of an error such that the interval ΔU contains the value of the error 95 times out of 100 (95% confidence level). An uncertainty interval thus indicates the range of magnitudes of the error, with its probability of occurrence and without information about its sign.

In the calculation of the numerical error the three main errors can be considered. They are: round-off error, iterative convergence error, and discretization error. Round-off errors occur due to the use of finite arithmetic on digital computers. The adverse effects of round-off error can be compensated by using more significant digits in the computation. Standard computers employ 32 bits of memory for each storage location. In a double precision calculation, available in commercial CFD codes, two storage locations are allocated for each number, thus providing 64 bits of memory. This type of error is few affected by the user choices and can be considered a bias error associated with the hardware used for the calculation.

Iterative convergence error arises due to incomplete iterative convergence of a discrete system. Iterative methods are generally required for complex nonlinear systems of equations, as the Navier-Stokes ones. The iterative procedure is typically used to calculate the unknowns of the discrete algebraic system arising from the discretization of the equations. When the number of unknown is very high, as in the case of engineering CFD simulation from thousands to millions, the iterative procedure is used to solve the system of unknowns starting from an initial guess. The longer one iterates, the closer one gets to the solution corresponding to that discretization. The criterion to evaluate the iterative convergence is usually based on the calculation of the residual of the discretized equations. The residual will approach zero (within machine round-off error) as the iterations converge. Residual calculations and plots are embodied in commercial CFD codes and, as convergence criteria, orders of 10^{-4} or lower are typically adopted. In Icing Wind Tunnel simulations with interest in the bulk region of the tunnel, far from the wall and the boundary layer, the simple geometry typically allow to reach those values for the residual and get iterative convergence.

While the iterative convergence assures the values of discretized unknowns have been sufficiently approximated by the iterative procedure, the approximation that the discretized variables provide respect the expected true solution if referred to the dicretization error. It can be defined as the difference between a numerical solution and the exact solution to the continuum partial differential equations. This difference arises from the conversion of the differential equations into an algebraic system of equations (i.e., the discretization process). Evaluation of the discretization error, associated with a given solution, might be needed during analysis of simulation results or for a model validation study [75]. This error assessment allows for obtaining an error estimate similarly as into experimental measurements. This error can then be expressed in terms of error estimate (e.g., the most likely value for the error is ±5%), an error band (e.g., a confidence level of 95% that the error is within ±8%), or an error bound (e.g., the error is guaranteed to be within ±8%). Another reason for evaluating the discretization error is to drive a grid adaptation process. Grid adaptation can involve locally adding more elements, moving points from a region of low error to a region of high error, or locally increasing the formal order of accuracy.

The estimation of the discretization error is practically done through the grid independence verification procedure. In this procedure the numerical solution is calculated on different grid with different size. Typically, three grids are used with a refinement ratio from coarser to finer grid that can be chosen by the user in relation to the computational cost of the simulation. The most appropriate values of the refinement ratio for industrial CFD are not yet fully established as discussed in Stern F & al [73]. Small values, very close to one, are undesirable since solution changes will be small and sensitivity to input parameter may be difficult to identify compared to iterative errors. Large values alleviate this problem; however, they also may be undesirable since the finest step size may be prohibitively small for the computational resources available. Also, as for small refinement values, solution changes for the finest grid size may be difficult to identify compared to iterative errors since iterative convergence could be more difficult for small cell size. Another issue can arise from interpolation to a common location, to compute solution changes, which introduces interpolation errors that are depending on the refinement ratio chosen. If doubling of halving the cell size, it might be expected to keep one location in common with the reference grid however, for industrial CFD, *refinement ratio* = 2 may often be too large. A good alternative may be a value of the refinement ratio around 1.3/1.4, as it provides fairly large parameter refinement ratio and at least enables prolongation of the coarse-parameter solution as an initial guess for the fine-parameter solution.

When the solution on at least three different grids is available the discretization error and the verification of the independence of the solution by the grid size can be estimated through the calculation of the Grid Convergence Index (GCI) defined by Roache [74]. In this work has been followed the procedure recommended by the ASME Journal of Fluid Engineering for calculating the GCI and for estimating the error. Details of the procedure can be found in the ASME guideline [75] and the main details will be discussed in the next chapter.

5.3.2 Grid convergence index

Using the solutions on more meshes with different level of refinement it is possible to obtain a higher-order estimate of the exact solution calculating the estimate with the Richardson extrapolation procedure. This approach is generally referred to the

extrapolation-based error estimate. The error on the discretized numerical solution can then be calculated in relation to the expected extrapolated solution.

Another procedure, often employed to estimate the discretized errors and verify the independence of the results by the grid size, is to compare the solutions on different meshes between them and verify that the differences are within the range required by the user. However, as discussed in Roy, the relative difference of the solutions can be misleading when used as error estimate. In principle the relative difference tells only how close each other the solution are, but not how far they are from a "real" expected solution.

Also, differently for the Richardson extrapolation method, that take in account the order of accuracy to calculate the expected solution, the relative comparison of the solutions on different meshes does not include it. As shown in Roy a relative difference of 5% in the solutions of two different meshes, can represent, when transferred to the Richardson extrapolation-based error estimate, an error of 0.71% for a formal second order accuracy scheme or an error of 9.1% for a first order accuracy scheme. This means that the relative difference has different meanings depending on the "effort" that is put on the calculation. A given relative difference with an first order accuracy scheme indicates that the margin of improvement are higher than for a second order accuracy scheme and then the solution if more far from the real "expected" one. For this reason is important to account for the order of accuracy in the calculation of the error, as done by the Roache's Grid Convergence index [76].

The Grid Convergence Index, or GCI, can be used as a method for uniform reporting of grid refinement studies and combines the often reported relative difference between solutions with the accuracy and refinement ratio effects from the Richardson extrapolation-based estimation. The GCI also provides an error band rather than an error estimate.

The procedure followed to calculate the GCI, from the ASME guideline, can be summarized as follow:

1. Define a representative cell, mesh or grid size *h*. For three dimensional mesh this can be done considering the average size of the discrete small volumes as:

$$h \equiv \left[\frac{1}{N}\sum_{1}^{N}\Delta V_{\mathrm{i}}\right]^{1/3} \qquad (5.1).$$

2. Select three significantly different set of grids, characterized by three values h_1, h_2, h_3 related by a grid refinement factor r ($r_{21}=h_2/h_1$, $r_{32}=h_3/h_2$). The choice of r is arbitrary and based on the experience. The value of 1.3 has been chosen in this thesis following the guideline of the ASME Journal of Fluid Engineering.
3. Run the simulations for three grids with same boundary condition and settings to determine the values of key variables important to the objective of the simulation study. In principle depending on the flow field variable, different grid size and refinement ratio would be required to get satisfactory accuracy of the final solution. In this work, with simulations concerning the water droplets dispersion in the geometry of the Icing Wind Tunnel, the turbulence kinetic energy has been chosen as key variable. The mean velocity variable, in this case, has been found to be not critical due the simply geometry analyzed.
4. Once the solution of the key variable has been computed on the three grids, calculate the apparent order of accuracy *p*, which is a general function of relative difference of the solutions on different grids, grid refinement factor and formal order of accuracy. For all the simulations the formal second order of accuracy, available in FLUENT, has been chosen to calculate the solution.
5. Once the apparent order of accuracy has been estimated, calculate the extrapolated values of the solution.
6. With the extrapolated values and the solution on the three grids, calculate the relative difference between the computed solution and the extrapolated one e_{ext} and the relative error between the solutions e_a.
7. With relative error e_a , apparent order of accuracy and grid refinement factor is possible to estimate the grid convergence index as:

$$GCI = \frac{1.25 e_a}{r^p - 1} \qquad (5.2).$$

Where 1.25 is a safety factor recommended by Roche. The GCI can then be plotted in form of error bar to indicate the uncertainty on the solution.

5.3.3 GCI of Cranfield Icing Wind Tunnel flow simulation

In this study, the vertical turbulence kinetic energy trend in the middle plane of the test section has been reported for the three solutions with error bars given by the GCI. The turbulence field has been resolved with the *k-e* model and with the Reynolds Stress Model (RSM) to further account for anisotropic effects in water droplets dispersion. Steady state simulation has been solved for the tunnel airflow and only the spatial discretization error is considered further. of The figure 5-3 show the trend of the turbulent kinetic energy profile along the vertical axis of the tunnel calculated of three grids with refinement ratio *r* constant and equal to 1.3. The turbulence model considered in this case is the *k-e* one.

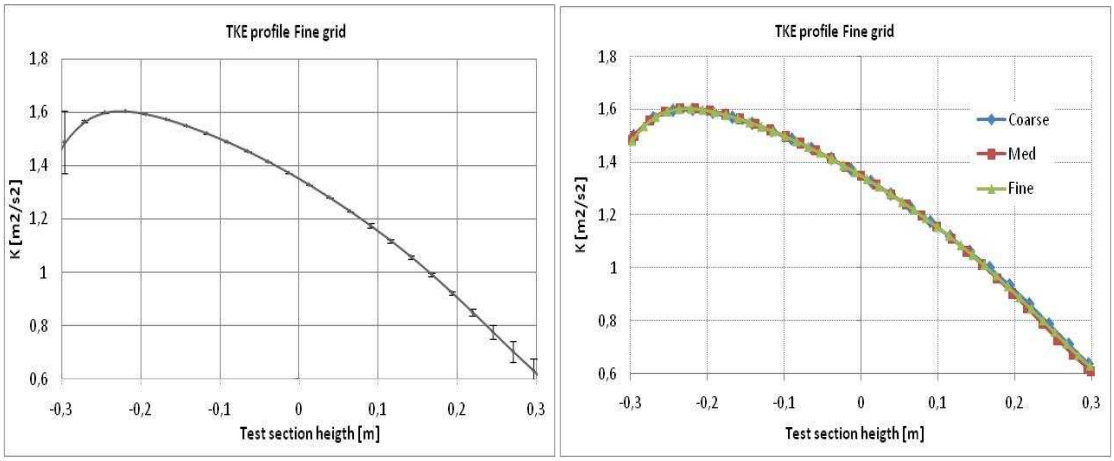

Figure 5-3a,2b : Turbulent kinetic energy trend (k-e)

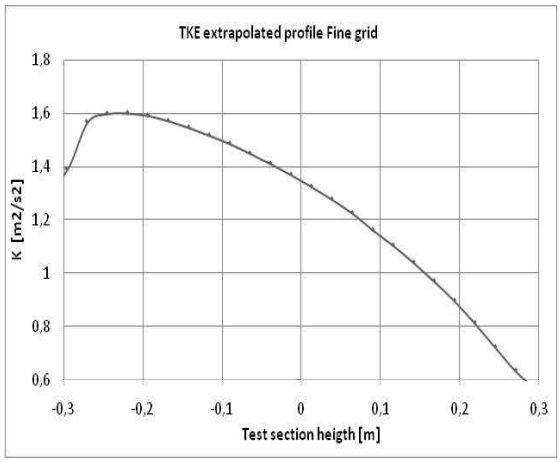

Figure 5-4: Turbulent kinetic energy extrapolated trend (k-e)

The GCI is plotted with error bars on figure 5-3a indicating that small uncertainties are related to the bulk region of the tunnel sufficiently far from the wall and boundary layer effect. Average values of these uncertainties are around 1%. The solution of the three grids is also reported in figure 5-3b showing very close results each other. However, despite the small relative differences, monotonic convergence of the solutions, with improvement associated with the finer grid has been found for the 85% of the points. The extrapolated trend of the solution, calculated with the Richardson extrapolation, is shown in figure 5-4. Very close agreement is found between the extrapolated and the calculated ones in the central part of the test section, far from the wall.

Results of the Reynolds Stress Model calculation are shown in figure 5-5a and 5-5b. The trend of turbulent kinetic energy with the trend of the diagonal components of the Reynolds Stress tensor are shown at the same location analyzed with the *k-e* model. The same grid sizes for the *k-e* simulation have been used for the RSM model.

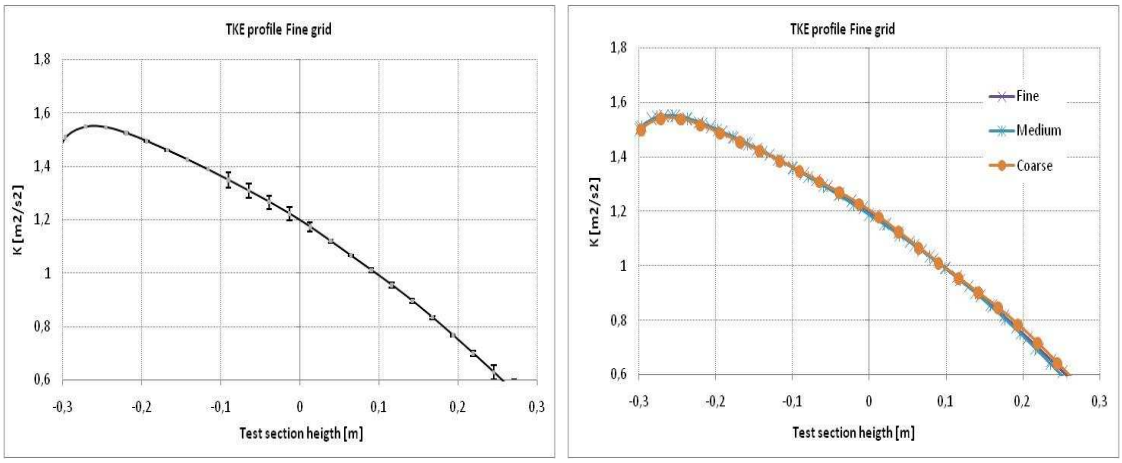

Figure 5-5a, 4b: Turbulent kinetic energy trend (RSM)

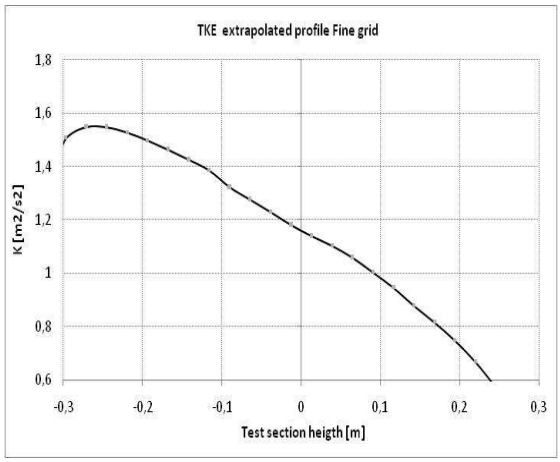

Figure 5-6: Turbulent kinetic energy extrapolated trend (RSM)

The average value of the error is in this case of the order of 1,5% in the bulk region of the tunnel. The extrapolated trend of the solution for RSM, calculated with the Richardson extrapolation, is shown in figure 5-6. Also in this case in the central part of the test section the difference between the extrapolated values and the calculated one is small, on the order of 3%.

Same results have been investigated for the component of the Reynolds Stress Tensor to verify their accuracy. The uu, vv, ww components trends have been analyzed on the same grid size used for the previous investigations. Next figures show their trend with error bars estimated from the GCI.

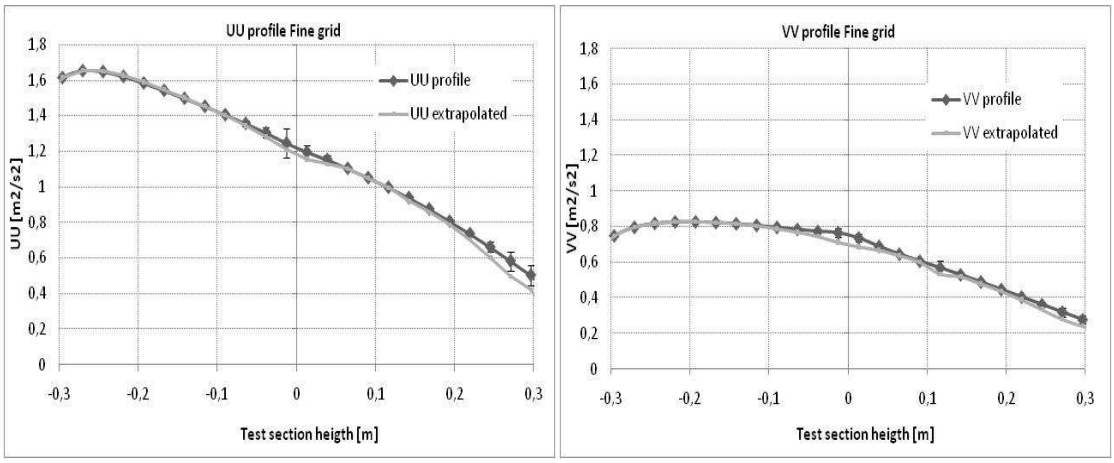

Figure 5-7a, 6b: UU and VV profiles

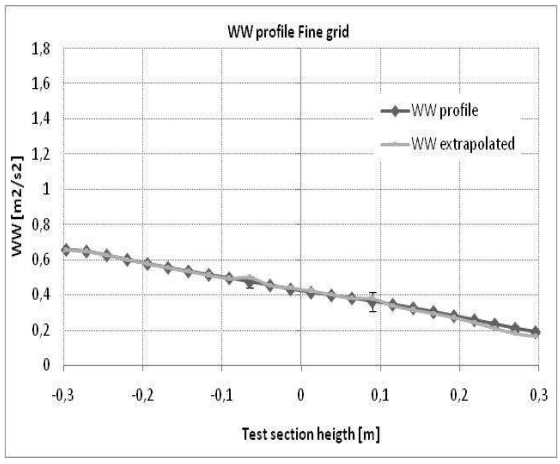

Figure 5-8: WW profile

The error of the components, calculated with the GCI, has been estimated to be on average of 1,7% for all the three components. Also, the average difference between the extrapolated values and the calculated one along the test section height is estimated to be approximately 2%, similarly for the three diagonal component uu, vv and ww.

Considering the small error percentage found on the solutions, for both *k-e* and RSM models, they have been used to describe the tunnel airflow and then to compute the water droplet dispersion. Also if the injection of a discrete phase can modify the flow field and consequently may require a new verification of the key variables, for the Icing Wind Tunnel case the small water volume fraction allows the flow field remaining unaffected by the presence of the water droplets. The verified flow field

calculations, previously shown, have then been used for water droplets dispersion computation.

5.4 Discrete Phase Simulation

5.4.1 Fluent Discrete Random Walk

Based on the calculation of the airflow, the particle trajectories are then computed in the Lagrangian reference frame integrating the particle equation of motion [16]. Droplet movement is dictated by the equations of motion for position and velocity. The position of the droplet can be solved by the following equation:

$$\frac{dx_p}{dt} = u_p \qquad (5.3).$$

where x_p is the particle location and U_p is the instantaneous particle velocity vector. The particle velocity is calculated by solving the standard equation of motion for a spherical droplet in the form:

$$\frac{du_p}{dt} = \frac{1}{\tau_p}\left(\bar{u}_f - u_p + g\right) + \frac{u'_f}{\tau_p} \qquad (5.4).$$

The particle acceleration is affected by only aerodynamic drag and gravity if the particle density is much greater than the gas density ($\rho_p > \rho_f$), as is the case herein. In addition, the particle loading is very small and droplet-droplet interactions terms and droplet effects on the airflow will be negligible.

To estimate the fluctuating component of the velocity, the formulation used in FLUENT is the eddy-lifetime model as described in the chapter [1.4.1 Fluid particle interaction] where the particle is assumed to interact with a discrete succession of eddies as it moves along the computational domains (Discrete Random Walk approach). A random number ξ, with normal distribution, is used to simulate the

stochastic perturbation of the airflow velocity as seen by the particle in a way to be consistent with the turbulent kinetic energy *k* available from RANS solution. For the *k-e* model, where the condition of isotropy in used, the fluctuations are calculated as follow:

$$\overline{u'} = \overline{v'} = \overline{w'} = \xi\sqrt{\frac{2}{3}k} \qquad (5.5).$$

For the RSM, instead, it is possible to take in account for anisotropy of the turbulence considering the fluctuations to be:

$$\begin{aligned} \overline{u'} &= \xi\sqrt{\overline{u'^2}} \\ \overline{v'} &= \xi\sqrt{\overline{v'^2}} \\ \overline{w'} &= \xi\sqrt{\overline{w'^2}} \end{aligned} \qquad (5.6).$$

This perturbation is then combined with the mean velocity value to compute the trajectories of statistically large number of droplets in order to obtain statistics moments of the dispersion process. Each eddy is characterized by a velocity, time scale τ_λ and length scale Λ that can be estimated by the local turbulent properties available by the RANS turbulence models:

$$\tau_\lambda = c_\tau \frac{k}{\varepsilon} \qquad (5.7).$$

,

$$\Lambda = c_\mu^{3/4} \frac{k^{3/2}}{\varepsilon} \qquad (5.8).$$

Where $c_\mu = 0.09$. The values of the constant for the time scale is not well know and a range of values has been proposed and used in the literature. Fluent code uses the values $\tau_\lambda = 0{,}15$ for *k-e* models and $\tau_\lambda = 0{,}30$ for the RSM. The interaction time (τ_{int}) between droplet and eddy (time step) is determined to be the minimum between the eddy life time ($2\tau_\lambda$) and the eddy crossing time τ_c . Its expression is:

$$\tau_{\text{int}} = \min(\tau_\lambda, \tau_c) \tag{5.9}$$

where:

$$\tau_c = -\tau \ln\left(1 - \frac{\Lambda}{\tau\left|u_f - u_p\right|}\right) \tag{5.10}$$

The advantage of the eddy lifetime model with this form of interaction time is that it can easily account for the crossing trajectory effects, particularly relevant for heavy particle dispersion. The integration of the particle equation of motion has been done with a trapezoidal second order scheme with automatic time step control depending on the desired level of accuracy, as allowed by FLUENT.

5.4.2 Test case for FLUENT Discrete Random Walk

The Discrete Random Walk model of fluid-particle interaction has been tested in the literature, validating its prediction against experimental results. Typically the DRW was implemented by other researchers in their own code and for this reason, though the model tested in the literature is conceptually similar to the one used by Fluent, an additional validation has been done here reproducing an experimental case with Fluent code. The objective of this validation was to underline and verify the settings of the code and the methods to use them for a measured test case, before to apply those settings for further predictions.

The test case has been chosen to be the Snyder & Lumley experiment [57]. In their work they measured the particle velocity autocorrelation and particle cloud variance of single spherical beads injected in a wind tunnel. The particles were chosen to have different inertia and consequently experience a range of different “crossing trajectory” effect. The particles used are summarized in the next table:

Particle Type	Diameter [μm]	Density [kg/m^3]	Time Constant [ms]
hollow glass	46.5	260	1.7
solid glass	87.0	2500	45.0
corn pollen	87.0	1000	20.0
copper bead	46.5	8900	49.0

Table 3: Snyder & Lumley particles

Because of the inertia of the particle, to avoiding the gravity effect on the particles path the tunnel was placed vertically with the flow upward. Grid generated turbulence was created adding a stationary grid with a flat mean velocity profile. The grid also contained a slot to house the particle injection tube. Particle were injected at the tunnel centreline 20 mesh lengths from the grid, with a mean velocity the same as the mean tunnel speed equal to 6.55 m/s. Measurement of the turbulence characteristic were acquired with the hot wire probe and reported into the paper for several stations along the tunnel.

To compare the Fluent model with the measurement, the geometry of the tunnel test section has been reproduced. The input plane has been chosen to be coincident with the first set of flow measurement acquired with the hot wire, so to be able to use that one as boundary conditions. The flow has then been calculated obtaining the turbulent statistic necessary for particle dispersion calculation. The injection of the particle has been specified as “single” injection and the number of stochastic tries chosen to limit the uncertainty of the particle cloud variance less than 10%. The Discrete Random Walk has been used to compute the particle trajectories. The trend of the particle cloud variance has been than calculated and compared with the experimental results.

A first comparison has been done between the measured and the calculated airflow characteristic to verify that the airflow solution resolved with Fluent match the measured one. The calculated turbulence kinetic energy trend and dissipation rate trend along the tunnel axis is shown in figure 5-9:

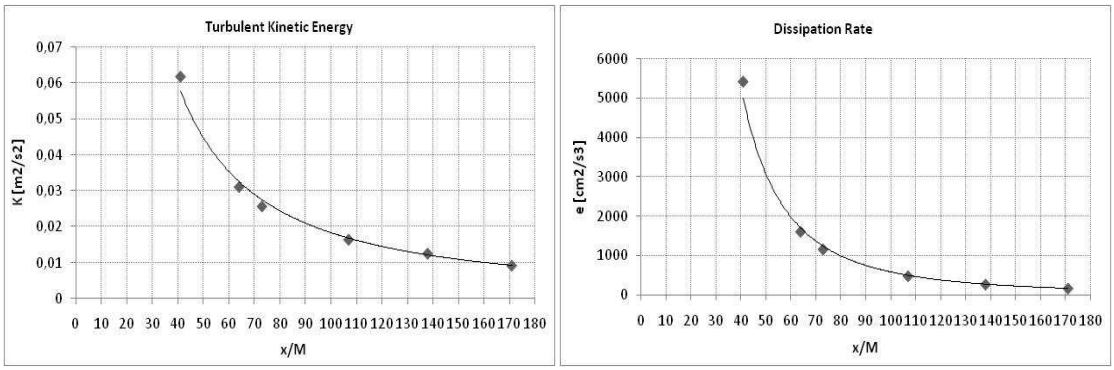

Figure 5-9: Turbulence kinetic energy and dissipation trends

A good agreement has been found between calculated trend (line) and measurements (dots) and in the case of grid generated turbulence the Fluent model has been found able to reproduce the flow field. Particle trajectories have then been calculated and the variance of the cloud of particles in plane normal to the tunnel axis has been computed from the number of stochastic tries. The figure 5-10 shows the trend of the variance along the tunnel axis:

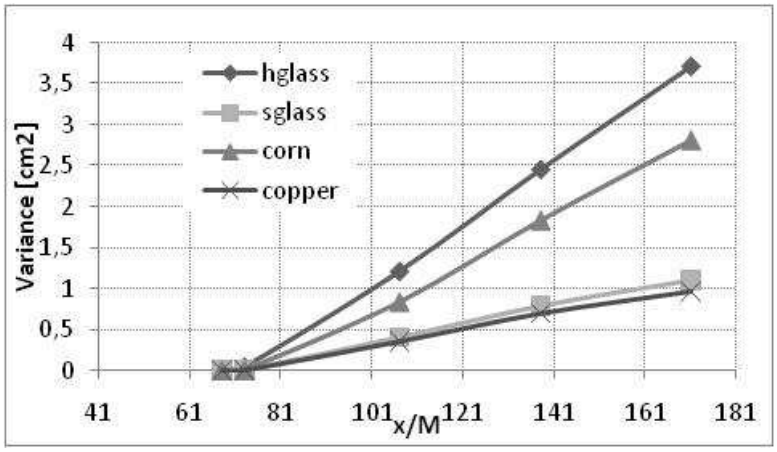

Figure 5-10: Variance of particle dispersion vs. Axial distance

In this calculation the Lagrangian time scale constant has been adjusted with the data coming from the experiment and the automatic time step choice has been applied. The result shows that with these settings the Fluent model is able to reproduce the measured dispersion with a reasonable level of accuracy.

In order to investigate the sensitivity of the model to the user settings and input parameters, different time scale constant and different particle injection velocities have been tried and compared to the baseline. A variation of 15% of the baseline has been considered for the timescale constant. Simulations have been done with the same injection properties and same numerical scheme of the baseline and the results are shown in figure 5-11a and 5-11b for a reduction and increasing of the time scale constant:

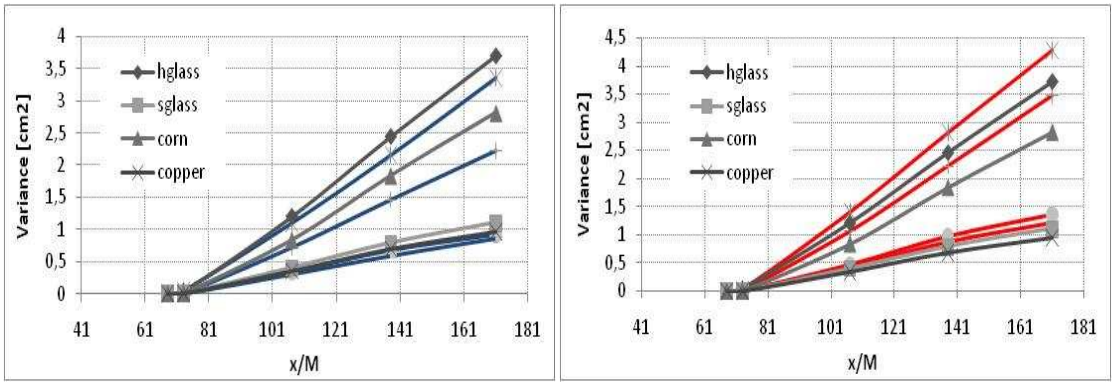

Figure 5-11a,b: Effect of time scale constant on the variance of the dispersion

The effect of the time scale constant is to monotonically affect the final particles dispersion (variance). It has been found a strong dependence of the particles dispersion on the choice of the time scale constant, where variation of the constant have produced difference of the dispersion, respect the baseline, around 20% for both increasing and reducing values.

The input parameters sensitivity has been tested with variations of the injection velocity of the particles. The injection velocity has been chosen because, when referring to an Icing Wind Tunnel, it is a parameter that is directly connected with the nozzle characteristics and operating conditions. It is dependent on the water pressure conditions and it is directly related to the nozzle mass flow. Local differences in the tunnel static pressure (non uniformity of the pressure profile) and differences in the pressure of the water rail connected to the nozzles or differences on the pressure of the single nozzles, might produce different local injection velocities. For this reason a preliminary investigation of their contribution and weight on the final particle dispersion has been done here. In this test the injection velocity has been increased of

15% respect to the baseline. The same Lagrangian time scale constant and numerical settings of the baseline have been used. The final particles dispersion is shown in figure 12:

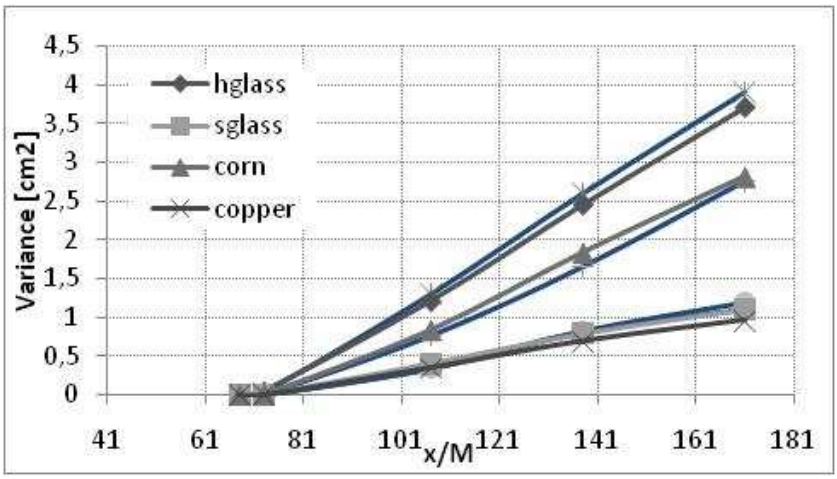

Figure 5-12: Effect of injection velocity on the variance of the dispersion

The relative difference on the variance respect to the baseline has been found to be less than 10% for the heavier particles (copper). For lighter particle, as the ones expected in Icing Wind Tunnel, the differences are on the order of 2%. For tracer particles the difference of the injection velocity is quickly dissipated close to the injection and a steady state with the surrounding fluid is quickly reached. This aspect is shown in figure 13 where the particle Reynolds number is shown for the two different injection velocities with the red line representing the higher one:

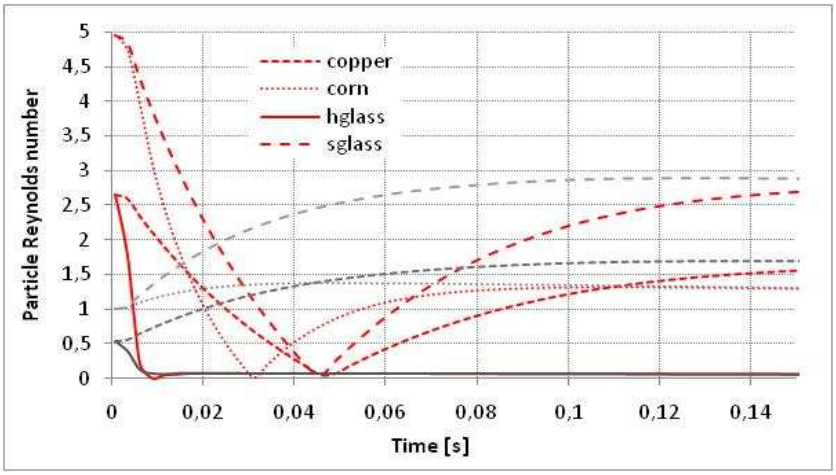

Figure 5-13: Particle Reynolds number vs. Time

For the hollow glass particle, with response time close to 2 milliseconds, the initial particles Reynolds number difference, due to the different injection velocity, is dissipated around 0,008 seconds after the injection.

The automatic numerical scheme has been found to be suitable to compute the particles dispersion in a wind tunnel and it has been used for computation in the Cranfield Icing Wind Tunnel. The injection velocity has been found to have a minor effect on the final particle dispersion when compare to the effect of the Lagrangian time scale constant. The Fluent discrete random walk formulation showed good result to calculate particles dispersion in homogeneous grid-generated turbulence as used in the experimental measurement and the model has been applied to Cranfield Icing Wind Tunnel.

The injection properties have been chosen in this test case as “single injection” option, which close reproduces the experiment. For Icing Tunnel case the injection is performed with nozzles, typically atomizing nozzles, which inject a cloud of droplets with characteristic velocity, cone angle and droplets size distribution. However the “single injection” option, combined with stochastic tries to reproduce the cloud, can be used as simplified approach also for Icing Tunnel simulation and its characterization will be discussed in the next chapter.

5.4.3 Injection Definition for Icing Tunnel simulation

For the sprays emanating from the nozzles, the resulting droplets are not a single diameter but instead can be characterized by a wide range of droplet sizes, from which an average droplet diameter can be determined. Depending on its size, each droplet, with its inertia, would have different dynamic behavior following different path. In this case the final distribution of water droplets would be then affected by the size distribution characterizing the nozzle’s spray.

In order to specify an injection type in Fluent, a model to be able to reproduce the nozzle characteristics would be required. Fluent has different type of injections that

can describe different type of spraying nozzles, including the atomizing pressure nozzles. However, for such representation the jet of air surrounding and interacting with the liquid sheet has to be simulated to obtain a proper representation of the spray. This would imply a detailed description of the local nozzle geometry and a detailed description of the nearby flow with great increasing of the computational cost and complexity of the simulation.

On the other side, if the size distribution is known, for example from experimental measurement, two approaches can be used to simulate the injection of water droplets. In the “single injection” approach the size of the droplet is fixed to its Mean Volumetric Diameter (MVD) and the cloud is obtained as a result of stochastic tries of the calculation of the droplet path. The cloud is then composed by a number of droplets (equal to the number of stochastic tries for calculations of trajectories) all with the same diameter (equal to the MVD).

When the spectrum of the droplets size distribution has to be included, the “file injection” can be used and the user has to create a file containing the information about positioning, velocity and sizes of the droplets [Fluent manual]. To obtain the size distribution of the droplets the Cumulative Distribution Function (CDF), or the percentage cumulative LWC, gives the fraction of mass (or LWC) contained in particles with diameter equal or less than a specified value. Experiments at Cranfield Icing Tunnel identified CDF curves for clouds with an MVD (Mean Volumetric Diameter) of 20 μm as shown in figure 5-14:

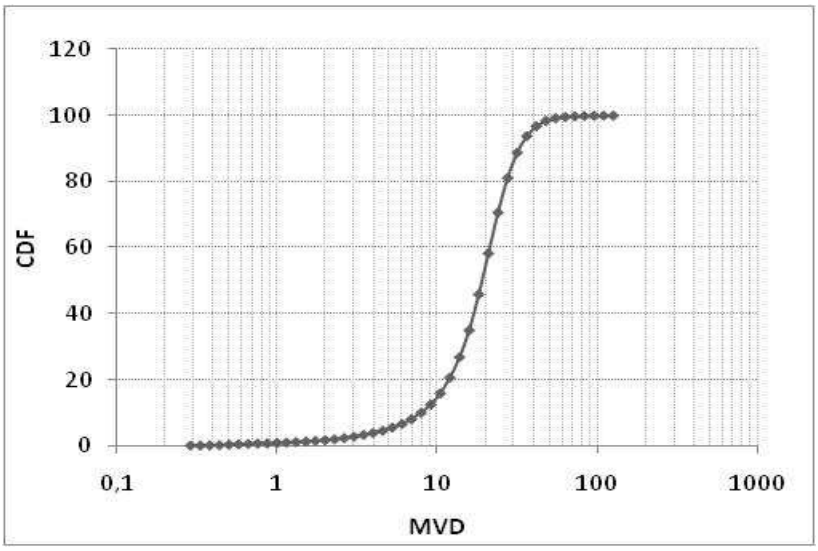

Figure 5-14: Cumulative distribution function vs. Mean Volumetric Diameter

It can be seen that the droplet diameter variation span a range between 0.3 and 125 microns. Using cubic splines, an interpolated curve was obtained for MVD vs. CDF. Using a linear Random Number Generator (between 0-1 with equal probability throughout the interval) and setting the generated random number equal to CDF, the corresponding diameter was found for each droplet injection event. A large number of droplets were injected in this manner to ensure a statistically large number of drops to cover the entire CDF range, and thus reproduce the same statistical distribution. An example of the injected cloud is shown in figure 5-15, where each droplet is identified by the position (x,y) and its size:

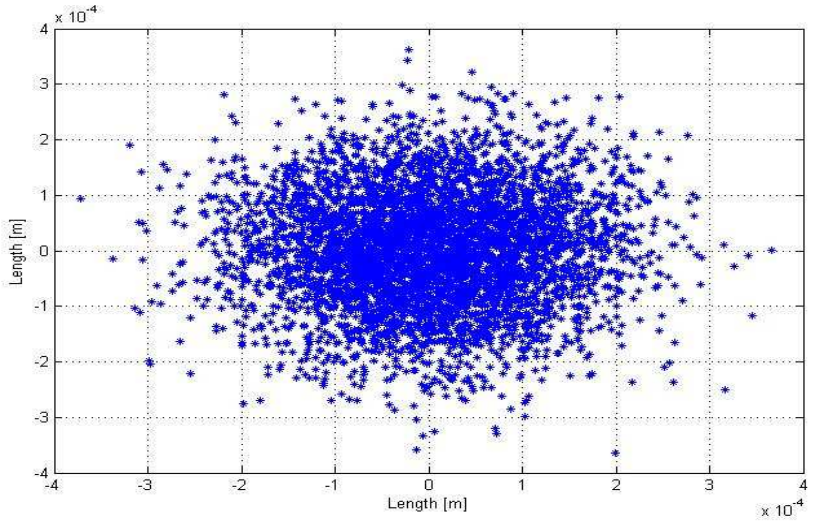

Figure 5-15: Simulated cloud of droplets

When the cloud has been statistically characterized by its CDF the dispersion of the droplets is calculated in the same way as done for the “single injection”. For each droplet, a stochastic number of trajectories are calculated to obtain a statistical representation of the droplet path. Differently from the “single injection” where the number of trajectories to be computed is N, when statistical representation of the injection is used, the number the number of trajectories is N x M, being M the number of droplets used to characterize the initial cloud. Because the computational cost greatly increases using the CDF to characterize the cloud, both the approaches have been used in the Cranfield Icing Tunnel calculation to investigate the sensitivity of the final solution respect the initial injection characterization.

6 Results of Cranfield IWT simulations

6.1 Introduction

The methodology and methods discussed in the previous chapters have been applied to the computation of water droplets dispersion in the Cranfield Icing Wind tunnel. Considering the low water droplets volume fraction (mush less than 10% of the air mass flow) and the consequent one-way coupling for the droplets-flow interaction, the first step was to obtain the airflow solution in the tunnel. The geometry and boundary conditions were determined as discussed in the paragraph 1.2.1. The verification of the tunnel airflow solution has been done as presented in the paragraph 1.3.3 for both the *k-ε* and RSM models. Once the airflow solution was available, the water droplets dispersion has been calculated with the DRW, where its validity was previously investigated in the test case of the paragraph 1.4.2. Two different injection types have been considered and used; respectively the “single injection” and the custom “file injection”. The droplets dispersion has been calculated in plane normal to the tunnel axis and the results compared with the experimental measurements. The discussion of the results is presented in the next paragraphs for the *k-ε* and RSM models.

6.2 Droplets dispersion with k-ε model

Calculations of water droplets dispersion have been performed with the airflow solution obtained with the *k-ε* turbulence model. The experimental measurements of the Icing Blade Test have been reproduced with the CFD for the conditions of velocity in the test section of 60 m/s and 40 m/s and for the three values of the LWC used. The measured turbulence statistics have been used to calculate the boundary condition as discussed in the paragraph 5.2.1 and the evolution of turbulent kinetic energy (k) and dissipation rate (ε) along the tunnel axis is shown in the next figures:

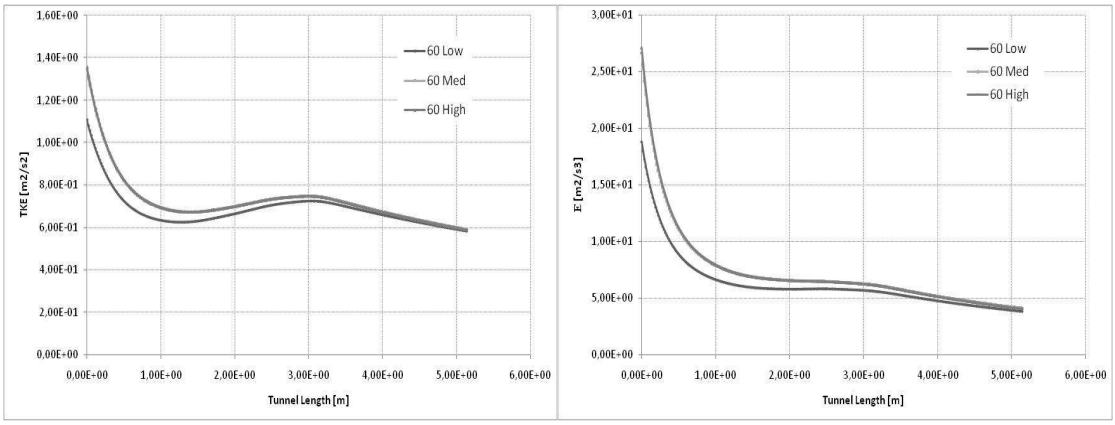

Figure 6-1a, b: k, ε along tunnel axis at 60 m/s

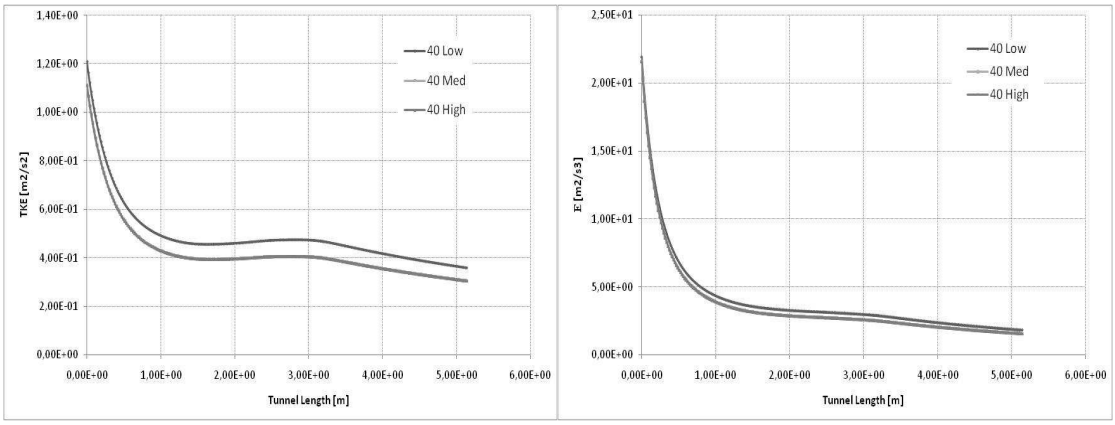

Figure 6-2a, b: k, ε along tunnel axis at 40 m/s

The decay of the turbulent kinetic energy, at the tunnel centreline, follows a power low trend approximately up to one meter far from the inlet plane. After that the increasing is due to the effect of the production terms, due to the tunnel contraction ratio and affected by the acceleration along the tunnel axis. Similar trend is shown by the dissipation rate. Low, medium and high LWC conditions show the same trend, at the tunnel centreline, with lines corresponding to different LWC valued overlapping for both the velocities of 40 and 60 m/s.

The water droplets have been injected in the flow at the input plane, which has been located at the pray bars location. The injection reproduce the spray bars from bar 1 (top of the tunnel) to bar 6 (bottom of the tunnel) with the nozzles configuration used in the

experimental measurements. Both the single injection and the file injection have been used and the results, in terms of droplets distribution, investigated.

6.2.1 "Single Injection" Case

The single injection has been specified for droplets size of 20 microns and the cloud has been characterized by stochastic tries of trajectory calculations. An example of the cloud representation is shown in figure 18:

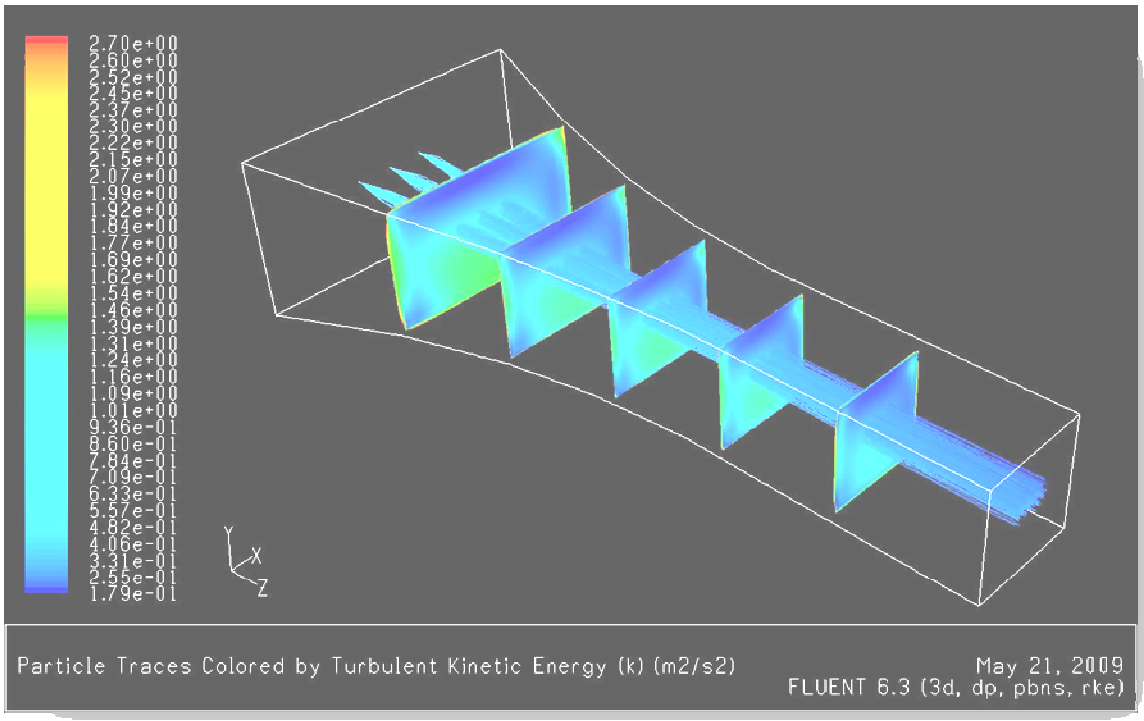

Figure 6-3: Droplets cloud from single injection

The cloud evolution along the tunnel has been measured calculating the standard deviation of the displacement of the droplets crossing reference planes vertical to the tunnel axis. The planes have been placed from 1 meter far from the spray bars, one each 40 centimetres. In the following figures is shown the evolution of the Y-axis standard deviation (Y-STD) of the cloud along the tunnel axis, for the velocity of 60 & 40 m/s

with respectively the three conditions of high, medium, low LWC i.e.: nozzles air pressures:

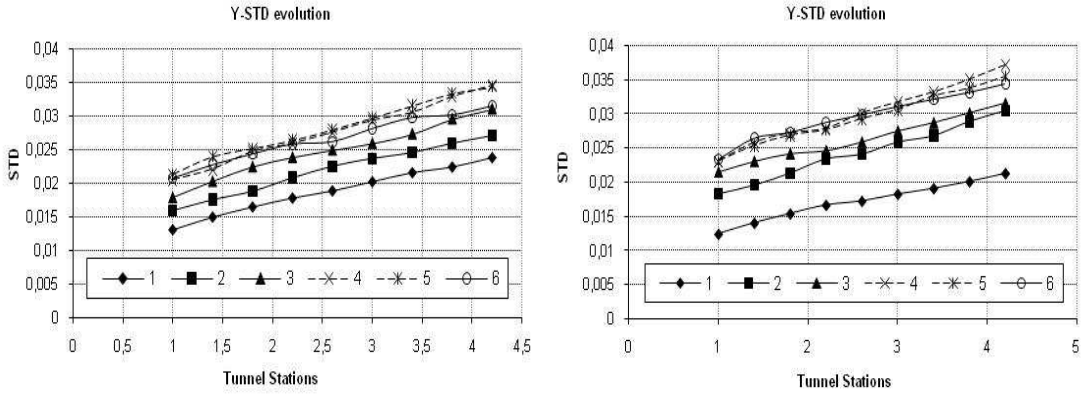

Figure 6-4 a, b: STD evolution 60 m/s (a) & 40 m/s (b) for High LWC

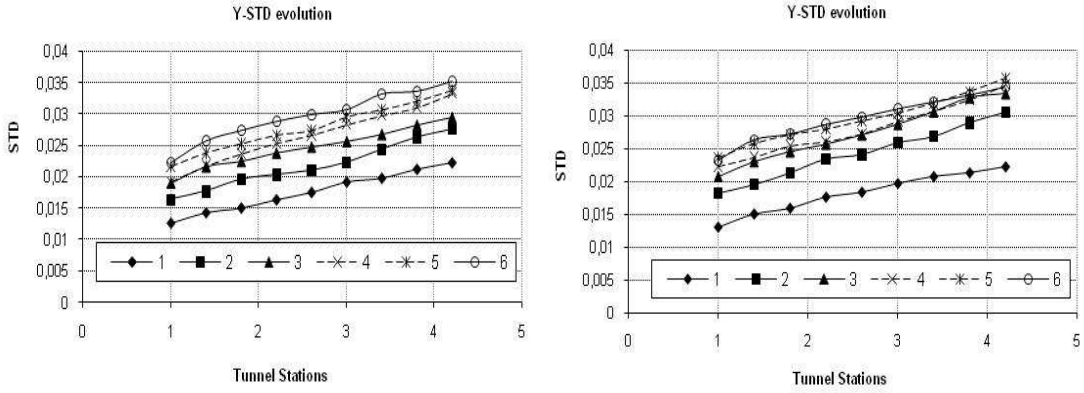

Figure 6-5 a, b: STD evolution 60 m/s (a) & 40 m/s (b) for Medium LWC

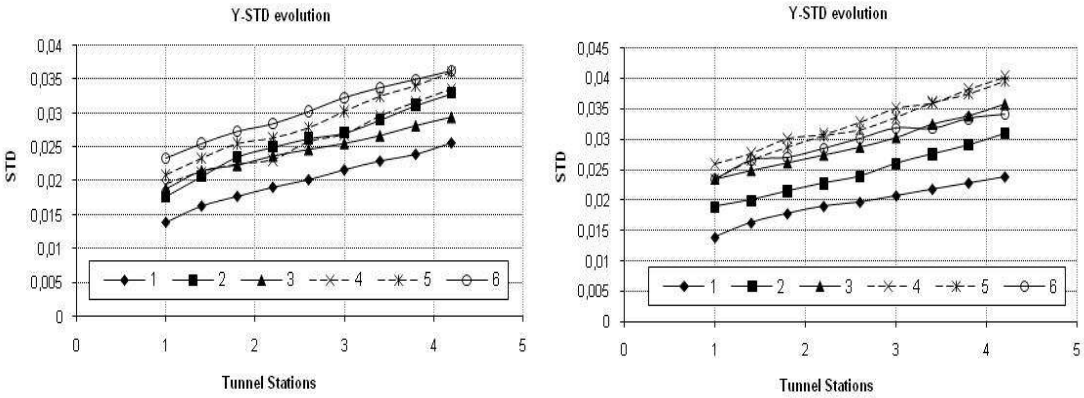

Figure 6-6 a, b: STD evolution 60 m/s (a) & 40 m/s (b) for Low LWC

The trend of the Y-STD is approximately linear along the tunnel axis for both the velocity conditions. The absolute value for the Y-STD increase for the bottom part of the tunnel where the measured turbulent kinetic energy was found to be higher. The positive contribution of the turbulent kinetic energy to the increasing of the standard deviation of the cloud is generally balanced by the contraction of the tunnel that squeezes the cloud. The slope of the STD trend is affected by both these contributions and the STD lines are slightly divergent with increasing the distance from the injection due to the higher turbulence at the bottom of the tunnel. However, depending on the tunnel geometry the contraction ratio effect can be dominant. This aspect can be seen considering the evolution of the X-axis standard deviation along the tunnel axis as shown in the next figures for the velocities of 60 and 40 m/s and respectively for high, medium, low LCW:

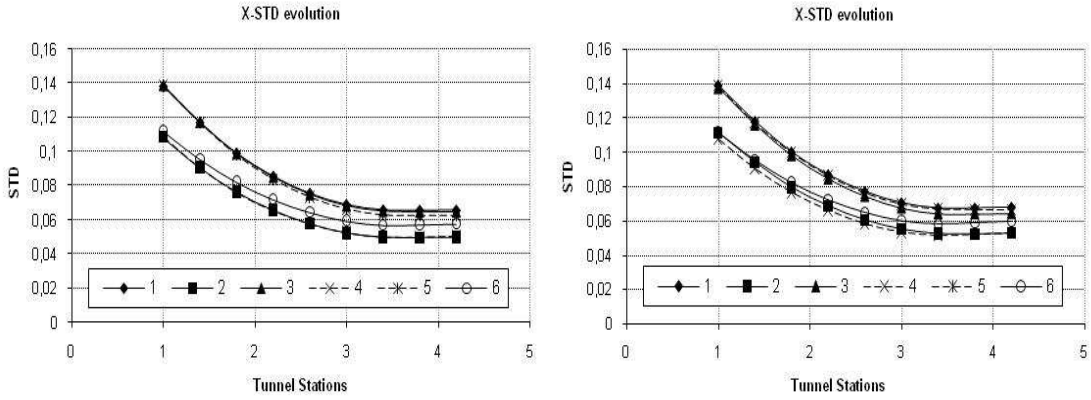

Figure 6-7a, b: X-STD evolution 60 m/s (a) & 40 m/s (b) for High LWC

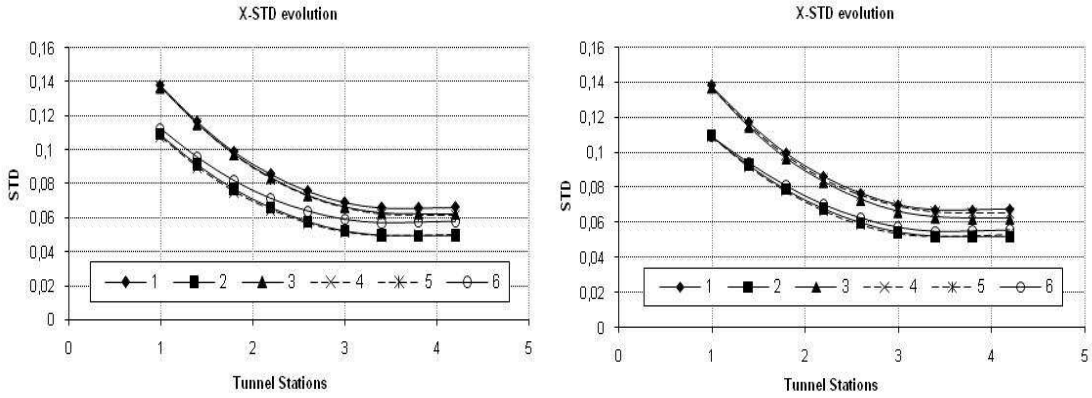

Figure 6-8a, b: X-STD evolution 60 m/s (a) & 40 m/s (b) for Medium LWC

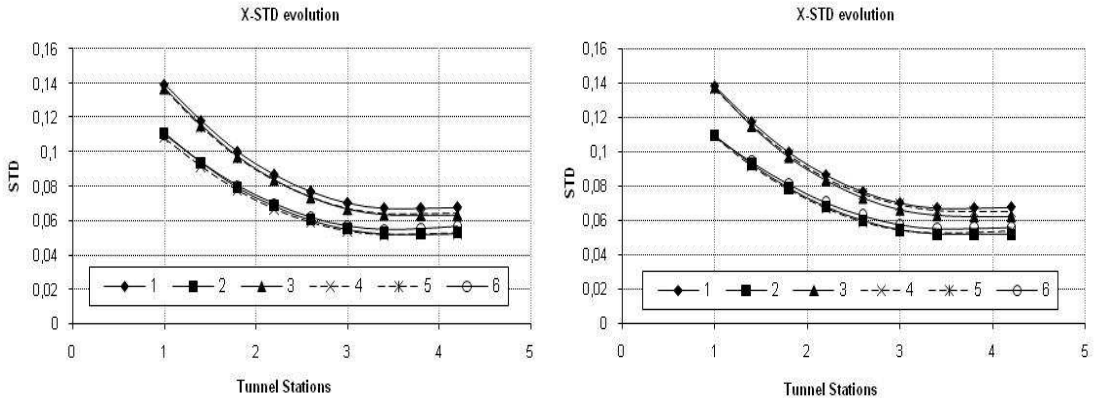

Figure 6-9a ,b: X-STD evolution 60 m/s (a) & 40 m/s (b) for Low LWC

In this case the contraction ratio effect reduces the X-axis spread of the cloud until the beginning of the straight section approximately 3 meters far from the injection. The trend of the X-STD then remain approximately constant during the first part of the test section where the droplets inertia effect on the trajectory balance the increasing dispersion effect due to the turbulence.

To compare the distribution with the experimental results the Y-axis standard deviation of the cloud has been investigated in a plane located at the same position of the icing blade during the experiments. The cloud distribution characteristics, as standard deviation and location of the mean value, have been calculated and reported for each of the spray bars. The Y-axis mean peak location comparisons are shown in the next table:

Bars	experiment	40	60
1	0.307	0.2918	0.2911
2	0.171	0.1751	0.1771
3	0.035	0.051912	0.054
4	-0.033	-0.058691	-0.058
5	-0.101	-0.1791	-0.1781
6	-0.169	-0.222345	-0.221958

Table 4: Position of the mean value of droplets distribution

The contribution of the nozzle air pressures to the peak location is of the order of 0.1% and then it does not significantly affect the location of the mean value. For this reason

an average value, calculated on the ensemble of the realization with the three different air pressures, has been reported. More significant, instead, is the contribution to the standard deviation of the distribution. The following graphs show the values of the standard deviation, normalized by the test section height (L), at the same icing blade location and for different spray bars (1 to 6), velocities (40 m/s and 60 m/s) and nozzle air pressure (low, medium, high).

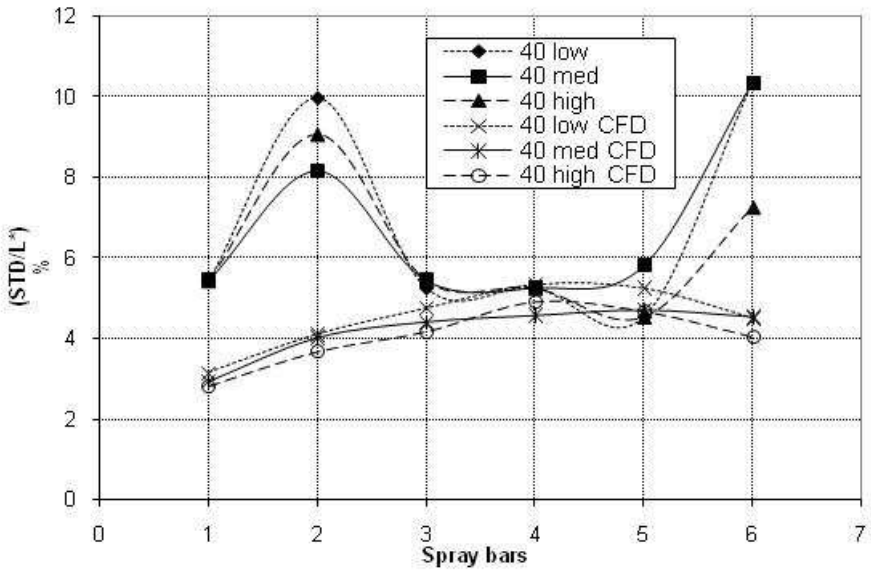

Figure 6-10: Experimental vs. Numerical STD trend at 40 m/s

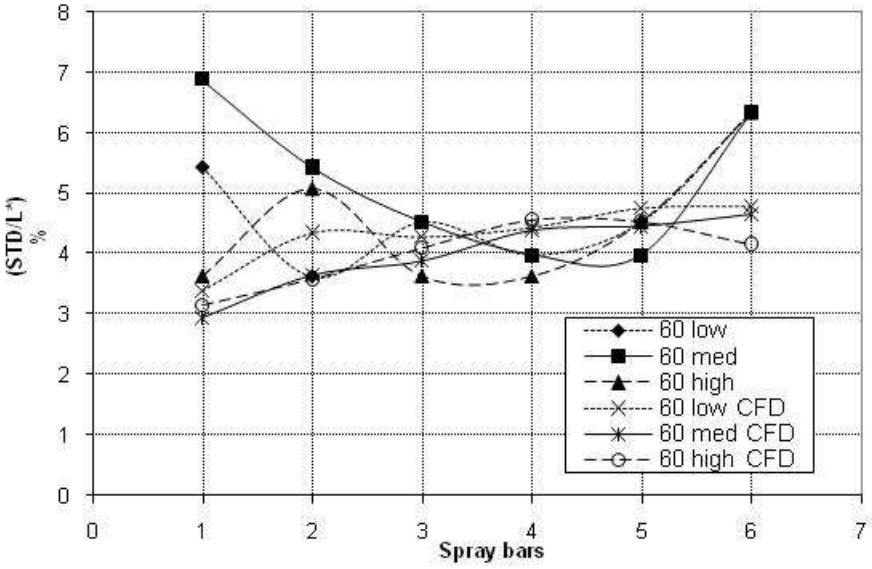

Figure 6-11: Experimental vs. Numerical STD trend at 60 m/s

The uncertainty of the standard deviation associated to the stochastic independent tries is about 2% and it is lower than the relative differences between the variances of the three air pressure solutions. The solver is able to reproduce the effect of the nozzle air pressure variations and original relative pressures differences of the order of 2%, for the values used during experimental measurements, have reflected, through different turbulence inlet profiles, in final STD differences less than 1% of the test section length. However, the accuracy of the model cannot catch higher variations of the standard deviation, more than 2% of the test section length. The trend at 60 m/s shows a higher accuracy if referred to the distinct solutions. However the value of the difference of the STD between CFD solutions and experiments is a fraction of the characteristic length scale of the test section making the model suitable for industrial applications.

The dispersion of water droplets along the X-axis has also been calculated in the test section reference plane and compared with the icing blade measurements performed with the blade in horizontal position in the test section, at heights corresponding to the mean position of the cloud. The velocity for this case was of 40 m/s. A representation of the X-axis behaviour of the cloud, produced by a row of nozzles for each spray bar and coming from CFD calculations, is shown in figure 6-12:

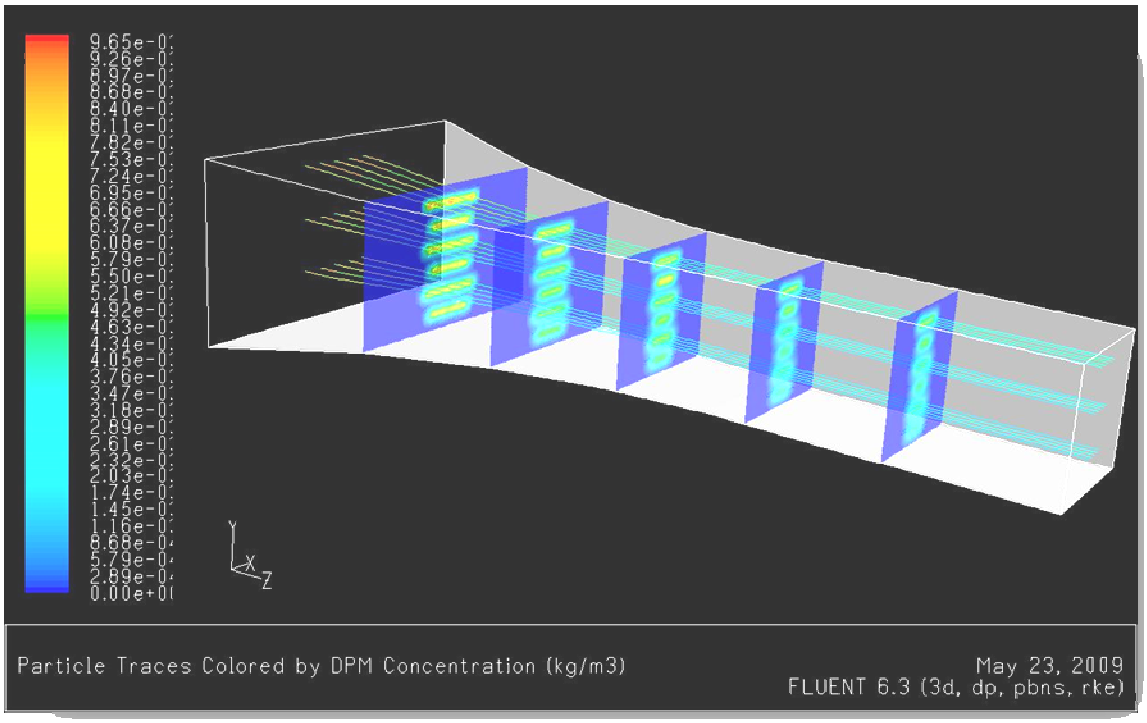

Figure 6-12: Overview of the cloud behaviour along the tunnel

The profile of the distribution along the X-axis has been calculated and presented in terms of LWC distribution. Results for each spray bar and three nozzles air pressures are shown in the next figures, from bar 2 to bar 6:

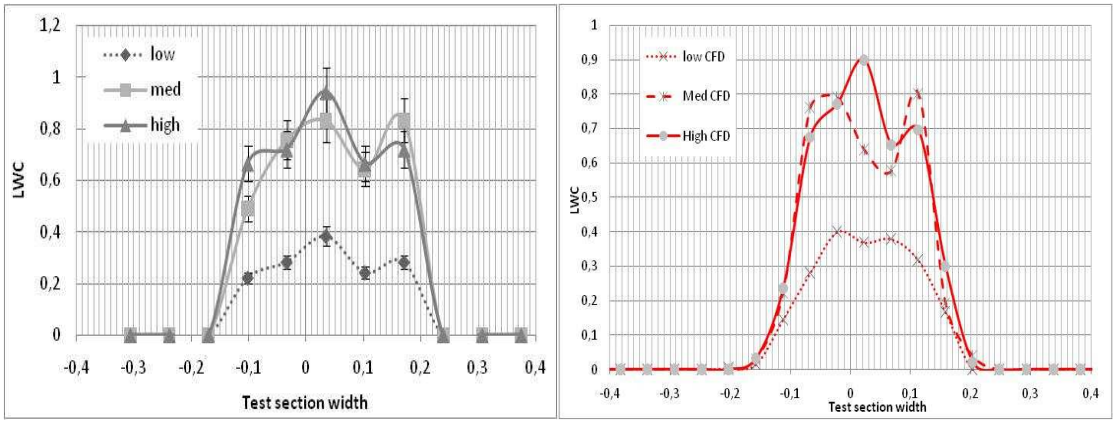

Figure 6-13a, b: bar 2, X-axis distribution, experiment (a), CFD (b)

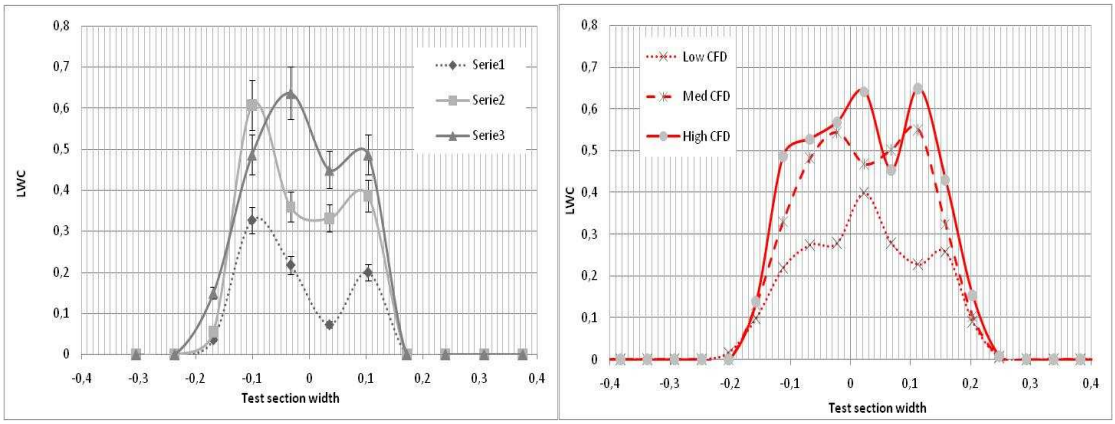

Figure 6-14 a, b: bar 3, X-axis distribution, experiment (a), CFD (b)

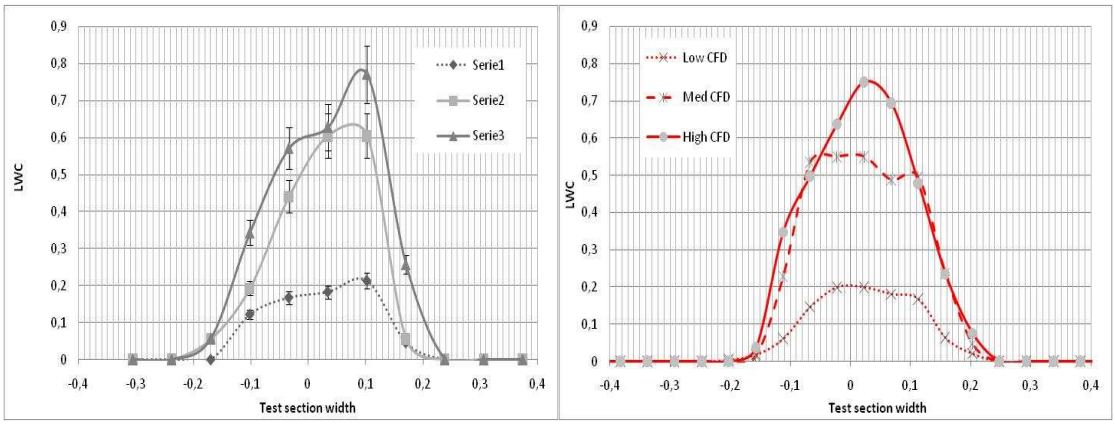

Figure 6-15 a, b: bar 4, X-axis distribution, experiment (a), CFD (b)

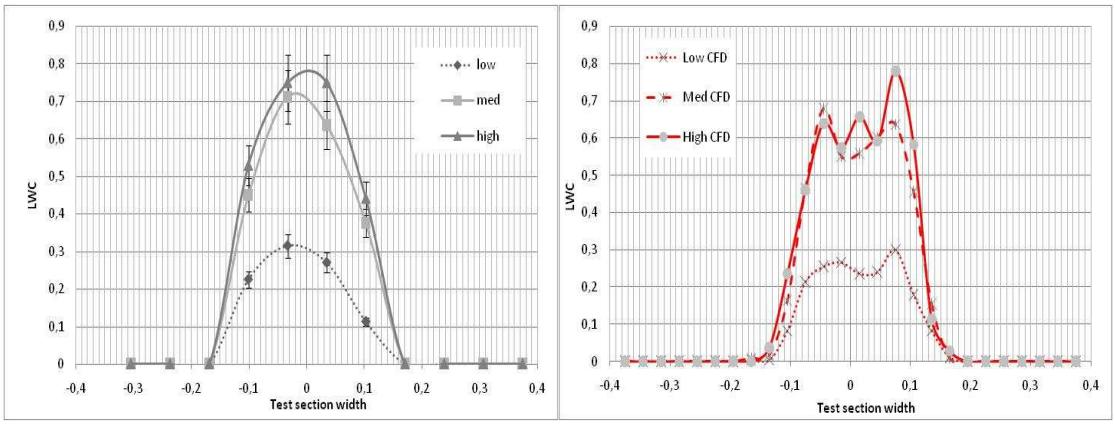

Figure 6-16 a, b: bar 5, X-axis distribution, experiment (a), CFD (b)

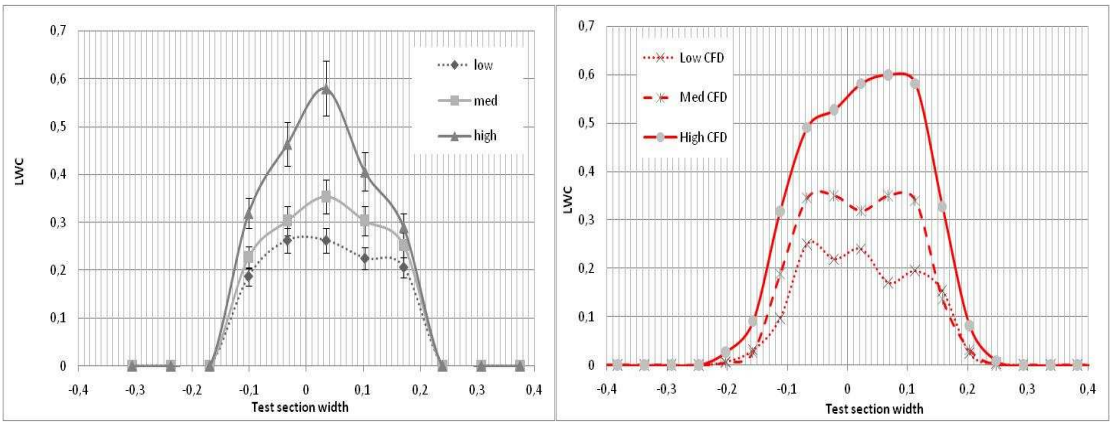

Figure 6-17 a, b: bar 6, X-axis distribution, experiment (a), CFD (b)

The CFD simulation performs a good result to reproduce the trend of the LWC distribution along the X–axis. The overall shape of the distribution is caught by simulation with better results for bars 2, 3 and 4, while bars 5 and 6 show more accentuate differences from the experiment. However the mean value of the distribution and its spread is well reproduced for all the spray bars. In terms of accuracy, local differences of LWC distribution between experiment and simulation can have average values around 10%. Both the cases of distribution along Y-axis and X-axis showed good agreement with experimental results with accuracy that can be suitable for industrial application and test support.

In order to verify the approach to simulate the injection with the “single injection” characterization, a comparison between the spray distribution close to the nozzle and the measurements acquired with the thermal probe has been done. The distribution of the cloud was calculated at the same location of the thermal probe measurements and the results compared in terms of standard deviation of the distribution (STD). The comparison has been done for the two values of the velocity, 40 m/s and 60 m/s, and for the three values of the nozzles air pressures used in the icing blade experiment. The calculated distribution, expressed in terms of frequency (Fr) of particles to be located at the interval (y, y+Δy), normalized by its maximum value (Fr max) is shown in figure 6-18 for the two velocities:

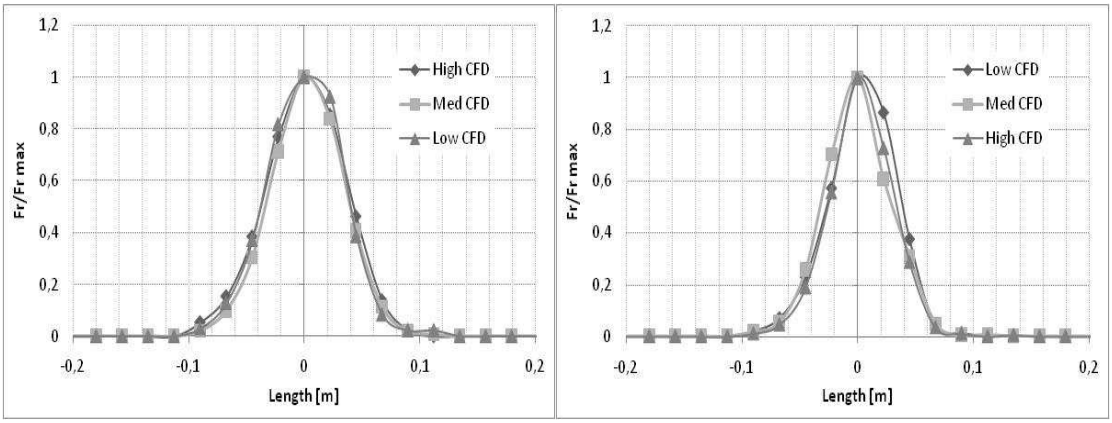

Figure 6-18 a, b: spray distribution, 40 m/s (a), 60 m/s (b)

As for the thermal probe experiment, where higher variations of nozzles air pressures were tested, the standard deviation has been found to be mainly not dependent on the nozzle air pressures. The values of the STD have been found to be on average 2.9 cm for the 40 m/s case and 2.7 cm for the 60 m/s one. The relative difference between them has been found to be consistent with the experimental measurement, with difference around 10%. The relative difference between the experiment and the CFD, for each value of the velocity, has been found to be of the order of 15% with an underestimation of the dispersion for the calculated cloud at the near nozzle field.

6.2.2 "File Injection" Case

In the single injection option the particle size is fixed to its MVD diameter and the cloud is composed by droplets of equal size. To improve the characterization of the injection the "file injection", as described in the paragraph 1.4.3 can be used. In this case a file containing the information about the cloud has to be created by the user following the Fluent user guide. To test the behaviour of this injection and to compare the result with the "single injection" type the water droplets dispersion has been calculated with the same airflow condition used for the "single injection". Results have been obtained for the velocity conditions of 40 and 60 m/s and for the three values of the nozzle air pressures. The droplet size distribution has been obtained by previous Cranfield Icing Tunnel measurements and the MVD was of 20 microns. The cloud

evolution has been monitored similar for the “single injection” case and the results for the Y-axis distribution are shown in the next figures:

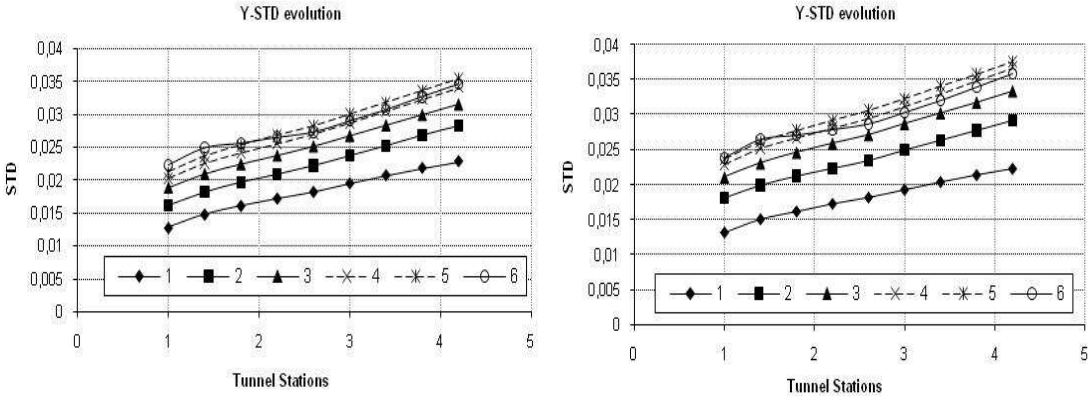

Figure 6-19 a, b: STD evolution 60 m/s (a) & 40 m/s (b) for High LWC (file injection)

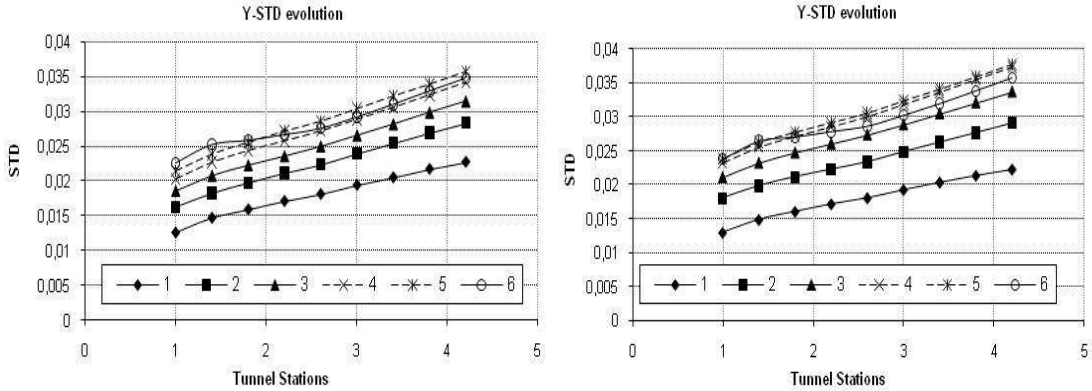

Figure 6-20 a, b: STD evolution 60 m/s (a) & 40 m/s (b) for Medium LWC (file injection)

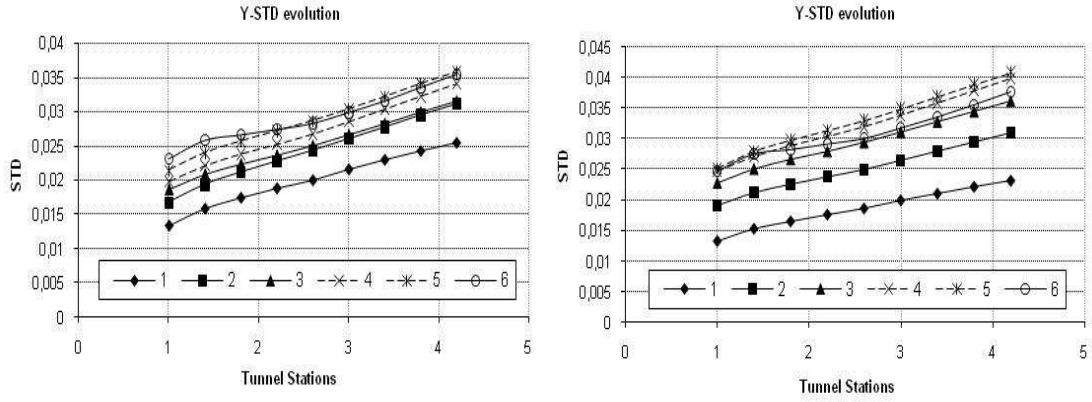

Figure 6-21 a, b: STD evolution 60 m/s (a) & 40 m/s (b) for Low LWC (file injection)

The trend is similar to the one obtained with the “single injection” specification. Also in this case the lines are slightly divergent confirming the same behaviour showed for the 20 microns-only droplets. The local errors between the values of the standard deviation of the solutions of “file injection” and “single injection” have been found to be generally less than 12% with strongly non-monotonic trend along the tunnel axis. The average of the error calculated on the ensemble of the errors at the reference plane along the tunnel axis for each spray bars is shown in figure 6-22 for the velocities of 40 and 60 m/s:

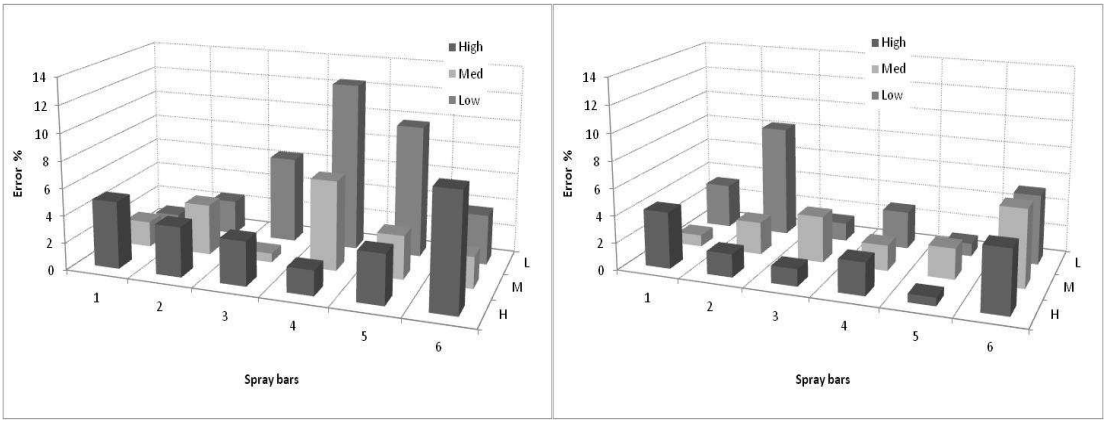

Figure 6-22a, b: Error % between different injection types, 40 m/s (a), 60 m/s (b)

The figures show as the error is mainly in the range of 2% and 4% , that is close to the statistical error associated to the stochastic computation of the trajectories and in this sense the two solutions do not show significant differences for the Y-axis cloud evolution.

The evolution of the X-axis distribution along the tunnel has also be found to be similar to the one of 20 microns-only droplets and also in this case mainly affected by the squeezing effect of the X-axis contraction ratio. The results for the standard deviation evolution are shown in the next figures:

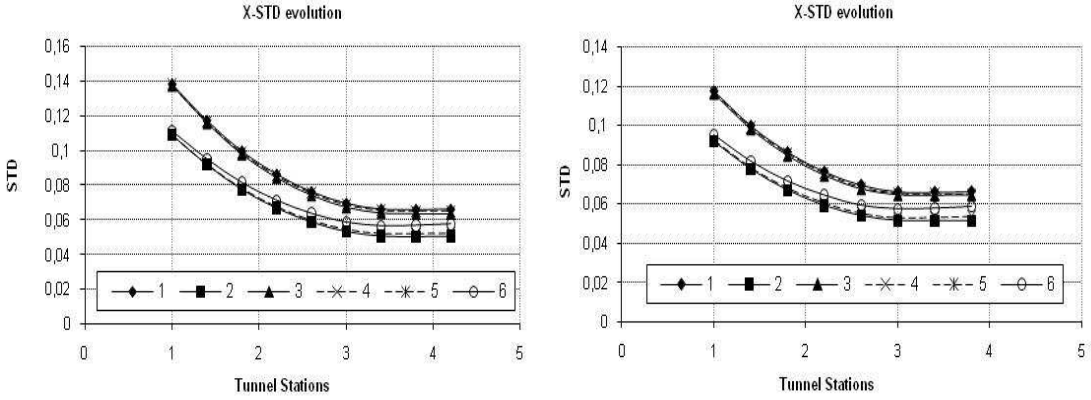

Figure 6-23 a, b: X-STD evolution 60 m/s (a) & 40 m/s (b) for High LWC

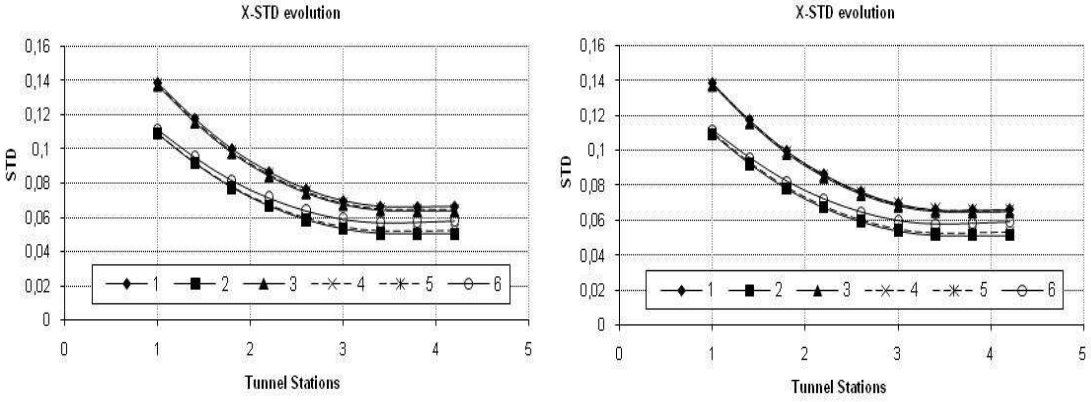

Figure 6-24 a, b: X-STD evolution 60 m/s (a) & 40 m/s (b) for Medium LWC

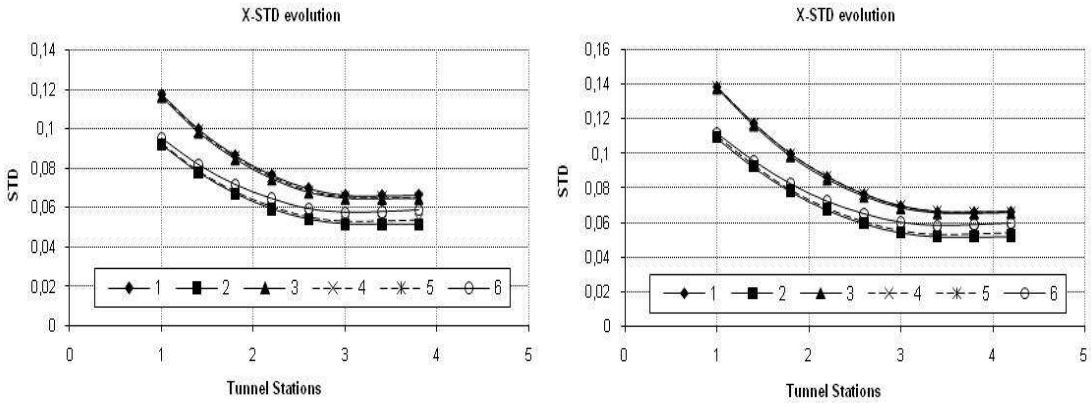

Figure 6-25 a, b: X-STD evolution 60 m/s (a) & 40 m/s (b) for Low LWC

The error of the X-axis standard deviation of the distribution between the solutions with the two injection types has been found to be generally less than 4%. The average value of the error, calculated on reference planes along the tunnel axis, is shown in the next figure for the two conditions of velocity, 40 and 60 m/s and for each spray bar.

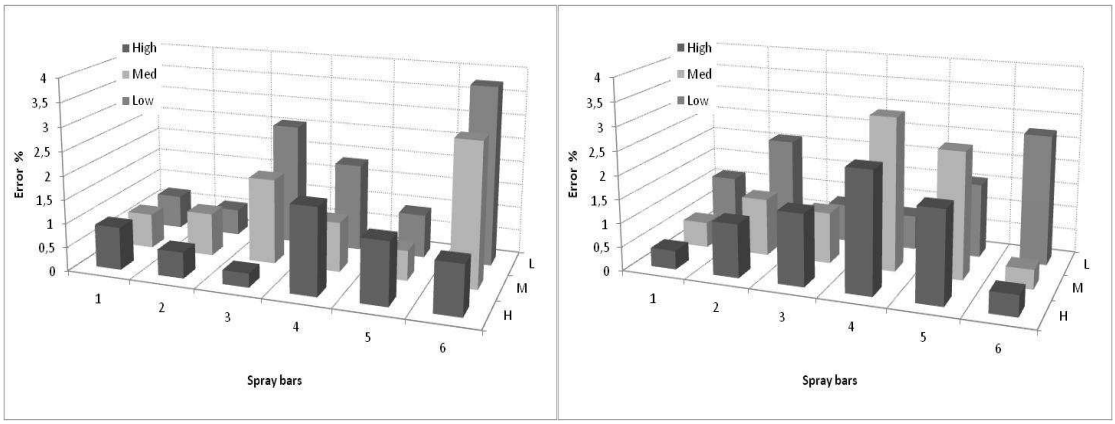

Figure 6-26 a, b: Error % between different injection types, 40 m/s (a), 60 m/s (b)

The figure 41 shows as the error is mainly in the range of the uncertainty due to the statistical calculation of the trajectories and also for this case the two injections provide the same type of results.

The results of the water distribution in the test section have been analyzed considering the Y-axis standard deviation for individual spray bars. As for the “single injection” case the results are expressed in terms of standard deviation, normalized by the test section height (L), for different spray bars (1 to 6), velocities (40 m/s and 60 m/s) and nozzle air pressure (low, medium, high). The following graph shows the values of the STD corresponding to the relative spray bar for the velocities of 40 and 60 m/s (compared with experimental measurement):

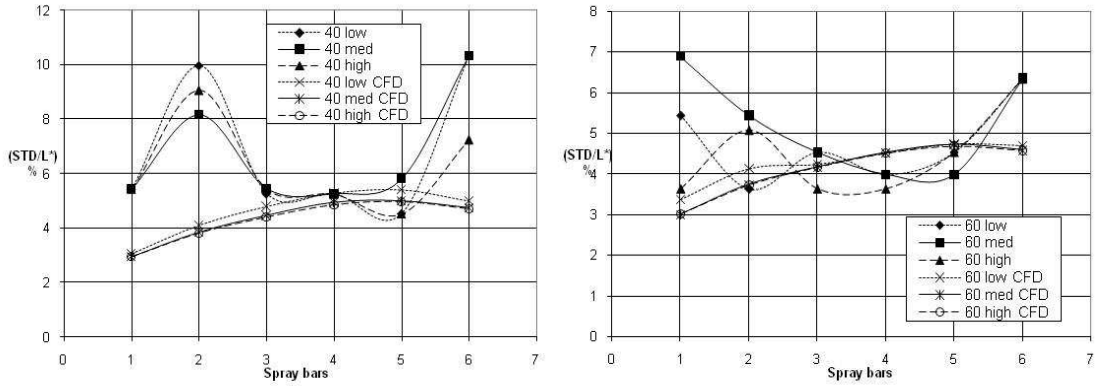

Figure 6-27 a, b: Y-axis normalized STD, 40 m/s (a), 60 m/s (b)

Similar trend to the 20 micron-only case has been found for the "file injection". Local relative differences have been estimated to be on average less than 5% of the "single injection" baseline. The error of the Y-axis standard deviation between the calculations with different injection type is shown in the next figure for the velocity conditions of 40 and 60 m/s:

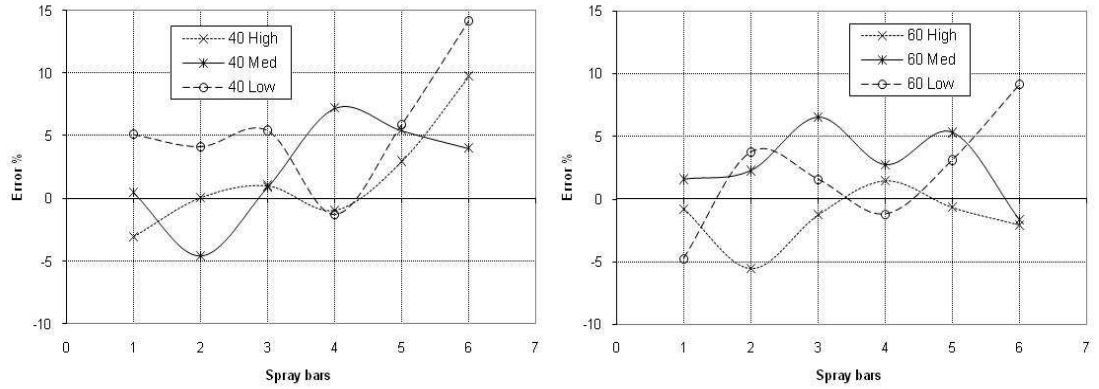

Figure 6-28 a, b: Y-axis relative error % between different injection types 40 m/s (a), 60 m/s (b)

Also in this case is not possible to identify a monotonic trend of the error, mainly because it is very close and affected by the statistical uncertainty on the standard deviation computation.

Considering the small relative differences of the calculations performed with the two injection types, both of them have given the same overall distribution, expressed in

terms of standard deviation of the statistical cloud. Relative errors of a fraction of the normalized standard deviation distribution indicate that the differences of the models produce not significant changes to improve the resolution of the cloud distribution on length scales proportional to the test section and then typically adopted during the tests.

6.3 Droplets dispersion with RSM

In order to include the effects of the anisotropy of the turbulence of the airflow solution and to extend those effects to the calculation of water droplets dispersion, additional simulations have been performed with the *Reynolds Stress* turbulence model (RSM). As for the *k-ε* model, the same conditions of velocity in the test section, 60 m/s and 40 m/s, and LWC, low, medium and high have been used. The boundary conditions at the input plane have been specified with the turbulent kinetic energy profile and the turbulent dissipation rate such as used in the *k-ε* model. However, depending on the details available from experimental measurements, the FLUENT code allows to specify singles values of the Reynolds Stress Tensor. In principle the *k-ε* boundary inlet conditions may require to be readjusted using the RSM in order to provide calculated values of turbulence statistics close to the experimental values, at the experimental measurement location. In the case of Cranfield Icing Tunnel it has been verified and will be shown further that the same input condition can be used within a reasonable level of accuracy.

When the turbulent kinetic energy profile is given as boundary condition the code automatically set the values of the anisotropic part of Reynolds Stress tensor to zero while the diagonal terms have the same value each other, equal to 1/3 of the turbulent kinetic energy. In this case, where no additional details are given for the Reynolds Stress Tensor, the assumption of isotropy is still used to specify the boundary conditions for the Reynolds Stress terms. However, the evolution of those terms along the tunnel would be then individually tracked and affected by the airflow regime and tunnel geometry. The evolution of turbulent kinetic energy (k), calculated as the sum of the diagonal components of the Reynolds Stress Tensor, and dissipation rate (ε) along the tunnel axis is shown in the next figures for the velocities of 60 m/s and 40 m/s:

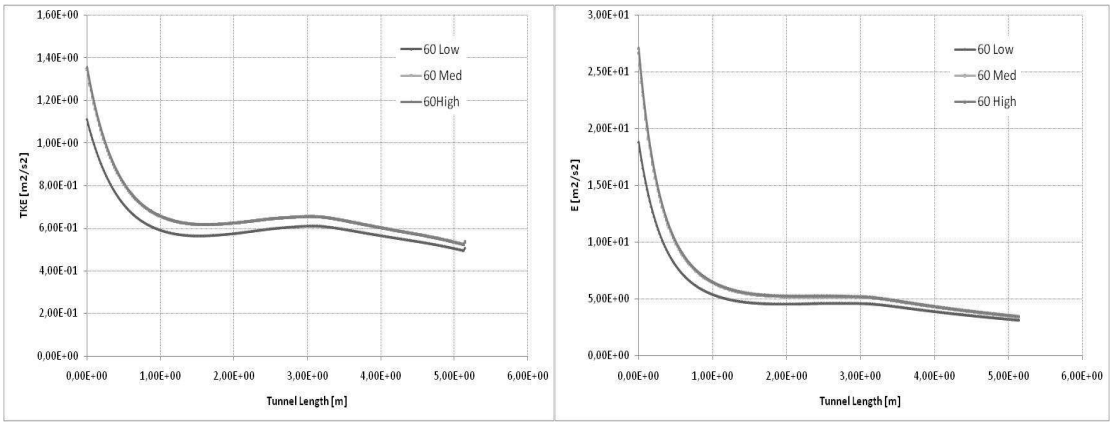

Figure 6-29 a, b: k, ε along tunnel axis at 60 m/s

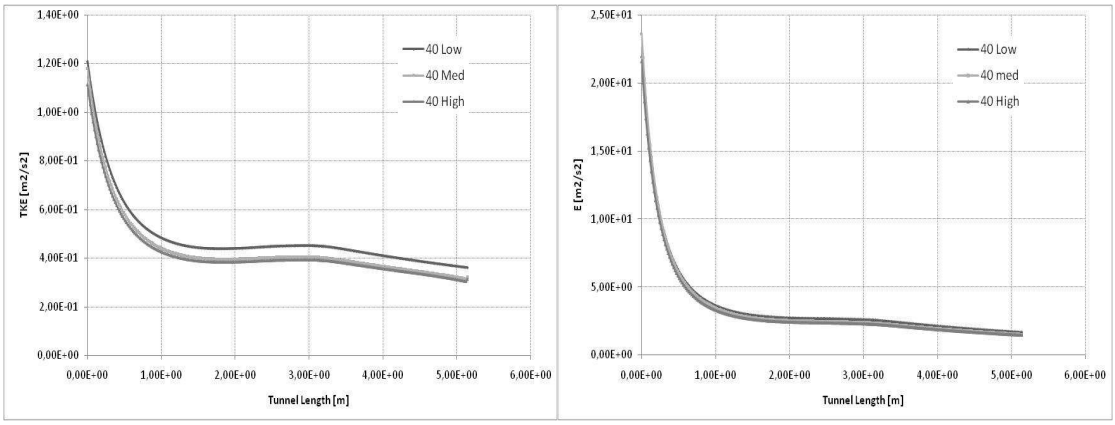

Figure 6-30 a, b: k, ε along tunnel axis at 40 m/s

The results of the turbulent kinetic energy and dissipation rate decay are similar to the ones obtained with the *k-ε* model. Same trend has been found for the decay along the tunnel axis with similar contribution to the production of the turbulent kinetic energy due to the tunnel contraction ratio. A comparison between the two solutions is shown in the following figures. They show the different percentage between the solutions with the two turbulence models, normalized by the value at the boundary inlet condition, for the velocities of 60 m/s and 40 m/s. Because the differences on the solutions, calculated with the three conditions of LWC, have been found to be very close each other, the average trend based on the ensemble of the three LWC trends, is reported.

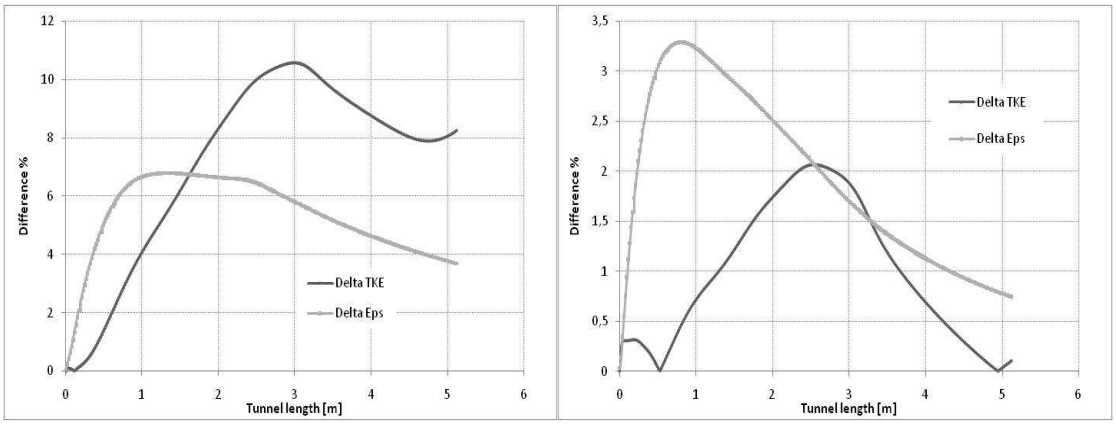

Figure 6-31 a, b: Difference % between RSM and k-e solutions 60m/s (a) 40m/s (b)

The difference percentage can be estimated to be on average 7% and 5% for the turbulent kinetic energy and dissipation rate at 60 m/s and 1% and 2% at 40 m/s. At the location of the experimental measurement plane, one meter downwind the spray bar, the error between the solution is generally less than 6.5% at 60 m/s and less than 3.2% at 40 m/s. This aspect confirm that the turbulent kinetic energy and dissipation rate profiles calculated with the RSM are close to the ones calculated with the *k-ε* model and, in this particular case, no adjustment of the inlet boundary profile is needed.

Besides the small relative difference between the turbulent kinetic energy of the two models, that in principle would affect the particles dispersion, another difference is based on the way the turbulent kinetic energy is distributed along the reference frame directions. For the *k-ε* model isotropy is assumed for the whole solution and the energy is equally divided on the three directions. For the RSM model the evolution of the Reynolds Stress terms is calculated along the tunnel and the energy can be differently divided along the three reference frame directions. The results of this energy distribution would affect the particles dispersion through the calculation of the fluctuating velocity that in the RSM is taken proportional to the Reynolds Stress components associated to X, Y and Z directions. The Reynolds Stress terms evolution, along the tunnel axis, is shown in the following figure and compared to the evolution of the turbulent kinetic energy calculated with the *k-ε* model. The values are normalized with the value of the variance of the fluctuation associated with the *k-ε* model. Both the cases of 60 m/s and 40 m/s are reported.

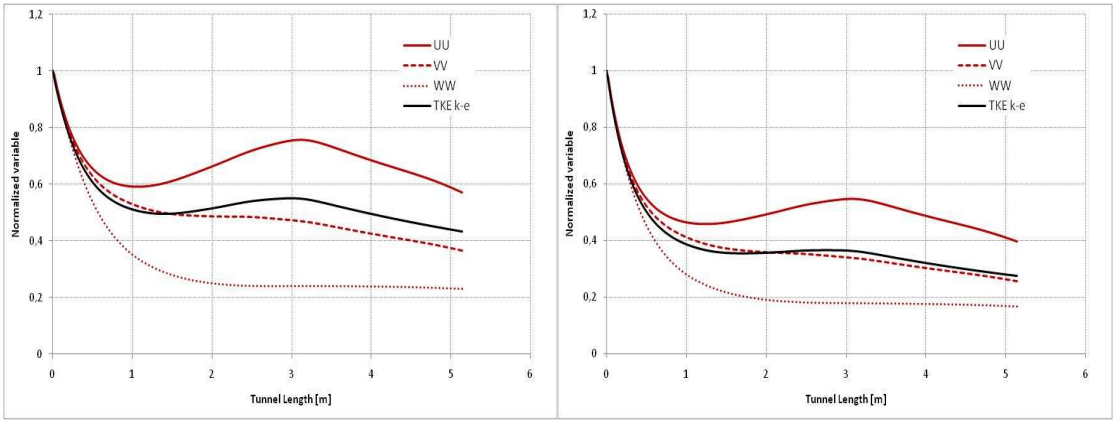

Figure 6-32 a, b: Reynolds Stress terms evolution 60 m/s (a) 40 m/s (b)

It can be seen that for the RSM at 60 m/s an higher variance is calculated for the fluctuating component of the velocity along the X-axis (UU component) respect the *k-ε* model, while for the Y-axis the associated variance is close to the one computed by the *k-ε* model using the turbulent kinetic energy. The variance along the tunnel axis (WW) is always lower than the one computed by the isotropic model, however, due to the higher difference with the mean velocity component, approximately two orders of magnitude, the impact of this fluctuating component on the residence time in the tunnel and then on the overall dispersion is negligible. For the 40 m/s case, similar trend has been found with the scale of variables shifted to lower values. The effects of these differences respect *k-ε* model may affect the overall particle dispersion through different calculation of the fluctuating components.

6.3.1 "Single Injection" case

As in the *k-ε* model the water droplets have been injected in the flow at the input plane, located at the spray bars location. The injection reproduce the spray bars from bar 1 (top of the tunnel) to bar 6 (bottom of the tunnel) with the same nozzles configuration of the *k-ε* model and then of the experimental measurements. Also in this case both the single injection and the file injection have been used to check the impact on the water droplets distribution. The single injection has been specified for droplets size of 20 microns and the cloud has been characterized by stochastic tries of trajectory calculations.

The Y-axis STD evolution, similarly at what shown for the *k-ε* model, is shown in the following figures:

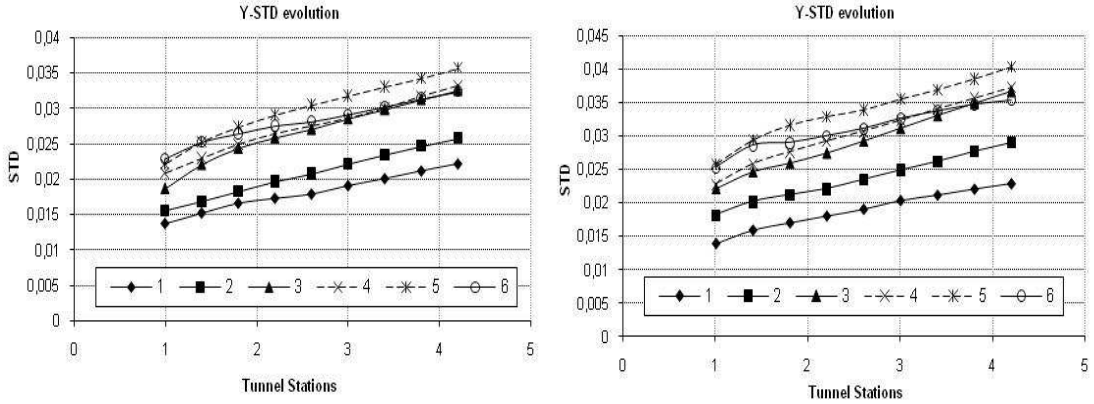

Figure 6-33 a, b: STD evolution 60 m/s (a) & 40 m/s (b) for High LWC (RSM)

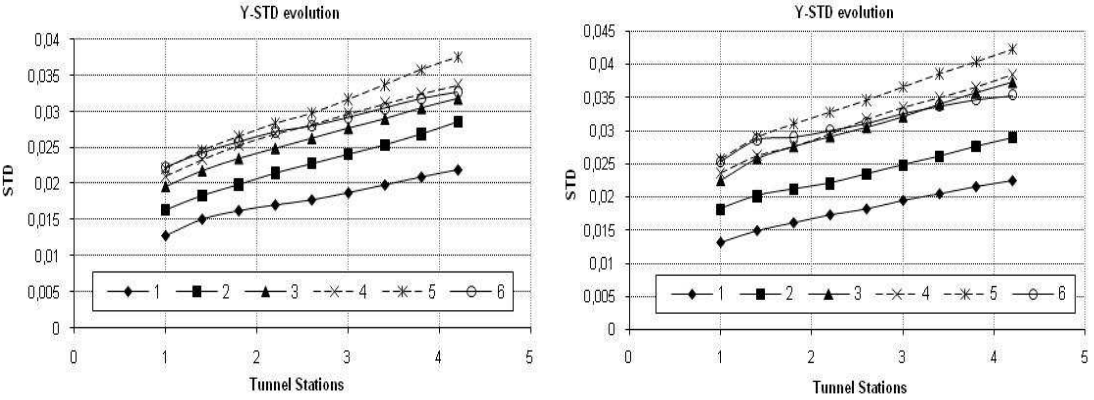

Figure 6-34 a, b: STD evolution 60 m/s (a) & 40 m/s (b) for Medium LWC (RSM)

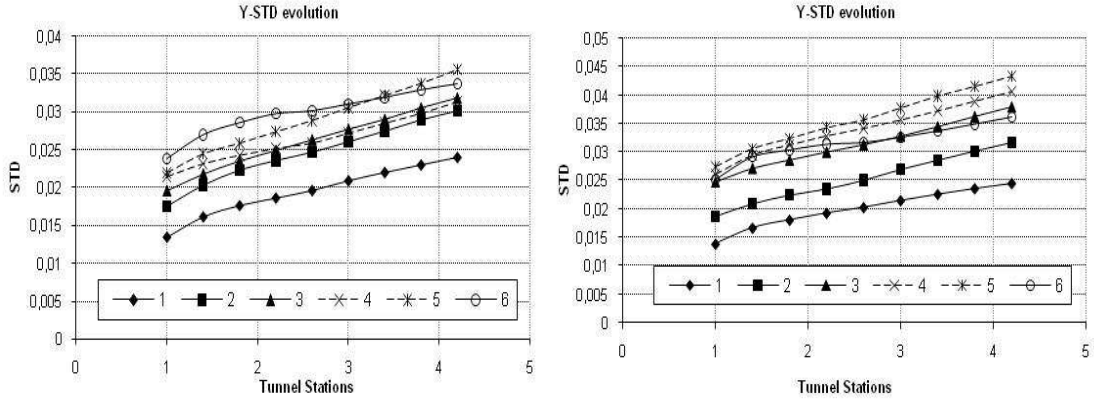

Figure 6-35 a, b: STD evolution 60 m/s (a) & 40 m/s (b) for Low LWC (RSM)

The trend of the Y-axis STD is quite close to the previous simulation with the assumption of isotropy and no significant difference can be recognized on macroscopic scale. Also in this case the bottom of the tunnel generally experience and higher slope for the STD trend, due to the higher local turbulence. Absolute values of the STD are also close to the ones calculated with the *k-ε* model, suggesting that the sensitivity of the model to small differences of the turbulence profiles, relative to the two different turbulence models, have a small impact on the overall particle dispersion.

The evolution of the X-axis STD for the case of 60 m/s and 40 m/s, with low, medium and high LWC is shown in the next figures:

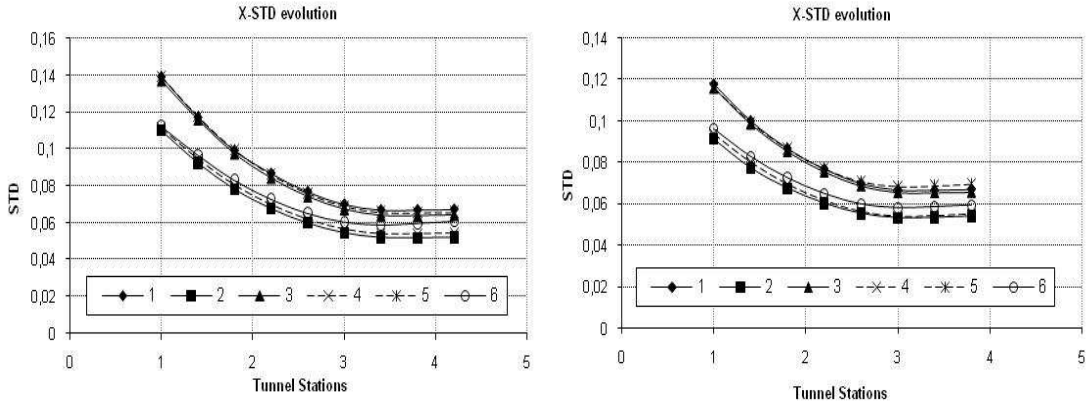

Figure 6-36 a, b: X-STD evolution 60 m/s (a) & 40 m/s (b) for High LWC (RSM)

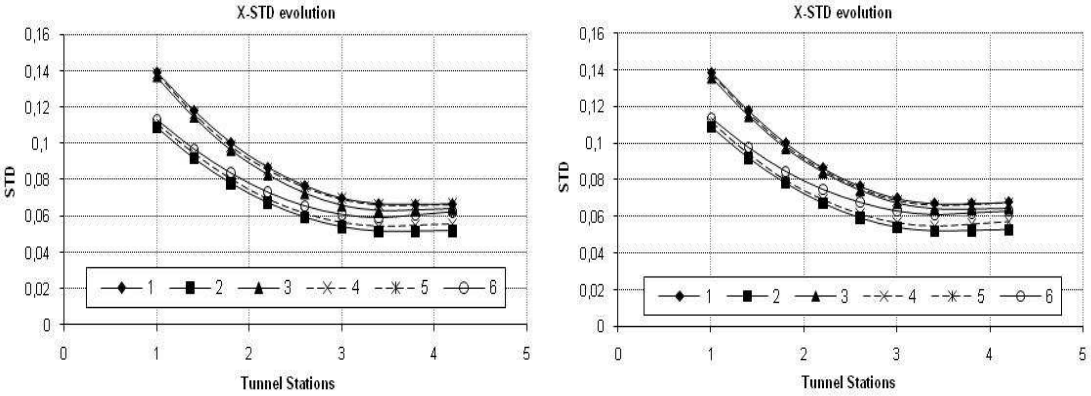

Figure 6-37 a, b: X-STD evolution 60 m/s (a) & 40 m/s (b) for Medium LWC (RSM)

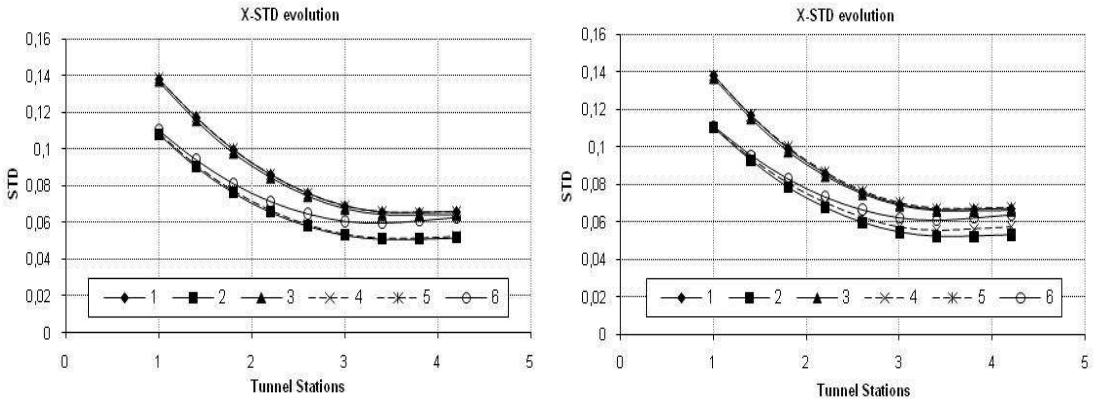

Figure 6-38 a, b: X-STD evolution 60 m/s (a) & 40 m/s (b) for Low LWC (RSM)

The evolution of the X-axis STD is mainly affected by the tunnel contraction ratio contribution and, though the variance of the X-axis fluctuations is higher for the RSM, his impact on the X-axis dispersion does not significantly affect the overall trend. As for the *k-ε* model, the trend is macroscopically the same for the three values of LWC (i.e.: nozzles air pressures) indicating that turbulence profile variations associated to the different choice of the nozzle air pressures does not produce significant impact on the particle dispersion when compared to the contraction ratio effect.

The overall Y-axis standard deviation of the cloud has been investigated in the plane located at the same position of *k-ε* model and it coincides with the experimental measurement plane. The cloud distribution characteristics, as standard deviation and location of the mean value, have been calculated for the reference velocity of 60 m/s and 40 m/s with the three values of LWC. The Y-axis mean peak location calculated with the RSM showed small differences with the position calculated with the k-e model. The difference percentage on the peak location, based on the ensemble of the realization with the three different air pressures, is shown in the next table:

Bars	40	60
1	0.477%	-0.275%
2	-0.632%	-0.625%
3	-7.66%	-1.971%
4	-0.331%	2.027%
5	-0.958%	-0.394%

6	0.577%	0.474%

Table 5: Difference % of the mean value for RSM and k-e

The difference between the model are bounded within 7% for 40 m/s and 1.9% for 60 m/s maximum values, both referring to the spray bar 3 location. In this case the RSM gives a prediction for the mean peak location slightly closer to the experimental measurement. However, such a small differences are close to the experimental uncertainty as well. The values of the standard deviation, normalized by the test section height (L), at the test section plane used in previous *k-ε* model and for different spray bars (1 to 6), velocities (40 m/s and 60 m/s) and nozzle air pressure (low, medium, high) are shown in the following figures (compared with experimental measurement):

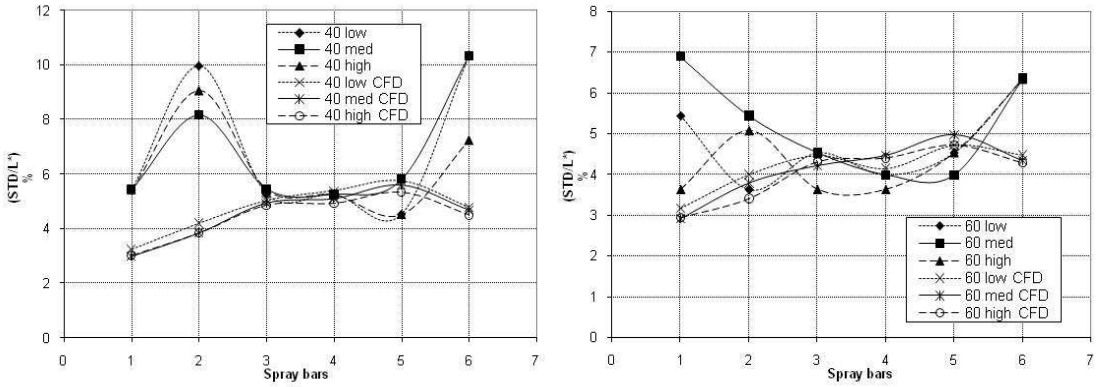

Figure 6-39 a, b: Y-axis normalized STD, 40 m/s (a), 60 m/s (b) (RSM)

The trend of the standard deviation for the Y-axis distribution in the test section is comparable with the ones obtained with the *k-ε* model and the accuracy of the RSM model is of the same order of the previous simulations. Also in this case the sensitivity of the model to the nozzles air pressures conditions reflects approximately in 1% difference in the STD as response to 2% difference of nozzles air pressure conditions. The differences of the STD respect to the one calculated with the *k-ε* model are shown in the following figure for the velocities of 60 m/s and 40 m/s:

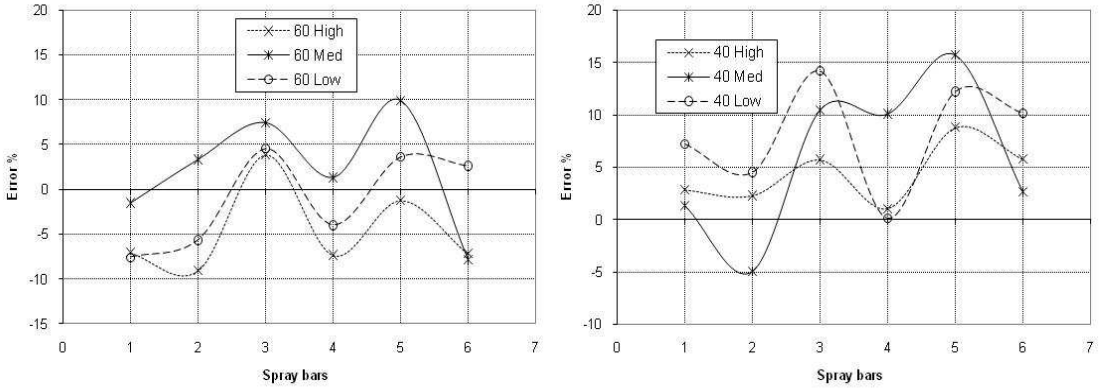

Figure 6-40 a, b: difference % between *k-ε* and RSM Y-axis STD (a) 60 m/s (b) 40 m/s

The relative difference between the two models are generally less than 10% for the 60 m/s case while reaches the peak around 15% for the 40 m/s condition. There is a general increase of the STD for the 40 m/s case while a more oscillating trend has been found for the 60 m/s case. However, these differences % between the solutions translate in length scales that are a maximum of 0.8 % of the test section length, with an average value around 0.4%, when calculated on the ensemble of all the spray bars.

The profile of the distribution along the X-axis has been calculated with the RSM, for the case of 40 m/s and presented in terms of LWC distribution, such as for the *k-ε* model. Results for each spray bar and three nozzles air pressures are presented in the following figures and compared with the experimental trend from bar 2 to bar 6:

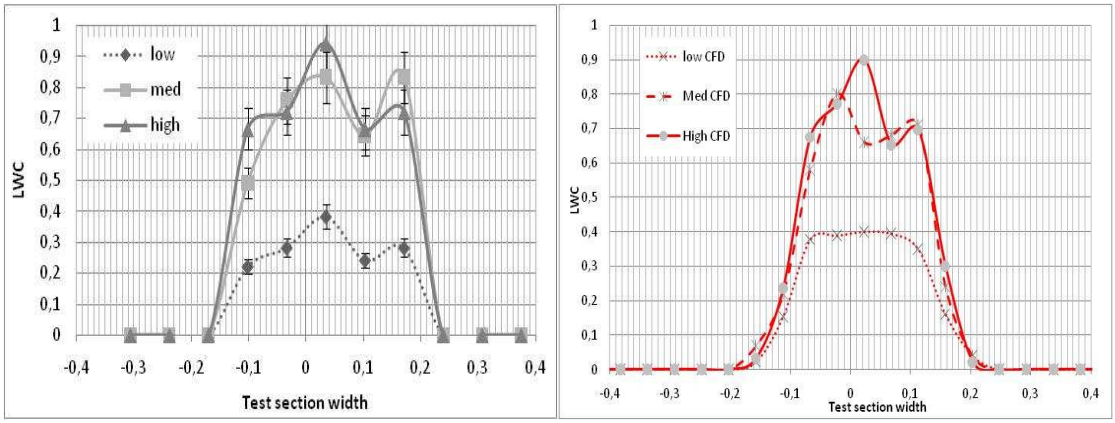

Figure 6-41 a, b: bar 2, X-axis distribution, experiment (a), CFD (b) (RSM)

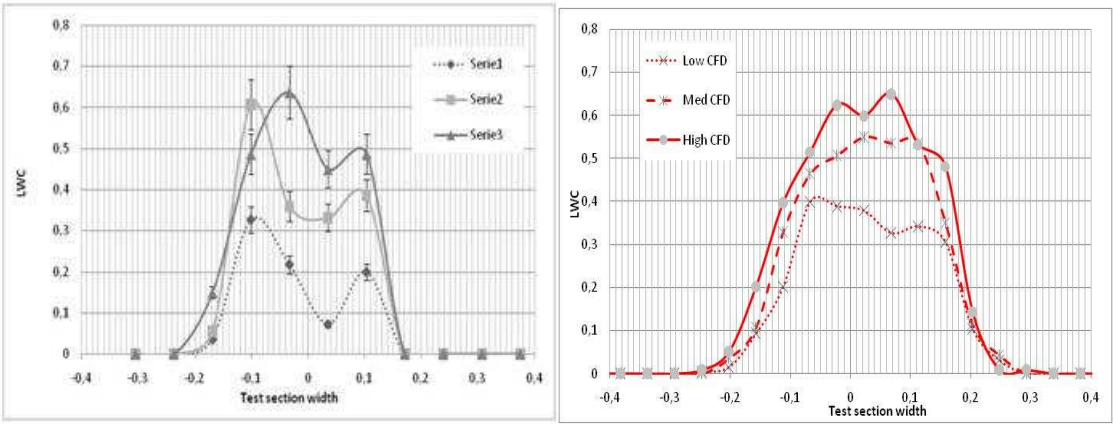

Figure 6-42 a, b: bar 3, X-axis distribution, experiment (a), CFD (b) (RSM)

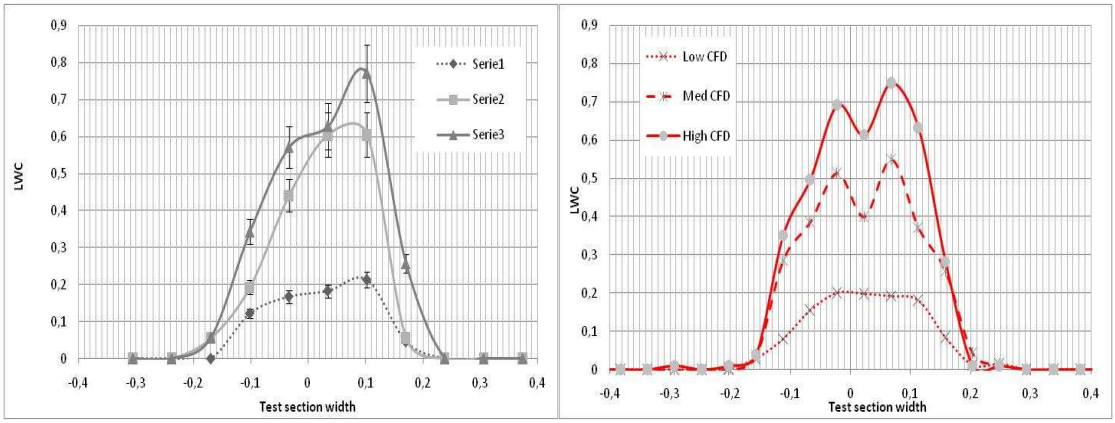

Figure 6-43 a, b: bar 4, X-axis distribution, experiment (a), CFD (b) (RSM)

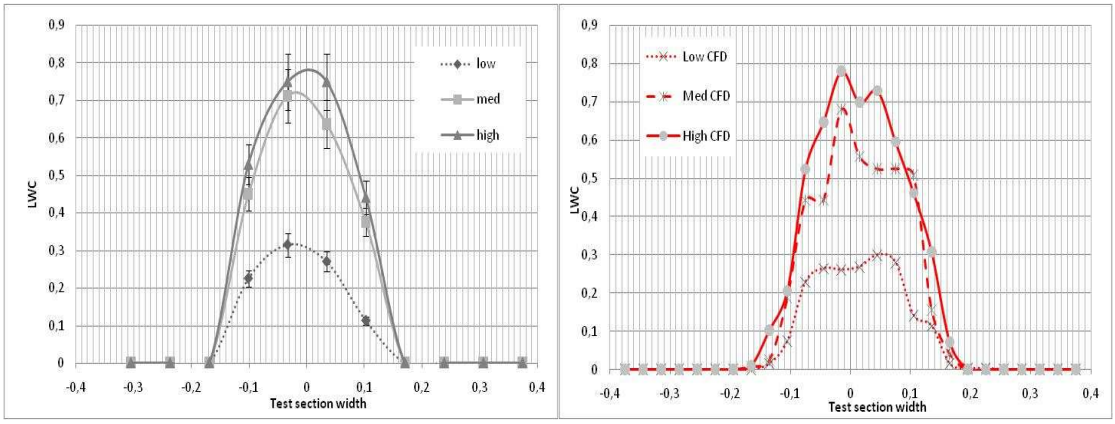

Figure 6-44 a, b: bar 5, X-axis distribution, experiment (a), CFD (b) (RSM)

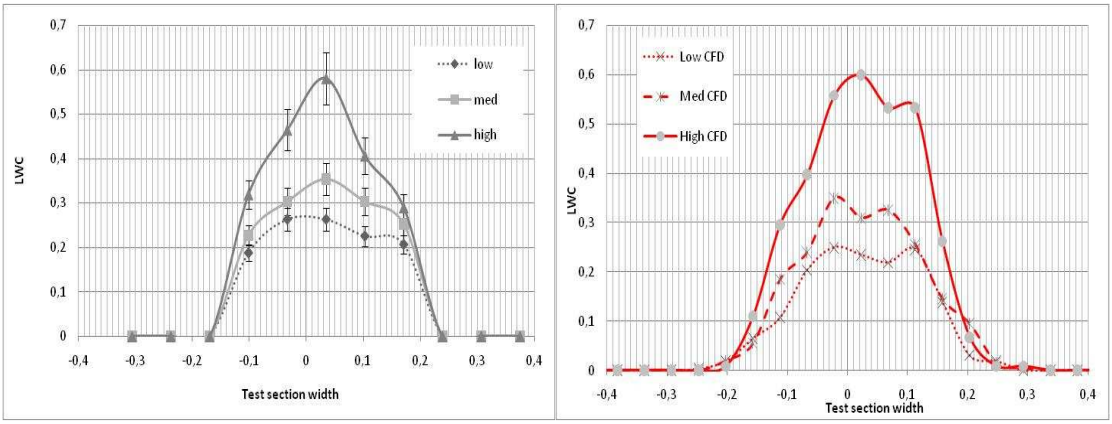

Figure 6-45 a, b: bar 6, X-axis distribution, experiment (a), CFD (b) (RSM)

The X-axis distribution calculated with the RSM performs well to approximate the experimental trend. The spread of the distribution is in close agreement with the experiment for all the spray bars and LWC cases. Compared to the *k-ε* solution, some differences arise in the shape of the distribution where the RSM describes peak with a higher X-axis resolution and generally approximate better the trend for the spray bars 5 and 6. However, within the stochastic nature of the water droplets dispersion, both the models provide good overall results for the X-axis water droplets distribution.

The behaviour of the simulated injection has been checked for the two values of the velocity, 40 m/s and 60 m/s, and for the three values of the nozzles air pressures. The calculated distribution, such as for the *k-ε* calculations, has been expressed in terms of frequency (Fr) of particles to be located at the interval (y, y+Δy), normalized by its maximum value (Fr max) and it is shown in the next figure:

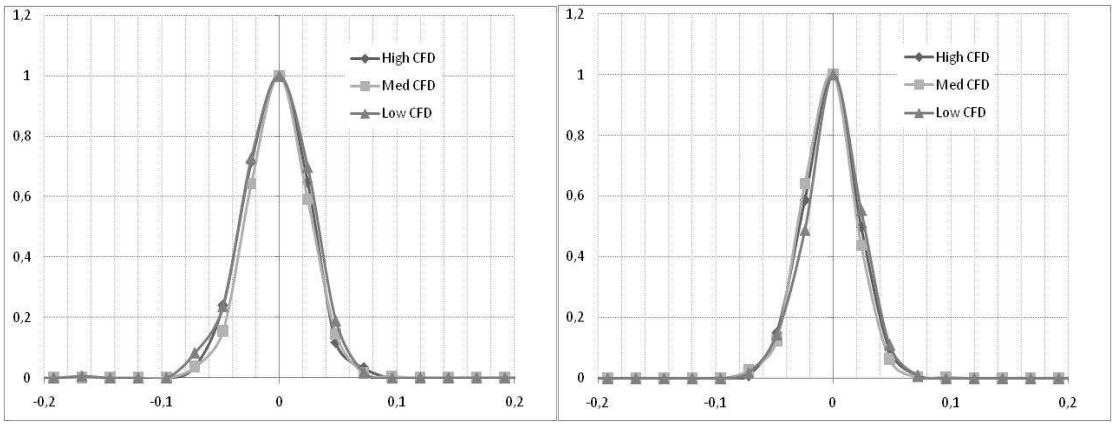

Figure 6-46 a, b: spray distribution, 40 m/s (a), 60 m/s (b)

The standard deviation of the distribution has been found to be around 2.8 cm for the 40 m/s case and 2.6 cm for the 60 m/s case. As for the *k-ε* model the relative difference between the velocities has been found to be consistent with the experimental trend with value around 10%. Small differences, compared to the *k-ε* model, have been found for the RSM calculation. Though the turbulent kinetic energy profile can evolve differently, at the input plane it has been chosen to be the same for the two model and only small differences (of few per cent) exist in the near nozzle region.

6.3.2 "File Injection" case

As in the previous simulations, the sensitivity to the injection type has been analysed comparing the results of the "single injection" with the "file injection" where the cloud characterization, in terms of droplets size distribution, has been kept the same as the *k-ε* simulations. Results have been obtained for the velocity conditions of 40 and 60 m/s and for the three values of the nozzle air pressures. The cloud evolution has been monitored at the same reference locations used previously for the "single injection" case. The results for the Y-axis standard deviation of the cloud distribution are shown in the next figures.

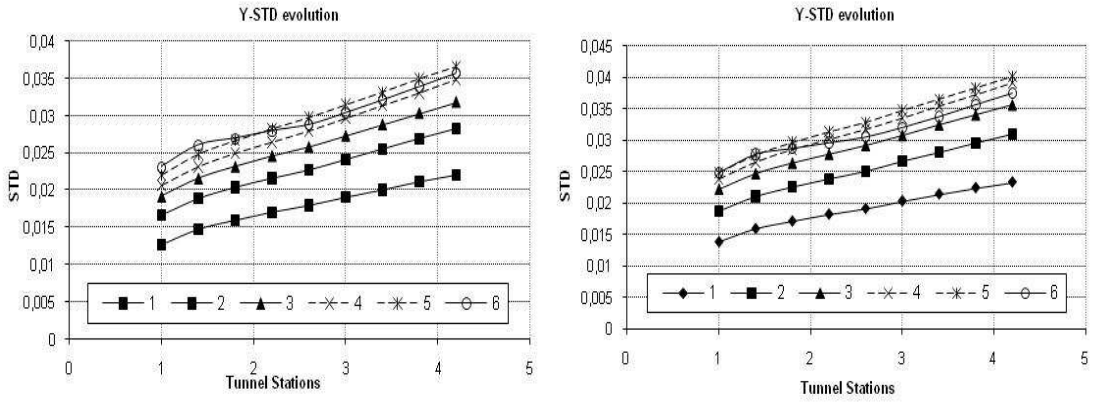

Figure 6-47 a, b: STD evolution 60 m/s (a) & 40 m/s (b) for High LWC (RSM file injection)

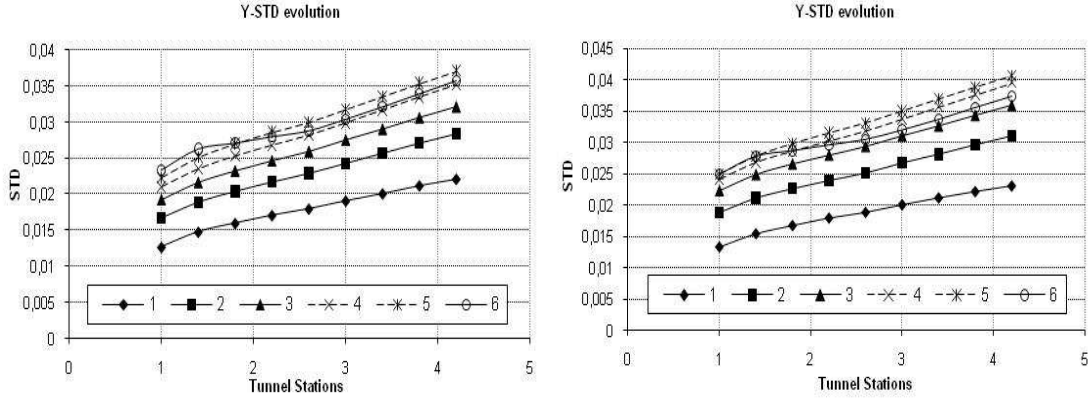

Figure 6-48 a, b: STD evolution 60 m/s (a) & 40 m/s (b) for Medium LWC (RSM file injection)

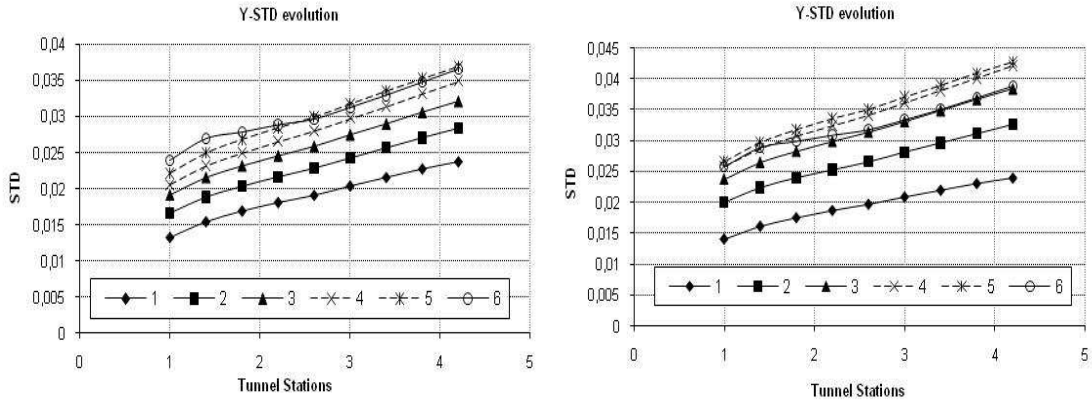

Figure 6-49 a, b: STD evolution 60 m/s (a) & 40 m/s (b) for low LWC (RSM file injection)

Also for the RSM the trend is similar to the one obtained with the "single injection" definition. The slightly divergent trend of the evolution along the tunnel axis is confirmed. The relative difference between the values of the standard deviation of the solutions of "file injection" and "single injection" has been found for the RSM to be less than 10%. The average difference, based on the ensemble of the local differences at the reference plane along the tunnel axis for each spray bars, is shown in next figures for the velocities of 40 and 60 m/s:

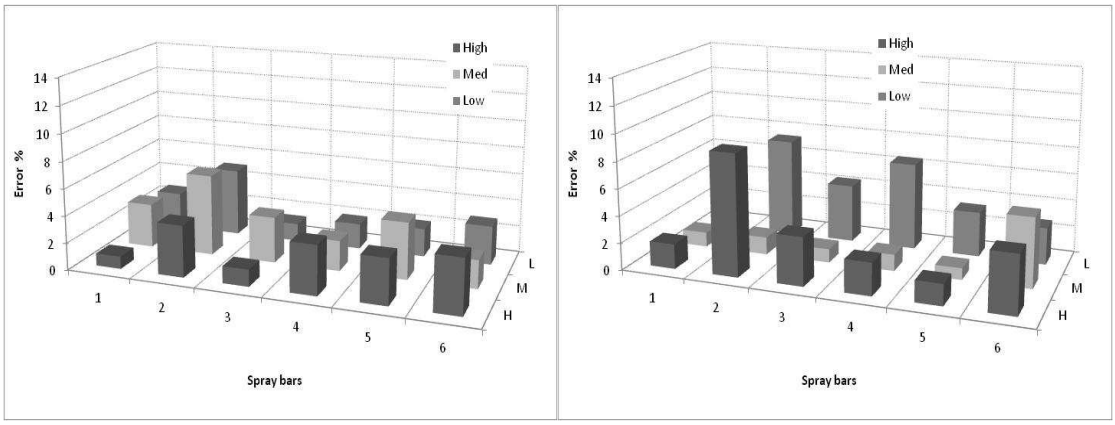

Figure 6-50 a, b: Y-STD error % between injection types, 40 m/s (a), 60 m/s (b) (RSM)

The difference between the models, as for the previous cases, appears to be randomly distributed with higher peaks present for the 60 m/s case. The average value can be estimated to be around 4% approximately for both the velocities case confirming that also for the RSM simulation not significant differences are experienced by the two injection types.

The trend of the X-axis standard deviation of the droplets distribution is shown in the next figures.

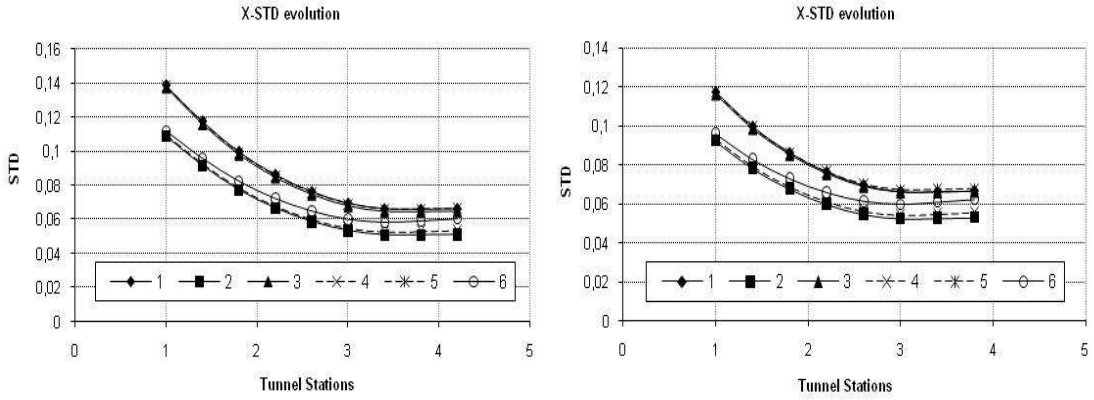

Figure 6-51 a, b: X-STD evolution 60 m/s (a) & 40 m/s (b) for High LWC (RSM file injection)

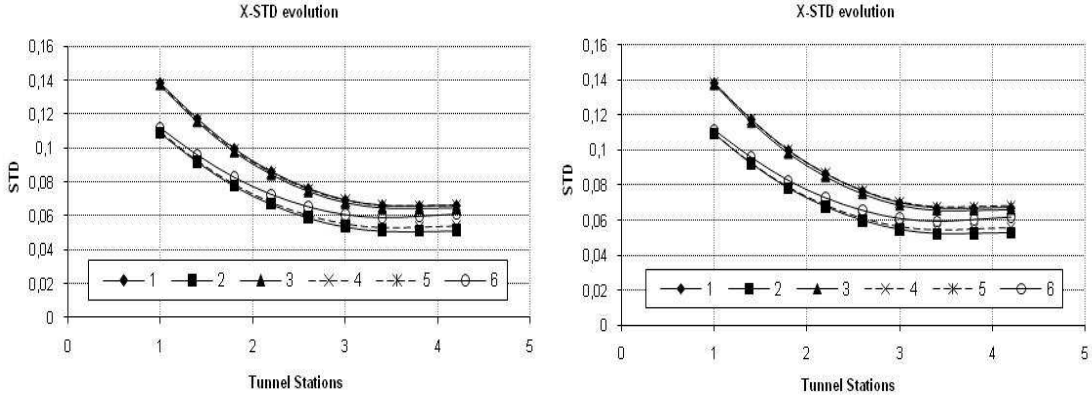

Figure 6-52 a, b: X-STD evolution 60 m/s (a) & 40 m/s (b) for Medium LWC (RSM file injection)

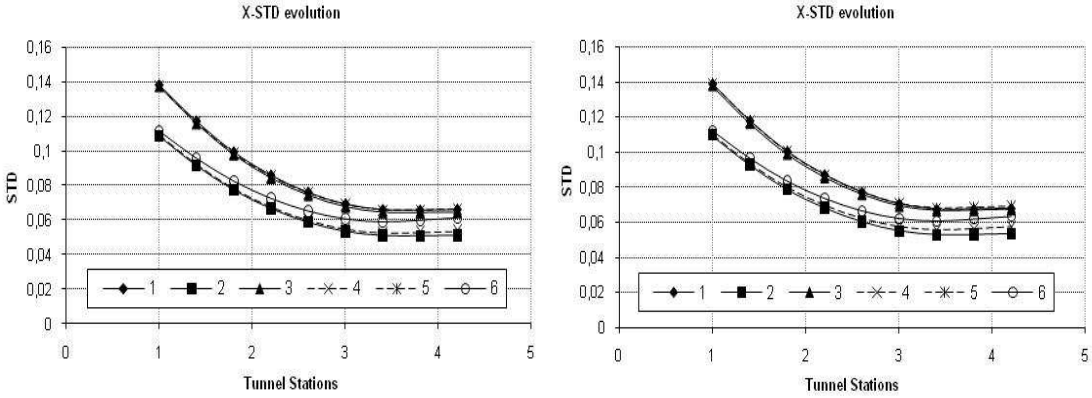

Figure 6-53 a, b: X-STD evolution 60 m/s (a) & 40 m/s (b) for Low LWC (RSM file injection)

The results show that no macroscopic differences exist between the trends calculated with the “single injection” and “file injection” types. The local differences are more associated to the random nature of the computation than to the different behaviour of the injections. The average values, based on the ensemble of the differences for the spray bars at the same reference location, are shown in the next figure for the velocities of 40 and 60 m/s.

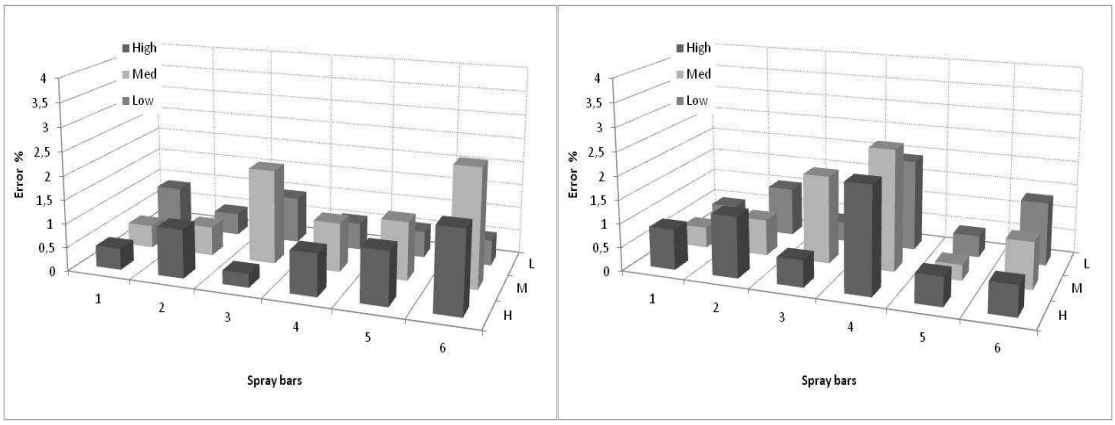

Figure 6-54 a, b: X-STD error % between injection types, 40 m/s (a), 60 m/s (b) (RSM)

The differences percentage for X-STD are lower that 2% being of the same order of the statistical uncertainty of the stochastic approach. Same result can then be assumed for both the injection types.

The results of the water distribution in the test section have been analyzed considering the Y-axis standard deviation for individual spray bars. Results are expressed in terms of standard deviation, normalized by the test section height (L), for spray bars 1 to 6, velocities of 40 m/s and 60 m/s and nozzle air pressure respectively low, medium and high. The Y-STD corresponding to the relative spray bar for the velocities of 40 and 60 m/s is shown in the next figure (compared with experimental measurement):

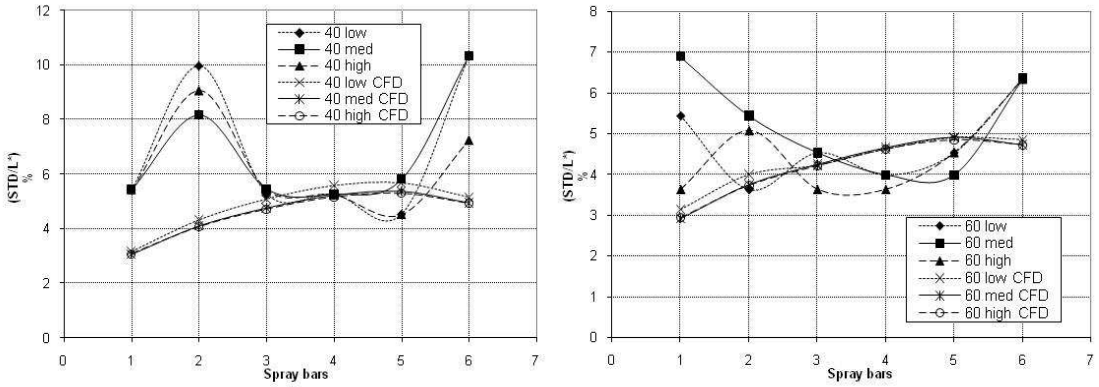

Figure 6-55 a, b: Y-axis normalized STD, 40 m/s (a), 60 m/s (b) (RSM file injection)

Also in this case the trend of the normalized standard deviation does not present significant differences if compared to the solution of the single injection case. The local difference compared to the solution of the RSM simulation and “single injection” is shown in the next figure for the both the velocity cases:

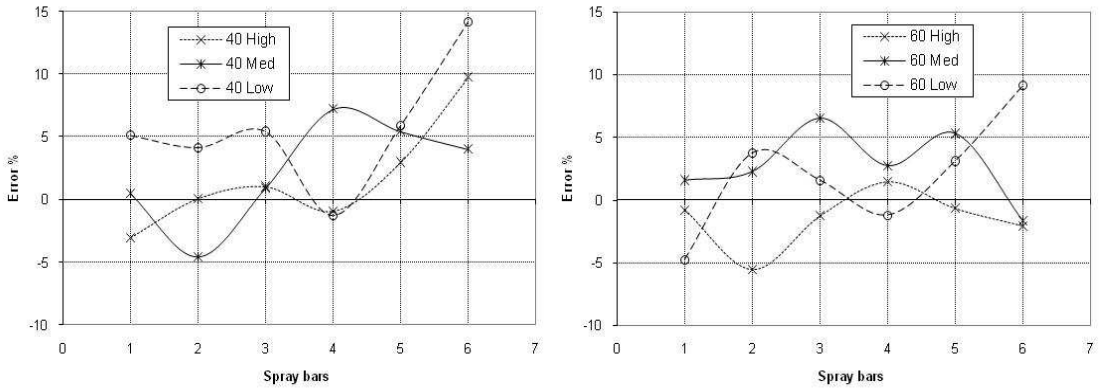

Figure 6-56 a, b: Y-STD relative error % between injection types 40 m/s (a), 60 m/s (b) (RSM)

The difference on the Y-STD is mainly around 5% for both the conditions of velocities with a peak close to 15% for the 40 m/s case. Such a relative differences can be considered negligible within the overall accuracy of the model for computation of particle trajectories and consequent dispersion. The average 5% difference on the normalized Y-STD reflects in a difference on cloud spread of about 0.4% of the characteristic test section length.

7 Discussion and Conclusion

7.1 Discussion on the methodology

This thesis presents a methodology to investigate and compute the water droplets distribution under condition and circumstances that are typically encountered in the Icing Tunnel environment.

7.1.1 Preliminary considerations on the flow regimes

In order to investigate which route should be followed to select the appropriate theoretical model to calculate the particle dispersion, a first analysis of the flow regimes has been done. This first process in the development of the methodology has been performed in parallel to the review of the existing theories concerning the discrete phase transport and turbulent dispersion. This is usually an iterative process. The overview of the discrete phase dispersion theories, generally applied to different research field as atmospheric research or combustion technologies, helps to identify the assumption used in the literature to build up those theories. At the same time the assumptions and the criteria that support them allow for selecting theories and models appropriate for the icing Tunnel case.

Once the criteria defining the way the flow field and the discrete phase interact each other have been identified, they should be applied to the local conditions characteristic of an Icing Tunnel. As shown in the chapter 2, criteria for particle-particle collision, particle-particle fluid dynamic interaction, one/two way coupling has been applied assuming a range of values for the variable characteristic of the Icing Tunnel environment. The Cranfield Icing Tunnel conditions did lie within that range. The result showed as the simplified version of the fluid particle interaction (one way coupling), without particle-particle interaction, can be used in the tunnel region sufficiently far from the near nozzle field. That region was identified, following the criteria, to be less than 50 cm from the injection point. This result showed that, though at a macroscopic point of view the Icing Tunnel fall within the dilute condition for particle loading, local regions can experience different regimes of loading.

This first process of the methodology would then allow for identifying the local flow regimes in the Icing Tunnel. Depending on those regimes the investigation would proceed selecting different approach or simplification for the local computation of particle dispersion. In this work has been chosen to not simulate the near nozzle field with a dedicated model but to describe the region with information coming from experiments.

7.1.2 Choice of numerical tools for engineering calculations

Once the flow regimes have been identified and the appropriate models to calculate the discrete phase dispersion have been selected, it is necessary to choose the numerical tools able to support the computation of the discrete phase motion. Because the numerical calculation are used, within the scope of this work, as possible support to icing test, the versatility of the numerical tools to reproduce different geometry and conditions with an user friendly capabilities should also be considered. As discussed in the chapter 3, while Direct Numerical Simulation and Large Eddy Simulation provide useful contribution on the scientific research on two phase flow, the Reynolds Average Navier-Stokes approach is still the common one for high Reynolds number flow encountered in Icing Tunnel case. This model has been used within this work.

In order to select the numerical codes, a preliminary investigation of the options available to numerically compute the discrete phase motion should be performed. The reason for this is that different numerical approaches, that satisfy the assumptions of the flow regimes, can be found. The first selection concerns the Eulerian or Lagrangian reference frame for discrete phase dispersion calculation. As has been discussed in the chapter 3, the overall condition of dilute loading of discrete phase typical of the Icing Tunnel allow for conveniently using the Lagrangian approach to calculate the discrete phase motion. In this case the particle motion is uncoupled with the carrier phase motion and the computation of trajectories can be done as post processing step. The injection of discrete phase can be performed within the computational domain specifying the injection characteristics of interest for the Icing Tunnel case as droplets size spectrum, water mass flow and injection velocity.

The discrete phase trajectory calculation has to include the effect of the turbulence on the estimation of the instantaneous carrier phase velocity fluctuation. The Stochastic Separated Flow approach is typically adopted within the RANS simulation, for this scope. The numerical code has to embody such a stochastic formulation. The selection of the stochastic model, whereas possible, should be based on the type of forces acting on the particle, details of the resolved turbulence field, isotropy of the flow and homogeneity of the flow. Within this work the only available model was the Discrete Random Walk implemented in Fluent.

7.1.3 Definition of flow details required for solution of Icing Tunnel case

When stochastic model are chosen for the estimation of the fluctuating component of the velocity, the solution of the turbulent field is required along the tunnel. This solution has to reproduce the real turbulent field encountered by the discrete phase along its trajectory. The calculation of the turbulence level in the tunnel has then to be linked to values of turbulence associated to the tunnel operating conditions under investigation. For the numerical calculation this aspect turns into a definition of an inlet turbulent profile that synthesizes the behaviour of the tunnel airflow. That profile would then be used to compute the turbulence solution along the tunnel by the numerical solver.

The characterization of the turbulent profile can be done with dedicated experiments. The choice of the location of the measurement plane should be related to the level of information that is required for the simulation. When the nozzle effects should be investigated the measurements should acquire such information. The main idea within this work was to investigate the effect of the nozzle sprays measuring the turbulence in a plane downwind the spray bars. This procedure would possible allow for obtaining a trend of the nozzles effect on the turbulence field versus the nozzle air pressures. For the small pressure differences object of this investigation a monotonic trend was not identifiable. The turbulence profiles acquired for each nozzle pressure condition have anyway been used to define the appropriate input condition required by the numerical solver.

The experimental procedure is, within this context, necessary to link the numerical model to the investigated case and to provide a description of the features necessary to properly characterize the flow field. The methods to perform the experiments and the level of details concerning those features are depending on the numerical methods that are going to be used thereafter and on the available experimental resources.

Experimental measurements are also required then to verify the numerical computation of the discrete phase dispersion. Discrete phase distribution profile, at defined conditions, can be used as test case. Within this work the acquisition of the profile has been done through the measurement of the ice shape along a defined profile (icing blade). This measurement is typically performed and easily implemented in Icing Tunnels for general test purposes. Also, validation of the near nozzle field description coming from a simplified numerical model should be performed in order to check the behaviour of the injection specification.

7.1.4 Calculation of the airflow solution and discrete phase dispersion with numerical tools

Once the numerical model has been set up and the input condition fully specified the solution of the carrier phase can be calculated. Depending on the interaction with the discrete phase the inter-phases exchange terms can be included during the calculation, whereas the numerical codes allows to do that. For Icing Tunnel application, with low volume fraction of droplets, the carrier phase solution can be computed without taking in account the contribution of the discrete phase. The carrier phase solution would provide the background for the calculation of the discrete phase trajectories.

In order to verify that the solution, corresponding to the chosen inlet condition, has been properly computed, a grid independence study should be performed. The choice of the variable to investigate is dependent to the local computational geometry and on the objective of the calculation. In relation of the Icing Tunnel case for computation of droplets dispersion the verification should concern the turbulence variables that would be used for trajectories calculation. The mean flow solution may also be

verified whereas the computational geometry would include elements which high geometrical complexity. Within this work the mean flow velocity has been found to be properly solved within the whole range of grid sizes tested. The turbulence variables have been chosen in relation to the turbulence model used within the solution of the carrier phase. The verification should be performed for any of the carrier phase solutions corresponding to different nozzle air pressures. However, it has been seen within this work that for small changes in nozzles air pressures, with consequent small changes in the turbulence profiles, the verification based on a baseline condition can be representative for the whole set of cases.

Once the solution of the carrier phase has been verified it would be possible to perform the discrete phase dispersion calculation. The carrier phase solution provides the background information about the flow field necessary for the calculation of discrete phase trajectories. The commercial codes provide automatic setting for the numerical accuracy related to the discrete phase trajectory calculation. The injection condition and the time scale constant can be changed or adjusted by the user. The original time scale constant in Fluent has been tuned to cover a range of application, whereas the proper value of the constant is still missing in the literature. Depending on the circumstances and conditions its value should be verified in order to be consistent with the characterization of turbulent quantities coming from the experiments. Within this work an additional verification of the impact of the constant on the model outcome has been done using the Snyder & Lumley experiment as benchmark.

7.2 Discussion on Cranfield Icing Tunnel simulations

Computational simulations of nozzle sprays in the Cranfield Icing Wind Tunnel at various conditions were conducted to apply and develop the methodology and to helping to understand the fluid physics associated with the test-section icing cloud.
The simulations have been solved with two different turbulence models for the carrier phase. As has been discussed in the chapter 3 the choice of the model in depending on the turbulence details required for the particle trajectories computation. In order to investigate the effects of the anisotropies, associated to the turbulence calculation and

affecting the discrete phase calculations, both the k-e models and RSM model have been used. The departure from isotropy of the turbulence solution may be affected by the tunnel geometry.

Both the solutions have to be able to represent the turbulent profile acquired with the experimental measurement. Within this work, it has been verified that the models reproduce the measured profiles, from the same inlet profile, with relative differences for turbulent quantities around 5%. The inlet profile has been kept the same and not re-adjusted for the RSM case.

The injection of water droplets has been done comparing two different injection types. The “single injection”, with droplets of the same size, represents an idealized configuration. It has the advantages to simplify the description of the injection, with consequent lower computational effort required for discrete phase trajectories calculations. In this work, it has been tested to verify its capabilities for Icing Tunnel application. To analyse the sensitivity of the droplets size spectrum on the discrete phase dispersion, a custom injection (“file injection”), containing information about the distribution function of the droplets size acquired with experiments, has been tested for the same condition of the “single injection”.

The computational droplet flux results at the test section were compared with measurements of the liquid water content taken at the same location with icing blade technique. For the spray clouds emanating from individual spray bar, comparisons of the computational and measured LWC results at the test section location indicate that the simulation does a reasonable job of tracking the size and location of individual nozzle clouds. The different input nozzles air pressures, low, medium and high, are recognized by the computational method, for the test cases chosen. They reflect the higher turbulence profile effects, during the decay period, near the spray bars, reproducing the nozzles presence in that region. This approach leads reasonable results, at least in situations where a superimposition of the separate contribution coming from nozzle and air turbulence can be applied.

Referring to the “single injection” both the k-e model and the RSM model provide similar trends of the water droplets distribution along the vertical and horizontal

directions in a plane normal to the tunnel axis. The effect of the different nozzle air pressures, of the order of 2%, for the values used during experimental measurements, have reflected, through different turbulence inlet profiles, in final STD differences less than 1% of the test section length. The level of the droplets dispersion prediction is close to the measurement but the trend with the spray bars cannot reproduce the local small effects. The accuracy of the models cannot catch higher gradient of the standard deviation, more than 2% of the test section length. The X-axis droplets dispersion trend along the tunnel axis is mainly affected by the X contraction that, for the Cranfield Icing Tunnel design, overcome the effect of the turbulent dispersion. The horizontal LWC distribution in the test section has been computed and compared to the experimental one. The CFD simulations perform a good result to reproduce the trend of the LWC distribution along the X–axis. Also in this case the two models perform quite close each other, with local differences of LWC distribution between experiments and simulations around 10%.

The local differences between the k-e and RSM models have been estimated. For the value of the mean position of the cloud the difference has been estimated to be around 7% for 40 m/s and 1.9% for 60 m/s maximum values, both concerning the spray bar 3 location. In this case the RSM gives a prediction for the mean peak location slightly closer to the experimental measurement. However, such a small differences are close to the experimental uncertainty as well. The relative difference between the two models in terms of standard deviation of the distribution instead is generally less than 10% for both the velocity conditions. There is a general increase of the STD for the 40 m/s case, respect the k-e model, while a more oscillating trend has been found for the 60 m/s case. However, these differences percentage between the solutions translate in length scales that are a maximum of 0.8 % of the test section length, with an average value around 0.4%, when calculated on the ensemble of all the spray bars. Concerning the horizontal distribution of the LWC the shape of the distribution the RSM describes peak with a higher X-axis resolution and generally approximate better the trend for the spray bars 5 and 6, characteristics of higher turbulence regions.

The custom “file injection” for both the k-e and RSM models has been used and investigated. Small relative differences on the solutions performed with the two injection types, with the same overall distribution predicted, have been found for both

the turbulence models. Relative errors of a fraction of the normalized standard deviation distribution indicate that the differences of the models produce not significant changes to improve the resolution of the cloud distribution on length scales proportional to the test section and then typically adopted during the tests. Local relative differences have been estimated to be on average less than 5% of the “single injection” baseline, both for the k-e model and the RSM model, which reflects in a difference on cloud spread of about 0.4% of the characteristic test section length.

The characterization of the near nozzle field, through the definition of a turbulence profile that would reflect the nozzle air pressures contribution to the turbulence, showed good result compared to the measurement of the jet spread. It has been verified an overall underestimation of the calculated standard deviation of the jet spread in the near nozzle field. However, those differences are less than 15% of the nozzle cloud indicating an overall good performance compared to the characteristic test section dimension.

7.3 Recommendations for future work

In order to improve the methodology and cover a wider range of possible icing tunnel operative conditions, as well as adding more specific procedures and methods to better describe additional physical process, some future works can be done following the same route. The very next steps in the methodology development can be summarized as follow:

- Considering the impact of the mean velocity profiles on the overall particle dispersion. Though it is reasonable to assume that the local streamline of a wind tunnel would follow the direction imposed by the tunnel wall geometry, a local description of the streamlines is necessary to include the effects of possible deviations. Local swirling regions and variation of the flow direction happening on length scale comparable to the tunnel diameter may be present in the Icing Wind Tunnel when operating close to the test section maximum speed. A characterization of the mean velocity vectors would then be useful to catch those phenomena. A measurement of the mean velocity components at

the input plane of the computational domain, similarly to the acquisition of the turbulence profile done within this work, may be used by the solver for computation of aerodynamic solution and droplet trajectory calculations. The FLUENT code allows for the specification of the velocity components at the boundary inlet plane.

- Considering different range of droplets sizes, especially including super cooled large droplets with diameter of the order of 100-200 microns. Droplets with higher inertia would help to identify the impact of the turbulence characterization, in terms of absolute values and details of the profiles, on the overall droplets dispersion. To validate the numerical simulations would be necessary to acquire droplets distribution in the test section corresponding to larger droplets size injection. The numerical simulation of the injection can be extended to larger droplets sizes for both the “single injection” and the “file injection” and used as done within this work.
- Considering the development of the inhomogeneity correction for droplets trajectories calculation within the Fluent code. Similar work has been done at the Paul Scherrer Institute for particles dispersion within bended pipes [78]. User Defined Function (UDF) have been written and included in the solver, as allowed by FLUENT. In the Icing Wind Tunnel case the main region of interest would be the bulk region of the tunnel and a simplified UDF may be used without additional and specific description of the boundary layer region.

REFERENCES

1. Gonsalez J.C. & Arrington E.A.: Aerodynamic calibration of the NASA Lewis icing research tunnel AIAA-98-0633
2. Gonsalez J.C. & Arrington E.A.: Aero-Thermal calibration of the NASA Glenn Icing Research Tunnel AIAA-2001-0233
3. Irvine T.B. & al.: Overview of the NASA Glenn icing research tunnel icing and flow quality improvements program AIAA-2001-0229
4. Gonsalez J.C. & Arrington E.A: 5-Hole flow angle probe calibration for the NASA Lewis icing research tunnel AIAA-96-2201
5. Ide R.F. & Oldenburg J.R.: Icing cloud calibration of the NASA Glenn icing research tunnel NASA/ TM2001-210689
6. Hinze, J. O. 1975. Turbulence (2nd Ed.) McGraw-Hill, New York
7. Tennekes
8. Pope S. B.: “Turbulent Flow”, Cambridge University press, 2000
9. Loth, E.: ”Numerical approach for motion of dispersed particles, droplets and bubbles”, Progress in Energy and Combustion Science 26 161-223, 2000
10. Stock DE.: Particle dispersion in flowing gases—Freeman scholar lecture. ASME Journal of Fluids Engineering 1996;118:4–17
11. Elghobashi, S. E., "On Predicting Particle-Laden Turbulent Flows," J. Applied Scientific Research, Vol. 52, 4, pp. 309-329 ,1994.
12. Elghobashi, S. E., and Truesdell, G. C., " On the two-way interaction between homogeneous turbulence and dispersed solid particles ; Part 1 : turbulence modification", Physics of Fluids, Vol. A5, pp. 1790-1801, 1993.
13. Eaton, J. K., and J. R. Fessler: Preferential concentration of particles by turbulence. *Int. J. Multiphase Flow,* **20,** 169–209 1994
14. Gore R. A., Crowe C. T. ; modulation of turbulence by a dispersed phase journal of fluids engineering , vol. 113, n^{o}2, pp. 304-307, 1991, american society of mechanical engineers, new york, NY
15. Taylor, G. I., Proceedings of the London Mathematical Society 20, 196, 1921

16. Shirolkar J.S et al.: Fundamental aspects of modeling turbulent particle dispersion in dilute flows, Prog. Energy Combust. Sci. vol. 22, pp. 363-399, 1996
17. Frenkiel, F. N., Etude statistique de la turbulence--fontions spectrales et coefficients de correlation, Rapport Technique, ONERA No. 34 ,1948.
18. Oesterle
19. Kampe de Feriet, J., Annal. Soc. Sci. Bruxelles 159, 145, 1939
20. Venkatram, A., Atmospheric Environment 22 (5), 865 ,1988
21. Yeung P.K.: LAGRANGIAN INVESTIGATIONS OF TURBULENCE, Annu. Rev. Fluid Mech, 34:115–42, 2002
22. Wang L.P. Stock D.E.: Dispersion of heavy particles by turbulent motion, American meteorological society , 1897, 1993
23. Yudine M.I.: Physical Considerations on Heavy-particle Diffusion, Advances in Geophysics, Volume 6, p.185, Published by Academic Press, Inc., New York, USA, 1959
24. Sato Y.,Yamamoto K. : Lagrangian measurement of fluid-particle motion in an isotropic turbulent field, Journal of Fluid Mechanics, **175**:183-199 Cambridge University Press, 1987
25. Wells MR, Stock DE. The effects of crossing trajectories on the dispersion of particles in a turbulent flow. Journal of Fluid Mechanics ;136:31–62, 1983
26. Loth E, Stedl J. Taylor and Lagrangian Correlations in a turbulent free shear layer. Experiments in Fluids ;26:1–6, 1999
27. Elghobashi S, Truesdell GC. Direct simulation of particle dispersion in a decaying isotropic turbulence. Journal of Fluid Mechanics; 242:655–700, 1984
28. Crowe T.C.: Multiphase flow handbook
29. Maxey, m. R. & Riley, j. J. Equation of motion of a small rigid sphere in a non-unifo flow. Phys. Fluids 26, 833-889, 1983.
30. Clift R, Grace JR, Weber ME. Bubbles, drops and particles, New York: Academic Press, 1978
31. S. A. Morsi and A. J. Alexander, ``An investigation of particle trajectories in two-phase flow systems", *J. Fluid Mech.*, **55**, 193-208 ,1972.
32. Fluent User Manual

33. Piomelli U. Introduction to the modeling of turbulence: large Eddy and direct simulation of turbulent flows. von Karman Institute for Fluid Dynamics, Lecture Series 1997-03, March 1997.
34. Piomelli U.: Introduction to the modeling of turbulence: largeEddy and direct simulation of turbulent flows. von Karman Institute for Fluid Dynamics, Lecture Series 1997-03, March 1997
35. Moin P. : Progress in large eddy simulation of turbulent flows. AIAA Aerospace Sciences Meeting, Reno, NV, AIAA-97-0749, 1997
36. Vandromme D. Introduction to the modeling of turbulence: turbulence modeling for compressible flows and acoustics. von Karman Institute for Fluid Dynamics, Lecture Series 1997-03, March 1997
37. Loth E. : Particles, drops and bubbles: fluid dynamics and numerical methods, Cambridge University Press, expected publication 2010
38. Wilcox D.C.: Turbulence modeling for CFD , La Canada, CA: DCW Industries, Inc , 1993
39. Baxter, L. L., Ph.D. Dissertation, Brigham Young University, Provo, Utah (1989).
40. Faeth, G. M., Proc. ASE-JSME Therm. Engng. Conf. 2, 517 (1983)
41. Gosman, A.D., Ioannides, E., 1981. Aspects of computer simulation of liquid-fueled combustors. 19th Aerospace Science Meeting, St Louis, MO, AIAA Paper 81-0323]
42. Graham, D.I., 1996. An improved eddy interaction model for numerical simulation of turbulent particle dispersion. ASME Journal of Fluids Engineering 118, 819 823
43. MacInnes, J.M., Bracco, F.V., 1992. Stochastic particle dispersion modeling and the tracer-particle limit. Physics of Fluids A 4, 2809 2824
44. Sawford B.L.: J. Climate Appl. Met. 24, 1152, 1987 Durbin P. A.: Phys. Fluids 23, 2151,1980)
45. Gardiner C. W. Handbook of Stochastic Methods for Physics, Chemistry, and the Natural Sciences, 2nd ed. (Springer-Verlag, Berlin, 1990)
46. Csanady, G.T., 1963. Turbulent diffusion of heavy particles in the atmosphere. Journal of Atmospheric Science 20, 201 208

47. Berlemont, A., Desjonqueres, P., Gouesbet, G., 1990. Particle Lagrangian simulation in turbulent flows. International Journal of Multiphase Flow 16, 19 34
48. Burry, D., Bergeles, G., 1993. Dispersion of particles in anisotropic turbulent flows. International Journal of Multiphase Flow 19, 651 664
49. Zhou, Q., Leschziner, M.A., 1991. A Lagrangian particle dispersion model based on a time-correlated stochastic approach. In: Gas Solid Flows, ASME FED Vol. 121, 255±260
50. Minier, J-P., Simonin, O. 1992. A numerical approach to cyclone separators. Report no. HE-44/92.02, ElectriciteÂ de France, Chatou]
51. Lu, Q.Q., Fontaine, J.R., Aubertin, G., 1993. A Lagrangian model for solid particles in turbulent flows. International Journal of Multiphase Flow 19, 347±367
52. Pozorski J., Minier J.P.: On the Lagrangian turbulent dispersion models based on the Langevin equation, International Journal of Multiphase Flow 24 (1998) 913 945
53. Bocksell T.L, Loth E. : Stochastic modeling of particle diffusion in a turbulent boundary layer, Int. J. Multiphase Flow **32**, pp. 1234–1253, 2006
54. Strutt H.C., Lightstone M.F.: Analysis of tracer particle migration in inhomogeneous turbulence, International Journal of Heat and Mass Transfer 49 2557–2566, 2006
55. J.S. Shuen, L.-D. Chen, G.M. Faeth, Evaluation of a stochastic model of particle dispersion in a turbulent round jet, AIChE Journal 29 (1983)
56. X.Q. Chen, Heavy particle dispersion in inhomogeneous, anisotropic, turbulence flows, International Journal of Multiphase Flow 26 (2000)
57. Snyder, W. H., and Lumley, J. L.: Some measurement of particle velocity autocorrelation functions in a turbulent flow, J. Fluid Mechanics, 48:41 (1971)
58. Robert F. Ide : Comparison of Liquid Water Content Measurement Techniques in an Icing Wind Tunnel, U.S. Army Research Laboratory, Glenn Research Center, Cleveland, Ohio,1999
59. U.S. Patent, patent number 4,890,494, Jan 02 1990
60. Gent R.W., Ford J.M., Moser R.J.: Results from super-cooled large droplet mass loss tests in the act luton icing wind tunnel, 41st aerospace sciences meeting and exhibit 6-9 January 2003, Reno, Nevada

61. Lekakis I.: Calibration and signal interpretation for single and multiple hot-wire/hot-film probes, Meas. Sci. Technol. 7, 1313–1333. Printed in the UK, 1996
62. Cheesewright R 1972 The application of digital techniques to hot-wire anemometry in highly turbulent flows Proc. DISA ConJ of Fluid Dyn. Meas. in the Indust. And Medical Eno. (Leicester University: University Press) Paper I1
63. Bruun H.H., Tropea C.: The calibration of inclined hot-wire probes, J. Phys. E: Sci. Instrum., Vol. 18, 1985. Printed in Great Britain
64. Bruun H H 1971b Linearization and hot-wire anemometry J. Phys. E: Sci. Instrum. **4** 8 15-20
65. Bruun H H 1976 A note on static and dynamic calibration of constant-temperature hot-wire probes J. Fluid Mech. **16** 154-5
66. BIPM, IEC, IFCC, ISO, IUPAC, IUPAP, OIML. Guide to the Expression of Uncertainty in Measurement. International Organisation for Standardization, Geneva, Switzerland. ISBN 92-67-10188-9, First Edition 1993
67. Finn E. Jørgensen: How to measure turbulence with hot-wire anemometers - a practical guide, Dantec Dynamics 2002
68. Bendat J.S., Piersol A.G. : Random Data Analysis and Measurement Procedures, Measurement Science and Technology, Vol 11 1825, 1999
69. Bruun H. H.: “Hot wire anemometry: Principles and signal analysis” Oxford University Press, 1995
70. Bradshaw, P.: Introduction to turbulence and its measurement
71. Glenn Howard: private communication
72. Batchelor, G. K. : “The theory of homogeneous turbulence”, Cambridge Press, 1956
73. Stern F. & al: Comprehensive Approach to Verification and Validation of CFD Simulations—Part 1: Methodology and Procedures, Journal of Fluids Engineering, vol. 123, December 2001,
74. Roache P.J.: Verification and validation in computational science and engineering, Hermosa Publishers, Albuquerque, NM , 1998.
75. Ismail B. C. : Procedure for Estimation and Reporting of Discretization Error in CFD Applications, Journal of Fluids Engineering Editorial Policy Statement on the Control of Numerical Accuracy

76. P.J. Roache, Perspective: a method for uniform reporting of grid refinement studies, J. Fluids Eng. 116 (1994) 405–413.
77. Bocksell T.L., Loth E. : “Random walk models for particle diffusion in free-shear flow”, AIAA Journal, Vol 39, No 6, June 2001
78. Dehby A.: Turbulent particle dispersion in arbitrary wall-bounded geometries: A coupled CFD-Langevin-equation based approach, International Journal of Multiphase Flow 34 (2008) 819–828
79. Gardiner C.W.: Handbook of stochastic methods for physics, chemistry, and the natural sciences, 3rd edition, Springer-Verlag, 2004
80. D.J. Thomson, Criteria for the selection of stochastic models of particle trajectories in turbulent flows. J. Fluid Mech. 180 (1987), pp. 529–556
81. Gillespie D.T.: Markov processes: An introduction for Physical Scientists – Academic Press, San Diego CA, 1992, 565 pp.